Autonomous Navigation for Satellite Formations

Advancing Missions Beyond Earth with Inter-satellite Radio Tracking

Turan, E.

DOI
10.4233/uuid:8b825b8d-7b3b-442b-bacd-19982f239058

Publication date
2024

Document Version
Final published version

Citation (APA)
Turan, E. (2024). *Autonomous Navigation for Satellite Formations: Advancing Missions Beyond Earth with Inter-satellite Radio Tracking*. [Dissertation (TU Delft), Delft University of Technology].
https://doi.org/10.4233/uuid:8b825b8d-7b3b-442b-bacd-19982f239058

AUTONOMOUS NAVIGATION FOR SATELLITE FORMATIONS

ADVANCING MISSIONS BEYOND EARTH WITH INTER-SATELLITE RADIO TRACKING

AUTONOMOUS NAVIGATION FOR SATELLITE FORMATIONS

ADVANCING MISSIONS BEYOND EARTH WITH INTER-SATELLITE RADIO TRACKING

Dissertation

for the purpose of obtaining the degree of doctor
at Delft University of Technology
by the authority of the Rector Magnificus prof. dr. ir. T.H.J.J. van der Hagen
Chair of the Board for Doctorates
to be defended publicly on
Monday 23 September 2024 at 17:30 o'clock

by

Erdem TURAN

Master of Science in Defense Technologies
Istanbul Technical University, Türkiye
born in Çorlu, Türkiye.

This dissertation has been approved by the promotors:

promotor: Prof. dr. E.K.A. Gill
copromotor: Dr. S. Speretta

Composition of the doctoral committee:

Rector Magnificus,	chairperson
Prof. dr. E.K.A. Gill,	Delft University of Technology, promotor
Dr. S. Speretta,	Delft University of Technology, copromotor

Independent members:

Prof. dr. L.L.A. Vermeersen,	Delft University of Technology
Prof. dr.ir. A.J. van der Veen,	Delft University of Technology
Prof. dr. M. Lavagna,	Politecnico di Milano
Prof. dr. C. McInnes,	University of Glasgow
Dr. J. Daşdemir,	University of Twente

This research was funded by the Ministry of National Education, Türkiye.

Keywords: Autonomous Navigation, Orbit Determination, Inter-satellite Link, Satellite-to-Satellite Tracking, Satellite Formations, Autonomous Operations

İstikbal göklerdedir.
The future is in the skies.

Mustafa Kemal Atatürk

CONTENTS

SUMMARY

Over recent years, there has been a growing interest in deep space missions involving small satellites. These missions have not only demonstrated their potential through remarkable achievements but have also spotlighted the critical role they will play in future space explorations. Simultaneously, satellite formations have gained popularity, opening up new possibilities for deep space exploration. Traditionally, these missions have relied heavily on ground-based radiometric tracking for navigation. However, ground-based operations pose several challenges, including limited tracking resources due to the increasing number of missions, and high operational costs. In response to these challenges, autonomous operations, with minimal or no human intervention, emerge as a beneficial strategy, and navigation stands as a key area that could greatly benefit from autonomous operations.

In this context, various autonomous navigation strategies exist, and one of them stands out as a promising approach: Crosslink navigation, using existing systems to provide navigation solutions based on inter-satellite measurements, which primarily offers relative navigation solutions but can also facilitate absolute navigation solutions when integrated with ground-based tracking. However, absolute state knowledge, crucial for tasks such as station-keeping, often relies on ground-based commands, limiting autonomy. Alternatively, Satellite-to-Satellite Tracking (SST) data can be used for absolute state estimation, where an on-board navigation filter estimates spacecraft position and velocity, i.e. with respect to a fixed reference frame. Previous studies have shown that depending on the orbital dynamics, SST-data can provide absolute state estimation. In other words, differences in accelerations of multiple spacecraft due to their motion in a non-homogeneous gravity field over time provide absolute navigation solutions in the SST-based Orbit Determination (OD) problem. However, this is not always straightforward, especially when inter-satellite measurements are not accurate, or the observation geometry is not optimal. Since inter-satellite measurements cannot always be collected due to operational constraints, careful planning of optimal tracking windows is required. This planning can be challenging when considering possibly conflicting operational needs, such as commanding. Moreover, since radio frequency measurement techniques are used to derive navigation data, system performances must be investigated, considering varying systematic and random errors. It remained a significant challenge to determine which types of navigation data—range, range-rate, or angle—yield the most effective navigation solutions across different deep space scenarios. Since real-time navigation solutions may be needed, designing a robust on-board estimation filter can be challenging, including decisions on which parameters to be estimated or neglected.

Given these complexities, this research investigated SST-based autonomous OD for satellite formations, consisting of small spacecraft, aiming to enhance current methodologies and explore new capabilities in both cislunar and deep space environments.

An analysis of 65 proposed missions, mainly targeting cislunar space and small celestial bodies for surface mapping and characterization purposes, revealed a predominant reliance on ground-based navigation, with only a few choosing autonomous methods. Diving into various deep space navigation techniques suitable for small satellites, such as optical, X-ray pulsar, and crosslink navigation, the dissertation detailed their operational principles and common error sources. A comprehensive categorization is provided for deep space navigation from data-collection, autonomy, and methods perspectives, including their advantages, disadvantages, and mission examples. Following that, the focus shifted to crosslink radiometric navigation using existing onboard communication systems, which can be adapted directly onto current missions. The survey results indicated that a majority of missions (>%58) utilize inter-satellite communication, with a significant portion able to benefit from autonomous crosslink radiometric navigation. Particularly effective around small bodies, in cislunar space and around Lagrangian points, this method can achieve remarkable accuracy within tens to hundreds of meters and millimeter per second in position and velocity, reducing navigation errors, complexity, and overall mission costs. Autonomy in this context opens possibilities for missions where direct communication with Earth is impractical.

The study subsequently focused on examining simple ranging algorithms, supported by a detailed review of the existing literature, due to the fact that the range data type provides marginally superior navigation solutions compared to other observational data types, specifically in cislunar space. This dissertation presents an extensive review of SST ranging methods, including their performance characteristics such as link budget, measurement error budgets, and error models. A crucial finding of this research was the importance of a simple yet reliable ranging method, especially considering the limitations in communication power available for small satellites. Consequently, the study investigated the data-aided ranging method, eliminating the need for separate ranging signals in the communication chain, offering a simplified approach over traditional ranging methods. Subsequently, the ranging performance was thoroughly examined, presenting that at high data rates, telemetry and telecommand signals could effectively substitute traditional ranging methods in SST. Furthermore, at lower data rates e.g., $< 10\,\text{kbps}$, data-aided ranging solutions are still sufficient to meet the majority of navigational needs for small satellite operations in deep space.

The fundamental aspects of SST-based autonomous on-board OD systems demand a comprehensive understanding of spacecraft dynamics, observation geometry, and tracking windows. This research has examined these aspects using a variety of performance metrics and methods, such as observability, Cramér-Rao Lower Bound (CRLB), Monte-Carlo, Covariance analysis, although it has become evident that no single metric universally applies to every scenario. Consequently, this dissertation has introduced and detailed specific metrics tailored to the research objectives, detailing their advantages, disadvantages, and implementation challenges. Using these metrics, a semi-analytical observability and covariance analysis was provided, along with a detailed performance analysis.

It was found that distinct spacecraft dynamics and optimized observation geometry enhance OD performance. Relying on overly simplified dynamic models may not suffice for accurate on-board system operation. Incorporating comprehensive models that ac-

count for all relevant perturbations can enhance system observability and, thus, estimation accuracy. Contrary to expectations, the measurement aspects, though crucial, exert a minimal impact on system performance compared to the orbital dynamics. Satellite formations in cislunar space are found to be less sensitive to measurement inaccuracies than observation geometry. For instance, the study of SST with a lunar orbiter demonstrated that even less accurate measurements could meet navigation requirements, e.g., $\sigma_r = 10\,\text{km}$ and $\sigma_v = 10\,\text{cm/s}$, supporting the use of simple data-aided ranging methods in such scenarios. This implies that desired OD performance can be achieved through meticulous planning of observation geometry or the on-board navigation filter, despite measurement inaccuracies. It has been shown that Lunar satellite network topologies, whether mesh or centralized consisting of three or more satellites, generally achieve the greatest benefit from autonomous navigation systems when they feature long inter-satellite links and short orbital periods. The integration of additional satellites to lunar network topologies is found to be effective in enhancing overall system performance.

Another vital aspect addressed was systematic errors. The analysis presented the necessity of either estimating or considering biases in the navigation filter, as neglecting these could lead to significant inaccuracies. It was found that, in cislunar space, consider filtering is more suitable for Halo / Halo formations, while estimating is preferable for Halo / Lunar formations, depending on mission configuration. It was also found that measurement bias has an impact on the optimal tracking windows. Additionally, the research explored observation data types, revealing that the suitability of a particular data type for navigation depends heavily on the mission profile. Generally, range observations were found to offer better performance compared to range-rate and angle data. Thresholds for these observations were also established, providing guidance on focusing on certain navigation data types based on the mission's specific requirements and profile. Various filtering techniques were investigated for their performance capabilities and complexities. A significant difference was not observed between different filtering techniques within the simplified dynamics, though advanced filters have shown improved performance in dealing with non-linearity around small solar system bodies.

As crucial as previous elements, the research addressed operational aspects, highlighting the critical role of optimal tracking windows, discussing on-board and off-board tracking strategies, and presenting an on-board data flow for error analysis and implementation, able to guide future mission design and operational planning of satellite formations in deep space.

SAMENVATTING

De afgelopen jaren is er een groeiende belangstelling ontstaan voor missies in de diepe ruimte met kleine satellieten. Deze missies hebben niet alleen hun potentieel aangetoond door opmerkelijke prestaties, maar hebben ook de cruciale rol benadrukt die ze zullen spelen bij toekomstige ruimteverkenningen. Tegelijkertijd hebben satellietformaties aan populariteit gewonnen, waardoor nieuwe mogelijkheden voor diepe ruimteverkenning ontstaan. Van oudsher waren deze missies voor navigatie sterk afhankelijk van radiometrische tracking op de grond. Operaties vanaf de grond brengen echter verschillende uitdagingen met zich mee, waaronder beperkte trackingmiddelen als gevolg van het toenemende aantal missies, en hoge operationele kosten. Als reactie op deze uitdagingen komen autonome operaties, met minimale of geen menselijke tussenkomst, naar voren als een nuttige strategie, en navigatie is een belangrijk onderdeel dat enorm zou kunnen profiteren van autonome operaties.

In deze context bestaan er verschillende autonome navigatiestrategieën, en één ervan springt eruit als een veelbelovende aanpak: Crosslink-navigatie, waarbij bestaande systemen worden gebruikt om navigatie-oplossingen te bieden op basis van intersatellietmetingen. Deze metingen bieden in de eerste plaats relatieve navigatie-oplossingen, maar kunnen ook absolute navigatie vergemakkelijken wanneer tracking op de grond geïntegreerd is. Absolute toestandskennis, die van cruciaal belang is voor taken als het bijhouden van stations, is echter vaak afhankelijk van instructies van de grond, waardoor de autonomie wordt beperkt. Als alternatief kunnen Satellite-to-Satellite Tracking (SST)-gegevens worden gebruikt voor het schatten van de absolute toestand, waarbij een navigatiefilter aan boord de positie en snelheid van het ruimtevaartuig schat, dat wil zeggen met betrekking tot een vast referentieframe. Eerdere studies hebben aangetoond dat SST-gegevens, afhankelijk van de orbitale dynamiek, een absolute toestandsschatting kunnen opleveren. Met andere woorden, verschillen in versnellingen van meerdere ruimtevaartuigen als gevolg van hun beweging in een niet-homogeen zwaartekrachtveld in de loop van de tijd bieden absolute navigatie-oplossingen in het op SST gebaseerde Orbit Determination (OD) vraagstuk. Dit is echter niet altijd eenvoudig, vooral wanneer metingen tussen satellieten niet nauwkeurig zijn of de observatiegeometrie niet optimaal is. Omdat metingen tussen satellieten niet altijd kunnen worden verzameld vanwege operationele beperkingen, is een zorgvuldige planning van optimale volginterval vereist. Deze planning kan een uitdaging zijn bij het overwegen van mogelijk tegenstrijdige operationele behoeften, zoals besturing. Omdat bovendien radiofrequentiemeettechnieken worden gebruikt om navigatiegegevens af te leiden, moeten de systeemprestaties worden onderzocht, waarbij rekening moet worden gehouden met variërende systematische en willekeurige fouten. Het bleef een grote uitdaging om te bepalen welke soorten navigatiegegevens (bereik, bereiksnelheid of hoek) de meest effectieve navigatieoplossingen opleveren in verschillende scenario's in de diepe ruimte. Omdat real-time navigatieoplossingen nodig kunnen zijn, kan het ontwerpen van een robuust ingebouwd

schattingsfilter een uitdaging zijn, inclusief beslissingen over welke parameters moeten worden geschat of verwaarloosd.

Gezien deze complexiteiten heeft dit onderzoek zich verdiept in op SST gebaseerde autonome OD voor satellietformaties, bestaande uit kleine ruimtevaartuigen, met als doel de huidige methodologieën te verbeteren en nieuwe mogelijkheden te verkennen in zowel cislunaire als diepe ruimteomgevingen.

Een analyse van 65 voorgestelde missies, voornamelijk gericht op de cislunaire ruimte en kleine hemellichamen voor oppervlaktekartering en karakteriseringsdoeleinden, bracht een overheersende afhankelijkheid van navigatie op de grond aan het licht, waarbij slechts enkelen voor autonome methoden kozen. Door te duiken in verschillende diepe ruimtenavigatietechnieken die geschikt zijn voor kleine satellieten, zoals optische, röntgenpulsaren crosslink-navigatie, heeft het proefschrift operationele principes en veelvoorkomende foutenbronnen gedetailleerd beschreven. Er wordt een uitgebreide categorisering gegeven voor navigatie in de diepe ruimte vanuit het perspectief van gegevensverzameling, autonomie en methoden, inclusief hun voordelen, nadelen en missievoorbeelden. Daarna verschoof de focus naar crosslink radiometrische navigatie met behulp van bestaande communicatiesystemen aan boord, die rechtstreeks kunnen worden aangepast aan huidige missies. De onderzoeksresultaten gaven aan dat een meerderheid van de missies (>%58) gebruik maakt van intersatellietcommunicatie, waarbij een aanzienlijk deel kan profiteren van autonome crosslink radiometrische navigatie. Deze methode is bijzonder effectief rond kleine lichamen, in de cislunaire ruimte en rond Lagrangiaanse punten en kan een opmerkelijke nauwkeurigheid bereiken binnen tientallen tot honderden meters en millimeters per seconde in positie en snelheid, waardoor navigatiefouten, complexiteit en totale missiekosten worden verminderd. Autonomie opent in deze context mogelijkheden voor missies waarbij directe communicatie met de aarde onpraktisch is.

De studie concentreerde zich vervolgens op het onderzoeken van eenvoudige algoritmen voor afstandmetingen, ondersteund door een gedetailleerd overzicht van de bestaande literatuur, vanwege het feit dat afstand data marginaal superieure navigatieoplossingen biedt in vergelijking met andere observationele datatypen, met name in de cislunaire ruimte. Dit proefschrift presenteert een uitgebreid overzicht van SST-afstandmeting methoden, inclusief hun prestatiekenmerken zoals linkbudget, meetfoutbudgetten en foutmodellen. Een cruciale bevinding van dit onderzoek was het belang van een eenvoudige maar betrouwbare meetmethode, vooral gezien de beperkingen in het communicatievermogen dat beschikbaar is voor kleine satellieten. Daarom onderzocht de studie de data-ondersteunde afstand meetmethode, waardoor de noodzaak voor afzonderlijke metingen in de communicatieketen werd geëlimineerd, wat een vereenvoudigde aanpak bood ten opzichte van traditionele meetmethoden. Vervolgens werden de afstand prestaties grondig onderzocht, waarbij werd aangetoond dat telemetrie- en telecommandsignalen bij hoge datasnelheden de traditionele bereikmethoden in SST effectief zouden kunnen vervangen. Bovendien zijn data-ondersteunde bereikoplossingen bij lagere datasnelheden, bijvoorbeeld < 10 kbps, nog steeds voldoende om te voldoen aan de meerderheid van de navigatiebehoeften voor kleine satellietoperaties in de diepe ruimte.

De fundamentele aspecten van op SST gebaseerde autonome OD-systemen aan boord

vereisen een uitgebreid begrip van de dynamiek van ruimtevaartuigen, observatiegeometrie en volgintervallen. Dit onderzoek heeft deze aspecten onderzocht met behulp van een verscheidenheid aan prestatiemetrieken en -methoden, zoals waarneembaarheid, Cramér-Rao Lower Bound (CRLB), Monte-Carlo en Covariantieanalyse, hoewel het duidelijk is geworden dat geen enkele metriek universeel van toepassing is op elk scenario. Vervolgens heeft dit proefschrift specifieke maatstaven geïntroduceerd en beschreven die zijn toegesneden op de onderzoeksdoelstellingen, waarbij de voordelen, nadelen en implementatie-uitdagingen ervan in detail worden beschreven. Met behulp van deze meetgegevens werd een semi-analytische waarneembaarheids- en covariantieanalyse uitgevoerd, samen met een gedetailleerde prestatieanalyse.

Het werd ontdekt dat de verschillende dynamiek van ruimtevaartuigen en de geoptimaliseerde observatiegeometrie de OD-prestaties verbeteren. Het vertrouwen op al te vereenvoudigde dynamische modellen is mogelijk niet voldoende voor een nauwkeurige werking van het systeem aan boord. Het integreren van uitgebreide modellen die rekening houden met alle relevante verstoringen kan de waarneembaarheid van het systeem en daarmee de nauwkeurigheid van de schattingen verbeteren. In tegenstelling tot de verwachtingen hebben de meetaspecten, hoewel cruciaal, een minimale impact op de systeemprestaties in vergelijking met de baandynamiek. Satellietformaties in de cislunaire ruimte blijken minder gevoelig te zijn voor meetonnauwkeurigheden dan observatiegeometrie. De studie van SST met een maanorbiter heeft bijvoorbeeld aangetoond dat zelfs minder nauwkeurige metingen aan de navigatievereisten zouden kunnen voldoen, bijvoorbeeld $\sigma_r = 10\,\text{km}$ en $\sigma_v = 10\,\text{cm/s}$, wat het gebruik van eenvoudige data-ondersteunde afstandsmethoden in dergelijke scenario's ondersteunt. Dit impliceert dat de gewenste OD-prestaties kunnen worden bereikt door een nauwgezette planning van de observatiegeometrie of het ingebouwde navigatiefilter, ondanks meetonnauwkeurigheden. Er is aangetoond dat maansatellietnetwerktopologieën, of ze nu verspreid of gecentraliseerd zijn, bestaande uit drie of meer satellieten, over het algemeen het grootste voordeel behalen uit autonome navigatiesystemen wanneer ze beschikken over lange inter-satellietverbindingen en korte omloopperioden. De integratie van extra satellieten in maannetwerktopologieën blijkt effectief te zijn bij het verbeteren van de algehele systeemprestaties.

Een ander essentieel aspect dat aan bod kwam, waren systematische fouten. De analyse bracht de noodzaak aan het licht om bias in het navigatiefilter in te schatten of in overweging te nemen, aangezien het negeren hiervan tot aanzienlijke onnauwkeurigheden zou kunnen leiden. Er werd vastgesteld dat filteren in de cislunaire ruimte geschikter is voor Halo/Halo-formaties, terwijl schattingen de voorkeur verdienen voor Halo/Lunar-formaties, afhankelijk van de missieconfiguratie. Er werd ook vastgesteld dat meetbias een impact heeft op de optimale trackingintervallen. Daarnaast onderzocht het onderzoek de soorten observatiegegevens, waaruit bleek dat de geschiktheid van een bepaald gegevenstype voor navigatie sterk afhankelijk is van het missieprofiel. Over het algemeen bleken afstandswaarnemingen betere prestaties te bieden vergeleken met snelheid- en hoekgegevens. Er werden ook drempelwaarden voor deze waarnemingen vastgesteld, die richtlijnen gaven voor het focussen op bepaalde soorten navigatiegegevens op basis van de specifieke vereisten en het profiel van de missie. Verschillende filtertechnieken werden onderzocht op hun prestatiemogelijkheden en complexi-

teit. Binnen de vereenvoudigde dynamiek werd geen significant verschil waargenomen tussen de verschillende filtertechnieken, hoewel geavanceerde filters verbeterde prestaties hebben laten zien bij het omgaan met niet-lineariteit rond kleine lichamen in het zonnestelsel.

Even cruciaal als voorgaande elementen was het onderzoek gericht op operationele aspecten, waarbij de cruciale rol van optimale trackingvensters werd benadrukt, trackingstrategieën aan boord en daarbuiten werden besproken, en een interne datastroom werd gepresenteerd voor foutanalyse en implementatie, die in staat is tot het sturen van missieontwerp en operationele planning van satellietformaties in de diepe ruimte in de toekomst.

NOMENCLATURE

ABBREVIATIONS

CN	Condition Number
CR	Convergence Ratio
UOI	Unobservability Index
ADEV	Allan deviation
AEKF	Adaptive Extended Kalman Filter
AIEKF	Adaptive Iterated Extended Kalman Filter
AIM	Asteroid Impact Mission
ASM	Attached Synchronization Marker
AU	Astronomical Unit
BER	Bit Error Rate
CAPS	Cislunar Autonomous Positioning System
CCSDS	Consultative Committee for Space Data Systems
CKF	Consider Kalman Filter
COPINS	CubeSat Opportunity Payload of Intersatellite Networking Sensors
CRLB	Cramér-Rao Lower Bound
CRTBP	Circular Restricted Three-body Problem
CSAC	Chip-scale atomic clock
CTL	Chip Tracking Loop
DDOR	Delta-Differential One-Way Ranging
DI	Deep Impact
DORIS	Doppler Orbitography and Radiopositioning Integrated by Satellite
DS1	Deep Space 1
DSN	Deep Space Network
DSS	Distributed Space Systems
DTE	Direct-to-Earth
EKF	Extended Kalman Filter
EM	Earth-Moon
EMXO	Evacuated Miniature Crystal Oscillator
ES	Earth-Sun
ESA	European Space Agency
ETP	Europa Tomography Probe
FIM	Fisher Information Matrix
FLOPs	Floating-point operations
GNSS	Global Navigation Satellite System
IEKF	Iterated Extended Kalman Filter
ISL	Inter-Satellite Link

ISS	International Space Station
ITU	International Telecommunication Union
IUKF	Iterated Unscented Kalman Filter
JAXA	Japan Aerospace Exploration Agency
JPL	Jet Propulsion Laboratory
LEO	Low Earth orbit
LiAISON	Linked Autonomous Interplanetary Satellite Orbit Navigation
LMCO	Lockheed Martin Corps
LOS	Line-of-Sight
LPF	Lunar Pathfinder
LQR	Linear-Quadratic Regulator
LRO	Lunar Reconnaissance Orbiter
LU	Length Unit
LUCE	Lunar CubeSats for Exploration
LUMIO	Lunar Meteoroid Impact Observer
MarCO	Mars Cube One
NASA	National Aeronautics and Space Administration
NORAD	North American Aerospace Defense Command
NRHO	Near Rectilinear Halo Orbit
OCXO	Oven-Controlled Crystal Oscillator
OD	Orbit Determination
OI	Orbit Insertion
OM	Observability Matrix
OP	Orbit Prediction
PDOP	Position Dilution of Precision
PLL	Phase Locked Loop
PN	Pseudo noise
PRARE	Precise Range And Range-Rate Equipment
PSO	Particle Swarm Optimization
RMS	Root Mean Square
RQ	Research Question
RSS	Root-Sum-Square
RTLT	Round-Trip Light Time
RTS	Rauch, Tung, and Striebel
S/C	Spacecraft
SDR	Software Defined Radio
SDST	Small Deep Space Transponder
SEP	Sun-Earth-Probe
SEXTANT	Station Explorer for X-ray Timing and Navigation Technology
SKF	Schmidt Kalman Filter
SKM	Station-Keeping Maneuver
SNR	Signal-to-Noise ratio
SRP	Solar Radiation Pressure
SST	Satellite-to-Satellite Tracking
STM	State Transition Matrix

SVD	Singular Value Decomposition
TCM	Trajectory Correction Maneuver
TCXO	Temperature Compensated Crystal Oscillator
TDRS	Tracking and Data Relay Satellite
TTC	Telemetry & Telecommand
TU	Time Unit
UKF	Unscented Kalman Filter
USO	Ultra-Stable Oscillator
UST	Universal Space Transponder

SYMBOLS AND NOTATIONS

$\bar{\mathbf{x}}$	Predicted State Vector
$\bar{P}$	Predicted State Estimation Covariance Matrix
$\bar{\sigma}_r$	Averaged Position Estimation Uncertainty
$\bar{\sigma}_v$	Averaged Velocity Estimation Uncertainty
β_{av}	Averaged Estimation Uncertainty within Satellite Formation
$\Delta_{\rho_{CO}}$	Clock offset
$\Delta_{\rho_{CRO}}$	Clock rate offset
$\Delta_{\rho_{TT}}$	Time-tag error
Δ_{rx}	Receiver line delay
Δ_{tx}	Transmitter line delay
ΔV_c	Delta-V
$\dot{\rho}$	Range-rate
$\hat{\mathbf{x}}$	Estimated State Vector
$\hat{\mathbf{x}}^s$	Smoothed State Vector
$\mathbf{a}$	Acceleration Vector
$\mathbf{b}$	Consider parameter vector
$\mathbf{r}$	Position Vector
$\mathbf{v}$	Velocity Vector
$\mathbf{x}$	State vector
$\mathscr{I}$	Fisher Information matrix
a	semi-major axis
C	Consider Covariance Matrix
e	eccentricity
H	Measurement Sensitivity Matrix
i	inclination
K	Kalman Gain
P	State Estimation Covariance Matrix
Q	Process Noise Covariance Matrix
R	Measurement Noise Covariance Matrix
Φ	State Transition Matrix
ψ	Ranging Signal Phase
ψ_R	Received Ranging Signal Phase
ψ_T	Transmitted Ranging Signal Phase

ρ	Pseudo-range
σ_ρ	Range Measurement Error
$\sigma_{\dot{\rho}_{GS}}$	Ground-based Range-rate Measurement Error
$\sigma_{\dot{\rho}}$	Range-rate Measurement Error
$\sigma_{\dot{\rho}_{SST}}$	Satellite-to-Satellite Range-rate Measurement Error
$\sigma_{\phi_{SST}}$	Satellite-to-Satellite Angle Measurement Error (Azimuth)
$\sigma_{\psi_{SST}}$	Satellite-to-Satellite Angle Measurement Error (Elevation)
$\sigma_{\rho_{data}}$	Data-aided Ranging Measurement Error
σ_{ρ_d}	Downlink Ranging Error
$\sigma_{\rho_{GS}}$	Ground-based Range Measurement Error
$\sigma_{\rho_{PN}}$	PN Ranging Measurement Error
$\sigma_{\rho_{SST}}$	Satellite-to-Satellite Range Measurement Error
$\sigma_{\rho_{TM}}$	Telemetry Ranging Measurement Error
$\sigma_{\rho_{tone}}$	Tone-based Ranging Measurement Error
σ_{ρ_u}	Uplink Ranging Error
σ_{exec}	Delta-V Execution Error
σ_{OD}	Orbit Determination Error
σ_{OI}	Orbit Insertion Error
σ_y	Allan deviation
τ	Round-trip Light Time
$\mathbf{h}$	Measurement model
$\mathbf{v}$	Measurement noise model
$\tilde{w}$	Process noise model
A	Area
B_l	Tracking Loop Bandwidth
c	Speed of Light
E_s/N_0	Code Symbol-to-Noise Ratio
f_{rc}	Range Clock Frequency
f_R	Received Frequency
$f_{T,0}$	Reference Frequency
f_T	Transmitted Frequency
G	Transponder Ratio
G_T	Transmitter Antenna Gain
$gbest$	Global-best solution by entire group
GM	Gravitational Coefficient
L_p	Polarisation Loss
L_T	Transmitter Path Losses
LB	Upper Bound
LB	Lower Bound
P_{nm}	Legengre Polynomials of degree n order m
P_r/N_0	Ranging Clock Signal-to-Noise Density Ratio
P_T	Transmitter Power
$pbest_i$	Personal-best solution by particle i
R_1	Cross Correlation Factor
T	Integration Time

T_{sd}	Telemetry symbol duration
T_{SST}	Satellite-to-Satellite Tracking Window Duration
az	Azimuth
el	Elevation
RAAN	Right Ascension of Ascending Node

1

INTRODUCTION

Over recent years, there has been a growing interest in deep space missions involving small satellites. These missions have demonstrated remarkable achievements, highlighting their significance in future space explorations. Parallel to this, satellite formations have gained popularity, opening up new possibilities for deep space exploration. Traditionally, ground-based radiometric tracking is the workhorse to establish the necessary navigation solution for these missions. However, ground-based operations pose several challenges, including limited tracking resources and an increasing number of missions. Additionally, ground-based tracking can be costly, whereas small satellites are expected to be at low cost. In response to these challenges, autonomous operations emerge as a beneficial strategy, and navigation stands as a key area that could greatly benefit from autonomous operations. This refers to the capability of a spacecraft to navigate with minimal or no human intervention. In this context, various autonomous navigation strategies exist, and one of them stands out as a promising approach: Crosslink navigation, using existing systems and providing navigation solutions for satellite formations based on inter-satellite measurements. This chapter introduces the state-of-the-art deep space autonomous navigation along with the past, present, and future of small satellites for deep space missions. The background and motivation of this research are provided, followed by the thesis goal and research questions. An outline of the dissertation is also presented, along with the research methodology.

Parts of this chapter have been published in:
E. Turan, S. Speretta, and E. Gill, "Autonomous navigation for deep space small satellites: Scientific and technological advances", *Acta Astronautica*, vol. 193, pp. 56–74, Apr. 2022. DOI: 10.1016/j.actaastro.2021.12.030

1

1.1. BACKGROUND AND MOTIVATION

In recent years, there has been a growing interest in deep space missions. The remarkable achievements of small satellites have been pivotal in this regard. These compact yet powerful satellites have successfully completed complex tasks such as rendezvousing with small solar system bodies, conducting asteroid flybys, and playing pivotal roles in data relay operations. Their success demonstrates their potential and supports their continued importance in future space missions.

Before diving into specifics, it is essential to define some key aspects, such as the definition of deep space: the International Telecommunication Union (ITU), responsible for standardizing telecommunication practices and available resources, categorizes *deep space* as regions extending beyond 2×10^6 km from the Earth [2]. This classification is crucial for several reasons, including the allocation of radio frequencies and the operational characteristics of spacecraft communication systems. While the ITU clearly defines deep space, they do not explicitly name the zone lying closer to Earth, resulting in a lack of an internationally recognized term for non-deep space missions such that this region includes space between Earth and the Moon (cislunar), Earth-Moon (EM), and Sun-Earth Lagrangian points. It should be noted that, historically, radio regulations have defined the deep space boundary as the lunar distance from Earth [3]. This study adopts a broader and more inclusive definition of deep space to avoid confusion with ITU and other existing definitions. In this context, deep space includes not just regions beyond 2×10^6 km from Earth but also cislunar space and the Lagrangian points of both the Earth-Moon and Sun-Earth systems.

Focusing on small satellites, they are typically characterized by low mass, usually less than 500 kg, with their specific classifications based on mass detailed in Table 1.1. The overall mission success rate and advancements in technology miniaturization led small satellite missions to be increasingly proposed by many entities, including universities, companies, and space agencies. The primary objective behind these mission studies is to facilitate cost-effective deep space exploration through the use of small satellites, leveraging their unique capabilities to facilitate a new exploration era. It is important to clarify that in this thesis, the terms *small satellites* and *small spacecraft* are used interchangeably, despite the nuanced distinction where *satellites* typically refer to objects orbiting celestial bodies, and *spacecraft* denote vehicles intended for extraterrestrial travel or operations beyond Earth's atmosphere.

Table 1.1: Small satellite classification in terms of mass [4].

Satellite categories	Mass range [kg]
Mini-satellites	100 –500
Micro-satellites	10 –100
Nano-satellites	1 –10
Pico-satellites	0.1 –1
Femto-satellites	0.01 –0.1

An important aspect of modern space missions is the use of Distributed Space Systems (DSS): these involve multiple spacecraft working in coordination, such as in formations or constellations, to achieve a common mission objective. DSS offer unique advantages in terms of coverage and mission flexibility: especially in deep space, DSS can enhance observational capabilities and provide robust communication networks. The use of small satellites in DSS configurations is increasingly popular due to their lower cost, reduced launch mass, and the flexibility they offer for mission design. These small satellites, when operating as part of a DSS, can achieve objectives that would be challenging, such as multi-point sensing, or impossible, such as forming a virtual instrument for a single larger spacecraft, opening up new possibilities for deep space exploration.

From the perspective of ground segment operations, small satellite missions pose several challenges, including the need for precise tracking within limited contact times, managing an increasing number of missions with limited tracking resources, and the limitations posed by on-board power for communications [5]. Furthermore, the need to simultaneously track multiple spacecraft within a tight schedule adds to the complexity in some cases. Traditional ground-based tracking can be costly, whereas small satellites are expected to be at low cost. In addition, ground-based tasks like station keeping and trajectory correction maneuvers, typically calculated on the ground and commanded to the spacecraft, necessitate a flight dynamics team, thereby increasing overall mission expenses. Given the goal of minimizing mission costs, integrating autonomous operations emerges as a beneficial strategy. In particular, autonomous capabilities enable satellites to make decisions and perform tasks with minimal or no human intervention [5], thereby enhancing operational efficiency, reliability, adaptability, and overall mission success while reducing mission costs.

Navigation stands as a key area that could greatly benefit from autonomous operations. Spacecraft navigation involves designing a reference trajectory, tracking the actual spacecraft position during the mission, and implementing maneuvers to align the spacecraft with the planned trajectory. The first aspect involves designing the intended flight path, while the second, OD and Orbit Prediction (OP), is crucial during the mission, involving tracking of the spacecraft past, present, and future positions. The final aspect involves correcting the spacecraft trajectory to align with the planned course. These operations, particularly OD and trajectory control, are traditionally dependent on ground-based systems such as ground-based tracking and communications, presenting considerable challenges. Autonomous navigation, therefore, emerges as a valuable solution, especially in deep space missions, where delays in radio signal transmission can be significant. There are other reasons apart from the previous ones. For instance, in scenarios like asteroid rendezvous, autonomous navigation becomes not just beneficial but potentially the only viable option due to the time lag in radio communications. In such cases, the spacecraft must be capable of tracking its trajectory and performing station-keeping tasks independently, enhancing operational efficiency and mission success. Overall, autonomous navigation refers to the capability of a spacecraft to navigate with minimal or no human intervention.

It should be noted that for a spacecraft to operate fully autonomously, it must collect and process navigation data on-board. This requirement is crucial as autonomy from the operation perspective implies operation with minimal or no human ground inter-

vention. Any process that involves transferring data from the ground to the spacecraft for navigation even if performed in an automated way, would still depend on ground support, which contradicts the definition of full autonomy. This leads to the concept of semi-autonomous navigation, where some aspects of navigation are autonomous but still require ground support. For instance, spacecraft could collect radio signals from ground-based systems and process the data on-board (one-way ranging). In contrast, fully autonomous on-board OD implies complete independence from ground systems. For instance, spacecraft could collect navigation data via an on-board camera and process it. In brief, autonomous OD and on-board navigation data collection are linked with each other, forming autonomous on-board OD.

Autonomous navigation methods have been widely researched in the scientific literature and several are proposed specifically for deep space missions [6]–[12]. These methods might utilize existing systems, such as communication links, or might necessitate the addition of new instruments, like cameras, to estimate the spacecraft position and velocity. Using existing systems offers cost and volume reduction advantages, making these methods especially advantageous for small satellite missions focused on miniaturization.

In missions involving multiple spacecraft, autonomous OD becomes even more critical, estimating their positions with respect to each other and/or with respect to a celestial body, adding another layer of complexity. In these missions, satellite-to-satellite tracking data could be used for navigation purposes. Since payload data in these missions typically follows a one-hop link configuration, being transferred first to a mothercraft and then to the ground, existing communication links can serve a dual purpose, also functioning as a source of navigation data. This would allow SST-based autonomous OD.

However, the design and implementation of an autonomous navigation system for deep space missions, especially for small satellite formations, presents several challenges, including accurately modeling the spacecraft dynamics in complex deep space environments, developing high-fidelity measurement models, performing simple yet accurate inter-satellite measurements, extracting navigation data efficiently, and designing robust on-board estimation filters. Furthermore, crucial decisions need to be made regarding which parameters to estimate, how to plan tracking windows, and how to design an orbital configuration, enabling accurate navigation solutions. Enhancing the autonomous capabilities of the spacecraft, enabling it to initiate tracking and perform station-keeping autonomously, is another critical aspect.

These aspects demand detailed studies and careful investigations, especially from the system performance perspective. As such, understanding system capabilities and ensuring the reliability and effectiveness of SST-based autonomous OD are crucial for the success of deep space missions. The following sections will delve deeper into the proposed deep space small satellite missions found in scientific literature, examining their specific navigation methodologies and the unique challenges they present. This exploration sheds light on the state-of-the-art in autonomous navigation for deep space missions and provides a path forward for future research and development in this critical area of space exploration.

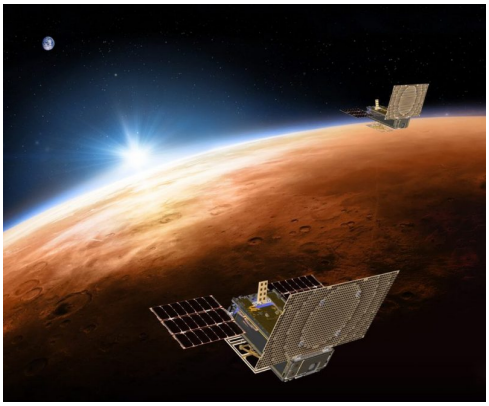

Figure 1.1: The first interplanetary CubeSat mission: MarCO [16].

1.2. PAST, PRESENT, AND FUTURE OF DEEP SPACE SMALL SATELLITE MISSIONS

This section provides a comprehensive overview of the evolution of deep space small satellite missions, encompassing past achievements, current advancements, and future prospects. Notably, parts of this and subsequent sections draw upon information previously published in [1], with the current study incorporating recent advancements in the field. Detailed information about various missions, including their specific objectives, can be found in Appendix A.

The history of interplanetary micro-spacecraft missions traces back to PROCYON, intended to flyby the asteroid 2000 DP_{107}, developed by Japan Aerospace Exploration Agency (JAXA). Launched in 2014 alongside Hayabusa-2, PROCYON marked a significant milestone in space exploration [13]. In 2018, Hayabusa-2 further extended its legacy by deploying three landers to the asteroid Ryugu, achieving a successful surface mission [14]. Prior to this, the European Space Agency (ESA) Rosetta mission had achieved a milestone with Philae becoming the first lander to land on a comet in 2014 [15]. Another groundbreaking mission was Mars Cube One (MarCO), the first interplanetary CubeSat mission, developed by Jet Propulsion Laboratory (JPL) and launched in May 2018 to accompany the InSight Mars lander [16]. Its twin 6U-sized CubeSats are depicted in Figure 1.1. It is important to mention that CubeSats are a class of miniaturized satellites with a form factor of 10 cm cubes (1U) often combined together to build bigger structures.

In 2022, CAPSTONE was launched into cislunar space to test and verify the calculated orbital stability planned for the Lunar Gateway station. The 12-unit CubeSat was designed to test an autonomous navigation system called Cislunar Autonomous Positioning System (CAPS), which estimates its position without relying on ground stations [17]. In the same year, the first Italian deep space CubeSat, LICIACube, observed the asteroid Dimorphos after DART impact [18].

The Artemis 1 (initially known as Exploration Mission 1) launch opened a window to Cislunar and deep space for ten 6U-CubeSats [20] (shown in Figure 1.2), each with

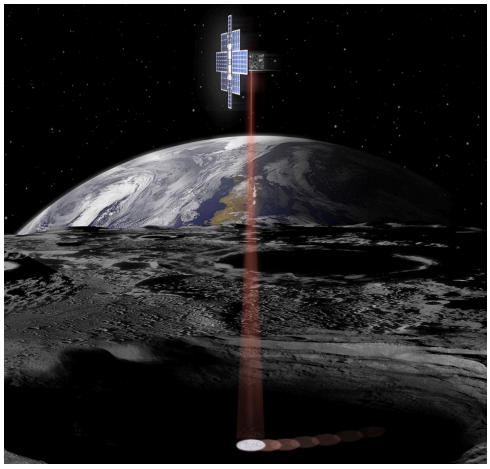

Figure 1.2: Lunar Flashlight will use its lasers to search for water on the Moon [19].

unique mission objectives on the way to the Moon. Three other CubeSats, Cislunar Explorer, Lunar Flashlight, and CU-E3, have missed the integration on the mission.

National Aeronautics and Space Administration (NASA) Planetary Science Deep Space SmallSat Studies (PSDS3) program funded 19 studies among the received 102 proposals [21], covering a range of destinations including Mars, Venus, and various small and icy bodies [22]. Additionally, the SIMPLEx program selected three proposals, HALO [23], DAVID [23], and MMO [24] for further technological development. Similarly, the Europa Clipper mission, designed to orbit Jupiter and conduct flybys of its moon Europa [25], is considering incorporating nano-satellites, Mini-MAGGIE [26], DARCSIDE [27], Sylph [28], and ETP [29] as secondary payloads to augment the mission.

The ESA General Studies Programme, through the third and fourth editions of the SysNova technical challenges, focused on deep space projects like CubeSat Opportunity Payload of Intersatellite Networking Sensors (COPINS) and Lunar CubeSats for Exploration (LUCE) [30]. COPINS initially supported the ESA Asteroid Impact Mission (AIM) mission, later renamed to HERA. Out of many competing concepts, five CubeSats – ASPECT,[31], DustCube [32], CUBATA [33], PALS [34], and AGEX [35] - were chosen for detailed studies, with Juventas and MILANI (formerly APEX) eventually selected for implementation [36]. For the LUCE mission, four CubeSats – LUMIO [37], MoonCARE [38], CLE [39] and VMMO [40] – were picked from numerous concepts. Additionally, a unique mission, M-ARGO, a standalone deep space CubeSat, has been designed for asteroid rendezvous and close proximity operations [30].

Apart from these specific missions, emerging concepts like space-based radio astronomy are exploiting recent advances in nano-satellites to explore low-frequency space arrays, investigating mostly unexplored frequency bands between 0.1-30 MHz [41]–[44], which cannot be observed due to man-made noise in the Earth's vicinity.

In summary, the near future holds exciting prospects for small satellites, with missions planned to a variety of destinations and objectives, as illustrated in Figures 1.3 and

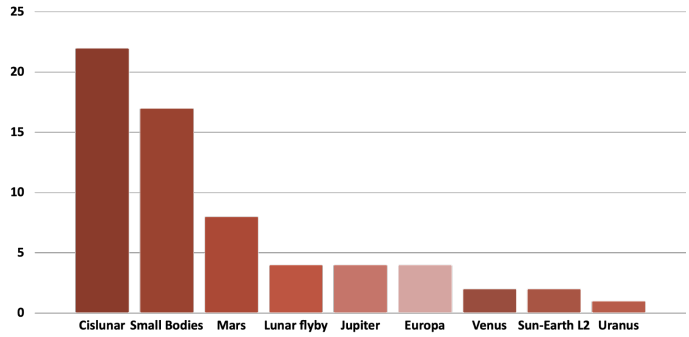

Figure 1.3: Mission destinations of small satellites operating in deep space, emphasizing the rising trend in cislunar space exploration.

1.4, respectively. Trends indicate a focus on lunar and small-body missions, primarily for surface mapping and characterization. This expansion of small satellite missions, as detailed in Table 1.2, represents a significant shift in deep space exploration, showing the potential of miniaturized technology.

1.3. STATE-OF-THE-ART IN DEEP SPACE NAVIGATION

This section provides the state-of-the-art navigation methods utilized in deep space exploration, with a particular focus on their classification based on autonomy, an in-depth look at SST-based autonomous navigation, and the enabling technologies involved.

The term *navigation* encompasses two critical processes: attitude and orbit determination: the former refers to the process of determining the orientation of a satellite as a function of time with respect to a reference frame, while the latter, the primary focus of this study, refers to the process leading to the satellite orbit, position, and velocity knowledge as a function of time, with respect to a fixed reference frame (absolute) or with respect to another spacecraft or moving object (relative). OD covers where the object was located in the past (definitive), is located at present, while OP covers where the object will be located in the future (predictive) [1]. In the context of this thesis, the terms *navigation* and *orbit determination* are used interchangeably, even though navigation generally implies guiding an object to a destination.

The study classifies navigation methods into two main categories: on-board and off-board. This is based on the location where navigation data is collected, processed, and stored, either on the satellite itself (on-board) or at a ground station (off-board). Since autonomous navigation implies navigation with minimal or no human input, these navigation approaches can be further divided into fully autonomous and semi-autonomous approaches. Fully autonomous navigation is characterized by on-board execution without any intervention from ground-based assets. An example would be an on-board camera tracking celestial bodies to provide data to the on-board navigation filter, thus estimating the spacecraft's position and velocity. Conversely, semi-autonomous navigation involves using ground-based assets for data collection and/or processing. A typical ex-

1

Table 1.2: Executed, ongoing, or planned deep space missions based on small satellites.

Cislunar		**Small Bodies**	
CAPSTONE	[17]	LICIACube	[18]
Lunar Ice Cube	[45]	Juventas	[36]
LunaH-Map	[46]	MILANI	[36]
Lunar Flashlight	[20]	ASPECT	[31]
ArgoMoon	[47]	Dust Cube	[32]
OMOTENASHI	[48]	PALS	[34]
Cislunar Explorers	[49]	CUBATA	[33]
EQUULEUS	[50]	AGEX	[35]
HALO	[23]	B1	[51]
WATER	[52]	B2	[51]
IMPEL	[53]	BIRDY-T	[10]
CubeX	[54]	AI3	[55]
LUMIO	[37]	NEA Scout	[20]
VMMO	[40]	M-Argo	[30]
CLE	[39]	DAVID	[23]
MoonCare	[38]	Ross	[56]
NanoSWARM	[57]	APEX	[58]
MiLuV	[59]	PRISM	[49]
BOLAS	[60]	**Venus**	
OLFAR	[41]	Cupid's Arrow	[61]
DSL	[42]	CUVE	[62]
Skyfire	[63]	**Jupiter**	
Lunar Flyby		SAEVe	[64]
CuSP	[65]	JUMPER	[66]
BioSentinel	[67]	PrOVE	[68]
CU-E3	[69]	VAMOS	[70]
Team Miles	[71]	**Uranus**	
Mars		SNAP	[72]
MarsDROP	[73]	**Europa**	
MAT	[74]	ETP	[29]
MARIO	[75]	Mini-Maggie	[26]
MarCO	[76]	DARCSIDE	[27]
MMO	[24]	Sylph	[28]
Aeolus	[77]	**Sun-Earth L2**	
MISEN	[78]	DEx	[43]
MIIAR	[79]	SULFRO	[44]

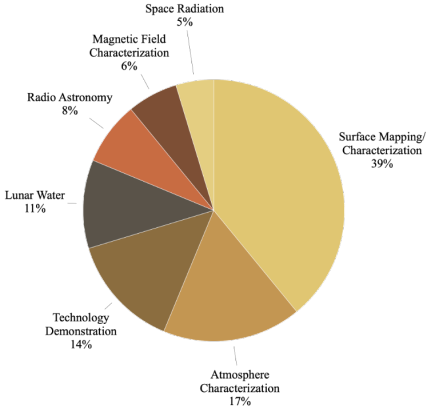

Figure 1.4: Mission objectives of small satellites operating in deep space, with a particular emphasis on the rising trend in surface mapping and characterization.

ample would be an on-board system that tracks the phase of a radio signal transmitted from a ground station and utilizes this for navigation purposes. In essence, autonomous navigation is only possible when data collection and processing are both conducted on-board. In contrast, non-autonomous navigation relies on observations and data processing conducted at ground stations, thus termed as off-board in this context. For instance, a ground-based asset could track the phase difference between the transmitted and received radio signals and use this for trajectory estimations. In brief, autonomous and non-autonomous approaches are closely linked with on-board and off-board data collection and processing. Therefore, this study interchangeably uses autonomous OD and on-board OD. Figure 1.5 presents a concept breakdown diagram showing various navigation approaches for deep space missions, while Figure 1.6 illustrates this categorization based on autonomy.

Autonomous navigation presents several advantages, including potential reductions in mission costs and improvements in performance. For instance, a Lunar CubeSat would require direct-to-Earth communications of 192 hours over one year, including payload downlink, nominal tracking, and emergency operations [80]. Mission costs can be significantly reduced by minimizing the dependency on ground-based operations. Furthermore, autonomous navigation systems can perform specific tasks more efficiently and effectively than ground-controlled systems, such as surface navigation of Mars rovers, by eliminating the latency for Earth-bound commands, which is around 14 minutes (one-way), allowing more time for scientific activities. Some tasks are only feasible through autonomous navigation. An example would be deep space rendezvous or flybys, where real-time human input is impossible due to long signal travel times. Historically, autonomous navigation has played a crucial role in missions such as Deep Space 1 (DS1) [6], [7], STARDUST [81], Deep Impact (DI) [82], all supported by JPL Autonomous Optical System [83], as well as SMART-1 [84], where the baseline approach was to com-

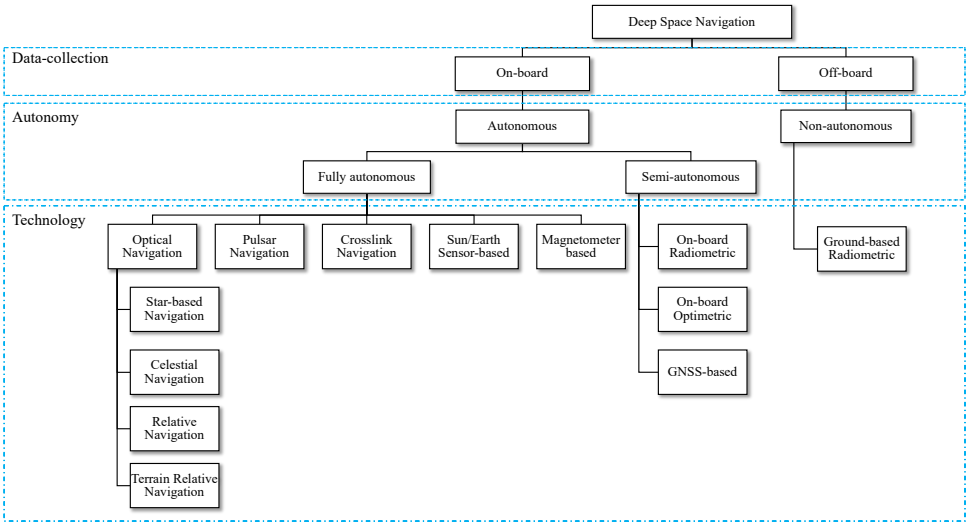

Figure 1.5: Classification of deep space navigation techniques by autonomy and data-collection source, detailing autonomous on-board approaches to non-autonomous ground-based operations.

pute spacecraft states and trajectory correction maneuvers using ground stations [85], [86], a method also employed in missions like Philae-Rosetta, HAYABUSA-1 [87], and the MarCO CubeSats [86].

The following subsections summarize these approaches, focusing on small satellite missions planning to employ these methods. Some options not considered for the missions examined in this study are grouped under other methods and detailed in Table 1.3. Figure 1.7 provides a visual representation of these methods. This study aims to provide a comprehensive understanding of the state-of-the-art in deep space navigation, emphasizing the evolving role and significance of autonomy in this domain.

1.3.1. AUTONOMOUS NAVIGATION

This section provides navigation strategies that are designed to operate independently of ground-based assets. These strategies focus on collecting OD data directly on-board the spacecraft, a technique that represents a significant shift towards autonomy in space missions.

OPTICAL NAVIGATION

Optical navigation refers to a variety of methods of determining the position and velocity of a spacecraft by using optical observations. This technique typically involves capturing images of celestial bodies or other known reference points, such as stars, planets, moons, or asteroids, and then using these images to calculate the spacecraft position and velocity [94]. This process is carried out by on-board cameras capturing images of nearby celestial bodies or distant stars. The software on the spacecraft then identifies familiar features within these images, like the surface of a planet, the edges of a moon, or specific star patterns. By comparing the observed positions of these features to their known

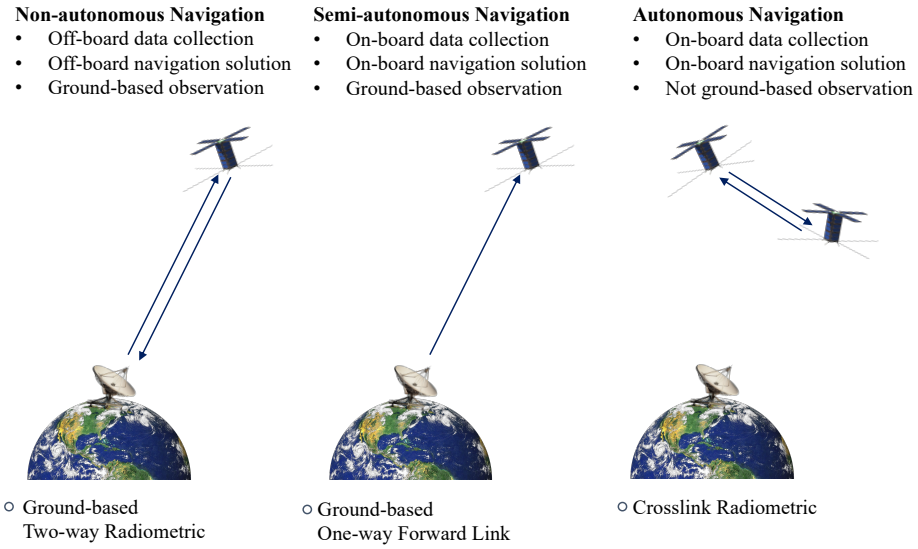

Figure 1.6: Illustration of deep space navigation categorization based on autonomy.

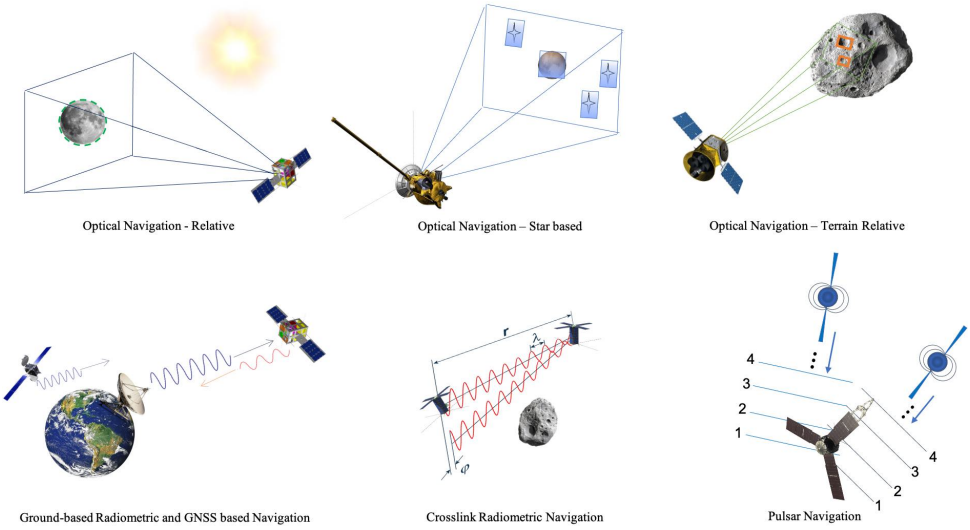

Figure 1.7: Illustration of deep space navigation strategies.

Table 1.3: Overview of Deep Space Navigation Strategies.

Navigation Technologies	Advantages	Disadvantages	Autonomy	Examples	References
Optical Navigation	Compatible with all mission phases Moderate to high accuracy	Moderate to high cost	Autonomous	BIRDY-T, LUMIO, Sylph, NEA-Scout, Juventas, IMPEL, DustCube, Cubata, PALS, M-ARGO	[88] [9] [89]
Pulsar Navigation	High accuracy	Sensor size Unavailable for rendezvous	Autonomous	CubeX, OLFAR	[54]
Crosslink Navigation	High accuracy Uses existing systems	Satellite formations only	Autonomous	CAPSTONE	[17]
Sun/Earth Sensor-based Navigation	Mature sensor Compatible with other systems	Limited availability	Autonomous	-	[90]
Magnetometer-based Navigation	Mature sensor Compatible with other systems	Available only in characterised magnetic fields	Autonomous	-	[12]
GNSS-based	High accuracy	Available only in Cislunar vicinity Sensor size	Semi-autonomous	-	[91]
Ground-based One-way Forward Link	High accuracy with optimetrics	High cost	Semi-autonomous	-	
Ground-based Two-way Radiometric	Heritage High accuracy	High cost	Non-autonomous	Lunar IceCube, LunaH-Map, EQUULEUS, JUMPER, OMOTENASHI, CuSP, Lunar Flashlight, Biosentinel	[92] [93]

locations in space, the spacecraft navigation system can compute its own position and velocity and autonomously correct its course to stay on the intended trajectory.

Optical navigation methods are broadly classified based on the target body apparent size in the captured image: unresolved center finding, resolved center finding, which utilizes multiple bodies, limb-based, which also uses range information, and surface landmark-based navigation, which calculates bearing to known landmarks [95]. These methods support various phases of a mission, including cruise, flyby, rendezvous, orbiting, and landing. Delving into the specific technologies, star-based and celestial navigation employ inertial pointing and bearing observations, while relative optical navigation produces bearing and position estimates concerning an observed object [96]. Terrain Relative Navigation combines on-board optical data with a map of the landing area to avoid landing hazards.

The performance of these optical navigation methods highly depends on the capabilities of the spacecraft optical sensors, with their resolution, sensitivity, and noise handling being key factors. The imagery utilized in vision-based navigation is subject to various types of noise, such as shot, read, fixed pattern, quantization noise, and dark current, which must be effectively handled [97].

In practice, missions like DS1, STARDUST, DI, and EPOXI used the JPL AutoNav [83], [98] system, incorporating these optical methods to achieve remarkable navigational accuracy. The DS1 mission, for instance, reported position accuracies of or better than 150 km and velocity accuracies to 0.2 km/s during its cruise phase [98].

Several deep space small satellite missions have or plan to incorporate optical navigation into their journeys. The BIRDY-T mission, for instance, is leveraging an In-Flight Orbit Determination (IFOD) system during its cruise to Mars, combining optical measurements with asynchronous triangulation and Kalman filtering to map its trajectory [88]. The LUMIO mission is another example, where the apparent size of the Moon in images is used to estimate the spacecraft's position and velocity in a Halo orbit around the Earth-Moon L2 point [9]. Similarly, the Cislunar Explorers mission intends to determine spacecraft locations in Cislunar space by analyzing the relative sizes and positions of the Earth, Moon, and Sun [99], [100]. The M-ARGO mission, too, is set to utilize miniaturized on-board optical sensors for Line-of-Sight (LOS) measurements to inform its navigation filter [89]. Under optimal observation conditions, M-ARGO's navigation accuracy is expected to be around 1000 km (3σ) for position and 1 m/s (3σ) for velocity components, respectively [89].

In summary, optical navigation stands out among navigation architectures for its moderate to high-accuracy solutions and its adaptability to various mission phases.

PULSAR NAVIGATION

Pulsar navigation is an advanced form of navigation for spacecraft that utilizes consistent and highly predictable signals from pulsars, which are rapidly spinning neutron stars, typically nearly 100 times a second, that emit beams of electromagnetic radiation, often in the form of radio waves or X-rays. This process is carried out with detectors, like X-ray or radio telescopes, capable of receiving the signals emitted by pulsars. Due to the stable emission intervals, these signals serve as highly accurate clocks, making them reliable navigational references. These timings are compared with the expected

arrival times at a known reference location, allowing the navigation system to triangulate the spacecraft precise position in space. This is similar to how Global Navigation Satellite System (GNSS) systems work, but instead of using satellites, it uses the signals from these distant celestial objects. A significant advantage of pulsar navigation is its autonomy, enabling spacecraft to navigate independently of ground-based assets, providing an opportunity to stabilize on-board clocks via the periodic pulse arrivals [101]. One notable application of this technology was the Station Explorer for X-ray Timing and Navigation Technology (SEXTANT) experiment, which demonstrated the capability to achieve position errors better than 10 km Root-Sum-Square (RSS) on the International Space Station (ISS) [102].

Compared to optical navigation, pulsar-based techniques have distinct advantages: higher signal stability, low background noise interference, and well-known locations make them more reliable and easier to detect than many optical signals. Pulsar navigation techniques include the pulsar elevation method, which utilizes the elevation angles and apparent diameter measurements to determine the distance which provides position determination with the help of multiple sources, and the limb occultation method, which relies on measuring how long a pulsar signal is obscured by a celestial body to deduce position [101].

However, pulsar navigation presents several challenges. The precision of timing measurements can be affected by various factors, including Poisson fluctuations, detector offsets, and local oscillator fluctuations, among others [103]. Despite these potential sources of error, the CubeX mission aims to validate the feasibility of pulsar navigation in a CubeSat form factor while in Lunar orbit. CubeX will employ two X-ray instruments: an X-ray Imaging Spectrometer and a Solar X-ray Monitor [54]. It is important to note that the detection of pulsar signals, which range from 100 MHz to a few GHz, typically requires substantial antenna sizes, often greater than 25 meters in diameter, which presents practical limitations for certain mission profiles [104].

In summary, pulsar navigation promises enhanced accuracy over optical navigation methods, with the potential for better than 0.1 km positional accuracy with 10^{-7} s timing and 10^{-4} arcsec pulsar position errors [101]. Its ability to stabilize on-board clocks with periodic pulsar signals is a significant benefit. However, the size of the required sensors and the integration time may limit its applicability during some mission phases, such as when in close proximity to other celestial bodies.

CROSSLINK NAVIGATION

Crosslink navigation is a method used to determine the relative positions and velocities of spacecraft within a satellite formation based on satellite-to-satellite tracking data. This technique is particularly useful for missions involving multiple spacecraft that must determine or maintain a precise configuration relative to each other, such as satellite constellations or deep space exploration missions. The process of crosslink navigation starts with transmitting radio or laser signals between spacecraft within the formation. The receiving spacecraft measures the characteristics of these signals via a one-way or two-way link, notably round trip light time or the Doppler shift. The round trip light time helps in determining the distance between spacecraft, while the Doppler shift provides information about the relative velocity. This information is then processed using algorithms to determine the relative or absolute positions and velocities of the spacecraft

within the formation. Notably, this computation can be done onboard each spacecraft, enhancing the autonomy of the formation. Additionally, crosslink navigation systems often incorporate error correction mechanisms to mitigate the influence of signal delay and noise, further refining the accuracy of navigational data.

Considering various systems, crosslink radiometric measurements often hold a significant advantage over optical or laser alternatives, especially in scenarios involving in small satellites in deep space. Radiometric systems, robust against environmental disruptions, do not require the high-precision pointing and direct line of sight that optical systems depend on, making them more suitable for the conditions of cislunar space where inter-satellite distances can reach up to the order of hundreds of thousands of km. Additionally, these systems are technologically less demanding, reducing the need for complex and power-intensive hardware that are a poor fit for small satellites which typically operate with limited power. The lower power consumption of radiometric measurements does not only preserve the onboard energy but also ensures continuous operation without compromising other mission-critical systems. Furthermore, the cost-effectiveness and proven track record of radiometric tracking offer a lower-risk and less expensive option for small satellites. Therefore, this study has solely focused on radiometric measurements for crosslink navigation.

A significant advantage of crosslink navigation is using existing components, such as radio tracking systems, eliminating the need for additional navigational instruments. While satellite-to-satellite tracking data primarily offers relative navigation solutions, it can also facilitate absolute state estimation when integrated with ground-based tracking. For instance, tracking one spacecraft from the ground and utilizing relative measurements can yield accurate positioning and velocities of all spacecraft in the formation with respect to a central body like Earth.

In specific mission configurations, satellite-to-satellite tracking data alone may be sufficient not only for relative but also for precise absolute positioning. Missions orbiting small solar system bodies, for example, can leverage inter-satellite range or range-rate measurements to achieve meter-level accuracy in position determination, i.e. with respect to a central gravitational body [11]. The dynamic environment around such bodies, with their irregular gravitational fields and significant third-body perturbations, like those found at Earth-Moon libration points, enables this accuracy. The ongoing CAPSTONE mission, for instance, tests a navigation architecture that utilizes inter-satellite measurements with Lunar Reconnaissance Orbiter (LRO) to estimate its absolute position in a Near-Rectilinear Halo Orbit around the Moon [17].

Despite its advantages, crosslink navigation is not without challenges. The accuracy of radiometric measurements, crucial for this technique, can be compromised by systematic errors, thermal noise, and the biases and drifts of onboard clocks. Additionally, the relative orbital geometry and, thus the measurement geometry can influence the navigation solution accuracy.

In summary, crosslink navigation offers distinct advantages for missions involving multiple spacecraft, particularly around small solar system bodies. Its ability to leverage existing communication systems without additional instruments makes it a cost-effective choice. However, this method is only suited for missions with several spacecraft.

OTHERS

This section presents alternative methods of autonomous OD that are suitable for specific mission types, highlighting their unique features and applicability to certain categories of deep space missions.

The concept of autonomous OD was initially proposed and analyzed by [105], [106] for Earth-orbiting spacecraft, employing a technique based on Sun/Earth sensors. One notable example is the Sun Doppler method, which involves measuring the Doppler shift of sunlight using a spectrometer combined with directional data from Earth and Sun sensors. Particularly useful for interplanetary spacecraft, the Sun Doppler method can provide a navigation solution with an accuracy of around 3 km in position [90], making it an attractive option for missions that require autonomous navigation capabilities.

Another strategy for autonomous OD is the use of a magnetometer measuring the local magnetic field and providing valuable data that can be used to estimate the spacecraft states. This method is especially useful for missions to destinations where the magnetic field has been well-characterized [12]. By analyzing the variations in strengths of the magnetic field, a spacecraft equipped with a magnetometer can estimate its position relative to the planetary body it is orbiting. This approach is particularly beneficial for missions to planets or moons with significant magnetic fields, where the data provided by the magnetometer can be crucial for navigation.

SEMI-AUTONOMOUS NAVIGATION

Semi-autonomous navigation includes strategies between fully autonomous and traditional ground-based approaches. These methods, including on-board radiometric and optimetric techniques, use a similar strategy, which involves receiving one-way forward radio or laser signals from ground stations to the spacecraft. This strategy allows spacecraft to partially determine their own position and velocity with a reduced dependence on continuous ground support, thus enhancing their operational independence while maintaining a high level of navigational accuracy.

The on-board optimetric method is a great example of this approach, where signals are sent to the spacecraft, and the necessary navigation data is processed on-board. This strategy has demonstrated its effectiveness in missions around the Moon, achieving meter-level accuracy in positioning [96], highlighting the potential applicability in other deep space mission scenarios.

Another approach for semi-autonomous navigation is the GNSS-based approach: this is highly effective in environments where Global Positioning System is already established. Currently, this applies to missions in Earth orbit and under certain conditions the cislunar space, including the L1 point orbits. In these regions, spacecraft can utilize signals from GNSS satellites to determine their position and velocity with a high degree of accuracy [91].

In brief, semi-autonomous strategies like on-board radiometric, optimetric, and GNSS-based navigation offer operational independence and a high degree of accuracy. They reduce the spacecraft dependence on ground-based navigation support. However, they still maintain a connection to Earth for critical navigational data. This approach is particularly advantageous in scenarios where full autonomy is not feasible, yet a high degree of operational independence is desired.

1.3.2. NON-AUTONOMOUS NAVIGATION

Ground-based radiometric navigation stands as the traditional and widely adopted non-autonomous navigation strategy for determining spacecraft states in deep space missions. This approach has been pivotal in these missions, including deep space observatories, missions targeting asteroids and comets, as well as various planetary explorations. This process starts with transmitting radio signals from the ground station to the spacecraft. These stations are typically part of a network, like Deep Space Network (DSN), distributed around the world. The spacecraft receives these signals and transmits back to the ground station, typically using a transponder. The time it takes for the signal to travel from the ground station to the spacecraft and back is measured. Additionally, the frequency of the received signal can be compared to the transmitted one to determine the relative velocity of the spacecraft with respect to the ground station. The angles to the spacecraft from the ground station can also be measured. By combining this data, the position and velocity of the spacecraft can be calculated. However, for deep space missions, the limitations of this method, such as time delays in signal transmission and the need for line-of-sight communication, become more significant. In the upcoming years, it is expected that numerous small satellite missions, including Lunar Ice Cube, LunaH-map, EQUULEUS, and others, will rely on traditional ground-based tracking for their navigational needs. This choice is influenced by the advantageous measurement geometry between Earth and the spacecraft destinations for the full mission duration.

When ground-based tracking is the baseline strategy for navigation, the frequency of tracking updates is a crucial factor in meeting mission requirements. Weekly tracking is generally sufficient for most deep space missions to maintain navigational needs. However, in scenarios with strict navigation requirements, like needing positional accuracy within 100 m and velocity accuracy of 0.1 cm/s, more frequent tracking intervals, such as every 2-3 days, may become necessary. This is the case for cislunar missions like Lunar IceCube [92].

Regarding measurement errors, achieving sub-meter level ranging accuracies is considered feasible, although it requires extended correlation and integration times [93]. Many small satellites, particularly those not requiring extreme accuracy in ranging measurements, may not need this. As in the case of crosslink radiometric navigation, the accuracy of radiometric measurements can be compromised by systematic errors and thermal noise. The performance in terms of range-rate varies in noise profile, ranging from approximately 0.01 mm/s and 10 mm/s depending on the Sun-Earth-Probe (SEP) angle [107].

Considering these measurement capabilities, ground-based navigation techniques provide solutions that meet a wide range of mission requirements. For example, the LRO around the Moon has achieved navigation accuracy of better than 0.5 km using this method, and the planetary Lucy mission has maintained a 5 km positional accuracy [95]. Thus, with its heritage, ground-based radiometric navigation will continue to be an essential strategy in deep space exploration.

1

1.4. THESIS GOAL AND RESEARCH QUESTIONS

The previous sections highlighted the growing interest in deep space small satellite missions, mainly focusing on satellite formations. This growing interest, coupled with constraints such as limited ground station availability, complex mission tasks, visibility issues, and rising costs, leads the missions to seek increased autonomy. As discussed previously, autonomous navigation is increasingly recognized as a critical solution in deep space missions, where significant delays in signal transmission can impact mission efficiency and success.

Autonomous navigation offers several key benefits, including improved performance, reliability, and cost reduction. Among the various autonomous navigation strategies discussed earlier, crosslink navigation stands out as a promising technology, especially for missions involving multiple spacecraft that need to maintain precise relative configurations, such as satellite constellations. A significant advantage of crosslink navigation is its ability to utilize existing on-board systems, such as radio tracking, which leads to improved cost efficiency.

The relationship between radio-tracking and communications for spacecraft is closely linked, as these systems often rely on the same or similar radio signals and technologies. Typically, both radio-tracking and communications use the same antennas and radio transmitters/receivers on the spacecraft. Communications primarily involve the exchange of data between the spacecraft and Earth. This includes sending scientific data, telemetry, and operational commands. The same radio signals used for communication can also carry tracking information, making crosslink navigation closely linked with radio communications.

The typical communications approach for satellite formations, where multiple satellites operate in close proximity, involves a combination of Inter-Satellite Link (ISL) and ground-based communications. Satellites within the formation use ISLs to communicate directly with each other. These links are crucial for maintaining formation, sharing sensor data, and coordinated maneuvers. ISLs can be based on various technologies, such as radio frequency or optical communications, with the choice depending on factors like power consumption and the distance between satellites. In deep space small satellite formations, radio frequency ISLs are the baseline due to power limitations in small satellites. In addition to ISLs, satellites in formation also communicate with ground stations. This Direct-to-Earth (DTE) communication link is used for several purposes: sending scientific data, measurement data, receiving operational commands, and status monitoring. The trend in deep space small satellite missions reveals a significant tendency towards using ISLs for telemetry, telecommand, or tracking, with approximately 58% of analyzed missions planning to use ISL. This trend is primarily driven by the limited power available for communications on small satellites. These missions can be categorized based on their link profile and destinations, as detailed in Table 1.4.

As previously discussed, SST data primarily offer relative navigation solutions, and it can also facilitate absolute navigation solutions when combined with ground-based tracking. Absolute state knowledge is crucial for tasks such as station-keeping with respect to a fixed reference frame. However, relying on ground-based commands for such operations takes the system away from autonomy. Alternatively, SST data can be used for absolute state estimation, where an on-board navigation filter estimates spacecraft

Table 1.4: Categorization of 65 satellites by their communication link profiles and destinations. Color coding represents the number of satellites: red for more than > 2 satellites, blue for exactly = 2 satellites, and black for a single satellite. Satellites marked in black within the inter-satellite link column indicate a crosslink with the mothercraft or carrier spacecraft.

	Inter-Satellite Link (ISL) Only	**Direct-to-Earth Link (DTE) Only**	**ISL & DTE Link**	**Total Number**
Cislunar	LUMIO, VMMO, CLE, MoonCare, NanoSWARM	Lunar Flash Light, Lunar Ice Cube, LunaH-Map, LunIR, ArgoMoon, OMOTENASHI, Cislunar Explorers, EQUULEUS, HALO, WATER, IMPEL, CubeX	MiLuV, BOLAS, OLFAR, DSL CAPSTONE	22
Mars	MarsDROP	MAT, MARIO	MarCO, MMO, Aeolus, MISEN, MIIAR	8
Small Bodies	Juventas, MILANI, ASPECT, Dust Cube, PALS, CUBATA, AGEX, B1, B2, BIRDY-T, AI3	NEA Scout, M-Argo, DAVID,Ross PrOVE, LICIACube	APEX, PRISM	19
Venus	Cupid's Arrow, SAEVe	CUVE, VAMOS		4
Jupiter		JUMPER		1
Uranus	SNAP			1
Europa	ETP, Mini-Maggie, DARCSIDE, Sylph			4
Sun-Earth L2			DEx, SULFRO	2
Lunar flyby trajectory		CuSP, BioSentinel, CU-E^3, Team Miles		4
Total Number	24	27	14	65

position and velocity i.e. with respect to a fixed frame.

Up to now, numerous studies have focused on SST-based absolute navigation [11], [108]–[110]. In two-body dynamics, which describes the motion of two bodies influenced primarily by their mutual gravitational attraction, relying solely on inter-satellite range measurements does not yield a complete absolute state estimation, leading to what is known as a rank defect problem [11]. This challenge continues even when relative range-rate measurements supplement range data, as the system remains unobservable. This issue extends to inter-satellite angle-only systems as well [111]. The relative orbital configurations of the spacecraft also impact system performance, with specific configurations causing the system to be less observable, such as two spacecraft orbiting on the same plane. However, modeling perturbations generally improve system performance.

In multi-body dynamics, SST-data provides an absolute state estimation when at least one of the spacecraft orbits has a unique size, shape, and orientation. This is especially relevant in regions with asymmetrical gravity fields, such as those encountered in the vicinity of a massive body, Lagrangian points or small solar system bodies. An asymmetrical gravity field here refers to a situation where the distribution of mass, and consequently the gravitational force, is not uniform in the vicinity of an object. In particular, the SST-based autonomous OD takes its strength from the differences in dynam-

ics, their unique orbits, and measurement geometry. For instance, spacecraft in orbits around small solar system bodies like asteroids are highly suited for crosslink navigation due to the significant effects of asymmetrical gravity fields. However, formations orbiting closer to primary bodies like Mars, which experience less asymmetric gravitational perturbations, may not be as well-suited to this strategy. Table 1.5 highlights that almost 81% of missions capable of inter-satellite communication could potentially benefit from crosslink navigation using their existing communication systems.

Table 1.5: Categorization of small satellite missions having inter-satellite links based on the applicability of satellite-to-satellite tracking based autonomous orbit determination architecture, red indicates > 2 number of satellites, blue = 2 satellites, black a single satellite (ISL with mothercraft)

	⟸ Weakly applicable		Highly Applicable ⟹
Cislunar		LUMIO, VMMO, CLE, MoonCare, NanoSWARM MiLuV, BOLAS, OLFAR, DSL CAPSTONE	
Mars	MarsDROP, MMO, Aeolus, MISEN, MIIAR		
Small Bodies			Juventas, MILANI, ASPECT, Dust Cube, PALS, CUBATA, AGEX, B1, B2, BIRDY-T, AI3 APEX, PRISM
Venus	Cupid's Arrow, SAEVe		
Uranus	SNAP		
Europa		ETP, Mini-Maggie, DARCSIDE, Sylph	
Sun-Earth L2		DEx, SULFRO	

Simply put, differences in accelerations of multiple spacecraft due to their motion in a non-homogeneous gravity field over time provide absolute navigation solutions in the SST-based OD problem. However, this is not always straightforward, especially when inter-satellite measurements are not accurate, or the observation geometry is not optimal. Since inter-satellite measurements cannot always be collected from the operational perspective, careful planning of optimal tracking windows is required. This planning can be challenging when considering possibly conflicting operational needs, such as commanding. Furthermore, since radio frequency measurement techniques are used to derive navigation data, system performances must be investigated, considering varying systematic and random errors. Additionally, it is unclear which navigation data among range, range-rate, or angle, provide superior navigation solutions in different deep space environments. Since real-time navigation solutions may be needed, designing a robust on-board estimation filter can be challenging, including decisions on which parameters to be estimated or neglected.

These complexities demand detailed studies and careful investigations, particularly

regarding the system performances. Therefore, this dissertation seeks to expand the current understanding of satellite-to-satellite radio-tracking based autonomous OD for small satellite formations in deep space. It focuses on various aspects of the OD problem, namely dynamics, measurements, and estimation, and aims to address the following Research Questions (RQs):

1. What are the current scientific and technological advances in autonomous navigation for small satellites missions in deep space?

   To understand the advancements in autonomous navigation for small satellites in deep space, the following steps will be taken:

   (a) A review of small satellites in deep space:

      i. Conduct a comprehensive review of deep space small satellites, focusing on their design, missions that have been undertaken, and the challenges they face.

      ii. Analyze past and ongoing missions to identify trends and advancements in small satellite technology.

   (b) Navigation and tracking system performance:

      i. Assess the current performance of navigation and tracking systems used for small satellites in deep space.

      ii. Compare various systems to understand their efficiency, accuracy, and limitations.

   (c) Autonomous navigation system needs and requirements:

      i. Define the specific needs and requirements for autonomous navigation systems for small satellites in deep space.

      ii. Consider factors such as mission duration, environmental challenges, and the need for precision in navigation.

2. What are the characteristics of a simple radio-tracking system for satellite formations in deep space?

   To explore the simplicity and effectiveness of radio-tracking systems for satellite formations in deep space, the study will focus on:

   (a) Radiometric measurements:

      i. Conduct a comprehensive review of radio-tracking systems, focusing on ranging concepts.

      ii. Analyze the limits of ranging performance that comply with the navigation system requirements.

      iii. Identify and define the key parameters that affect ranging performance.

   (b) A simple ranging concept:

      i. Provide a straightforward concept for ranging within satellite formations.

      ii. Discuss the simplicity and feasibility of this concept for practical use.

3. How can we describe the fundamental aspects and design principles of a satellite-to-satellite tracking-based autonomous on-board orbit determination system for satellite formations in deep space?

   To investigate the fundamental aspects and principles behind designing an SST-based autonomous on-board OD system, the study will focus on:

   (a) SST-based OD:
      i. Discuss the characteristics of SST-based OD.
      ii. Provide OD models, including dynamic, measurement, and estimation aspects.

   (b) System performance analysis:
      i. Provide system performance analysis techniques.
      ii. Investigate how various factors impact the overall system performance, including:
         A. Orbital configuration.
         B. Dynamical environment and errors.
         C. Measurement geometry, accuracy, precision, and interval.
         D. Clock bias, drift, and aging.
         E. Navigation filter selection, design, and parameters.
         F. Number of spacecraft.
         G. Network topology.
      iii. Apply the basic ranging concept and evaluate the navigation system's performance.

   (c) Operational constraints:
      i. Develop a comprehensive plan for SST-based tracking in satellite formations.
      ii. Explore strategies to optimize tracking intervals.
      iii. Provide a data flow for SST-based autonomous navigation systems.

1.5. METHODOLOGY AND THESIS OUTLINE

This thesis focuses on SST-based autonomous OD for small satellite formations in deep space. It is structured into several chapters, each addressing specific aspects of this research.

Chapter 1 begins with an extensive review of the historical and future context of small satellite missions in deep space. Part of this first RQ (1.a. and 1.b.) is answered, highlighting autonomy as a crucial factor in enhancing mission capabilities. This chapter analyzed 65 proposed and flown deep space small satellite missions, revealing a focus on cislunar and small solar system bodies for surface mapping and characterization. The chapter highlighted the predominant reliance on ground-based navigation, noting that only a few missions have chosen autonomous methods, with crosslink navigation emerging as a promising strategy. Chapter 2 answers the remaining part of the first RQ

(1.c) by presenting the requirements and needs for autonomous navigation from scientific and operational perspectives. This chapter discusses radiometric measurement techniques, including ranging strategies, and how range, range-rate, and LOS data are derived from radiometric measurements, along with their error sources and enabling technologies. This chapter addresses the second RQ (2.a) and introduces a simple ranging concept (2.b), based on a comprehensive literature review of techniques and error sources. Chapter 3 introduces how SST-based autonomous OD works, studies conducted so far, challenges, and OD models, answering RQ 3.a. Chapter 4 focuses on performance analysis methods, including observability, CRLB, Monte-Carlo, and covariance analysis, addressing RQ 3.b.i. In this chapter, semi-analytical observability and covariance analysis are also conducted. Chapter 5 presents the key findings of the dissertation, addressing RQ 3.b. It details SST-based autonomous OD performance with sensitivity and performance analyses for various scenarios. Chapter 6 explores operational aspects and tracking planning for both ground-based and on-board systems, answering RQ 3.c. Finally, a summary, limitations, and outlook are given in Chapter 7, along with the key innovations resulting from this work. The thesis outline, publications, and RQs can be seen in Figure 1.8.

The methodology adopted throughout the dissertation combines analytical and numerical approaches, along with comprehensive literature reviews. The first and second chapters are mainly based on reviews conducted through an extensive examination of journals, conference proceedings, and resources from governmental organizations, universities, and the LUMIO phase 0 and phase A design studies. In chapter 3, analytical methods are applied to dynamical models, such as the Circular Restricted Three-body Problem (CRTBP), and to measurement models for range measurements, while numerical models are used for state propagation and high-fidelity dynamics, primarily using Matlab. In high-fidelity dynamical analyses, planetary ephemeris files are used to determine the location of solar system objects. Semi-analytical and numerical approaches are compared with each other, especially for State Transition Matrix (STM) calculations, detailed further in Appendix C. Additionally, filter complexities are presented analytically, illustrating the required number of numerical operations per estimation loop. In Chapter 4, the semi-analytical strategy is employed for in-depth system observability and covariance analysis. The chapter also compares different navigation data types using analytical derivations for measurement models and numerical approaches for results. Recognizing that estimation or covariance results alone may not provide a complete picture, the dissertation employs various performance analysis tools. This strategy ensures consistency across all metrics and aims to prevent biased results, particularly in the analyses presented in Chapter 5. In the last chapter, a heuristic optimization approach is implemented for the tracking windows planning, considering operational challenges. This approach yields near-optimal results, then numerically compared with nominal tracking strategies. It is important to note that the parameters used throughout the thesis reflect realistic mission scenarios derived from academic publications and real-world projects in which the author is involved. Lastly, no commercial orbital propagation or orbit determination tool is used in this work, but, instead, the software has been developed, allowing for a detailed approach to the specific needs of SST-based autonomous OD for small satellite formations in deep space.

1

Figure 1.8: Thesis Outline (journal papers, conference papers)

Chapter 1
Introduction
RQ-1
Turan, E., Speretta, S., & Gill, E. (2022). Autonomous navigation for deep space small satellites: Scientific and technological advances. *Acta Astronautica*, *193*, 56-74. https://doi.org/10.1016/j.actaastro.2021.12.030

Chapter 2
Radiometric Tracking
RQ-1, RQ-2
- Turan, E., Speretta, S., & Gill, E. (2022). Autonomous navigation for deep space small satellites: Scientific and technological advances. *Acta Astronautica*, *193*, 56-74. https://doi.org/10.1016/j.actaastro.2021.12.030
- Turan, E., Speretta, S., & Gill, E. K. A. (2022). Autonomous Navigation Performance of Cislunar Orbits considering High Crosslink Measurement Errors. In *2022 IEEE Aerospace Conference, AERO 2022* (IEEE Aerospace Conference Proceedings; Vol. 2022-March). https://doi.org/10.1109/AERO53065.2022.9843772
- Turan, E., Speretta, S., & Gill, E. (2023). Performance analysis of crosslink radiometric measurement based autonomous orbit determination for cislunar small satellite formations. *Advances in Space Research*. https://doi.org/10.1016/j.asr.2022.11.032

Chapter 3
Satellite-to-Satellite Tracking-based Autonomous Radiometric Orbit Determination
RQ-3
- Turan, E., Speretta, S., & Gill, E. (2022). Autonomous navigation for deep space small satellites: Scientific and technological advances. *Acta Astronautica*, *193*, 56-74. https://doi.org/10.1016/j.actaastro.2021.12.030
- Turan, E., Speretta, S., & Gill, E. (2023). Performance analysis of crosslink radiometric measurement based autonomous orbit determination for cislunar small satellite formations. *Advances in Space Research*. https://doi.org/10.1016/j.asr.2022.11.032

Chapter 4
Performance Analysis Methods
RQ-3
Turan, E., Speretta, S., & Gill, E. (2023). Performance analysis of crosslink radiometric measurement based autonomous orbit determination for cislunar small satellite formations. *Advances in Space Research*. https://doi.org/10.1016/j.asr.2022.11.032

Chapter 5
Autonomous Navigation Performance for Satellite Formations in Deep Space
RQ-1, RQ-2, RQ-3
- Turan, E., Speretta, S., & Gill, E. (2023). Performance analysis of crosslink radiometric measurement based autonomous orbit determination for cislunar small satellite formations. *Advances in Space Research*. https://doi.org/10.1016/j.asr.2022.11.032
- Turan, E., Speretta, S., & Gill, E. K. A. (2022). *Performance Analysis of Radiometric Autonomous Navigation for Lunar Satellite Network Topologies*. 11th International Workshop on Satellite Constellations and Formation Flying, Milan, Italy.
- Turan, E., Speretta, S., & Gill, E. K. A. (2022). *Radiometric Autonomous Navigation for Cislunar Satellite Formations*. NAVITEC 2022.
- Turan, E., Speretta, S., & Gill, E. K. A. (2022). Autonomous Crosslink Radionavigation for a Lunar CubeSat Mission. *Frontiers in Space Technologies*, *3*, [919311]. https://doi.org/10.3389/frspt.2022.919311

Chapter 6
Operational strategies and navigation data flow
RQ-3
Turan, E., Speretta, S., & Gill, E. (2023). Particle Swarm Optimization based Tracking Window Planning for Cislunar Orbiters Performing Autonomous Radiometric Navigation, IAC 2023

Chapter 7
Conclusion

2

RADIOMETRIC TRACKING

Radiometric tracking stands as a vital technique for enhancing the capabilities of satellite formations operating in deep space. This chapter provides the details of satellite-to-satellite (SST) tracking from a radiometric measurement standpoint, highlighting the significance of accurate inter-satellite data for effective Orbit Determination (OD). Central to this discussion are three principal data types: range, range-rate, and Line-of-Sight (LOS) angles. Each measurement type is carefully analyzed, with an emphasis on the underlying measurement and error models that support their integration into an autonomous onboard OD strategy. The discussion extends to various mission and tracking scenarios that highlight the application and significance of these measurements, setting the stage for a comprehensive understanding of their role in deep space missions. Concluding the chapter, an overview of enabling technologies presents the tools and innovations that make inter-satellite radiometric tracking feasible.

Parts of this chapter have been published in:
E. Turan, S. Speretta, and E. Gill, "Autonomous navigation for deep space small satellites: Scientific and technological advances", *Acta Astronautica*, vol. 193, pp. 56–74, Apr. 2022. DOI: 10.1016/j.actaastro.2021.12.030
E. Turan, S. Speretta, and E. Gill, "Autonomous Navigation Performance of Cislunar Orbits considering High Crosslink Measurement Errors", in *2022 IEEE Aerospace Conference (AERO)*, IEEE, Mar. 2022, pp. 1–11. DOI: 10.1109/aero53065.2022.9843772
E. Turan, S. Speretta, and E. Gill, "Performance analysis of crosslink radiometric measurement based autonomous orbit determination for cislunar small satellite formations", *Advances in Space Research*, vol. 72, no. 7, pp. 2710–2732, Oct. 2023. DOI: 10.1016/j.asr.2022.11.032

2

This chapter provides the details of radiometric tracking techniques for satellite formations in deep space, focusing on both ground-based and space-based tracking methodologies. It elaborates on several types of navigation data, including range, Doppler, and angle observables, highlighting their derivation from radiometric methods. For each type of navigation data, the methodology includes both the observed and calculated values of observables, thereby establishing a comprehensive understanding of operational challenges and solutions. The chapter further discusses various sources of measurement errors and operational limitations, providing insights into current state-of-the-art systems for radiometric tracking. Aimed at enhancing the understanding of autonomous onboard OD from a satellite-to-satellite tracking perspective, this chapter sets the stage for the subsequent detailed exploration of autonomous navigation in the following chapters.

Initiating with a brief introduction to the navigation process, the chapter emphasizes the pivotal role of satellite-to-satellite tracking in autonomous navigation and, thus, in this dissertation. These introductory paragraphs aim to prepare the reader for a deeper dive into the nature of observables, which form the critical link between practical tracking operations and theoretical navigation models. Although a more detailed investigation on autonomous navigation follows in the next chapter, an initial overview here sets the stage for deeper insights into the process.

In this context, repeating one more time, OD refers to the process leading to the satellite orbit, position, and velocity knowledge as a function of time, with respect to a fixed reference frame (absolute) or with respect to another spacecraft or moving object (relative). This process also covers where the object was located in the past (definitive), is located at present, and will be located in the future (predictive) [1].

From a ground operations perspective, the navigation workflow, depicted in Figure 2.1, unfolds through iterative OD steps, starting with an a priori spacecraft trajectory [114]. This initial step involves computing the expected values of these tracking observables based on nominal trajectory and precise observable models. Differences between these calculations and actual tracking data form the basis for data residuals, which, in an ideal scenario of model accuracy, would display a Gaussian distribution due to measurement noise. However, model inaccuracies imprint distinct patterns on the residuals, guiding adjustments in model parameters via estimation procedures, hence optimizing trajectory solutions. This highlights the importance of accurately understanding measurement errors, as these errors directly impact the OD accuracy and the execution of necessary maneuvers.

As the application transitions to satellite-to-satellite tracking-based autonomous navigation, Figure 2.2 illustrates this similar process through which observations are collected and utilized for orbit determination on a primary spacecraft, also known as the mothercraft. This process highlights the necessity for accurate spacecraft dynamic models, precise measurement models, and robust navigation filters to ensure reliable autonomous navigation without human intervention. A more detailed exploration of these themes will be given in Chapter 3.

Subsequent sections in this chapter will discuss observation methodologies and their processings, alongside a detailed examination of error sources. Discussion extends to both observed and computed values of radiometric observables, categorized into range,

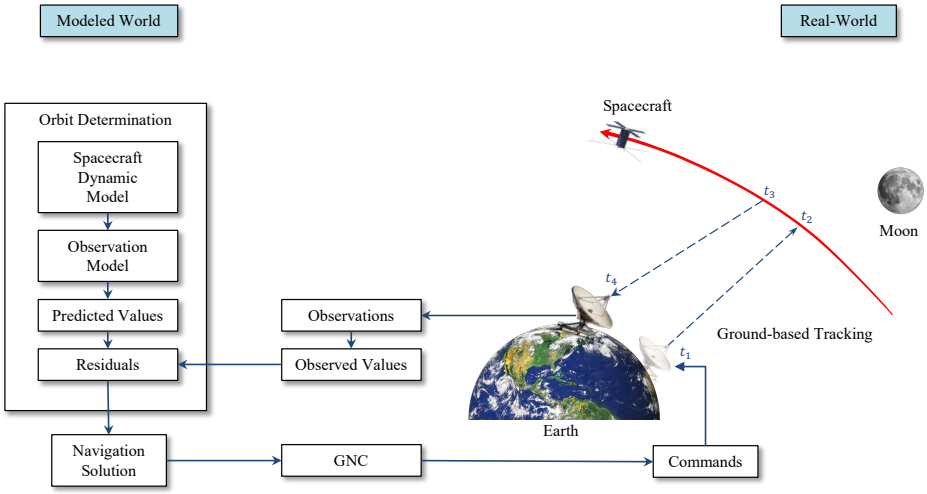

Figure 2.1: Simplified ground-based tracking and corresponding orbit determination process, inspired by [114]. This process involves the computation of the observed values of the observations and the computed (predicted) values of the corresponding observations and uses the observed-minus-computed residuals, along with the partial derivatives of the computed values of the observables with respect to the estimation vector, to determine the spacecraft trajectory. Based on the estimated trajectory, the optimal trajectory control can be calculated and the corresponding command can be delivered to the spacecraft.

Doppler, and angular data, incorporating operational considerations and measurement errors. Starting with an in-depth analysis of range observations, this chapter aims to equip the reader with a thorough understanding of radiometric tracking's fundamental principles and applications for satellite formations in deep space.

2.1. RANGE MEASUREMENTS

Ground-based tracking for ranging purposes involves measuring the round-trip time between a spacecraft and a tracking station on Earth to determine the spacecraft's position and velocity. This process is essential for maintaining accurate knowledge of the spacecraft's orbit for navigation, mission planning, and safety. In particular, this process starts with the tracking station sending a radio signal to the spacecraft. This signal is often a specific frequency or code that can be easily identified when it turns. Upon receiving the signal, the spacecraft either reflects it back or generates a response signal and sends it back to the Earth station. For the latter, the onboard transponder modifies the signal, changing its frequency or encoding a timestamp before sending it back, which helps differentiate it from other signals and reduces ambiguity. The ground station receives the echoed signal after it travels the round-trip distance between the Earth and the spacecraft. The time taken for this round-trip journey is precisely measured.

Satellite-to-satellite tracking (SST) within the context of satellite formations involves precise measurement of the time a signal takes to travel between two spacecraft to derive their relative distances. This technique is an adaptation of ground-based ranging methods but is applied between satellite formations. During such operations, a transmitting

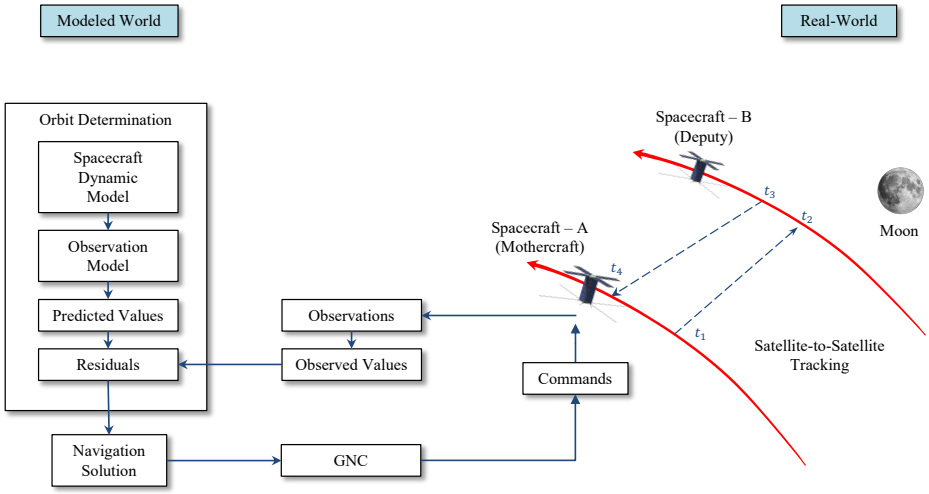

Figure 2.2: Simplified satellite-to-satellite tracking and corresponding orbit determination process. Similar to ground-based tracking, this process involves the computation of the observed values of the observations and the computed (predicted) values of the corresponding observations and uses the observed-minus-computed residuals, along with the partial derivatives of the computed values of the observables with respect to the estimation vector, to determine the trajectory of spacecraft within formation. Based on the estimated trajectory, the spacecraft can be controlled with respect to the intended trajectory. In the satellite-to-satellite tracking case, the system model involves more than one spacecraft dynamics.

satellite, often designated as the mothercraft, emits a radio frequency signal towards a secondary satellite, called the deputy. Upon reception, the deputy satellite's response is dictated by its onboard equipment. If equipped with a transponder, the deputy satellite actively processes and retransmits the signal back to the mothercraft with a different frequency. This retransmission process leverages the spacecraft's transponder to maintain phase coherence between the uplink and downlink signals, despite their differing frequencies. The frequency change is guided by the transponder's turnaround ratio, a predefined value that depends on the frequency bands utilized for the uplink at the mothercraft and the downlink from the deputy. This phase coherence is essential for ensuring the accuracy of the ranging process by preserving the integrity and phase relationship of the signals, thereby facilitating precise distance measurements.

Moreover, the ranging process can employ either a constant or a dynamically adjusted uplink (ramped) frequency to counteract the Doppler effect, ensuring minimal frequency deviation as the signal reaches the spacecraft. This technique, known as uplink Doppler compensation, adds a layer of complexity to data analysis, particularly for scenarios involving time-varying frequencies. Tracking systems today are adept at managing both constant and variable uplink frequencies. Nonetheless, this investigation predominantly considers scenarios with static uplink frequencies, sidestepping the complex mathematical formulations necessary for analyzing time-varying frequency data. This also emphasizes the practical challenges and considerations associated with Doppler compensation in ranging methodologies.

In scenarios where the deputy satellite serves as a radar target, the system relies on radar-based ranging techniques, where signal strength diminishes at the fourth power of the distance between the satellites. This rapid attenuation poses significant challenges for distance measurements across long inter-satellite distances. Conversely, transponder-based SST ranging benefits the advantages of signal regeneration and retransmission by the deputy, with signal strength degradation proportional to the square of the distance, enabling more robust and accurate measurements across long distances. The essence of SST ranging hinges on the precision of time measurement for the signal's round trip between the mothercraft and the deputy. This delay directly correlates to the inter-satellite distance, considering the constant speed of light for signal propagation.

SST ranging systems may operate in different configurations, such as two-way or one-way. One-way SST ranging operations involve the transmission of a signal from one satellite to another without expecting a return signal. While one-way operations offer a simpler approach to SST ranging by eliminating the need for a signal to be returned to the originating satellite, they impose stringent requirements on time synchronization that can be challenging to meet in practice. Two-way operations, though potentially more complex, provide advantages in terms of error correction and reduced reliance on precise synchronization, making them more suitable for applications requiring high accuracy in distance measurements between spacecraft. These SST-ranging methods are often called direct approaches. The choice of configuration depends on mission requirements, spacecraft capabilities, and the desired accuracy levels.

Besides *direct* ranging methods that measure the time it takes for a signal to travel from one satellite to another and/or back, *indirect* ranging techniques offer alternative ways to deduce this critical information. Indirect methods may include the utilization of GNSS or ground-based observations for Earth-orbiting satellites [115]. These approaches often involve the subtraction of two sets of position data (GNSS-only) or range observables (ground-based tracking) to ascertain the inter-satellite distance. While GNSS measurements or ground-based tracking data can serve this purpose for satellites orbiting Earth, deep space missions must rely on ground-based assets for indirect inter-satellite ranging. These inter-satellite ranging strategies are summarized in Figure 2.3, along with technologies available.

These operations encounter several challenges that can affect ranging accuracy and reliability. SST operations are sensitive to various systematic errors, including biases in the signal generation and reception hardware, inaccuracies in the onboard clock, and errors in the spacecraft's attitude control. These errors can introduce biases in the time-of-flight measurements, leading to inaccuracies in the determined distances (which can be as high as a few microseconds [116]). Furthermore, the signal transmitted between satellites can reflect off other surfaces, leading to multipath interference where multiple signals arrive at the receiver at slightly different times. Another significant challenge in ranging operations is the repetitive nature of the radio frequency signal, which introduces distance ambiguity. This ambiguity necessitates compensation through advanced algorithms, as the system can only measure distance within a wavelength without ambiguity resolving techniques. The system performance is also constrained by the capabilities of the onboard hardware, including the power of the transmitters, sensitivity of the receivers, and the accuracy of the onboard clocks. Enhancements in hardware tech-

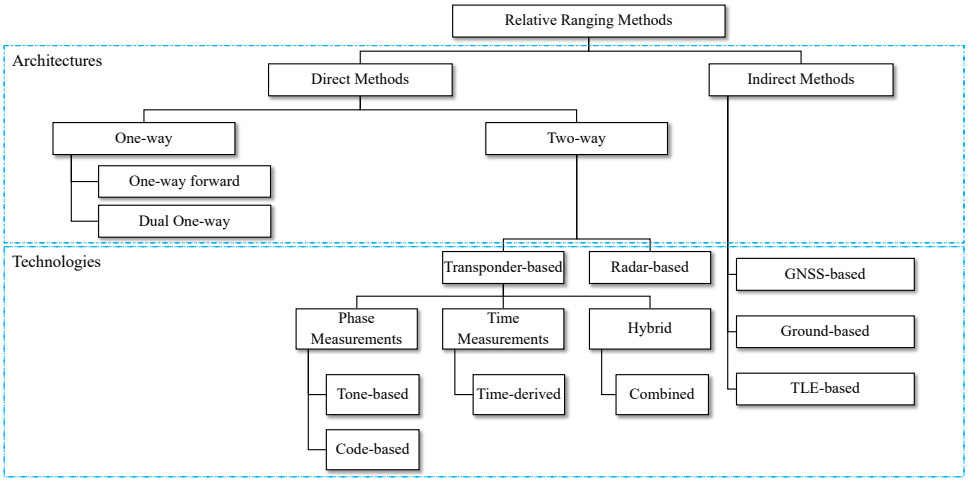

Figure 2.3: Inter-Satellite Ranging Methods.

nology can lead to improvements in SST performance but come with increased cost and development time.

The computed value of two-way range is a measure of the round trip signal time between a set of two or more participants and uses a single clock on the initiating participant to determine the elapsed time of signal transit. While the basic model is common to many two-way tracking systems, different systems handle time delays and precision differently. Also, if and how the round trip signal time delay is converted to a range or distance unit varies among tracking systems. Considering two spacecraft, each equipped with a transponder and antenna, a timeline representing the two-way range measurement is given in Figure 3.8. Based on this timeline, a two-way range measurement is given by:

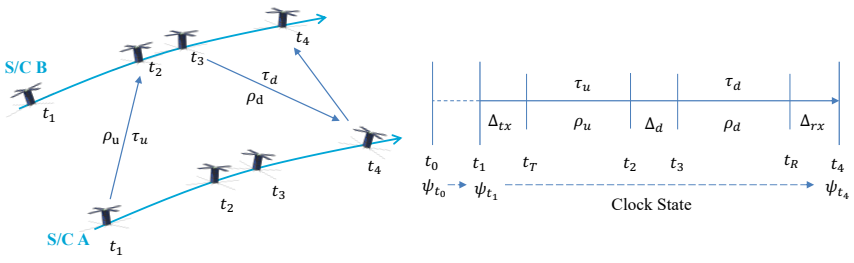

Figure 2.4: Two-way measurement time-line

$$\begin{aligned}\tau &= \tau_u + \tau_d + \tau_x \\ &= \Delta_{tx} + \frac{\rho_u}{c} + \Delta_d + \frac{\rho_d}{c} + \Delta_{rx}\end{aligned} \tag{2.1}$$

where

$$\begin{aligned}\tau_u &= \frac{\rho_u}{c} \\ \tau_d &= \frac{\rho_d}{c} \\ \tau_x &= \Delta_{tx} + \Delta_d + \Delta_{rx}\end{aligned} \tag{2.2}$$

$$\begin{aligned}\rho_u &= c(t_2 - t_T) = |\mathbf{r}_2(t_2) - \mathbf{r}_1(t_T)| \\ \rho_d &= c(t_R - t_3) = |\mathbf{r}_1(t_R) - \mathbf{r}_2(t_3)|\end{aligned} \tag{2.3}$$

where Δ_{tx} and Δ_{rx} are the transponder transmit and receive line delays on the S/C-A, respectively. Δ_d is the line delay on the S/C-B, returning the ranging signal. Both terms in Eq. 3.22 need to be solved via the fixed-point iteration, which can be found in [117].

The following subsections dive into details of ranging techniques, starting from phase observations and continuing with time, as well as hybrid measurements.

2.1.1. PHASE MEASUREMENTS

This section discusses the details of phase measurements, emphasizing the phase delay introduced by the time of flight for any transmitted periodic signal between a transmitter and a receiver. Grounded in a review of extensive literature, this discussion, referenced from [118]–[125], is dedicated to two-way operations, following an introduction to the challenges associated with one-way ranging and the importance of time synchronization detailed in preceding paragraphs.

Two-way ranging involves measuring the time delay for a signal's round trip between two nodes, which could either be within a spacecraft formation or between a ground station and a spacecraft. Specifically, in SST, the signal modulates the phase of an uplink carrier from the *mothercraft*, is demodulated by the *deputy* spacecraft, and then used to modulate the phase of a downlink carrier back to the mothercraft. This process can be either *transparent* or *regenerative*. In a transparent operation, the received signal at the deputy is filtered, amplified, and directly modulated onto the downlink signal. Conversely, a regenerative process involves the deputy generating a clean copy of the uplink signal in phase with the received version before modulating the downlink phase. Regardless of the method, the essence of two-way ranging is the deputy echoing the uplink signal back to the mothercraft, eliminating the need for precise clock synchronization between the spacecraft.

A pivotal advantage of this two-way operation lies in its ability to accurately determine the two-way time delay (τ) without the need for synchronizing clocks between the spacecraft. This is achieved by calculating the delay from the two-way phase delay experienced by the signal during its round trip. However, phase measurements introduce their own complexities, including ambiguity in every phase measurement, known only within one cycle of the ranging signal, and additional delays through the signal path.

The two-way delay is thus determined by the difference between the phase of the transmitted ranging signal (ψ_T) at the transmitting electronics of the mothercraft and the phase of the received ranging signal (ψ_R) at the receiving electronics of the mothercraft, measured at the reception time (t_R). This process involves correlating the downlink ranging signal with a local model at the mothercraft. The resulting phase difference ($\Delta\psi$) represents the round-trip time, which is the sum of the one-way uplink (τ_u) and downlink (τ_d) times, providing a fundamental basis for accurate range determination in SST operations (see illustration given in Figure 2.5).

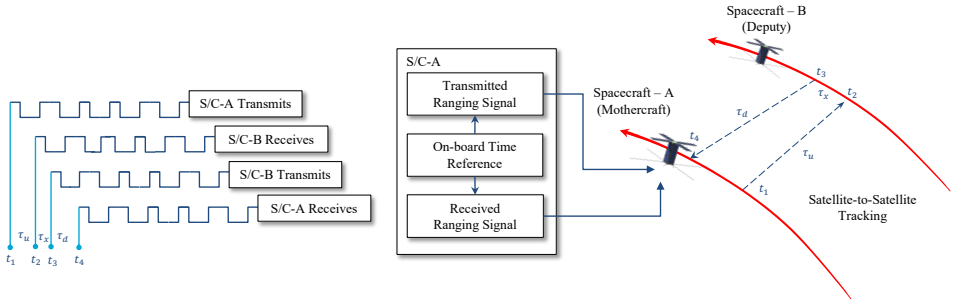

Figure 2.5: An illustration of the satellite-to-satellite tracking-based two-way ranging from the timing perspective, presenting the round-trip light time equal to the sum of the one-way uplink and downlink light times. Inspired by [122].

The following equation is the fundamental theorem of calculus [123]:

$$\psi_T(t_R) - \psi_T(t_R - \tau(t_R)) = \int_{t_R-\tau(t_R)}^{t_R} \frac{\mathrm{d}\psi_T}{\mathrm{d}t}\, dt \tag{2.4}$$

It is critical to understand that the phase of the ranging signal measured at the receiver $\psi_R(t_R)$, was originally present at the uplink antenna a time $t_R - \tau(t_R)$ ago, thereby establishing the connection between the transmitted and received signals:

$$\psi_R(t_R) = \psi_T(t_R - \tau(t_R)) \tag{2.5}$$

By employing the above relations, one can deduce that the difference in the transmitted and received signal phases corresponds to the integrated history of the transmitted signal's frequency over the round-trip time. Using Eq. 2.4 and 2.5

$$\psi_T(t_R) - \psi_R(t_R) = \int_{t_R-\tau(t_R)}^{t_R} \frac{\mathrm{d}\psi_T}{\mathrm{d}t}\, dt \tag{2.6}$$

In 2.6, only the lower limit on the definite integral ($t_R - \tau(t_R)$) is unknown. The left-hand side, $\psi_T(t_T) - \psi_R(t_R)$, is the difference between the ranging signal phase at the uplink antenna location at time t_T and the phase at the receiving antenna location at time t_R, derived from signal correlation. Given that the frequency history of the transmitted ranging signal ($\psi_T(t)$) is logged, the objective becomes determining the precise starting point on the timeline for the definite integral such that, once integrated over the

signal's frequency history, it equates to the observed difference in phase. This would give the round-trip delay τ at time t_R.

Notably, in previous research, the phase of the ranging signal is represented as an unwrapped phase form. Typically, a coherent receiver tracks the phase modulo 2π. However, as the phase varies it could also track an unwrapped phase in which the phase is allowed to increase without limit. This is critical since ranging measurements are derived from observations of unwrapped phases, and also, for illustrative purposes, it provides insights into the ranging process.

To further elucidate the two-way ranging process, Figure 2.6, as mentioned in [123], visualizes the timing based on unwrapped phase measurements. Through this graphical representation, the phase difference is converted into the two-way time of flight using the reference signal frequency, providing insights into the calculation of the distance between the spacecraft based on phase measurements. This illustration shows the sloped lines representing the phase of the transmitted ($\psi_T(t)$) and received ($\psi_R(t)$) signals over time, with the vertical line indicating the phase difference ($\Delta\psi = \psi_T(t_R) - \psi_R(t_R)$) at the reception time (t_R) and the horizontal line depicting the round-trip time, which can be calculated as $\tau = \Delta\psi / f_{T,0}$.

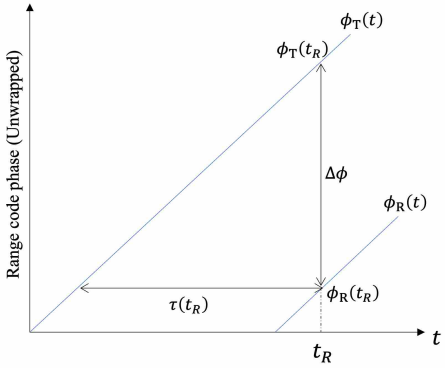

Figure 2.6: Timing in two-way ranging [123], highlighting that the sloped lines represent the phase of the transmitted ($\psi_T(t)$) and received ($\psi_R(t)$) signals over time, with the vertical line indicating the phase difference ($\Delta\psi = \psi_T(t_R) - \psi_R(t_R)$) at the signal reception time (t_R) and the horizontal line depicting the round-trip time, which can be calculated as $\tau = \Delta\psi / f_{T,0}$.

In [126], further elaboration on the two-way time of flight is provided:

$$\tau = \frac{1}{f_{T,0}}(\psi_T(t_R) - \psi_T(t_T)) - (\Delta\tau_\beta + \Delta\tau_x + \Delta\tau_y) \tag{2.7}$$

where $f_{T,0}$ is the reference signal frequency, while $\Delta\tau_\beta$ and $\Delta\tau_x$ represent biases due to Doppler shift and oscillator phase deviations over the two-way time interval. The uncalibrated systematic delays are represented as $\Delta\tau_y$. Eq 2.7 is derived from the fact that the transmitted ranging frequency can be represented as follows:

$$\frac{\mathrm{d}\psi_T}{\mathrm{d}t} = f_T(t) \approx (1 + \beta(t) + y(t)) f_{T,0} \tag{2.8}$$

where $\beta = \dot{\rho}/c$ determines the Doppler pre-compensation shift, while y is the normalized frequency deviation due to noise and the phase shift integral over the two-way time interval with $t_T = t_R - \tau(t_R)$. Introducing Eq.2.8 into Eq. 2.6 gives [126]:

$$\begin{aligned}\int_{t_T}^{t_R} \frac{\mathrm{d}\psi_T}{\mathrm{d}t} dt &= \int_{t_T}^{t_R} (1+\beta(t)+y(t)) f_{T,0} dt \\ &= f_{T,0}(\tau + \Delta\tau_\beta(t_r,\tau) + \Delta y(t_r,\tau))\end{aligned} \tag{2.9}$$

where $\Delta\tau_\beta(t_r,\tau)$ and $\Delta y(t_r,\tau)$ represent biases due to Doppler shift and oscillator phase deviations over the two-way time interval.

The two-way delay measurements based on Eq 2.7 introduce random errors, mainly in $(\psi_T(t_R) - \psi_T(t_T))$ as random noise (thermal noise) due to signal correlation, oscillator phase deviations $\Delta\tau_x$ over the two-way time interval (negligible). These random and systematic errors will be discussed in the following sections. Since thermal noise figures are dependent on the signal structures used in the ranging process, the upcoming part will provide insights into these key aspects.

SIGNAL STRUCTURES

Ranging signal structures, pivotal in both ground-based and SST operations, are classified into tone-based, code-based, or hybrid systems, blending both techniques. Historically, tone-based systems have been extensively utilized within ground-based operations, exemplified by the sequential ranging technique standard in the DSN [127]. This approach employs a sequence of sinusoidal tones to resolve distance ambiguity, with the ambiguity resolution directly tied to the period of the lowest-frequency tone transmitted. The key to this method's precision lies in the highest frequency tone used, often referred to as the range clock.

Distinct from tone-based systems, code-based ranging employs Pseudo noise (PN) codes, offering advantages in terms of ambiguity resolution and precision through the use of code sequences rather than simple tones. The hybrid approach combines elements of both, leveraging the precision of tone-based measurements with the ambiguity resolution capabilities of code-based systems.

Figure 2.7 in the literature provides a comprehensive overview of the various phase measurement techniques utilized for ranging, spanning from signal replication-based tone standards such as Sequential tone [119], ESA-tone [128], and USB tone [129], to direct phase measurement standards like INMARSAT tone and Lockheed Martin Corps (LMCO) tone [129]. Also included are pseudo-ranging standards, notably the JPL PN code and CCSDS T4B and T2B codes [2], alongside hybrid approaches like the ESA code standard [121].

Regarding Tone-ranging systems, signal replication methods employ transmitting a major tone alongside several minor tones. In direct phase measurement methods, tones are transmitted sequentially from the lowest to the highest frequency. The ESA tone, also known as ESA 100K, stands as a prime example of this methodology which can be seen in Figure 2.8.

The process begins with the transmission of the highest frequency tone, the major tone, which is then acquired by the primary transmitter source. The Phase Locked Loop (PLL), a crucial component in this setup, recovers the transponded major tone signal.

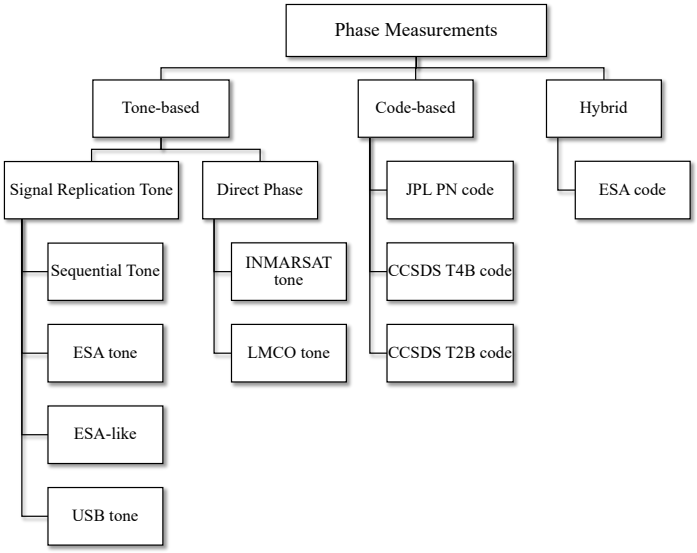

Figure 2.7: Phase measurement standards.

Through frequency division, a replica of the first minor tone is generated from this major tone, marking the first step in a sequence designed to systematically incorporate and then replace minor tones until the full spectrum has been transmitted. The precision of this system hinges on the recording of the phase difference between each received minor tone and its replicated version, ultimately leading to phase measurement on the major tone and the initiation of ambiguity-solving processes. These measurements are time-tagged, and Doppler is compensated during this process in specific configurations [130].

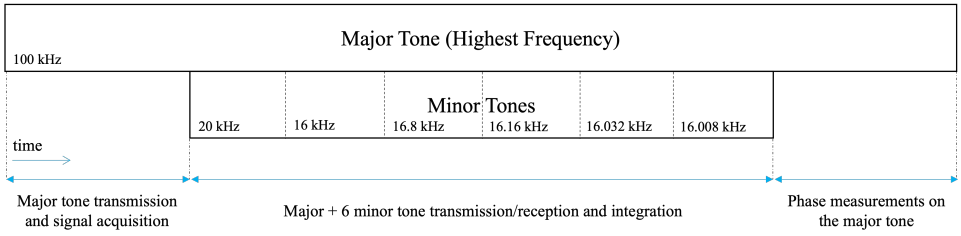

Figure 2.8: ESA Tone Standard Operational Timeline.

A key insight from this is that higher frequency tones, or major tones, are preferred for phase shift measurements due to their shorter wavelength, which translates to lower ranging error compared to lower frequency tones. Therefore, a major tone is used for phase shift measurement. Since the observed phase shift is given by $\psi_T = 2\pi n \psi_{MT}$, where n is the number of complete cycles of tone f_m in tone f_{m+1}, tone-ranging systems use more than one minor tone for ambiguity resolution. Thus, the non-ambiguous

major tone phase shift can be given as [129]

$$\psi_T = (n_m k_{m-1} k_{m-2} ... k_2 + n_2 k_2 + n_1) 2\pi + \psi_{MT} \tag{2.10}$$

where n_m is the number of complete cycles on each minor/major tone process (after Doppler compensation and corrections), k_m are matching ratios, and ψ_{MT} is phase measurement on the major tone. For instance, considering the ESA tone standard, n_1 represents the cycles at first measurement between the first tone (highest tone at the same time) f_1 (100 kHz) and the first minor tone f_2 (20 kHz) and it can be found via the following relation

$$\frac{-\pi}{k} + \frac{2\pi n}{k} < \Psi_2 - \frac{\Psi_1}{k} < \frac{\pi}{k} + \frac{2\pi n}{k} \tag{2.11}$$

The duration of the ranging process, influenced by various operational parameters such as the measurement sampling ratio, integration time, and the number of measurements on the major tone, underscores the procedural depth of tone-based systems [130]. An illustration of tone-based system architecture can be seen in Figure 2.9. Furthermore, the consideration of relative motion between the transmitter source and spacecraft necessitates precise Doppler compensation, facilitated by the Phase Locked Loop (PLL) or similar tracking mechanisms. The PLL bandwidth should be selected, as explained in [130], such that it is wide enough for tolerating the high relative motion but also low enough to allow performances at low Signal-to-Noise ratio (SNR).

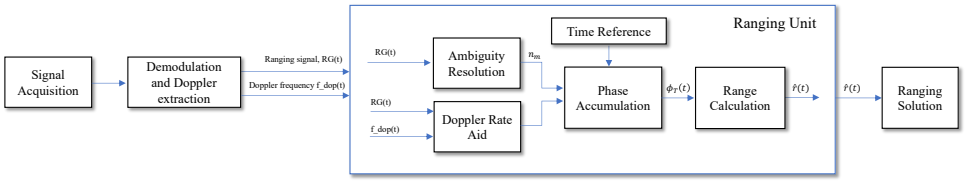

Figure 2.9: Tone-based Ranging System Architecture [130].

PN ranging offers a sophisticated approach to satellite tracking by leveraging the properties of PN sequences for accurate measurements. This method modulates a PN range code, utilizing binary phase shift keying to encode the ranging signal with a half-sine or square pulse shape. Crucial to this method is the concept of measuring the signal phase in units of chips, controlled by a range clock that dictates the timing of each chip. For typical configurations, a range clock frequency of 1 MHz results in a chip rate of 2 Mchips/s and a code period close to 0.5 s, allowing for the resolution of ambiguity through post-processing.

The operation sequence of a PN ranging system unfolds with the continuous broadcast of a pseudo-noise sequence. This sequence is a logical of six binary periodic PN components, each serving a distinct role in resolving ambiguity. Among these components, the range clock is distinguished as the major tone, its phase-locked replica produced by a digital PLL to align with the major tone cycles within the ranging span. The defining aspect of a PN sequence lies in its code length, signified by N, with variations like N=2 for the Weighted-Voting Balanced Tausworthe (T2B) and N=4 for T4B, each tailored to either optimize integration time or enhance ranging precision.

The PN components, a total of six, present a spectrum of periodic patterns, contributing to the composite ranging signal's overall structure (see [120] for further details). This complexity allows for a high degree of correlation between the range clock and the emitted ranging sequence. Operational advantages of PN ranging come from its robustness to low SNR and its superior correlation properties [129]. This resilience is particularly valuable given the challenges posed by significant increases in round-trip time, which can necessitate the re-initiation of tone-based measurements [2]. By correlating the received composite PN code with local replicas of component codes, the system provides accurate ranging.

In addition to tone or code-based ranging systems, the ESA code standard introduces a hybrid approach, combining PN codes for ambiguity resolution with a major tone for range measurements. This sequence involves the sequential transmission of a tone modulated by a series of codes. By correlating each transmitted code with the demodulated version, the system calculates the number of tone cycles in the range, thereby facilitating accurate distance measurements. Further details about the code programming and ranging sequence can be found in [130].

SYSTEM PERFORMANCE

The performance of a ranging system is intricately affected by both *random* and *systematic* errors, with range jitter—predominantly caused by thermal noise—playing a significant role. Thermal noise affects system performance in two major ways: it introduces inaccuracies in range measurements and can lead to signal acquisition failures. Specifically, inaccuracies arise during the correlation process between the received ranging signal and the local model of the range clock, while acquisition failures are linked to unsuccessful correlations between the received signal and local models used for ambiguity resolution. The concept of the probability of acquisition highlights the likelihood that a range measurement will be successfully completed without failure, with elevated thermal noise levels increasing the risk of measurement failures [2].

Distinct ranging standards possess unique correlation and acquisition characteristics, thus influencing system performance differently. Critical parameters affecting this performance include the range clock frequency (f_{RC}), which represents the highest frequency component of the ranging signal, and the integration time (T), denoting the duration of measurement on the range clock and inversely related to the tracking loop bandwidth (B_{RL}). Additionally, the signal-to-noise density ratio (P_R/N_0) plays a crucial role, indicating the power ratio of the ranging signal to the noise power per unit bandwidth.

The range measurement error (σ_ρ) due to thermal noise for PN ranging, expressed in meters for a one-way open tracking loop scenario, can be calculated as follows [2], [124]:

$$\sigma_{\rho,PN} = \frac{c}{f_{RC} A_c R_1 \sqrt{32\pi^2 T (P_r/N_0)}} \tag{2.12}$$

where A_c represents the fractional loss of correlation amplitude due to frequency mismatch, with coherent operations (where the transponder maintains phase coherence between incoming and outgoing signals) having $A_c = 1$, and non-coherent operations falling between 0 and 1. The cross-correlation factor R_1 is pivotal for correlating against

Table 2.1: PN ranging jitter performances.

	T2B	T4B	JPL
σ_ρ [m]	1.4633	0.9780	0.9619

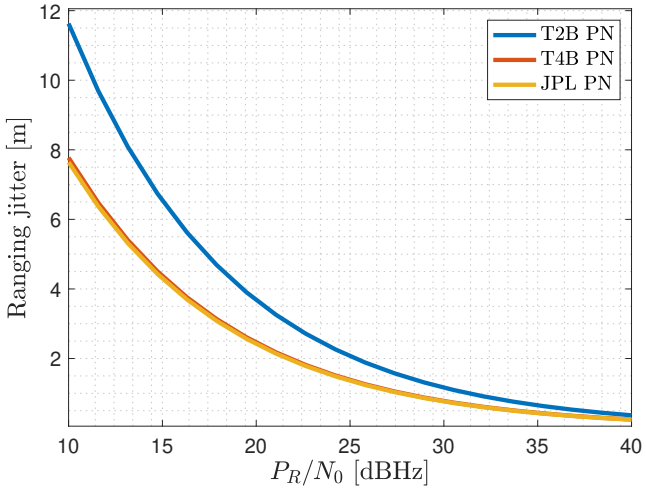

Figure 2.10: PN ranging jitter performances (one-way, $T = 0.5s$).

the range clock, with varying values depending on the PN code used, such as $R_{1,T2B} = 0.6274$, $R_{1,T4B} = 0.9387$ and $R_{1,JPL} = 0.9544$ [2].

For instance, given a P_R/N_0 of 25 dB, a sinewave range clock with a chip rate of (F_c) 2.068 Mchips/s ($f_{RC} = 1/F_c$), and an integration time (T) of 1 s, the ranging performance will differ based on the cross-correlation factor as provided in Table 2.1 (see Figures 2.10 and 2.11 for varying P_R/N_0 and range clock frequencies). Longer integration times for the range clock can diminish range measurement errors attributable to thermal noise. However, extending the integration time for components used to resolve ambiguities increases acquisition likelihood, though at the expense of potentially prolonging the measurement duration and thus limiting the number of range measurements achievable during a tracking session. This trade-off necessitates careful consideration of available P_R/N_0 levels to optimize ranging performance.

It should be noted that Eq. 2.12 is given for an open-loop architecture. The open-loop architecture is characterized by a fixed receiver bandwidth and does not require a tracking loop for delay estimations on the ranging clock [124], allowing for longer integration times not constrained by onboard tracking jitter. This architecture is especially suited for ground-based applications due to its need for synchronization between the chip rate and the carrier frequency.

Conversely, the closed-loop architecture incorporates a mechanism to lock onto the

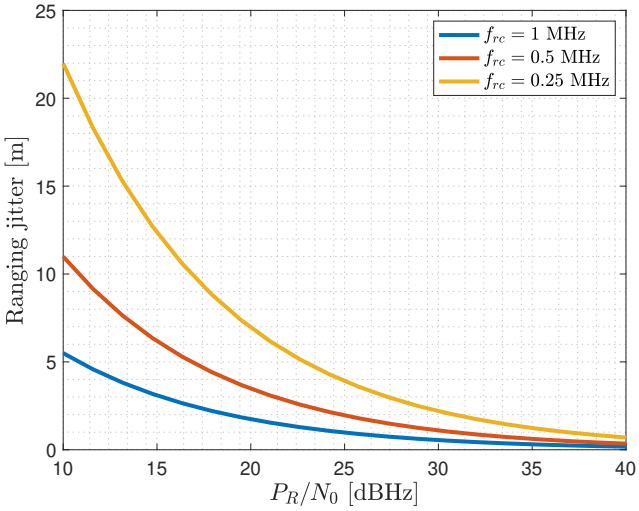

Figure 2.11: Ranging jitter performances based on different range clock frequencies (one-way, $T = 1s$).

received signal's phase, progressively reducing its bandwidth as its performance is given:

$$\sigma_{\rho,PN} = \frac{1}{\sqrt{2}} \frac{c}{8 f_{rc}} \sqrt{\frac{B_L}{(P_{RC}/N_0)}} \tag{2.13}$$

This architecture's performance, factoring in the Chip Tracking Loop (CTL), suggests that similar outcomes can be achieved between open and closed-loop systems if the condition $2B_L = 1/T$ is met [124]. In practical applications, particularly in ground-based tracking, the preference for an open-loop system implies a larger integration time, leading to a significant difference in bandwidth ($B_L >> 1/T$), allowing the use of the performance equation given in Eq. 2.12. It is worth noting that these equations are based on the sinewave range clock. The squarewave counterparts can be found in [2], [124].

Radio-navigation transponders, commonly used in large satellites, generate a downlink carrier that is phase-coherent with the uplink signal, optimizing ranging performance. However, small satellites may lack the capability for coherent operations, resorting to non-coherent PN ranging. This non-coherence introduces a measurable range bias due to discrepancies in chip rates between the replica and received codes [124], which can be mathematically modeled:

$$\rho_{\text{bias}} = \frac{c \Delta f_{cp} T}{4 f_{cp}} \tag{2.14}$$

where Δf_{cp} is the difference in frequency between the received chip rate and the local chip rate.

Similar to PN ranging systems, the range measurement error σ_ρ, in meters (1σ Root Mean Square (RMS) one-way, open tracking loop) for the tone-based ranging is given as

[2]:

$$\sigma_{\rho,tone} = \frac{c}{f_{RC} A_c \sqrt{32\pi^2 T(P_r/N_0)}} \tag{2.15}$$

PN ranging and Tone-based ranging variance, integration times, and crossover power have been compared in [120]: PN ranging provides superior performances when SNR is higher than 2 dB – Hz in terms of range variance and integration time. Here in Figure 2.12, the two methods have been compared assuming the equal probability of acquisition and various range errors (1σ) highlighting the integration time difference between the two methods and similar findings are presented: PN ranging allows more measurements to be done in a given tracking period. The trend shows that tone-based ranging could be relatively preferable over PN ranging at low ranging SNR together with higher accuracy.

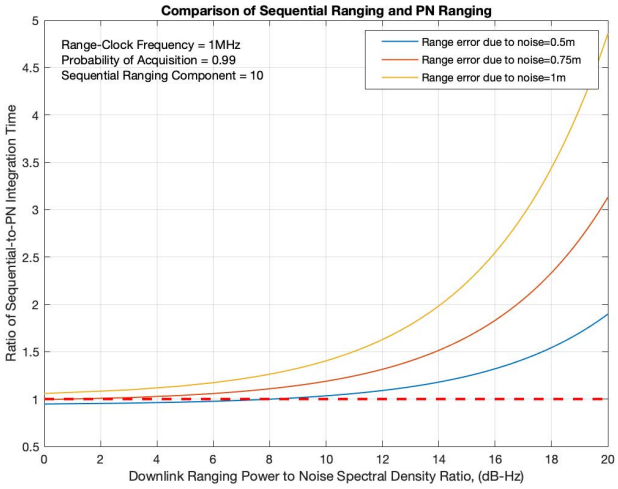

Figure 2.12: Integration Time Comparison between Tone and PN Ranging. This graph illustrates the preferred operational zones for Tone-based and PN ranging methods. Notably, for conditions above the designated horizontal threshold line, PN ranging offers superior performance and efficiency compared to Tone-based ranging.

Clock instability is a notable source of error in radiometric tracking, impacting the accuracy of ranging measurements significantly. In Eq. 2.7, oscillator phase deviation $\Delta\tau_x$ over the two-way time interval was introduced. The stability of frequency standards over time is typically assessed using the two-sample Allan variance, which quantifies the variance of fractional frequency deviations between consecutive measurements [114]. This measure helps in evaluating the precision of onboard clocks, which are crucial for accurate timing in satellite operations and it is represented as [114]:

$$\sigma_y^2(\tau) = \frac{1}{2} < (\bar{y}_{k+1} - \bar{y}_k)^2 > \tag{2.16}$$

where $\bar{y}_k$ and $\bar{y}_{k+1}$ are measurements of fractional frequency deviation, with averaging time, τ. The fractional frequency deviation is computed by subtracting the oscillator

Table 2.2: Available Space Clocks and Properties adapted from [131].

Clock	$\sigma_y(1s)$	$\sigma_y(1000s)$	Drift (per day)	TRL	Power [W]	Mass [kg]	Lifetime [years]
OCXO	5×10^{-10}	8×10^{-12}	7×10^{-10}	9	3	0.075	>20
USO	1×10^{-13}	1.5×10^{-13}	1×10^{-11}	9	6.5	2	>20
CSAC	3×10^{-10}	1×10^{-11}	3×10^{-11}	9	0.12	0.035	>11
MAC	3×10^{-11}	1×10^{-12}	2.5×10^{-11}	9	6.3	0.1	17
GNSS Rb	2×10^{-12}	7×10^{-14}	5×10^{-14}	9	39	6.4	>20
GNSS Cs	1.2×10^{-11}	8.5×10^{-13}	1×10^{-14}	9	40	16.6	>10
GNSS PHM	7×10^{-13}	2.2×10^{-14}	1×10^{-15}	9	60	18.2	>12
Active HM	2.5×10^{-13}	3×10^{-15}	3.6×10^{-14}	8	-	-	-
DSAC	1.5×10^{-13}	1.5×10^{-14}	3×10^{-16}	7	56	19	5
DSAC-FO	1×10^{-13}	3×10^{-15}	1×10^{-15}	5	34	10	>10

Table 2.3: An example list of commercial CSACs [133]

	$\sigma_y(1s)$	Mass [kg]	Size [cm^3]	Power [W]
Microsemi SA45.s	3×10^{-10}	0.035	17	0.12
Spectratime mRO-50	4×10^{-11}	0.075	50	0.36
Teledyne TCSAC	3×10^{-10}	0.042	23	0.18

phase errors at the beginning and at the end of the averaging interval and then dividing by the product of the nominal frequency times the averaging interval [114].

There are several types of onboard clocks, including Oven-Controlled Crystal Oscillator (OCXO), Ultra-Stable Oscillator (USO), and Chip-scale atomic clock (CSAC), each with distinct characteristics regarding power consumption and performance. While this study did not delve into the detailed pros and cons of each clock type, the CSAC was chosen as a baseline due to its energy efficiency and suitable drift characteristics for missions with constrained power resources. Available space clocks and corresponding properties can be seen in Table 2.2 adapted from [131]. An example list of commercially available CSACs can be found in Table 2.3. For instance, the Iris radio on the CAPSTONE mission utilizes a CSAC, demonstrating an Allan deviation (ADEV) around 4×10^{-11} at one second and a daily drift of 2.4×10^{-8} [132], figures that serve as a baseline for clock-related effect simulations.

The impact of clock instability on two-way range data is significant, but its effect is negligible for two-way operations due to the relatively short round-trip times involved. The effect of clock instability on the two-way range data is approximately:

$$\Delta\tau_x = \Delta\rho_x/c = \sqrt{2}\tau\sigma_y(\tau) \tag{2.17}$$

where $\sigma_y(\tau)$ is the Allan deviation with a sample time τ. For instance, a maximum round trip time is on the order of 10 000 km (assuming SST between Earth-Moon L1 and L2 Halo orbiters), which yields a two-way time of flight $\tau = 2\rho/c$ on the order of 0.001 s. Assuming a clock with short-term stability of 1×10^{-10} and τ =0.8 s, $\Delta\tau_x$ =1.13×10^{-10} s ($\approx$ 3.39 cm) can be observed. Compared to thermal errors, which are on the order of meters, clock instability's contribution to overall measurement uncertainty can often be neglected in two-way operations. In addition, phase drift can be neglected, thanks to the relatively short round-trip time.

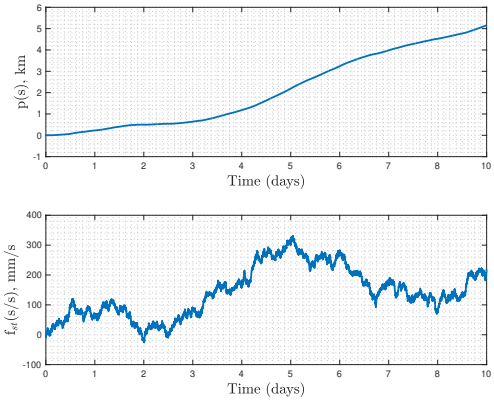

Figure 2.13: Stochastic clock errors based on a two-state clock model following the analysis given in [134]. In the analysis, $\sigma_y(\tau)$ was set to $4\,e-11$ (for the white frequency noise σ_{wf} due to the integration time below 1000s), and $4\,e-12$ (for a random walk frequency σ_{rwf} due to the integration time above 10000s), respectively.

Even though this study is based on two-way operations, the author thinks it is beneficial to provide clock models critical for one-way operations. This would improve understanding of the two-way ranging and limitations that can pop up in one-way operations. To illustrate stochastic clock noise in one-way operations, Figure 2.13 represents phase and frequency errors, reaching up to equivalents of 6 km and 4 cm/s after ten days, respectively (Analysis followed the approach given in [134]).

In particular, clock instabilities become critically relevant in one-way operations, where differences in clock epoch offsets and clock rate offsets between transmitting and receiving nodes introduce significant errors. In this case, the clock offset can be modeled as:

$$\Delta\rho_{CO} = c\Delta T \tag{2.18}$$

and the clock rate offset can be modeled as:

$$\Delta\rho_{CRO} = c\tau\Delta\dot{T} \tag{2.19}$$

where ΔT and $\Delta\dot{T}$ represent unknown time-tag error and clock rate offset. In addtion, an unknown time-tagging error of ΔT would result in a range error [114]:

$$\Delta\rho_{TT} = \dot{\rho}\Delta T \tag{2.20}$$

In addition to random errors, systematic errors arising from group delays, instrumental delays, antenna multipath effects, and atmospheric conditions like tropospheric delays (for ground-based systems) can significantly impact the accuracy of range measurements. These errors can either be calibrated or estimated during the orbit determination process. Instrumental biases are hardware-dependent and can vary depending

on the system. In ground-based deep-space tracking operations, station biases are typically less than 5 m [107], [135]. It is reasonable to assume that on-board systematic delays can be modeled in the same order of magnitude since measurement biases are, in general, calibrated on the ground.

2.1.2. TIME MEASUREMENTS

Inter-satellite distance computation can also be achieved through time transfer methods between nodes, leveraging proximity space links for short-range radio communications. These links facilitate data exchange among various space assets, including spacecraft, landers, rovers, orbital constellations, and orbiting relay stations, supporting both stationary and mobile operations. The Proximity-1 Space Link Protocol, as defined by the Consultative Committee for Space Data Systems (CCSDS), plays a crucial role in this process by offering two essential timing services: timestamping transfer frames for time synchronization and transmitting time information to distant nodes [136].

These timing services enable a time correlation function critical for maintaining coordinated operations among diverse space assets. Time tagging and time transfer capabilities require that a Proximity-1 transceiver accurately log the timing of the final bit's trailing edge of the Attached Synchronization Marker (ASM) for both incoming and outgoing Transfer Frames. Furthermore, these transceivers must be capable of sharing time information with distant nodes, facilitating precise time correlation across the space network. Time correlation is the alignment and synchronization of time references among spacecraft and ground assets, addressing the potential drift caused by clock inaccuracies and differing drift characteristics.

The importance of these timing services lies in their ability to support the exchange of time between satellites and the derivation of time-derived ranging measurements. This approach is particularly relevant in addressing the physical limitations inherent in space operations, such as the stability of onboard clocks. Dedicated algorithms for efficient and reliable time exchange and processing, as proposed in the literature [137], [138], are instrumental for leveraging space data links effectively. These algorithms are particularly valuable for spacecraft operating in the vicinity of Mars and the Moon, where precise time synchronization is essential for mission success.

In brief, the Proximity-1 protocol and subsequent developments in time transfer techniques provide a robust framework for computing inter-satellite distances and ensuring coordinated operations among space assets [136]. By leveraging these technologies and algorithms, space missions can achieve precise time synchronization and time-derived ranging, enhancing the overall efficacy and reliability of space data links.

Time-derived ranging is an essential technique for ISL-based applications, offering a detailed process for determining the distance between spacecraft. As illustrated in Figure 2.14, the process begins when S/C A transmits a signal to S/C B, marking the transmission time with a timestamp, t_1. Upon receiving this signal, S/C B records the reception time as t_2. The procedure is then mirrored, with S/C B sending a signal back to S/C A, which are timestamped as t_3 at transmission and t_4 at reception, respectively.

Utilizing these four successive timestamps, the Round-Trip Light Time (RTLT) and the time offset between the spacecraft can be accurately calculated [137]. This calculation is essential for determining the actual distance between the spacecraft, with the pre-

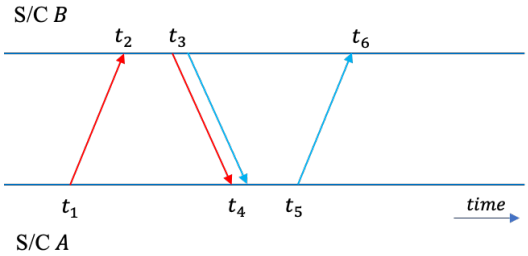

Figure 2.14: Time-Derived Ranging Measurement Process. This illustration details the sequence for calculating inter-satellite distances through time-derived ranging, emphasizing the exchange of timing information between spacecraft to measure distances.

cision of these time tags being heavily reliant on the onboard master clock's frequency. This method underscores the significance of the spacecraft's clock in the ranging process, where its drift from the nominal value can impact the accuracy of the measurements.

The resolution of the time-derived measurements is directly tied to the frequency of the onboard master clock. For example, the Electra Transceiver, utilized by Mars orbiters and landers, incorporates an USO operating at approximately 76 MHz. This high-frequency operation allows for a timing resolution of about 15 ns, equivalent to a resolution of approximately 4.5 m, without necessitating signal averaging [139]. Similarly, the Iris V2 transponder, employed by cislunar CubeSats, utilizes a Temperature Compensated Crystal Oscillator (TCXO) with a 50 MHz frequency, achieving a 20 ns resolution, or about 6 m.

Further advancements in time-derived ranging have been explored, such as the method proposed by [140], which leverages ping requests for RTLT measurements, simplifying the process by eliminating unnecessary steps to ensure repeatable measurements. This approach, tested on satellite radio hardware, demonstrated a ranging accuracy of 0.156 km under strong signal conditions (Bit Error Rate (BER) of around $<10^{-5}$) and 0.303 km under realistic worst-case scenarios (BER of around 10^{-4}) at a 10 kbps data rate. It is important to note that the data rate plays a crucial role in this context. Furthermore, research by Foster et al. [141] has shown the feasibility of conducting range measurements using communication radios between a satellite and a ground station, achieving a 1σ error of 650 m for each range observation.

These developments highlight the potential and challenges of implementing time-derived ranging in space applications. By leveraging advanced timing and processing techniques, spacecraft can achieve precise distance measurements crucial for navigation and mission planning, even in the absence of ground-based support.

2.1.3. HYBRID MEASUREMENTS

Hybrid ranging methods have emerged as a significant advancement in satellite tracking, combining various techniques to improve the accuracy and efficiency of measuring the RTLT. One such method, telemetry ranging, offers a novel alternative to the tradi-

tional two-way ranging process. Introduced in [122], telemetry ranging eliminates the re-transmission of the conventional ranging signal. Instead, it utilizes telemetry data alone to modulate the downlink carrier, providing the essential timing information required for estimating the RTLT. This process is streamlined by directly reporting uplink signal phase measurements within successive telemetry frames, thus simplifying the generation of ranging measurements. It should be noted that telemetry ranging is based on phase measurements, collecting on deputy transmitted to the mothercraft. However, in this dissertation, due to differences from traditional two-way code/tone-based ranging methods, telemetry ranging has been considered a hybrid ranging method. Despite its advantages, telemetry ranging still requires a traditional uplink ranging signal, limiting the end-to-end system performance. To overcome this limitation, techniques such as telecommand/telemetry ranging [125] or a simplified data-aided ranging have been developed. These methods eliminate the need for an uplink ranging signal by deriving timing information from the telecommand signal, offering a more efficient approach to satellite ranging. The subsequent sections of this dissertation will delve deeper into these hybrid ranging methods, exploring their capabilities and applications in autonomous navigation.

TELEMETRY-BASED RANGING

Telemetry-based ranging, or Telemetry ranging, is similar to the traditional two-way code/tone-based ranging method, relying on phase samples [118], [122], [123]. From the satellite-to-satellite tracking perspective, the traditional ranging uses the difference between the phase of the transmitted ranging signal (ψ_T) at the transmitting electronics of the mothercraft and the phase of the received ranging signal (ψ_R) at the receiving electronics of the mothercraft, measured at the reception time (t_R). This process involves correlating the downlink ranging signal with a local model at the mothercraft. The resulting phase difference ($\Delta\psi$) represents the round-trip time, which is the sum of the one-way uplink (τ_u) and downlink (τ_d) times. These traditional ranging methods require a certain amount of on-board power for the ranging signal, which can limit the power available for telemetry and telecommand (see Figure 2.15). This is particularly significant for the telemetry stream.

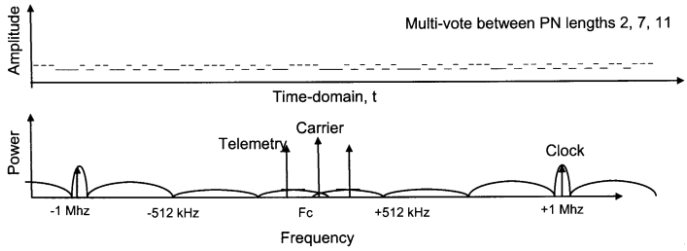

Figure 2.15: PN spectrum within the conventional ranging [120].

In telemetry-based ranging, the system derives the RTLT directly from the telemetry stream, thus eliminating the need for a dedicated downlink ranging signal [118]. This innovation not only conserves onboard power but also streamlines the process by remov-

ing the need for phase measurement at the mothercraft's receiving end (ψ_R). Instead, phase measurements are sourced from the deputy's reception (ψ_{dp}), similar to one-way phase measurements, but with a significant distinction: Phase recordings on the deputy are not time-stamped onboard. Instead, each phase sample $\psi_{dp}(t_{dp})$, captured at the deputy and corresponding to a specific telemetry frame's start at t_{dp}, is transmitted to the mothercraft, with the mothercraft measuring the telemetry frame's arrival time (t_r) and phase difference ($\Delta\psi$). In this case, a master frame that triggered the phase sample on the deputy can be used to identify the sample $\psi_{dp}(t_{dp})$ on the mothercraft [122]. In telemetry ranging, similar to Eq. 2.5, the phase measured at the deputy $\psi_{dp}(t_{dp})$, ($t_R = t_{dp} - \tau_d$), was originally present at the uplink antenna at time t_T as $\psi_T(t_T)$, i.e. $\psi_{dp}(t_{dp}) = \psi_T(t_T)$ and thus, the round-trip time can be derived similarly to Eq. 2.6 as:

$$\psi_T(t_R) - \psi_{dp}(t_{dp}) = \int_{t_R-\tau(t_R)}^{t_R} \frac{\mathrm{d}\psi_T}{\mathrm{d}t}\,dt \tag{2.21}$$

To further elucidate the two-way ranging process, Figure 2.16, as mentioned in [123], visualizes the timing based on unwrapped phase measurements. This illustration shows the sloped lines representing the phase of the $\psi_T(t)$ and $\psi_{dp}(t)$ signals over time, with the vertical line indicating the phase difference $\Delta\psi = \psi_T(t_R) - \psi_{dp}(t_{dp})$ and the horizontal line at t_R depicting the round-trip time, which can be calculated as $\tau = \Delta\psi / f_{T,0}$. Through this graphical representation, the phase difference is converted into the two-way time of flight using the reference signal frequency, providing insights into the calculation of the distance between the spacecraft based on phase measurements. In this case, the two-way time of flight given in Eq. 2.7 can be adjusted as:

$$\tau = \frac{1}{f_{T,0}}(\psi_T(t_R) - \psi_{dp}(t_{dp})) - (\Delta\tau_\beta + \Delta\tau_x + \Delta\tau_y) \tag{2.22}$$

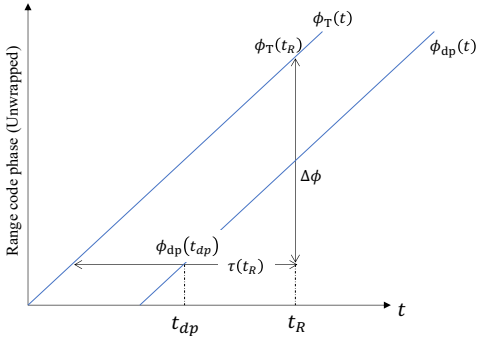

Figure 2.16: Timing in the telemetry ranging [123], highlighting that the sloped lines represent the phase of the transmitted from the mothercraft ($\psi_T(t)$) and received ($\psi_R(t)$) signals from the deputy over time, with the vertical line indicating the phase difference $\Delta\psi = \psi_T(t_R) - \psi_{dp}(t_{dp})$ and the horizontal line at t_R depicting the round-trip time, which can be calculated as $\tau = \Delta\psi / f_{T,0}$. Note that phase samples on the deputy are not time-tagged. The ranging signal phase is sampled at different locations, but the mothercraft on-board clock is used to calculate the round-trip time.

In telemetry ranging, a unique aspect is the absence of time tagging for the phase sample by the deputy satellite. This omission means that calculations rely solely on the mothercraft's onboard clock, ensuring stable RTLT measurements. This configuration is particularly beneficial when maximizing the downlink's power for telemetry transmission is crucial, effectively eliminating any potential conflict between telemetry and ranging signals. Furthermore, this method's independence from the ranging chip rate for the telemetry symbol rate allows all transmitted energy to focus on data transmission, enhancing efficiency [118], [122], [123]. The functional block diagram can be seen in Figure 2.17, illustrating the concept for satellite-to-satellite tracking purposes.

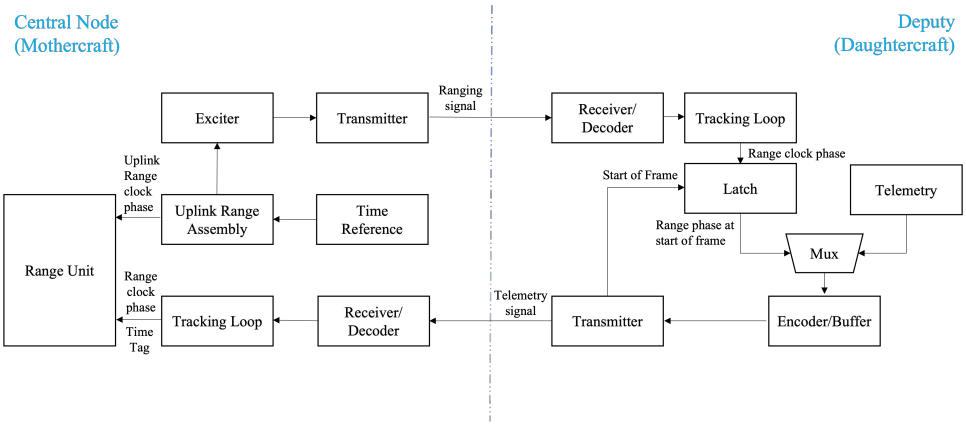

Figure 2.17: Functional Block Diagram of Telemetry Ranging for Satellite-to-Satellite Tracking. Adapted from [3], this diagram has been specifically reorganized to illustrate the process of telemetry ranging in the context of satellite-to-satellite tracking.

The performance of telemetry-based ranging, similar to traditional methods, hinges on various factors including the signal structure, integration time, T, SNR of the ranging signal, and the ranging clock frequency f_{rc}. For telemetry-based ranging, considering a square wave as the uplink range clock and a Binary Phase Shift Keying (BPSK)-modulated telemetry signal, the end-to-end performance can be represented as follows [118]:

$$\begin{aligned} \sigma_{\rho_{TM}} &= \sqrt{\sigma_{\rho_u}^2 + \sigma_{\rho_d}^2} \\ \sigma_{\rho_u} &= \frac{c}{8 f_{rc}} \sqrt{\frac{B_L}{(P_{RC}/N_0)}} \\ \sigma_{\rho_d} &= \frac{4\,c\,T_{sd}^2}{\pi\,T\,E_S/N_0} \end{aligned} \tag{2.23}$$

where σ_{ρ_u} and σ_{ρ_d} represent the uplink and downlink ranging errors, respectively. T_{sd} is the telemetry channel symbol duration, E_S/N_0 the code symbol-to-noise ratio. Eq. 2.23 given here assumes that the relative velocity between satellites v_r is negligible, e.g., $c >> v_r$. In Eq. 2.23 encompasses both uplink and downlink ranging errors, with the former tracking via a chip tracking loop on the deputy and the latter through a

correlator-based approach on the mothercraft. The overall error is then derived as a root sum square of the uplink and downlink errors.

Figure 2.18 illustrates the telemetry ranging performance across different data rates, considering varying radiometric parameters and compare it with traditional ranging performance, demonstrating that telemetry-based ranging might offer advantages at higher data rates. This insight highlights the method's versatility and potential suitability for missions requiring efficient data transmission alongside precise navigation. Additionally, a comparative analysis between the jitter in uplink ranging (predominantly associated with pseudo-random noise codes) and downlink ranging jitter relative to telemetry data rates is illustrated in Figure 2.19 and it offers insights into the operational preferences for different ranging methods based on data rate scenarios. This analysis underlines that traditional ranging methods might be more preferable at lower data rates. Adjustments in the ranging clock frequency f_{RC} or improvements in the symbol-to-noise ratio E_S/N_0 could further influence the threshold given in the figure.

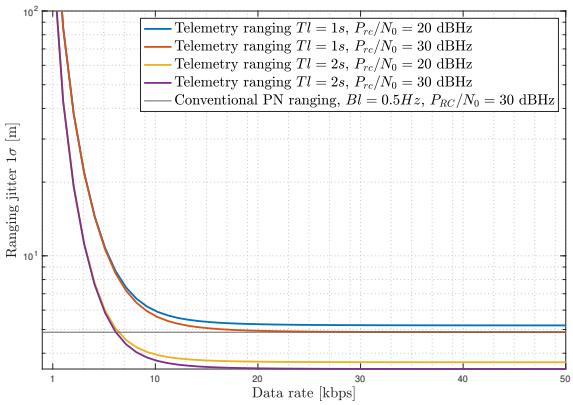

Figure 2.18: Telemetry Ranging Performance Versus Data Rate.

DATA-AIDED RANGING

The discussion on radiometric measurements has evolved from traditional phase-based methods, where the round-trip time is calculated from phase differences, to innovative telemetry and data-aided ranging techniques that streamline the process, making it more efficient for missions with constrained resources. In phase measurements, the round-trip time is determined by the difference between the phase of the transmitted ranging signal (ψ_T) and the phase of the received ranging signal (ψ_R) measured at the reception time (t_R). The resulting phase difference ($\Delta\psi$) represents the round-trip signal travel time. Traditional ranging methods, which typically require separate telemetry and ranging sessions due to limited onboard power, face challenges in simultaneously conducting ranging and high-rate telemetry transmission. This limitation is particularly pronounced in small satellites, where power availability for crosslink communications is critical. The introduction of telemetry ranging, as discussed in the previous section, of-

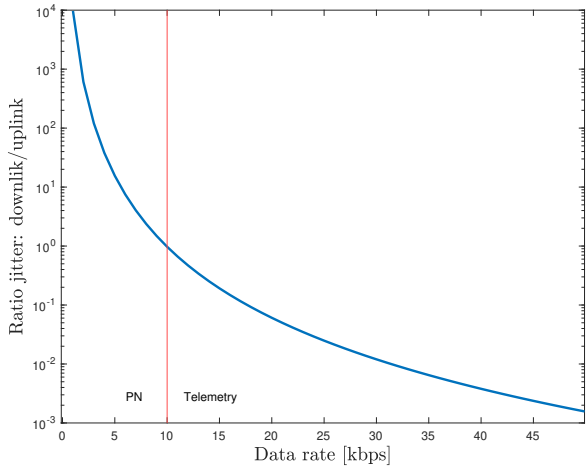

Figure 2.19: Telemetry Ranging Versus PN Ranging. Figure represents the ratio of uplink ranging jitter (related to PN ranging code) and downlink ranging jitter with respect to the telemetry data rate for illustration purposes, indicating that conventional ranging methods are more suitable at low data rates and vice versa. Note that there are several other factors may affect the threshold.

fers a solution by allowing the simultaneous execution of ranging and telemetry without the need for additional power allocation to a dedicated downlink ranging signal, thus optimizing the power available for telemetry.

In [125], the telemetry ranging concept has been extended by also eliminating the uplink PN ranging signal, which has been replaced by a data-bearing telecommand signal. This dissertation follows a similar structure given in [125] and defines this technique as *data-aided ranging*. The concept introduced in [125] involves measuring the code delay of the uplink command sequence, counting the number of symbols, and incorporating the measured command delay into a downlink telemetry, then recovering the command delay along with the codeword delay via a symbol tracking loop in the receiver end. This technique's performance hinges on various factors, such as the length of codewords and the symbol rate, with potential to achieve ranging accuracy in the meter level under optimal conditions, e.g. around 10 m ranging jitter is expected at a symbol-rate of 10 ksps with a symbol SNR of 15 dB and higher symbol rates yields less than a meter-level ranging error [125]. It has been stated in the telemetry ranging framework that chip or symbol timings can be recovered via a correlator or a tracking loop, e.g., uplink PN ranging signal can be tracked via a chip-tracking loop on the deputy. In short, a correlator-based approach can be used in the data-aided ranging framework. In a simple way, assuming uplink telecommand symbol timing is recovered with a correlator on the deputy, and likewise on the downlink telemetry at the mothercraft, data-aided ranging jitter can be

given as follows (assuming error-free decoding and without any delay):

$$\begin{aligned}\sigma_{\rho_{TCTM}} &= \sqrt{\sigma_{\rho_u}^2 + \sigma_{\rho_d}^2} \\ \sigma_{\rho_u} &= \frac{4\,c\,T_{sd,tc}^2}{\pi\,T_{dp}\,E_S/N_0} \\ \sigma_{\rho_d} &= \frac{4\,c\,T_{sd,tm}^2}{\pi\,T_m\,E_S/N_0}\end{aligned} \tag{2.24}$$

where $T_{sd,tc}$, $T_{sd,tm}$ are the symbol duration for uplink (telecommand) and downlink (telemetry), respectively. Correlator integration times are T_{dp} (deputy) and T_m (mothercraft), respectively.

Considering different ranging methods, it becomes evident that the choice of ranging technique significantly influences the operational performance and applicability of each method to specific mission requirements. The comparison of theoretical performances across conventional PN, telemetry-based, and data-aided ranging methods reveals a clear trend: Higher data transmission rates directly correlate with improved accuracy in ranging measurements. This relationship underscores the crucial role of data transmission capabilities in determining the suitability and effectiveness of each ranging technique.

Figure 2.20, which presents the expected theoretical performances of these ranging methods, clearly illustrates this point. Data-aided ranging at high data rates emerges as superior in terms of accuracy, highlighting the benefits of leveraging existing telecommunication streams for ranging purposes. This approach not only maximizes the use of onboard power but also simplifies the system architecture by eliminating the need for separate ranging signals.

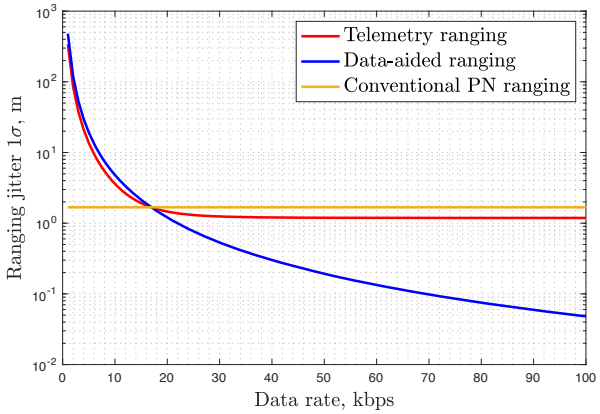

Figure 2.20: Performance of Satellite-to-Satellite Ranging Methods by Data Rate.

This chapter's comprehensive review of SST ranging methods (see Figure 2.21 for an overview) offers a critical evaluation of each technique's performance characteristics, advantages, and limitations, as summarized in Table 2.4. While traditional PN and

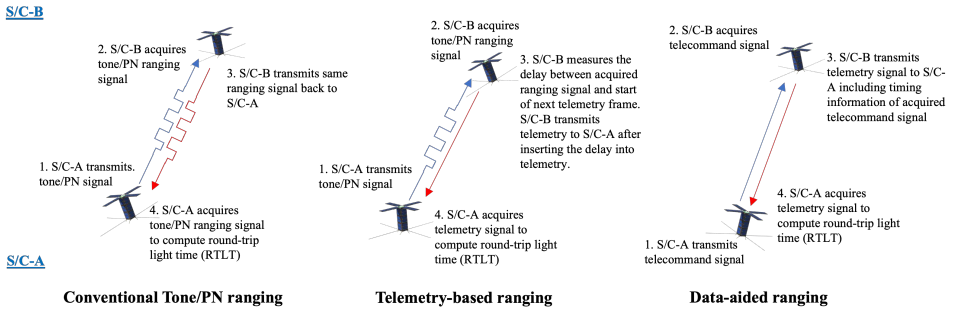

Figure 2.21: Overview of SST Ranging Methods. This figure presents a comparison of available SST ranging techniques, illustrating that while conventional PN/Tone ranging relies on a ranging signal for both uplink and downlink, Telemetry-ranging removes the necessity for a downlink ranging signal, and Data-aided ranging operates without a dedicated ranging signal entirely.

Table 2.4: Comparison of Satellite-to-Satellite Ranging Methods.

Ranging Methods	Advantages	Disadvantages
PN/Tone Ranging	Meter level accuracy Heritage	Limits the power for telemetry Interference between telemetry and ranging signals
Telemetry-based Ranging	Sub-meter level accuracy at high telemetry data rates (>Mbps) Ranging signal is not required on the downlink	Limited performance due to the uplink-ranging signal Interference between telecommand and ranging signals
Data-aided Ranging	Sub-meter level accuracy at high data rates (>Mbps) Ranging signal is not required on both uplink and downlink	Limited performance at a low data rate (<10 kbps)
Time Transfer	Simple design	Limited performance Sensitive to time-tagging errors

tone-based ranging methods have established their utility in various applications, they encounter practical limitations when applied to small satellite formations and missions with constrained operational parameters. These constraints often stem from the design of the spacecraft and the mission's operational requirements, particularly in managing tracking, telecommanding, and telemetry sessions.

Operational considerations, such as the availability of tracking windows, can significantly impact the choice of ranging method. For missions where tracking opportunities are limited, integrating ranging measurements into telecommand and telemetry sessions via telemetry or data-aided ranging methods can offer a pragmatic solution. This integration allows for more efficient use of mission time and resources, aligning with the goal of achieving reliable and accurate navigation data within the constraints of mission design and execution.

The following sections will delve deeper into these operational aspects and explore additional radiometric observation types, broadening the understanding of the diverse methodologies available for enhancing the performance of autonomous on-board OD in satellite formations.

2.2. RANGE-RATE MEASUREMENTS

Doppler tracking between satellites provides a pivotal means for determining the relative velocity between two spacecraft. This technique leverages the Doppler effect, which describes the change in frequency of a wave in relation to an observer moving relative to the source of the wave. The Doppler shift, a direct consequence of the relative motion between the transmitting mothercraft and the receiving deputy satellite, plays a critical role in this process. In essence, Doppler measurements represent the average shift observed over a designated time interval, as instantaneous measurements are not physically possible.

In particular, the Doppler shift is measured by counting accumulated cycles of zero-crossings between the received frequency f_r and the transmitted frequency f_t (reference frequency) over a count time [117]. The Doppler shifted received frequency, fr is:

$$f_R = f_T(1 - \frac{\dot{\rho}}{c}) \tag{2.25}$$

where $\dot{\rho}$ is the range rate, and c is the velocity of light. The instantaneous Doppler shift is then:

$$\Delta f = f_R - f_T = -f_T \frac{\dot{\rho}}{c} \tag{2.26}$$

In the two-way operation, a signal is transmitted from the mothercraft with frequency f_t and is received by the deputy with a certain Doppler shift. A transponder on the deputy coherently transmits the received signal back to the mothercraft. In this case, the Doppler shift can be given as:

$$\Delta f \approx -2 f_T \frac{\dot{\rho}}{c} \tag{2.27}$$

The average Doppler shift $\Delta \bar{f}$ in this case is:

$$\Delta \bar{f} = \frac{1}{\Delta T} \int_{t_1}^{t_2} -2 f_t \frac{\dot{\rho}}{c} dt = -\frac{2 f_T}{c \Delta T} (\rho(t_2) - \rho(t_1)) \tag{2.28}$$

where ΔT is the averaging interval given by $t_2 - t_1$.

In practice, the observed value is the number of accumulated cycle counts over a given interval [117], [126]:

$$\begin{aligned} N &= \int_{t_1}^{t_2} (f_T(t) - f_R(t)) dt \\ &= \int_{t_1}^{t_2} (\dot{\psi}_T(t) - \dot{\psi}_R(t)) dt \\ &= f_{t,0}(\tau_2 - \tau_1) + \Delta N_r + \Delta N_s \end{aligned} \tag{2.29}$$

where ΔN_r and ΔN_s represent random and systematic errors. An average range rate measurement $\bar{\dot{\rho}}$ is then modeled as [117]:

$$\bar{\dot{\rho}} = \frac{1}{2} \frac{c(\tau_2 - \tau_1)}{t_2 - t_1} = \frac{\rho_2 - \rho_1}{t_2 - t_1} \tag{2.30}$$

where ρ_1 and ρ_2 represent the two-way range values at time t_1 and t_2.

The noise of two-way Doppler data is expressed by phase noise and clock instabilities [114]. Clock instability, in particular, can impose significant limitations on the accuracy of Doppler measurements, depending on the onboard clock's performance. Considering a count time τ, the range-rate error due to frequency instability is given by [114]:

$$c < (\bar{y}_{k+1} - \bar{y}_k)^2 >^{1/2} = \sqrt{2} c \sigma_y(\tau) \tag{2.31}$$

For instance, with specific reference to the Iris radio on the CAPSTONE mission, the ADEV of 4×10^{-11} at 1 s indicates that frequency instability could introduce a range rate error in the order of 1 mm/s. On the other hand, measurement errors for two-way coherent Doppler includes the effect of jitter introduced by the deputy receiver. The thermal noise in this case can be approximated by [2]:

$$\sigma_V = \frac{c}{2\sqrt{2}\pi f_c T} \sqrt{\frac{1}{\rho_L} + \frac{G^2 B_L}{(P_C/N_0)}} \tag{2.32}$$

where f_C is the downlink carrier frequency in Hz, G is the transponding ratio, P_C/N_0 uplink carrier to noise spectral density ratio in Hz and ρ_L is the downlink carrier loop signal-to-noise ratio. While plasma noise and atmospheric effects typically do not impact SST operations significantly, they are crucial considerations for ground-based measurements. Additionally, rounding numerical errors and mechanical noise, primarily associated with ground antennas, can also contribute to the total error in Doppler measurements [107]: 1.9×10^{-2} mm/s for Rosetta and 1.5×10^{-2} mm/s for Cassini, however, a limited extent due to their relatively minor impact on overall performance.

In the context of mission proposals like the Europa Clipper's Europa Tomography Probe (ETP), two-way coherent X-band Doppler data becomes a vital component of OD processes [29], leveraging the suppression of instability by a factor $\pi T/\tau \ll 1$ over timescales exceeding the RTLT to achieve accuracy comparable to ground-based systems, 0.012 mm/s with an integration time τ of 60 s.

2.3. LINE-OF-SIGHT MEASUREMENTS

The measurement of LOS angles between a transmitter and receiver utilizes the phase shift or time delay of a signal as illustrated in Figure 2.22 [142]. This is particularly useful in scenarios where two antennas are mounted on a baseline at a certain distance, b, on small satellites. Given the size constraints of these satellites, the baseline is often shorter than the signal's wavelength, which simplifies the observations by eliminating ambiguity associated with the wavelength. Notably, the acquisition of two distinct LOS angles necessitates the deployment of at least three antennas.

The measurement method considers the signal's arrival times at the antennas and the corresponding phase shift or time delay between these arrivals. This information facilitates the calculation of the angle, θ, which represents the angle between the direction towards the signal source and a line perpendicular to the baseline. The relationship between the time delay Δt and the angle θ can be represented mathematically. If the signal reaches the first antenna at time t and the subsequent antenna at $t + \Delta t$, with an

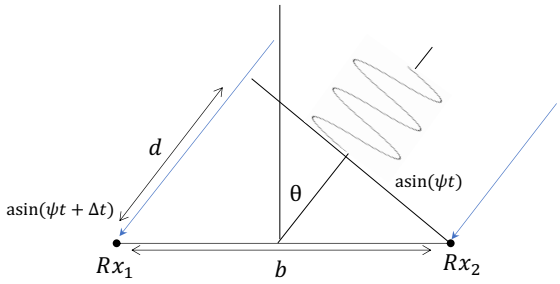

Figure 2.22: LOS measurement via two-antennas

associated phase shift $\Delta\psi$, the angle θ can be determined by [142]:

$$\Delta t = \frac{b}{c}\cos\theta \tag{2.33}$$

$$\Delta\psi = \frac{2\pi b}{\lambda}\sin\theta \tag{2.34}$$

These equations indicate that the LOS measurement's accuracy is influenced by the baseline's length and the accuracy of the time-delay or phase-shift measurements. By analyzing the variance of the time delay and phase shift equations, a relationship between the range measurement accuracy σ_ρ and the LOS measurement accuracy σ_θ can be established. Recalling that the variance of a continuous random variable X is defined as:

$$\mathrm{Var}[X] = \mathrm{E}[(X - \mathrm{E}[X])^2] = \mathrm{E}[X^2] - (\mathrm{E}[X])^2 \tag{2.35}$$

for constants a and b:

$$\mathrm{Var}[a + bX] = b^2\mathrm{Var}[X] \tag{2.36}$$

Taking the variance of both sides of Eqn. 2.33 for the time-delay-based approach:

$$\mathrm{Var}[\Delta t] = \frac{b^2}{c^2}\mathrm{Var}[\cos\theta] \tag{2.37}$$

A variance of $\cos\theta$ is given as:

$$\mathrm{Var}[\cos\theta] = \mathrm{E}[\cos^2\theta] - (\mathrm{E}[\cos\theta])^2 \tag{2.38}$$

where

$$\mathrm{E}[\cos\theta] = \sum_{k=0}^{\infty}\frac{(-1)^k}{2k!}\mathrm{E}[\theta^{2k}] = \sum_{k=0}^{\infty}\frac{(-1)^k}{2k!}\sigma^{2k}(2k-1)! = e^{-\sigma_\theta^2} \tag{2.39}$$

and

$$\begin{aligned}
\mathrm{E}[\cos^2\theta] &= 1-\mathrm{E}[\sin^2\theta] \\
&= 1-(\frac{1}{2}(1-\mathrm{E}[\cos 2\theta])) \\
&= 1-(\frac{1}{2}(1-\sum_{k=0}^{\infty}(-1)^k\frac{2^{2k}}{2k!}\mathrm{E}[\theta^{2k}])) \\
&= 1-(\frac{1}{2}(1-\sum_{k=0}^{\infty}(-1)^k\frac{2^{2k}}{2k!}\sigma^{2k}(2k-1)!)) \\
&= \left(\frac{1+e^{-2\sigma_\theta^2}}{2}\right)
\end{aligned} \tag{2.40}$$

Inserting Eq. 2.39 and 2.40 into 2.38 results in:

$$\mathrm{Var}[\Delta t] = \frac{b^2}{c^2}((\frac{1+e^{-2\sigma_\theta^2}}{2})-e^{-2\sigma_\theta^2}) = \frac{b^2}{c^2}(\frac{1-e^{-2\sigma_\theta^2}}{2}) \tag{2.41}$$

The relationship between the range measurement variance σ_ρ^2 and the LOS measurement variance σ_θ^2 is given as:

$$\sigma_\theta^2 = -\frac{1}{2}\ln\left(1-2\left(\frac{\sigma_\rho}{b}\right)^2\right) \tag{2.42}$$

It can be seen that, for a LOS measurement, the baseline must exceed the range measurement error, $b > \sqrt{2}\sigma_\rho$, requiring high measurement accuracy or a significantly large baseline, which is challenging to achieve on small satellite missions due to size constraints. Considering a range measurement error of 1 m as a best-case scenario, a minimum antenna baseline of 1.4 m is required, which is not quite possible on small satellites. Similar the relationship between phase-shift measurement error and LOS measurement error can be found by taking the variance of both sides of Eq. 2.34. A further details can be found in [113]. Note that, time-delay and phase-shift measurement errors can be converted as $\sigma_{\Delta t} = \sigma_{\Delta\psi}\lambda/2\pi c$.

2.4. TRACKING SCENARIOS

In the preceding discussions, the focus has been on detailing radiometric observables and the methodologies for measuring these within the context of SST, including an assessment of error sources and modeling as detailed in Table 2.5. These radiometric observables serve a pivotal role in the OD process, which is fundamental for achieving accurate trajectory estimations. The focus of OD efforts is often guided by specific navigation requirements which hinge on accuracy, availability, and continuity. These criteria are vital for tailoring navigation solutions to the unique demands of each mission, influenced by various factors such as mission goals, mission phases, measurement system capabilities, spacecraft functionality, and technological advancements.

The derivation of OD requirements is significantly shaped by the mission's scientific goals, which can introduce wide-ranging variations in navigational needs across different missions. For instance, considerations might be weighted heavily towards the implications of station-keeping costs, which pertain to the propellant necessary for spacecraft maneuvers to maintain or correct its orbit. This analysis deeply considers the potential risks arising from uncertainties in the spacecraft's orbital dynamics. Utilizing stochastic models for OD, Orbit Insertion (OI) errors, and maneuver execution, coupled with Monte Carlo simulations, provides a deeper understanding of the propellant needs for maintaining the spacecraft's intended course and position.

OD performance is influenced by several factors, including dynamical modeling inaccuracies, the choice of estimation filters, and the efficacy of measurement techniques. Detailed discussions on navigation requirements and OD models will be given in the next chapter. However, this section will delve into a broad system analysis flow from the perspective of radiometric measurements. The performance of SST is influenced by various radiometric parameters, which, in turn, impact OD outcomes.

As stated in previous chapter, the link between inter-satellite communication and radiometric measurements is crucial. Consequently, OD system analysis might encompass radiometric parameters in its framework. A suggested analysis flow could start with link budget analysis, as depicted in Figure 2.23, showing a simplified system analysis block diagram applicable to autonomous OD scenarios. This flow begins with an assessment of the inter-satellite link budget under worst-case scenarios, progressing to an evaluation of radiometric ranging performance. Specifically, ISL budget analysis for a given mission scenario determines the supportable data rate in the current setup, enabling the prediction of expected performance for data-aided ranging or alternative measurement methodologies. This process is intricately linked to OD performance, encapsulating dynamics, measurements, and estimation processes (see Chapter 3). OD outcomes can be assessed using various analytical methods, including Monte Carlo simulations, CRLB, or covariance analysis (see Chapter 4). The system's analysis might necessitate iterative processes to ensure compliance with defined requirements, encompassing operational constraints, scientific objectives, and Delta-V budget considerations. Notably, station-keeping cost estimates are influenced by OD performance, alongside OI and maneuver execution accuracy. While the scope of system analysis can extend further, for instance, to include attitude estimation impacts, the focus here remains on three primary drivers. Operational constraints in this context refer to tracking window durations, visibility, pointing requirements, and related operational challenges. This comprehensive system analysis flow underscores the iterative nature required for effective OD system construction, providing a framework for addressing the technical complexities associated with such systems. It should be noted that the presented data flow serves as a guide for system analysis and technical aspects of OD data flow will be provided in chapter 6.

Building on the foundational aspects of system analysis, the initial step involves a thorough assessment of the ISL budget, a factor paramount to the system performance. The link budget encapsulates a detailed calculation of the cumulative gains and losses encountered within a communication system, ensuring that the signal transmitted is robust enough to be acquired by the receiver despite the inherent challenges of dis-

Table 2.5: Radiometric Measurement Error Models and Corresponding Error Budgets.

Radiometric Observable	Error Source	Description	Error Model
Range	Thermal noise (Random)[a]	PN Ranging, (Uplink/downlink only Chip Tracking Loop)	$\sigma_{\rho,PN} = \frac{1}{\sqrt{2}} \frac{c}{8 f_{rc}} \sqrt{\frac{B_L}{(P_{RC}/N_0)}}$
		Tone Ranging, (Uplink/downlink only Open Tracking Loop)	$\sigma_{\rho,tone} = \frac{c}{f_{RC} A_c \sqrt{32\pi^2 T (P_r/N_0)}}$
		Telemetry-based, (Correlator, end-to-end)	$\sigma_{\rho_{TM}} = \sqrt{\sigma^2_{\rho_u} + \sigma^2_{\rho_d}}$, $\sigma_{\rho_u} = \frac{c}{8 f_{rc}} \sqrt{\frac{B_L}{(P_{RC}/N_0)}}$, $\sigma_{\rho_d} = \frac{4 c T^2_{sd}}{\pi T E_S/N_0}$
		Data-aided, (Correlator, end-to-end)	$\sigma_{\rho_{TCTM}} = \sqrt{\sigma^2_{\rho_u} + \sigma^2_{\rho_d}}$, $\sigma_{\rho_u} = \frac{4 c T^2_{sd,tc}}{\pi T_{dp} E_S/N_0}$, $\sigma_{\rho_d} = \frac{4 c T^2_{sd,tm}}{\pi T_m E_S/N_0}$
	Systematic Errors	Chip rate mismatch	$\Delta\rho = \frac{c \Delta f_{RC} T}{4 f_{RC}}$
		Group delays	N/A
		Instrumental delays	Depends on instrument, <5 m
		Clock bias, drift, and aging	Depends on clock, $\sigma_y(\tau)$<5e-11
		Clock instability	$\Delta\rho = \sqrt{c\tau}\sigma_y(\tau)$
		Clock offset	$\Delta\rho_{CO} = c\Delta T$
		Clock rate offset	$\Delta\rho_{CRO} = c\tau\Delta\dot{T}$
		Time tag error	$\Delta\rho_{TT} = \Delta T \dot{\rho}$
Range rate	Thermal noise (Random)	Tracking loop (Two-way)	$\sigma_V = \frac{c}{2\sqrt{2}\pi f_c T} \sqrt{\frac{1}{\rho_L} + \frac{G^2 B_L}{(P_C/N_0)}}$
	Systematic Errors	Group delays	$\sigma_{V,SEP} = \frac{0.73 c \sqrt{C_{band}} \sin(SEP)^{-1.225}}{f_C T^{0.175}}$
		Clock instability	$\sigma_V = \sqrt{2} c \sigma_y$
Line-of-Sight	Random Errors	Time delay/Phase-shift-based	$\sigma_\theta = \sqrt{-\frac{1}{2}\ln\left(1 - 2\left(\frac{\sigma_\rho}{b}\right)^2\right)}$

[a]Note that equations given in the table for conventional ranging methods might be different for specific cases such as a square-wave ranging signal.

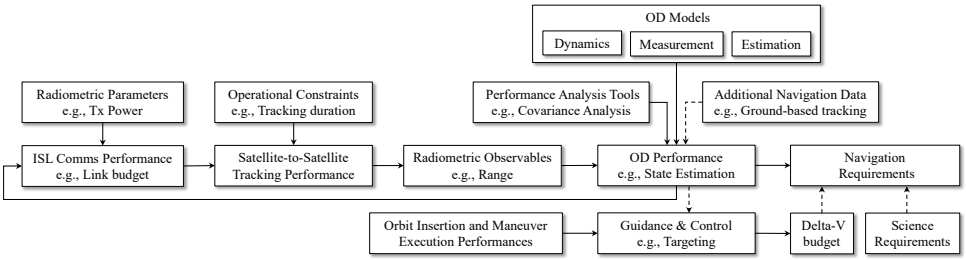

Figure 2.23: System Analysis Block Diagram Overview. The process begins with an examination of the inter-satellite radio communication link budget, followed by the generation of radiometric observables under operational constraints, including tracking and visibility windows. The OD models then calculate computed values, allowing for the calculation of residuals. Using performance analysis tools, the OD performance is assessed, and radiometric parameters can be optimized based on these findings. Note that OD models, performance analysis tools, and corresponding OD performances will be presented in the subsequent chapters.

tance and required data rates. This meticulous process incorporates an array of elements, including transmitter power (P_T), transmit antenna gain (G_t), free-space path loss, receiver antenna gain (G_R), receiver sensitivity, and potential losses due to cables and negligible atmospheric attenuation for space-based communications.

A pivotal aspect of the link budget is its role in determining the feasibility and reliability of the communication link, guiding the optimization of system parameters such as antenna dimensions to meet the mission's communication needs. Of particular interest is the inter-satellite distance, which directly influences communication capabilities and measurement precision. An alteration in distance, for example, a tenfold increase, from 100 km to 1000 km, results in a significant 20 dB shift in free space path loss (FSPL), represented by:

$$\text{FSPL(dB)} = 20\log_{10}(\frac{4\pi df}{c}) \tag{2.43}$$

This change not only affects the link budget due to FSPL but also dramatically alters the data rate by a factor of 100. In scenarios where telemetry-ranging is employed for satellite-to-satellite tracking, such a distance adjustment necessitates an additional 20 dB gain for every tenfold increase in distance to maintain comparable ranging accuracy in downlink measurements.

Contemporary technology has facilitated various implementations of ISL, showcasing their potential in real missions. For instance, the Rosetta-Philae link exemplified two-way S-band communications capable of reaching up to 16 kbps across 150 km [143]. Additionally, the OLFAR constellation case study demonstrated the feasibility of achieving 48 Mbps data rates over a 90 km separation [143]. These examples underscore the profound influence of inter-satellite distance on the attainable ISL data rates at different transmit powers, as depicted in Figure 2.24.

In light of these considerations, it becomes evident that the inter-satellite distance is a principal determinant in shaping the mission profile. It dictates the achievable data rates and, by extension, the overall effectiveness of the communication system within the mission's operational framework. Consequently, a thorough investigation into mission profiles, taking into account varying distances and their implications on link budget

and system performance, is indispensable for the successful planning and execution of space missions.

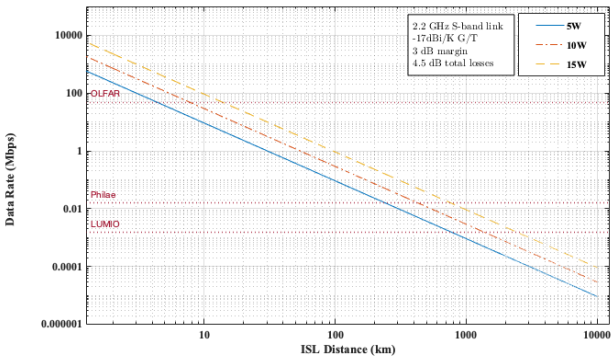

Figure 2.24: S-band Data Rates as a Function of Inter-Satellite Distances and Transmit Powers. This graph demonstrates how data rates vary with changes in inter-satellite distances, highlighting the impact of different transmit powers on achievable data rates.

Deep space missions involve various phases depending on the mission profile, including:

- Cruise (towards a point)
- Flyby (small bodies or planets)
- Rendezvous (docking)
- Orbiting (planets, small bodies, or Lagrangian points)
- Landing (planets, small bodies)

The scope of this thesis is deliberately focused on the orbiting phase of missions within the cislunar region (targeting Lunar and Lagrangian orbiters) and in proximity to smaller solar system bodies. This concentration stems from the inherent limitations of SST during the cruise phase of missions, where it fails to offer a reliable navigation solution. In contrast, the orbiting phase around Earth and detailed SST scenarios in the cruise phase are left for discussion in Chapter 5, aiming to shed light on the potential performance outcomes. A specific case study presented revolves around a lunar CubeSat mission, examining the communication dynamics between a lunar orbiter and an Earth-Moon L2 Halo orbiter. It is crucial to acknowledge that the inter-satellite distances between L1/L2 Halo orbits and lunar orbits fall within a similar range ($< 1 \times 10^6$ km), thus the discussion will primarily revolve around a link between the lunar orbiter and an Earth-Moon L2 Halo orbiter to represent a worst-case scenario.

In addition to this research study, the author participated in a lunar CubeSat mission study called LUMIO; designed to observe, quantify, and characterize meteoroid impacts by detecting their flashes on the lunar far side at an EM L2 Halo orbit. This part of

the study is based on experience gathered during the phase-0 and phase-A design studies, focusing on the communication and radio navigation systems integral to the Lunar CubeSat project. The findings and methodologies outlined here are adaptable to similar mission contexts in the cislunar space, underscoring the broader applicability of the research. Detailed OD performance for this mission scenario will be presented in Chapter 5.

As studied in [80], the operational design of the radiometric navigation system integrates communication hardware to feature both ISL and DTE links. The DTE link, primarily designed for the downlink transmission of payload data, also incorporates ranging and tracking capabilities for standard operational scenarios over distances approximating ~ 480 000 km. This includes a DTE link from the CubeSat to the Sardinia Deep Space Antenna, achieving data rate performances up to 450 kbps at maximal separation distances, facilitated through the X-band with an inclusive 3 dB margin (see [80] for further details).

Moreover, the ISL serves as a redundant command link, eliminating the necessity for a dedicated deep-space class ground station by utilizing commercial resources instead. This approach ensures optimal visibility performance, albeit with restricted data rate capabilities. The SSTL Lunar Pathfinder (LPF) spacecraft emerges as a critical component within this framework, acting as a relay satellite. Data rates ranging between 0.5 kbps-4 kbps are anticipated, contingent on the relative distances spanning from 31 000 km to 89 000 km, predicated on S-band specifications, 9 dBW link, and inclusive of a 3 dB safety margin. It is critical to note that the ISL configuration has not been specifically tailored for SST or telemetry functionalities, indicating that enhancements such as a larger antenna or increased onboard transmission power could further optimize system performance.

Utilizing two-way operations for baseline measurements, the mission scenario dives into analyzing performance under two distinct measurement error frameworks: One reflecting the high accuracy typically associated with conventional pseudo-noise ranging methods and another mirroring the challenges posed by low data-rate, data-aided ranging methods. A pivotal step in enhancing the mission's navigational accuracy involved reconfiguring the radiometric parameters to suit the demands of the SST-based OD, notably improving upon the initial configuration that yielded a 2700 m (1σ) ranging accuracy. This optimization hinged on augmenting the uplink data rate and symbol duration through an enhanced antenna configuration and increased transmit power.

The distinction between the two measurement scenarios extends beyond measurement errors, delving into their operational impacts. While prolonged tracking arcs are typically desirable for accuracy, practical constraints often limit continuous tracking. Such constraints may emerge from operational necessities, including Telemetry & Telecommand (TTC) and station-keeping intervals. In certain scenarios, integrating the ranging signal within telemetry or telecommand signals presents a feasible solution, thereby mixing telemetry, telecommand, and tracking within a single operational window. However, traditional ranging techniques necessitate a dedicated portion of onboard power for the ranging signal, which could consequently restrict telemetry capabilities. This presents a significant challenge for small satellites with limited onboard power resources, necessitating the strategic planning of operations across distinct time frames, as de-

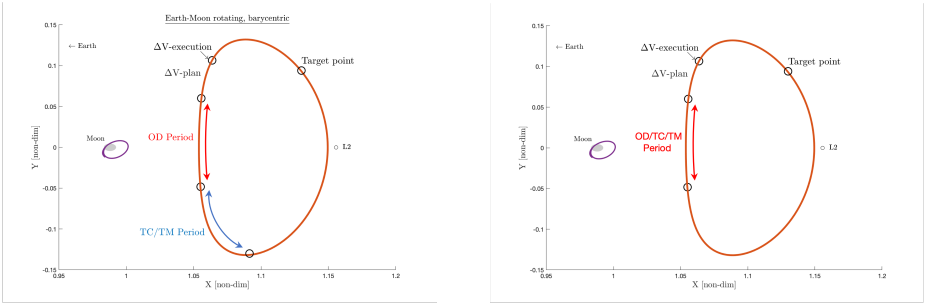

(a) Conventional ranging-based.

(b) Data-aided ranging-based.

Figure 2.25: Operational Time Windows Illustration. This figure highlights how data-aided ranging or telemetry-ranging could simplify mission operations, potentially allowing for extended periods of tracking, telemetry, and telecommand sessions. It underscores the operational flexibility and efficienct that these ranging methods bring to mission operation management.

picted in Figure 2.25a.

Conversely, telemetry-ranging or data-aided ranging approaches offer the potential to entirely eliminate the dedicated ranging signal. This strategy enables the reallocation of the full power capacity towards telemetry or telecommand functions. In such configurations, the time windows for TTC and SST overlap, facilitating the simultaneous execution of all pertinent operations, as illustrated in Figure 2.25a. Additionally, this approach allows for the possibility of extending the total duration dedicated to SST/TTC/OD operations, thereby collecting additional navigation data and enhancing telemetry transmission. The critical challenge here revolves around the trade-off between *achieving accurate ranging within limited tracking windows or opting for less accurate ranging accompanied by extended tracking arcs*, e.g., a 3-hour session of SST based on PN ranging with an expected error of 3 m (1σ), or extended 6-hour session employing Data-aided ranging, with performances of 100 m (1σ). Chapter 5 will delve deeper into these considerations, exploring the influence of measurement errors and geometric configurations on overall system performance. To facilitate this investigation, it is critical to establish radiometric measurement parameters that account for worst-case conditions, such as those based on the maximal inter-satellite distances encountered in cislunar space, with a fixed data-rate determined for the specified scenario.

The nominal radio parameters are presented in Table 2.6. Note that 4 kbps representing the worst-case scenario is given in the table. This data rate is inherently dependent on the distance between the satellites and can escalate to 100 kbps in scenarios where orbiters are in closer proximity, such as formations around small solar system bodies. The choice of S-band as the baseline frequency for inter-satellite communications is predicated on the findings of [80], which highlighted the comparative power and volume efficiencies of S-band radios over X-band counterparts, as further illustrated in Table 2.7.

It is important to note that this differentiation in data rates, tailored to specific inter-satellite distances, directly influences the radiometric measurement errors. Thus, the baseline parameters outlined may be subject to adjustments based on the unique requirements and constraints of individual mission scenarios within this work.

In brief, the procedure presented in this work could contribute to helping the mission design of small satellites in deep space. In particular, various system parameters in mission design including antenna size, ranging clock frequency, data rate, OD frequency, filter selection, and other parameters could be handled in a single loop. The following chapters of this thesis will pivot around the foundational structure established in this section, further delving into these aspects with an emphasis on their practical implications and operational efficiency.

2.5. ENABLING TECHNOLOGIES

This section delves into the current state and future prospects of inter-satellite radio links, essential for autonomous on-board OD leveraging the communication systems integral for telecommand, telemetry, and tracking. In the current state, small satellites in deep space utilized two radios: the PROCYON (X-band) and the IRIS (X-band) [144]. PROCYON's radio stands out for its tone generator for range and range rate measurements and ΔDOR orbit determination capabilities, supported by a robust 15 W power output [145]. In contrast, the IRIS transponder, a product of JPL's innovation for the MarCO mission, supports sequential/PN ranging, Delta-Differential One-Way Ranging (DDOR), and Doppler with a 4 W RF output.

The updated V2.1 IRIS Transponder, set to be employed in six CubeSats as part of the Artemis-1 mission, was designed to support communications over distances ranging from up to 180 Mkm and achieve downlink data rates up to 6.25 Msps [146], which is substantially beyond the Artemis-1 CubeSats' requirement of 256 kbps. This advancement is poised to enhance proximity operations and inter-satellite communication significantly [147]. In addition, an experimental one-way uplink ranging has also been implemented, allowing formations to perform ranging simultaneously on the same uplink ranging signal [148].

The CAPSTONE mission has employed Iris radio for DTE communications and Tethers Unlimited's SWIFT SLX radio for crosslink purposes, utilizing the LRO at an output power of 2 W in the S-band [149]. This mission's objectives include the evaluation of one-way ranging with the DSN and crosslink ranging experiments, with ground test results aligning closely with theoretical predictions, highlighting one-way radiometric range precision between 0.38 m and 2.21 m and a range rate of 11 mm/s at a 60-second integration time [150].

Moreover, the OMOTENASHI CubeSat, another Artemis-1 participant, will incorporate a new X-band transponder, succeeding PROCYON's transponder, to provide advanced navigation capabilities alongside a P-band transceiver for amateur operators [151]. In addition, the CU-E3 mission aims long-distance communications reaching over 4 million km [69], [152].

Several other small satellite radios, identified for potential use in cislunar missions [92], can be considered for radio-navigation. Notably, the Tethers Unlimited SWIFT-RelNav SDR system enables promising crosslink communication and ranging accuracy of 10 cm at 12 Mbps [154]. The MASCOT and Hayabusa-2 missions showcased UHF band communication via the lightweight Parent-COM transceiver (<< 100 g), achieving data rates up to 37 kbps [155]. The PRISMA mission's success in inter-satellite data transmission and accurate ranging measurements, 1 cm, further exemplifies the progress in this

Table 2.6: Summary of Typical Radiometric Measurement Parameters and Corresponding Errors. This table presents the specific parameters and associated errors for radiometric measurements, focusing on formations consisting of Lunar/EML2 Halo orbiters. It is noted that Lunar/EML1 Halo configurations are expected to yield comparable results. Additionally, in formations where satellites are in close proximity, such as formations around small solar system bodies, data rates can reach up to 100 kbps and higher, which contributes to reduced measurement errors.

	Parameter	**Value**	
		Downlink	Uplink
Inter-Satellite Link (ISL) Budget	Frequency, f	2200 MHz	2100 MHz
	TX power, P_t	3 dBW	3 dBW
	TX path losses, L_t	1 dB	1 dB
	TX antenna gain, G_t	6.5 dBi	23.6 dBi
	Polarisation loss, L_p	0.5 dB	0.5 dB
	Data rate	4000 bps	500 bps
	Required E_b/N_0	2.5 dB	2.5 dB
	Link Margin	3 dB	3 dB
	Inter-satellite distance	$<1 \times 10^6$ km	
Inter-Satellite Radiometric Measurement Parameters (ISL)	Symbol rate, $1/T_{sd}$	4000 sps	2700 sps
	Correletor integration time, T_l	0.5 s	
	Symbol-to-noise ratio, E_s/N_0	−1 dB	
	Modulation	BPSK	
	Transponding ratio, G	1	
	Range clock frequency, f_{rc}	1 MHz	
	Ranging code	PN, T4B	
	Ranging clock power over noise spectral density, P_{rc}/N_0	25 dBHz	
	Loop Bandwidth, B_L	1 Hz	
	Chip rate difference, Δf_{chip}	100 Hz	
	Clock instability, $\sigma_y(1s)$	4×10^{-11}	
	Clock error on range	on the order of 1 cm	
	Clock error on range-rate	on the order of 0.1 mm/s	
Ground-based Radiometric Measurement Parameters	Tx Frequency f	7200 MHz	
	Ranging Code	PN, T4B	
	Range clock frequency	1 MHz	
	P_{rc}/N_0	30 dBHz	
	Loop Bandwidth, B_L	0.25 Hz	
	Minimum elevation angle	5 deg	
Measurement Error Budget 1σ, (two-way)	Inter-satellite range meas. error, $\sigma_{\rho_{STT}}$	1-100m	
	Inter-satellite range-rate meas. error, $\sigma_{\dot{\rho}_{STT}}$	1 mm/s	
	Ground-based range meas. error, $\sigma_{\rho_{GS}}$	1 m	
	Ground-based range-rate meas. error, $\sigma_{\dot{\rho}_{GS}}$	0.1 mm/s	
	Satellite-to-satellite angle meas. errors, $\sigma_{\phi_{SST}}, \sigma_{\varphi_{SST}}$	40 arcsec	

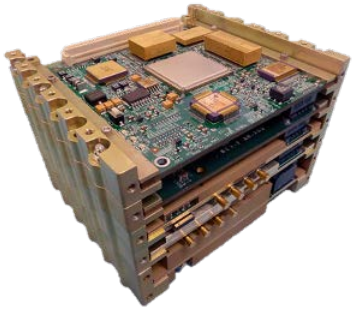

Figure 2.26: JPL IRIS V2.1 Transponder [153].

domain.

Looking ahead, CNES's initiative to develop miniaturized ISL for exploration missions [155], informed by insights from PRISMA and others, indicates a move towards more sophisticated and accurate navigation solutions. The development leverages the Syrlinks S-band transponder as a hardware foundation, aiming for sub-10 m ranging error and enhanced data transmission rates (128 kbps). This effort also introduces the potential for multipoint ISL, facilitating simultaneous communication with multiple satellites.

Reference missions like Juventas anticipate inter-satellite data rates of up to 460 kbps in the S-band at a 2 W output power, with estimated crosslink measurement accuracies with HERA of 1 m in range and 1 mm/s in range-rate [156], highlighting the ongoing innovation in small satellite radio technology. Additionally, radios employed on larger missions, such as the Small Deep Space Transponder (SDST) (utilized in Deep Space 1, Deep Impact, and InSight [157]), Frontier, Universal Space Transponder (UST), and UST-lite others [158], [159], though more voluminous, present viable options for enhancing small satellite missions' navigation capabilities. Table 2.7 summarizes the capabilities of selected small satellite radios, underscoring the diverse and evolving landscape of radio navigation technologies poised to support future deep space exploration missions.

2.6. SUMMARY

This comprehensive chapter described the radiotracking architectures, technologies, and their integration into the SST-based OD framework. It categorizes SST ranging methods into three distinct approaches: phase, time, and hybrid measurement methods, including conventional pseudo-noise (PN)/Tone ranging, telemetry-ranging, data-aided ranging, and time-derived ranging. A central focus is placed on the collection along with available standards, computation, and strategic incorporation of radiometric observables into OD, aiming to determine low-cost, reliable systems suited for small satellite formations. Operational constraints, inherent to such missions, are considered to highlight operational benefits, drawbacks, and expected performances carefully. Mission tracking scenarios and a system analysis flow diagram were presented to facilitate a realistic mission analysis, underscoring the practical application of these methodologies

Table 2.7: A Brief Overview of Satellite Radios.

	Mass [kg]	Volume [cc]	Frequency bands	Data Rate (up to)	Link
JPL Iris	1	560	UHF X / X	6.25 Msps	DTE
General Dynamics SDST	3.2	3386	X /X Ka	30 Msps	DTE
JHU/APL Frontier	2.1	2050	S/X/Ka	150 Msps	DTE
JHU/APL Frontier Lite	0.4	320	UHF/C	10 Msps	DTE
JPL UST Lite	3.0	2700	UHF/S/X/Ka	300 Msps	DTE / ISL
Clyde Space STX	0.08	138	S	2 Mbps	DTE
Tethers Unlimited SWIFT-SLX	0.38	350	S	15 Mbps	DTE / ISL
Tethers Unlimited SWIFT-XTS/KTX	0.5	375	X/Ka	300 Mbps	DTE
Syrlinks/ EWC27	0.225	207	X	5 Mbps	DTE
Syrlinks/ EWC31	0.25	260	S	2 Mbps	DTE / ISL
Tethers Unlimited SWIFT-RelNav SDR	0.38	350	X	12 Mbps	DTE / ISL
Blue Canyon Technologies SDR	N/A	N/A	UHF S X Ka	100 Mbps	DTE, ISL

in the design and execution of small satellite missions in deep space.

Key findings from this chapter include:

- An extensive review of ranging methods for the purpose of SST in section 2.1 alongside their performance metrics, providing a detailed overview as depicted in Figure 2.21.
- A detailed presentation of inter-satellite radio parameters, measurement error budgets, and error models, summarized in Table 2.6 and 2.5.
- A preference for data-aided or telemetry ranging methods over conventional tone/PN methods for small satellites in deep space, attributed to the operational efficiencies in power allocation for telemetry and the ability to conduct tracking and telemetry simultaneously, allowing also more time for scientific activities and particularly beneficial in close proximity operations and high data rate transmissions.
- A simplifed system analysis flow that bridges the gap between radiometric considerations and navigation system performance.

3

SATELLITE-TO-SATELLITE TRACKING-BASED AUTONOMOUS ORBIT DETERMINATION

Recent advancements have introduced various innovative strategies for autonomous spacecraft navigation. Among these, Satellite-to-Satellite Tracking (SST)-based Autonomous Orbit Determination (OD) emerges as a particularly promising approach, using existing systems and providing navigation solutions for satellite formations based on inter-satellite measurements. Starting with an overview of the general OD problem, this chapter introduces a detailed exploration of the SST-based OD process, addressing the challenges, methodologies and existing knowledge gaps. Additionally, it outlines the specific navigation requirements and goals for small satellite missions in deep space. The chapter offers extensive OD models, including dynamical, measurement, and estimation aspects, setting the stage for the following chapters of this dissertation. It also evaluates the computational demands associated with on-board processing algorithms, crucial for real-time applications in autonomous navigation.

Parts of this chapter have been published in:
E. Turan, S. Speretta, and E. Gill, "Autonomous navigation for deep space small satellites: Scientific and technological advances", *Acta Astronautica*, vol. 193, pp. 56–74, Apr. 2022. DOI: 10.1016/j.actaastro.2021.12.030
E. Turan, S. Speretta, and E. Gill, "Performance analysis of crosslink radiometric measurement based autonomous orbit determination for cislunar small satellite formations", *Advances in Space Research*, vol. 72, no. 7, pp. 2710–2732, Oct. 2023. DOI: 10.1016/j.asr.2022.11.032

3.1. ORBIT DETERMINATION

In space, the motion of objects follows distinct trajectories, commonly referred to as orbits. An orbit, in essence, describes the translational motion of an object as it is influenced by the gravitational pull exerted by larger mass bodies, such as planets and moons. It can be represented in state vector format as position and velocity or as orbital elements [160]. The ability to accurately define these orbits lies at the core of Orbit Determination (OD), a discipline within the field of space science and engineering that ensures the successful navigation and operation of spacecraft.

In this context, OD refers to the process leading to the satellite orbit, i.e., position, and velocity knowledge as a function of time, with respect to a fixed reference frame (absolute) or with respect to another spacecraft or moving object (relative). OD covers where the object was located in the past (definitive), is located at present, and will be located in the future (predictive) [1]. In other words, OD is the process of determining the position and velocity of an object at specific times with respect to a defined coordinate system and seeks to answer the following critical question:

- How does an estimator incorporate measurements and determine an orbit that provides the best fit to the collected data, considering the dynamics of a satellite's orbital motion?

The OD problem has been studied by scientists for centuries: many methods have been developed since Gauss addressed the OD problem utilizing least squares estimation in 1795 [161]. This technique uses data collected for a given time period and then processes it all together to obtain an offline solution. In 1960, Kalman addressed the challenge of handling noisy measurements and process noise in dynamic systems by providing a solution known as filtering [162]. Since then, various numerically stable and efficient filtering techniques have been proposed.

The OD process involves dynamical models, which describe the forces acting on the spacecraft, and measurement models, which represent how measurements are computed (See Figure 3.1). Estimation techniques then utilize the differences between actual and modeled measurements to generate an estimated state vector, containing position, velocity, and possibly various other parameters, including force model parameters, measurement biases, and clock-related parameters. In this process, OD methods comprise three key phases: **predicting**, involving the estimation of future states based on existing information and observations, **filtering**, which derives the current state information using a combination of present and past data, **smoothing**, where past states are improved by using all available observations. In this study, the term *filtering* is used to refer to both Kalman-type methods and sequential-batch methods as given in [163]. It should also be noted that least squares and batch least squares are given as smoothing techniques due to their solution belonging to a particular epoch time [163].

In typical ground-based OD, tracking stations employ various techniques to collect data about the spacecraft trajectory. As detailed in Chapter 2, it is important to understand that these measurements are imperfect and are distributed around the spacecraft's *true* trajectory. A prime example of this is radiometric tracking, which starts the transmission of radio signals from a ground station directly to the spacecraft. Upon receiving these signals, the spacecraft then retransmits them back to the ground station. The time

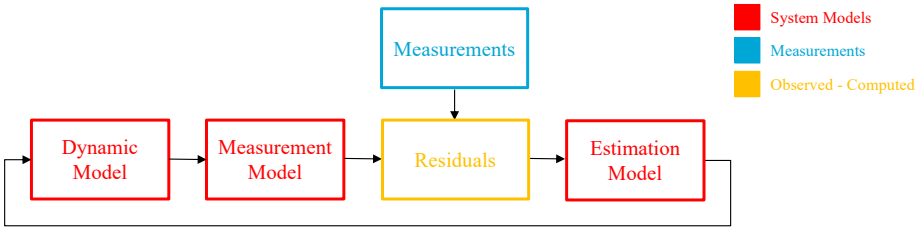

Figure 3.1: Simplified Orbit Determination Process.

it takes for the signal to travel from the ground station to the spacecraft and back is measured (see Figure 3.2). Moreover, by analyzing the frequency of the received signal in comparison to the one transmitted, the relative velocity of the spacecraft with respect to the ground station can be measured. Additionally, the angle from the ground station to the spacecraft can also be measured. Collected data is then processed, and an *estimated* trajectory is produced along with its uncertainty. In this context, the navigation filter plays a critical role by combining information from the dynamics and the measurements to obtain the most accurate estimate possible. Following the estimation phase, the trajectory correction process starts by implementing maneuvers to align the spacecraft with the planned trajectory, which is commonly called the *nominal* orbit. As the spacecraft is guided to remain close to its *nominal* orbit, non-optimal estimations can lead to increased propellant consumption and potential deviations from the intended path. Thus the OD accuracy and subsequent corrections are not just crucial for scientific operations but also for operational efficiency and mission success.

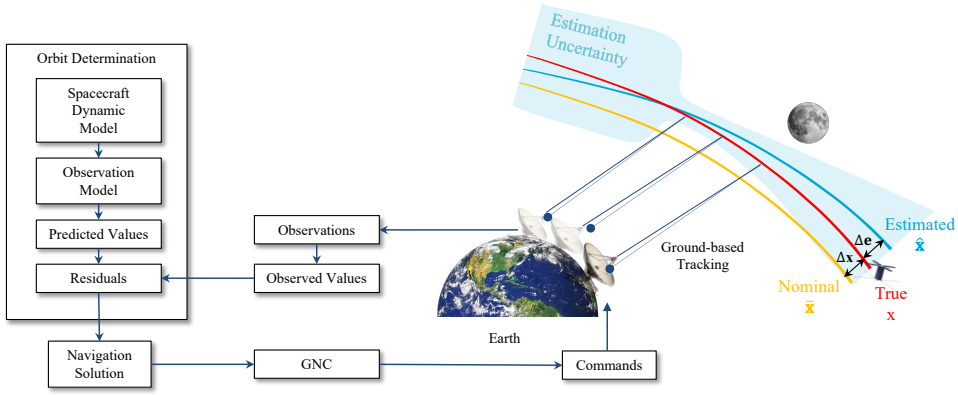

Figure 3.2: Simplified illustration of the ground-based orbit determination, representing that measurements given as dots are not perfect and contain errors. Nominal states

OD methods encompass a variety of algorithms divided into two main categories: batch and sequential processing. The former processes a batch of observations together, considering associated measurement uncertainties, and aims to find the state vector that

Table 3.1: Comparison of the data processing algorithms.

Aspect	Batch	Sequential
Processing approach	Collectively	Incrementally
Timing	Offline/Post-processing manner	Real-time/Near real-time
Complexity	Higher computational resources	Less computational resources
Estimation Updates	A single refined OD solution	Continuous refinement
Requirements	Initial state estimation Partial derivatives (force and meas.models)	Initial state estimation and associated uncertainty Partial derivatives (force and meas.models) except UKF
Sensitivity	Fit span	Initial state estimation

minimizes the weighted sum of squared differences between the computed observations and the actual measurements. By having different weights to different measurement types, the algorithm gives more importance to accurate and reliable observations while not taking into account less reliable measurements. In other words, the batch-weighted least squares algorithm iteratively adjusts the initial estimate of the state vector using a weighted least squares approach until convergence to a solution is achieved. Sequential processing instead involves updating the estimation incrementally as new data is received. Table 3.1 provides a comparison of these approaches.

Both approaches have their own advantages and are suitable for different scenarios: sequential processing is beneficial for real-time applications where timely updates are crucial, while batch processing is useful for offline applications. If the *true* and *estimated* orbits significantly differ due to linearization assumptions, both algorithms may yield divergent solutions where the calculated trajectories notably deviate from the actual or expected path of the object in space. The choice between them depends on the mission requirements, available resources, and timing constraints of the OD task at hand. It is worth noting that sequential processing requires an accurate initial state, which is often provided by batch-processing previous measurements.

As discussed in Chapter 1, from the ground segment operations standpoint, deep space missions pose several challenges, including the need for precise tracking within limited contact times, managing and increasing number of missions with limited tracking resources, and others [5]. Traditional methods of ground-based tracking, while effective, often cause significant costs, a notable concern for missions deploying cost-sensitive small satellites. Furthermore, essential ground-based activities such as station keeping and executing trajectory correction maneuvers, which are typically calculated on Earth and then transmitted as commands to the spacecraft, require the expertise of a flight dynamics team, thereby increasing overall mission expenses. Given the goal of minimizing mission costs, integrating autonomous operations stands out as a strategically advantageous approach. Autonomy, in this context, enables satellites with the ability to independently make decisions and execute tasks with minimal to no human intervention [5], significantly enhancing operational efficiency, reliability, adaptability, and ultimately, the success rate of the mission, while reducing mission costs. Specifically, on-board autonomy is defined by the capability of the space segment to manage nominal or contingency operations without ground segment intervention for a given period of time [164]. With autonomy levels as outlined in Table 3.2 [164], where higher levels correspond to decreased ground-based intervention, this study aims to achieve full autonomy, particularly at levels E3 and E4, to realize the self-sufficient, cost-effective space

Table 3.2: Mission execution autonomy levels taken from [164]

Level	Description	Functions
E1	Mission execution with ground control; limited onboard capability for safety issues	Real-time control from ground for nominal operations Execution of time-tagged commands for safety issues
E2	Execution of pre-planned, ground-defined, mission operations on-board	Capability to store time-based commands in an on-board scheduler
E3	Execution of adaptive mission operations on-board	Event-based autonomous operations Execution of on-board operations control procedures
E4	Execution of goal-oriented mission operations on-board	Goal-oriented mission re-planning

missions.

OD is a key field that could greatly benefit from autonomous operations, as depicted in Chapter 1. Autonomous navigation, as introduced, offers several advantages, including the potential for significant cost savings and improvements in performance. Notably, autonomous navigation systems can perform specific tasks more efficiently and effectively than ground-controlled systems, making some operations exclusively viable through autonomy. Chapter 1 categorized navigation methods into on-board and off-board based on where the navigation data is collected, processed, and stored. Since autonomous navigation implies navigation with minimal or no human input, these navigation approaches have been further divided into fully autonomous and semi-autonomous approaches. Fully autonomous navigation, which operates independently of ground-based interventions, aligns with the E3 and E4 levels of mission execution autonomy. SST-based autonomous OD would be a typical example of on-board OD, which is studied in the following section in detail.

3.2. SST-BASED AUTONOMOUS ORBIT DETERMINATION

Building on the understanding of OD and the critical role of autonomous operations introduced in the previous section, this part dives into a specific method of autonomous navigation: SST-based autonomous OD. SST is a technique where two or more spacecraft track each other, thereby enabling the collection of measurements from which relative position and/or velocity can be deduced. This method is particularly advantageous for missions involving multiple spacecraft that are required to maintain precise configurations relative to each other, such as satellite constellations or deep space exploration missions.

The SST-based OD process initiates with the transmission of radio or laser signals between the spacecraft within the formation, or through visual-based tracking systems. Focusing on radiometric tracking systems, which are central to this study, the receiving spacecraft evaluates the characteristics of these signals, whether through one-way or two-way communication links. Notable measures include the round trip light time and the Doppler shift; the former assists in calculating the inter-spacecraft distance, while the latter provides information on their relative velocities. Subsequently, this information is processed using algorithms to determine the relative or absolute positions and velocities of the spacecraft within the formation. Significantly, this computation can be autonomously conducted on board each spacecraft, thereby enhancing the formation's operational independence.

A notable benefit of SST-based OD is its reliance on existing system components, such as radio tracking systems, thus eliminating the need for supplementary navigation instruments. While SST data fundamentally provides relative navigation solutions, it can also support the estimation of absolute states when integrated with ground-based tracking efforts. For example, by tracking a single spacecraft from the ground and employing relative measurements, the precise positioning and velocities of all formation spacecraft relative to a central body, like Earth, can be accurately determined. Absolute state knowledge is crucial for tasks like station-keeping with respect to a fixed reference frame. However, relying on ground-based commands for such operations takes the system away from autonomy. Alternatively, SST data can be used for absolute state estimation, where an on-board navigation filter estimates spacecraft position and velocity within the formation with respect to a fixed frame. Figure 3.3 illustrates the conceptual diagram of SST-based OD. In brief, this study defines that:

- SST-based autonomous OD is a method where multiple spacecraft track each other to estimate the state of each spacecraft on-board in real-time with respect to a fixed reference frame, thereby advancing the autonomy of space missions.

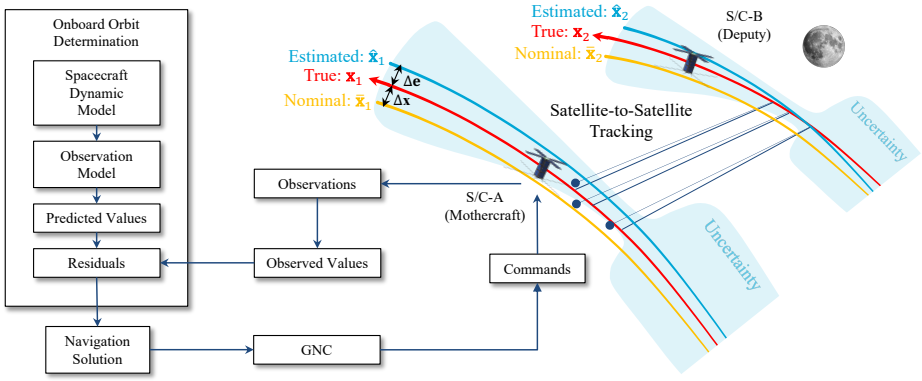

Figure 3.3: Simplified illustration of SST-based orbit determination, showing measurements as dots distributed around the true orbit, indicating their imprecision. The spacecraft collects these measurements to estimate the real-time state of each spacecraft with respect to a gravitational body, such as the Moon in this case. These estimations enable trajectory corrections towards nominal orbits.

Despite its advantages, SST-based autonomous OD introduces its own set of challenges, one of which is system observability. This is an important aspect, providing information on whether all orbital elements can be accurately estimated from the available measurements. It should be noted that relative measurements might not always yield a complete absolute state estimation or may only provide partial absolute state information. Such comprehensive state information is crucial for operations like station-keeping or for effectively commanding spacecraft from the ground. The absence of complete state information can adversely impact the success of a mission. In the context of OD involving a formation of two spacecraft, $i = 1, 2$, the estimation process focuses on the

position **r** and velocity **v** states of each spacecraft. In such scenarios, the challenge lies in ensuring that the following state vector can be fully determined:

$$\mathbf{x} = \begin{bmatrix} \mathbf{r}_1 & \mathbf{v}_1 & \mathbf{r}_2 & \mathbf{v}_2 \end{bmatrix}^T \tag{3.1}$$

To date, numerous studies have focused on SST-based absolute OD [11], [108]–[110]. In two-body dynamics, which describe the motion of two bodies influenced primarily by their mutual gravitational attraction, relying solely on inter-satellite range measurements does not yield a complete absolute state estimation, leading to what is known as a rank defect problem [11]. This challenge continues even when relative range-rate measurements supplement range data, as the system remains unobservable. This issue extends to inter-satellite angle-only systems as well [111].

The configuration of the spacecraft in their orbits significantly affects the observability of the system. For instance, two spacecraft orbiting on the same orbital plane tend to make the system less observable due to the lack of diverse measurement geometries. Previous research has shown that while inter-satellite range measurements can provide information about the orbital size and shape, they fall short of providing absolute orbital orientations, leaving critical parameters like the Right Ascension of Ascending Node (RAAN) unobservable [11]. To address this, some studies have explored various orbital configurations and found that non-coplanar elliptical orbital configurations provide the most observable geometrical condition in two-body dynamics [108]. Additionally, [110] has shown that the unobservability of RAAN can be solved by implementing third-body perturbation and solar radiation pressure models.

Expanding to multi-body dynamics reveals that absolute state estimation becomes feasible with SST-data when spacecraft occupy orbits with distinct sizes, shapes, and orientations [11]. This is particularly relevant in environments characterized by asymmetrical gravity fields, such as those around Lagrangian points or small solar system bodies (see Figure 3.4), where the gravitational forces exerted on a spacecraft are not uniform and vary over time while the spacecraft orbits. Since the navigation filter uses partials of spacecraft dynamics, e.g., STM, differences in spacecraft dynamics are beneficial from the estimation perspective. This will be further discussed in Chapter 4. Here, Figure 3.5 illustrates the three main cases from the dynamical perspective. It is worth noting that observable situations could easily be turned into unobservable if measurement errors are high and/or orbital configurations are not optimal. However, a detailed investigation of these aspects remains lacking in the literature.

SST-based autonomous OD benefits from the dynamic differences between spacecraft, their unique orbital paths, and the geometry of their measurements. It has been observed that increased inter-satellite distances and a greater number of nodes within formation enhance system observability [11], [113], improving OD performances while having satellites on the same orbital plane drastically reduces it [108], [165]. Studies have also explored the phase angle between satellites, as highlighted in the context of cislunar orbiters in [11], revealing that phase angles close to 0 and 180 degrees are not particularly useful. Comprehensive studies have demonstrated the capabilities of SST-based OD over the past decade [11], [109], [165]–[170]: A summary of the relevant mission concept studies can be seen in Table 3.3.

While SST-based OD offers promising accuracy for navigation solutions, this is not

Table 3.3: Brief overview of SST-based OD in the scientific literature.

Author	Mission Orbit	Number of S/C	Tracking	Inter-satellite Observables	Estimation Technique	Position Accuracy	Velocity Accuracy
Hill (2008)	Earth-Moon L2 Halo-Low Lunar Orbiter	2	SST-only	Range (RF)	EKF	Halo S/C 78.68 m (RSS) Lunar Orbiter 2.93 m (RSS)	Halo S/C 5.3×10^{-4} m/s (RSS) Lunar Orbiter 2.59×10^{-3} m/s (RSS)
Hill (2008)	Lunar Frozen Constellation	3	SST-only	Range (RF)	EKF	Sat1 - 1905.68 m (RSS) Sat2 and Sat3 N/A	N/A
Hill (2008)	Hybrid EM L2 Frozen Orbit Constellation	2	SST-only	Range (RF)	EKF	Halo S/C 87 m (RSS) Frozen Orbiter 9.8 m (RSS)	Halo S/C 0.4×10^{-3} m/s (RSS) Frozen Orbiter 1.4×10^{-3} m/s (RSS)
Hill (2008)	Earth-Moon L1 LEO Constellation	2	SST-only	Range (RF)	EKF	Halo S/C 512 m (RSS) LEO S/C 11 m (RSS)	N/A
Leonard (2012)	Asteroid(433 Eros)	2	SST+GT	Range, Doppler (RF)	EKF	Sat1 55.92 m (RMS) Sat2 37.46 m (RMS) Around 10 m with DSN	Sat1 5.6×10^{-3} m/s (RMS) Sat2 3.5×10^{-3} m/s (RMS)
Hesar (2012)	Asteroid(433 Eros)	2	SST/GT	Range, Doppler (RF)	EKF	Sub-meter level	N/A
Hesar (2015)	Earth-Moon L2 Halo-Surface Asset	2	SST+GT	Range, Doppler (RF)	EKF	Order of 10 m	N/A
Fujimoto (2016)	Asteroid(433 Eros)	11	SST-only	Range, Angles, Angle Rate (Visual)	EKF	Order of 1 m	$\sim 10 \times 10^{-4}$ m/s
Stacey (2018)	Asteroid(433 Eros)	3	SST-only	Range, Doppler, Angles, Angle Rate (RF+Visual)	UKF	Order of 1 m	$\sim 10 \times 10^{-6}$ m/s
Wang (2019)	DRO in cislunar space Lunar Orbitter	2	SST-only	Range (RF)	EKF	Order of 100 m	$\sim 10 \times 10^{-4}$ m/s
Tong (2019)	Observability analysis in the two-body dynamics	2	SST-only	Range (RF)	UKF	Order of 100 m	$\sim 10 \times 10^{-1}$ m/s

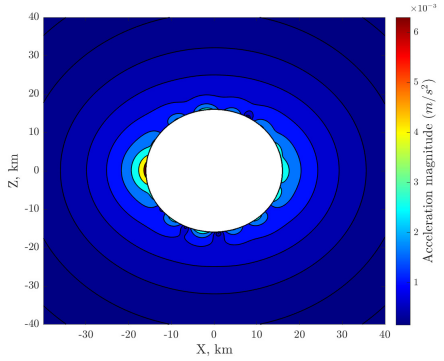

Figure 3.4: Asymmetrical gravity field of Eros (433) on the X-Z plane.

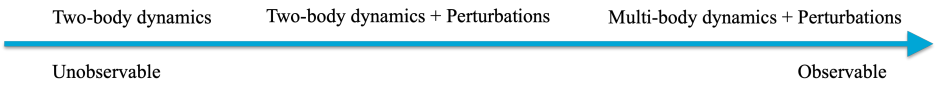

Figure 3.5: Observability aspect in SST-based absolute state estimation.

always straightforward, especially when inter-satellite measurements are not accurate or the observation geometry is not optimal. The impact of measurement errors on OD performance in these applications remains a critical unknown. Additionally, it is unclear which navigation data among range, range-rate, or angle, provides superior navigation solutions in different deep space environments.

The reliance on radio frequency measurement techniques to collect navigation data introduces another layer of complexity, necessitating a comprehensive analysis of system performances in terms of both systematic and random errors. The value of adding additional spacecraft into the network to improve OD accuracy also remains an open question, including the strategic selection of spacecraft for collecting navigation data (mothercraft). Given that it is not always feasible to collect inter-satellite measurements due to operational constraints, the planning of optimal tracking windows becomes a challenging task. This planning must take into account other operational requirements, such as commanding and control activities, further complicating the situation.

Moreover, the need for real-time navigation solutions introduces the challenge of designing a robust on-board estimation filter. This requires making decisions about which parameters should be estimated, which should be considered, and which may be neglected to ensure the system works optimally under various conditions.

Addressing these complexities requires detailed studies and careful investigations, particularly regarding system performance. Consequently, the subsequent chapters of this thesis are dedicated to exploring the following aspects in depth, shedding light on existing gaps in the literature:

- Dynamics: Orbital configuration, geometry, network topologies, tracking windows.

Table 3.4: Navigation requirements for various orbit regimes [50], [95], [132], [135], [171], [172]

Orbit	Ground-based tracking	ΔDOR	CELNAV/Optical	Requirement/Source
Lunar, in view	200 m at 2 days	1 km at 1 day	0.5 km at 0.5 days	0.5 km, LRO
Lunar, far side	N/A	N/A	0.5 km at 0.5 days	0.5 km, LRO
Sun-Earth Libration	4-32 km at 3 weeks	1 km at 1 day	5-15 km at 3 days	8 km, WFIRST 5 km, Lucy
Planetary	8-15 km at 3 weeks	1 km at 1 day	5-10 km at 3 days	2.8 km and 2 m/s, MARS 2020 (Cruise) 5 km (Crosstrack) and 0.2deg MARS 2020 (Entry)
Small body	20.5 m (Transverse)	N/A	N/A	20 m, 85 m, 7 m / OSIRIS-REx (Bennu) 1 km and 1cm/s / ARTEMIS
Earth-Moon Libration	N/A	N/A	N/A	1.27 km and 1.8 cm/s RSS /EQUULEUS (L2) 1 km and 1 cm/s / LUMIO (L2) 10 km and 10 cm/s / CAPSTONE (NRHO)

- Measurement: Errors, systematic bias, radiometric parameters, data type.
- Estimation: Filtering techniques, performance.

As mentioned in Chapter 2, the ultimate goal is to meet the navigation requirements, which often consider factors such as accuracy, availability, and continuity to ensure that navigation systems meet the specific needs and constraints of the intended application. In particular, they are subject to various factors, including mission objectives, mission phases, available measurement systems, spacecraft capabilities, and available technology. In [95], navigation requirements and capabilities are presented for various orbit regimes. Here, they are given in Table 3.4 together with other studies in the scientific literature to illustrate the needs of existing missions.

Although the literature does not offer a one-size-fits-all requirement for similar missions, the table sheds light on the specific navigation needs of various deep space missions. For instance, LRO requires a positional accuracy of 0.5 km, a goal that can be achieved with two days of ground-based tracking data, thereby reaching a positional accuracy of up to 200 m. This table also highlights the performances of alternative navigation methods, such as ΔDOR which employs a pair of distant ground antennas to track a transmitting object, measuring the time difference of signal arrivals to determine location, as well as optical navigation that relies on bearing to known celestial objects captured by an onboard camera system to estimate the spacecraft's position and velocity, as previously discussed in Chapter 1.

Scientific objectives can significantly influence OD requirements, potentially leading to vast differences in the requirements for different missions. In certain scenarios, the considerations for OD requirements may primarily revolve around the costs associated with station-keeping, which in essence, concerns to the propellant needed for the spacecraft to perform maneuvers to maintain its intended orbit. A critical factor in this analysis is the consideration of potential risks, including uncertainties in the spacecraft's orbital dynamics. By employing stochastic models for OD, OI, and execution errors, and conducting Monte-Carlo simulations, it is possible to gain valuable insights into the amount of propellant required for maintaining the spacecraft's desired position and trajectory.

Previous research has provided the station-keeping cost estimations for missions like EQUULEUS, a CubeSat mission in an Earth-Moon L2 Halo orbit [173]. These studies have considered OD and OI errors with assumed values, and factored in maneuver ex-

ecution errors, leading to varied annual station-keeping propellant requirements based on the specific orbital family. For instance, the annual station-keeping costs for EQUULEUS have been estimated to range between 12.65 m/s to 29 m/s [173], with a subsequent study indicating a reduced cost of 7.4 m/s for the same mission [50]. Similarly, for the LUMIO mission, designed for lunar observation from an Earth-Moon L2 Halo orbit, the estimated Delta-V required for annual station-keeping is around 4.3 m/s [171]. Such missions are meticulously planned to ensure that the required orbit can be maintained with minimal propellant, a critical consideration given the limited capacity for carrying additional propellant onboard.

To effectively manage these costs and ensure mission feasibility, it is essential to understand how OD errors impact station-keeping costs. This understanding can facilitate the establishment of specific OD requirements for missions, taking into consideration the Delta-V costs. The calculation is based on solving a Linear-Quadratic Regulator (LQR) problem, aiming to minimize the weighted sum of the Delta-V magnitude and the deviation from the reference orbit at predetermined target points. The optimal Delta-V can be calculated as follows [173]:

$$\begin{aligned} \Delta V_c(t) &= -\sum_{i=1}^{M} (\alpha_i \mathbf{e} + \beta_i \mathbf{p}) \\ \alpha_i &= [I_{3\times3} + R_i B_{t_i t_c}^T B_{t_i t_c}]^{-1} R_i B_{t_i t_c}^T B_{t_i t_0}, \\ \beta_i &= [I_{3\times3} + R_i B_{t_i t_c}^T B_{t_i t_c}]^{-1} R_i B_{t_i t_c}^T A_{t_i t_0}. \end{aligned} \tag{3.2}$$

where $\mathbf{e}$ and $\mathbf{p}$ are velocity and position perturbations, respectively. A and B are upper left and right parts of the State Transition Matrix (STM), respectively. M is the number of target points, and R_i is a weighting scalar with respect to i-th target point. More details about the target point method applied to Halo orbits can be found at [173].

In the context of an Earth-Moon L2 Halo orbiter scenario, the analysis given in Table 3.5 illustrates a significant correlation between OD error and the annual station-keeping costs. Specially, if the 1-sigma OD error reaches approximately 5 km for position and 5 cm/s for velocity, the annual Delta-V costs could exceed 10 m/s. Consequently, aiming for an OD accuracy of 1 km in position and 1 cm/s in velocity (1σ) can be considered acceptable, aligning with the requirements of other similar missions. It is important to note that the outcomes of such an analysis can vary based on several factors, including the chosen orbit, the number of target points and the placement of these target points. For example, the CAPSTONE mission, which operates in a Near Rectilinear Halo Orbit (NRHO), a more stable orbit compared to others, requires navigation knowledge of up to 10 km and 10 cm/s (3σ). Therefore, this study sets a goal to achieve better than 1 km and 1 cm/s (1σ) OD accuracy for the mission scenarios analyzed within the Earth-Moon system.

When considering missions around small bodies or during planetary cruises, the requirements for OD accuracy vary significantly depending on the specific target body or destination: it is not possible to provide a single requirement that fits all. However, in general, the orbital phase of a small-body mission would require an accurate OD solution. For example, as given in the table, OD accuracy requirements for the OSIRIS-REX mission were set significantly 1-2 orders of magnitude lower than those for previous mis-

Table 3.5: Annual station-keeping cost for an Earth-Moon L2 Halo orbiter, depending on the various OD and OI error levels.

Case	σ_{OD} [m]	σ_{OD} [m/s]	σ_{OI} [m]	σ_{OI} [m/s]	σ_{exec} [m]	Mean annual Delta-V [m/s]	Std (1σ) of annual Delta-V [m/s]
A	100	0.001	100	0.001	5%	0.77	0.05
B	500	0.05	500	0.05	5%	3.91	0.28
C	1000	0.01	1000	0.01	5%	7.85	0.54
D	5000	0.05	5000	0.05	5%	39.36	2.57
E	10000	0.1	10000	0.1	5%	79.22	6.36

sions [172], indicating a level that is difficult to reach. This is also true for the MARS 2020 mission during cruise aiming to enter the Martian atmosphere with a maximum OD uncertainty of 2.8 km in position and 2 m/s in velocity (3σ) [135]. Previous studies on autonomous OD have suggested that a positional accuracy of 5-100 km during the cruise phase is desirable for such missions [88]. Based on these considerations, this study aims to achieve the following OD accuracy (1σ) targets across different mission types:

- Cislunar: Order of 1 km and 1 cm/s
- Small solar system body: Order of 0.1 km and 0.1 cm/s
- Planetary: Order of 10 km and 1 m/s

In general, missions with human and/or surface observing objectives require accurate navigation solutions, while libration and planetary cruise fall into the lower accuracy category [95]. Table 3.6, adapted from [95], categorizes navigation categories based on accuracy, distinguishing between absolute definitive and absolute predictive navigation estimates. The former denotes a navigation estimate that encompasses a period during which measurements are available, thus offering an accurate description of the spacecraft's position and velocity relative to a fixed reference frame. The absolute predictive comes into play when the navigation estimate extends into a time frame where no measurements are readily available. Both are essential in navigation, providing insights into spacecraft dynamics. It is worth noting that the accuracy levels within each category can vary depending on the particular application.

Table 3.6: Navigation categories in terms of accuracy [95]

Navigation Category	Lower Accuracy	Accurate	High Accuracy	Precise
Absolute Definitive	100 - 300 m	5 - 40 m	50 cm - 10 m	1 mm - 50 cm
Absolute Predictive (1 day)	1 km	75 - 500 m	5 - 50 m	5 cm - 5 m

3.3. ORBIT DETERMINATION MODELS

The following sections of this chapter will present the OD models used in this dissertation: dynamical, measurement, and estimation models.

From a dynamic perspective, force modeling is a complex task due to all the perturbations from various sources. Multi-body (high-fidelity) modeling is essential for real SST-based autonomous OD applications, as two-body dynamics alone are inadequate

due to the rank defect problem. However, analyzing simplified models can provide insights into the application. Consequently, both high-fidelity and simplified dynamical models will be explored in subsequent sections. The discussion will then shift to measurement models, which include range, range-rate, and line-of-sight observables. Finally, the chapter will introduce estimation models, focusing on the algorithms used for on-board sequential data processing. These models are critical for real-time OD, enabling spacecraft to autonomously navigate and maintain their intended orbits.

3.3.1. DYNAMICAL MODELS

The dynamics of a satellite orbiting a primary celestial body, such as Earth, are described using a primary-centered inertial coordinate system. This system accounts for the gravitational force exerted by the primary body, along with perturbations from various secondary sources. These secondary forces include the gravitational influences of other solar system bodies, atmospheric drag, and solar radiation pressure. This dissertation adopts the notation outlined in [174]. The positions of a satellite at any given time t, denoted by $x_i(t)$, $y_i(t)$, and $z_i(t)$, form the basis of the satellite's position vector, $\mathbf{r}_i$, for satellites $i = 1,2$. Thus, the velocity vector, $\mathbf{v}_i$, comprises the derivatives of these positions over time, denoted as $\dot{x}_i$, $\dot{y}_i$, and $\dot{z}_i$. The propagation of the satellite's state vector $\mathbf{x}$, given in Eq. 3.1, over time is governed by the following differential equation:

$$\frac{\mathrm{d}\mathbf{x}(t)}{\mathrm{d}t} = f(\mathbf{x}, t) \tag{3.3}$$

The following equation of motion (provided here for a single satellite) models the problem:

$$\begin{bmatrix} \frac{\mathrm{d}\mathbf{r}}{\mathrm{d}t} \\ \frac{\mathrm{d}\mathbf{v}}{\mathrm{d}t} \end{bmatrix} = \begin{bmatrix} \mathbf{v} \\ \mathbf{a}_C + \mathbf{a}_S + \mathbf{a}_P + \mathbf{a}_D + \mathbf{a}_{SRP} \end{bmatrix} \tag{3.4}$$

where $\mathbf{r}$ and $\mathbf{v}$ is the position and velocity vector of the spacecraft at time t. The term $\mathbf{a}_C$ in the equation denotes the gravitational acceleration exerted by the primary celestial body, including acceleration due its asymmetric gravitational field. Additionally, $\mathbf{a}_S$ and $\mathbf{a}_P$ represent the accelerations due to gravitational forces from the Sun and another solar system body, such as the Moon, respectively. These bodies are considered point masses for the simplification, yet their gravitational influence is significant enough. Solar radiation pressure $\mathbf{a}_{SRP}$ and atmospheric drag $\mathbf{a}_D$ are two other critical forces modeled in the equation. The gravitational potential of the primary body, crucial for calculating $\mathbf{a}_C$, is expressed through spherical harmonics, which allows for a detailed representation of the primary's gravitational field as follows:

$$U(x,y,z) = \frac{GM}{r}\left\{1 + \sum_{n=2}^{\infty}\sum_{m=0}^{n}\left(\frac{R}{r}\right)^n P_{nm}(\sin(\varphi))\left[C_{nm}\cos(m\lambda) + S_{nm}\sin(m\lambda)\right]\right\} \tag{3.5}$$

where GM, the gravitational coefficient, R, the reference radius, typically denotes the mean radius of the primary body, and $\mathbf{r}$, the position vector, represents the satellite's location relative to the center of the primary body. Additionally, C_{nm} and S_{nm} are the gravitational coefficients for the gravity model, respectively, and φ and λ are the geocentric latitudes and the longitude of the satellite in the body fixed frame. The Legendre polynomials P_{nm} of degree n and order m further refine the gravitational model by accounting

for the non-uniform distribution of the mass within the primary body. To accurately calculate the forces acting on the satellite, the acceleration vector derived from spherical harmonics must be transformed into the inertial frame. This transformation allows for understanding the satellite's dynamics in a reference frame that is not rotating with the primary body. The acceleration due to the primary body, which includes the fundamental two-body effect, encapsulates the direct gravitational attraction between the satellite and the primary body, modified by the detailed gravitational potential captured by the spherical harmonics given as [109]:

$$\mathbf{a}_C = \mathbf{a}_{2-\text{body}} + \mathbf{a}_{\text{nonspherical}} \tag{3.6}$$

where

$$\mathbf{a}_{2-\text{body}} = -\frac{GM}{r^3}\mathbf{r} \tag{3.7}$$

and

$$\mathbf{a}_{\text{nonspherical}} = \nabla(U - \frac{GM}{r}) \tag{3.8}$$

For the Sun's gravitational influence, the acceleration, $\mathbf{a}_S$, experienced by a satellite is expressed as follows:

$$\mathbf{a}_S = GM_S\left(\frac{\mathbf{s}-\mathbf{r}}{|\mathbf{s}-\mathbf{r}|^3} - \frac{\mathbf{s}}{|\mathbf{s}|^3}\right) \tag{3.9}$$

where $\mathbf{r}$ and $\mathbf{s}$ are the geocentric coordinates of the satellite and the Sun, respectively. GM_S is the gravitational coefficient of the Sun. Similarly, the gravitational acceleration resulting from another solar system body, also treated as a point mass, is modeled as:

$$\mathbf{a}_P = GM_P\left(\frac{\mathbf{p}-\mathbf{r}}{|\mathbf{p}-\mathbf{r}|^3} - \frac{\mathbf{p}}{|\mathbf{p}|^3}\right) \tag{3.10}$$

where $\mathbf{p}$ is the geocentric coordinates of the point mass. The acceleration due to atmospheric drag can be expressed as follows:

$$\mathbf{a}_D = -\frac{1}{2}\rho_d v_r C_D \frac{A}{m}\mathbf{v}_r \tag{3.11}$$

where ρ_d denotes the atmospheric density, A represents the frontal area of the spacecraft, C_D is the drag coefficient and v_r is the spacecraft velocity with respect to the atmosphere.

Finally, the acceleration due to Solar Radiation Pressure (SRP) is as follows:

$$\mathbf{a}_{SRP} = P_{SRP} C_R \frac{A}{m}\frac{\mathbf{r}_s}{|\mathbf{r}_s|^3}\text{AU}^2 \tag{3.12}$$

where P_{SRP} and C_r are the solar radiation pressure at one AU and coefficient of reflectivity, respectively. The cross-sectional area of the spacecraft is given as A. The vector describing the spacecraft's position relative to the Sun is given as $\mathbf{r}_s$.

CIRCULAR-RESTRICTED THREE-BODY PROBLEM

In certain mission scenarios, particularly those occurring in cislunar space and around Lagrangian points, the motion of spacecraft can be effectively simplified using the Circular Restricted Three-body Problem (CRTBP). This dynamical model provides a framework for analyzing the motion of a small object under the gravitational influence of two larger celestial bodies, such as a planet and its moon. Within the CRTBP, these larger bodies are assumed to orbit around their mutual center of mass in circular paths defined by the radius r_{12} while the smaller body, considered to be of negligible mass, is treated as a point mass. Key assumptions of the CRTBP include:

- Circular orbits: The two larger bodies are assumed to move in perfectly circular orbits around their mutual barycenter without any eccentricity.
- Neglected third-body mass: The mass of the smaller object is considered negligible compared to the two larger bodies.
- Co-rotating frame: A rotating coordinate system is employed, known as the co-rotating frame, in which the two larger bodies appear to be stationary while the smaller object's motion is analyzed.
- No external forces: This simplified model assumes that there are no external forces acting on the system, such as perturbations from other celestial bodies or atmospheric drag.

The CRTBP employs a non-inertial, co-moving reference frame to facilitate the analysis of the third body's motion. This reference frame (see Figure 3.6) is centered at the barycenter of the two primary masses, with the x-axis extending from the barycenter towards the second primary body P_2. The positive y-axis is aligned with P_2's velocity vector, indicating the direction of motion, and the z-axis stands perpendicular to the orbital plane, completing the three-dimensional frame of reference.

In this model, the third body, designated as P_3 with mass m_3, is so small in comparison to the primary masses m_1 and m_2 (representing P_1 and P_2, respectively) that its gravitational influence on them is negligible. This assumption allows the model to focus solely on the effects of the two primary bodies' gravitational fields on the motion of the third body. The motion of this third body, P_3 is then described by Newton's second law, providing equations that account for the combined gravitational pull of the primary bodies while factoring in the third body's infinitesimal small:

$$m_3\ddot{\mathbf{r}} = \mathbf{F}_1 + \mathbf{F}_2 \tag{3.13}$$

where $\mathbf{F}_1$ and $\mathbf{F}_2$ are the gravitational forces exerted on m_3 by m_1 and m_2, respectively and it can be written in the following form [175]

$$m_3\ddot{\mathbf{r}} = -\frac{Gm_1m_3}{r_1^3}\mathbf{r}_1 - \frac{Gm_2m_3}{r_2^3}\mathbf{r}_2 \tag{3.14}$$

where G is the universal gravitational constant. Note that the absolute acceleration of m_3 requires differentiation in the inertial frame [176]. By using the characteristic quantities $l^* = r_{12}$ and $t^* = \sqrt{l^{*3}/G(m_1+m_2)}$, Eq. 3.14 can be normalized and the following the equations of motion for the CRTBP [176] can be found as:

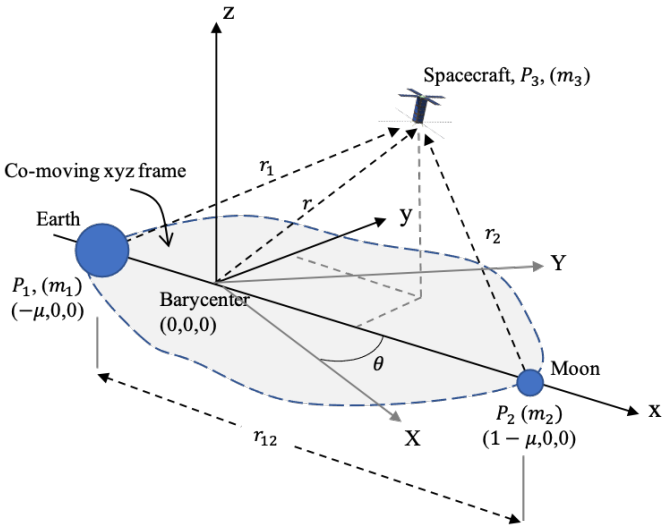

Figure 3.6: Formulation of the Circular Restricted Three-Body Problem: a rotating, non-dimensional coordinate frame [175].

$$\ddot{x} - 2\dot{y} = x - (1-\mu)\frac{x+\mu}{r_1^3} - \mu\frac{x+\mu-1}{r_2^3} \tag{3.15}$$

$$\ddot{y} + 2\dot{x} = (1 - \frac{1-\mu}{r_1^3} - \frac{\mu}{r_2^3})y \tag{3.16}$$

$$\ddot{z} = (\frac{\mu-1}{r_1^3} - \frac{\mu}{r_2^3})z \tag{3.17}$$

where $r_1 = \sqrt{(x+\mu)^2 + y^2 + z^2}$, $r_2 = \sqrt{(x+\mu-1)^2 + y^2 + z^2}$, and x, y and z represent normalized variables, respectively. As an example, in the Earth-Moon system, the gravitational parameter μ, time conversion, and length conversion parameters are 0.01215, 4.343 days/nondim time and 384 747.96 km/nondim length, respectively.

This simplified approach, encapsulated by the CRTBP, offers valuable insights into the trajectories and potential stable points within the system, such as the Lagrangian points where the gravitational forces balance the centrifugal force. There are five equilibrium points: three of them are collinear, and trajectories are unstable around these points. It should be noted that the effects of eccentricity of P_1 and P_2 are ignored in this problem as this would introduce additional complexities due to the time-varying distances between bodies.

Previous research into the dynamics of the three-body problem has revealed the existence of several quasi-periodic and periodic solutions [177]. Among these solutions, Libration point orbits, particularly Halo and Lyapunov orbits, stand out for their unique

characteristics and application in space exploration. Halo orbits represent a class of periodic trajectories that exist within the framework of the CRTBP, offering stable paths around the Lagrangian points where gravitational forces and orbital motion balance out.

This study delves into the SST-based OD at various Halo orbits, prompting the need to explain the methodology behind their computation. The process of deriving a Halo orbit typically involves differential correction methods, which adjust the initial conditions and parameters of a spacecraft's trajectory. These adjustments aim to fine-tune the spacecraft's path, ensuring it aligns closely with the desired Halo orbit. A notable method for the computation of Halo orbits is Howell's approach [177], which leverages specific characteristics of these orbits. For instance, it considers conditions where, at half of the orbital period, the velocity components v_x and v_z should equate to zero, indicating a moment of symmetry in the orbit. A change in the y position's sign triggers an adjustment in v_x and v_z, setting $\delta v_x = -v_x$ and $\delta v_z = -v_z$, upon which differential correction is applied. This process is mathematically represented as [177]:

$$\begin{pmatrix} \delta \dot{x} \\ \delta \dot{z} \end{pmatrix} = \left[\begin{pmatrix} \Phi_{43} & \Phi_{45} \\ \Phi_{63} & \Phi_{65} \end{pmatrix} - \frac{1}{\dot{y}} \begin{pmatrix} \ddot{x} \\ \ddot{z} \end{pmatrix} \begin{pmatrix} \Phi_{23} & \Phi_{25} \end{pmatrix} \right] \begin{pmatrix} \delta z_0 \\ \delta \dot{y}_0 \end{pmatrix} \tag{3.18}$$

where Φ represents the STM from t_0 to t_k, illustrating how the system's state changes over time from the initial state at t_0 to a subsequent state at t_k. The STM is governed by:

$$\dot{\Phi}(t_k, t_0) = A(t)\Phi(t_k, t_0) = \frac{\partial f(x,t)}{\partial x}\Phi(t_k, t_0) = \begin{bmatrix} 0_{3\times3} & I_{3\times3} \\ G(t) & 2\Omega \end{bmatrix} \Phi(t_k, t_0) \tag{3.19}$$

where

$$G(t) = \begin{bmatrix} \frac{\partial \ddot{x}}{\partial x} & \frac{\partial \ddot{x}}{\partial y} & \frac{\partial \ddot{x}}{\partial z} \\ \frac{\partial \ddot{y}}{\partial x} & \frac{\partial \ddot{y}}{\partial y} & \frac{\partial \ddot{y}}{\partial z} \\ \frac{\partial \ddot{z}}{\partial x} & \frac{\partial \ddot{z}}{\partial y} & \frac{\partial \ddot{z}}{\partial z} \end{bmatrix} \qquad \Omega = \begin{bmatrix} 0 & 1 & 0 \\ -1 & 0 & 0 \\ 0 & 0 & 0 \end{bmatrix} \qquad \Phi(t_0, t_0) = I$$

Leveraging this formulation, the study computes orbits within the CRTBP framework, examining a variety of orbital configurations. More details about generating Halo orbits can be found at [176]. Table 3.7 presents the initial conditions and characteristics of these orbits, including orbital period T and Jacobi constant C_j which is a conserved quantity, meaning it remains constant over time for a given system due to the consequence of the system's symmetry and the conversation laws of mechanics (see [11]). Figure 3.7 presents corresponding trajectories considered in this study. Throughout this thesis, these initial conditions form the basis for generating orbits within the CRTBP, where the performance of SST-based OD in these orbits is carefully analyzed.

DYNAMICAL MODEL ERRORS

In the OD process, recognizing and accounting for various dynamical model errors is crucial due to the inherent imperfections and simplifications present within mathematical models. These errors, caused by multiple sources, introduce uncertainties into the OD process, each affecting the accuracy of orbit predictions and corrections in different ways:

Table 3.7: Selected Lagrangian point orbiters with their periods and Jacobi constants (Southern and northern Halo configurations have the same values).

Orbit	T [days]	C_j	Normalized Initial Conditions
L_2 Halo a.	14.14	3.09	[1.1582 0 -0.1289 0 -0.2107 0]
L_2 Halo b.	13.77	3.06	[1.1473 0 -0.1514 0 -0.2199 0]
L_1 Halo a.	12.10	3.08	[0.8306 0 -0.1184 0 0.2334 0]
L_1 Halo b.	11.98	3.04	[0.8354 0 -0.1424 0 0.2527 0]
L_2 NRHO	6.87	3.04	[1.0274 0 -0.1856 0 -0.1147 0]
L_1 NRHO	7.83	3.00	[0.9245 0 -0.2180 0 0.1233 0]
L_2 Lyapunov	18.72	3.01	[1.2200 0 0 0 -0.4275 0]
L_1 Lyapunov	18.81	3.00	[0.7688 0 0 0 0.4813 0]

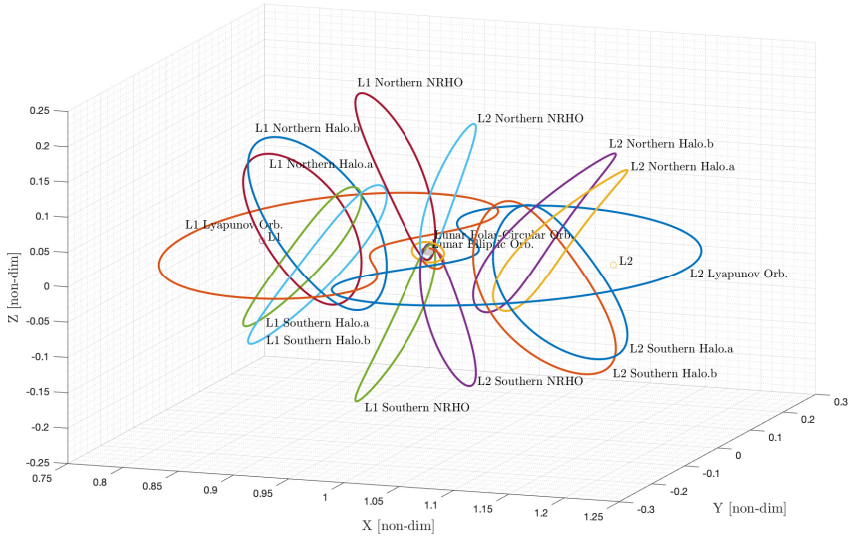

Figure 3.7: Cislunar orbital trajectories within the CRTBP framework considered in this study.

- Gravitational modeling errors: These types of errors are primarily related to uncertainties in the knowledge of the asymmetrical gravity fields of celestial bodies.
- Atmospheric drag modeling errors: Uncertainty in the atmospheric density, spacecraft orientation, and mismodelled spacecraft shape are the main sources. However, this is not relevant in deep-space applications.
- Solar Radiation Pressure Modeling Errors: SRP errors arise from several factors, including inaccuracies in the spacecraft reflection properties and uncertainties in the solar radiation flux. In addition, errors in attitude estimation may lead to incorrect information on the spacecraft orientation and thus calculated forces acting on the spacecraft via SRP. Furthermore, incorrect modeling of the spacecraft's

shape can introduce additional errors.

- Thrust modeling errors: This is because it is not possible exactly to know the magnitude, direction, and duration of the thrust. Such errors in modeling thrust can lead to deviations from the intended orbit, necessitating corrections and potentially increasing the mission's propellant requirements.

Addressing these dynamical model errors requires detailed calibration, validation of models against the data, and the development of robust and reliable estimation techniques capable of compensating for these uncertainties. By systematically accounting for these sources of error, the OD process can be refined. In this study, maneuver execution errors are modeled as 5% of their nominal values, aligning with assumptions made in previous missions (5% in EQUULEUS and 1% in ARTEMIS [50]).

3.3.2. MEASUREMENT MODELS

This section provides a mathematical representation of the relationship between the spacecraft state and the measurements derived from observation systems. In this case, observation models describe how state variables of the spacecraft are transformed into the observed quantities. The measurement model, a fundamental component of this framework, is represented by the following equation:

$$\mathbf{y}_k = \mathbf{h}(\mathbf{x}_k) + \mathbf{v}_k, \quad \mathbf{v}_k \sim N(\mathbf{0}, R) \tag{3.20}$$

where $\mathbf{y}_k$ represents the observed measurements at time t_k, while $\mathbf{h}$ denotes the deterministic part of the measurement model. This deterministic component transforms the state variables, $\mathbf{x}_k$, into the ideal observable quantities, incorporating necessary adjustments such as light-time correction and systematic errors. Furthermore, $\mathbf{v}_k$ represents the stochastic error contributions caused by multiple sources, which might include sensor inaccuracies, thermal noise, and computational errors in data processing. The error term $\mathbf{v}_k$ is modeled as a normally distributed random variable with zero mean and covariance matrix R, denoted by $N(\mathbf{0}, R)$.

The subsequent section will explore specific measurement models that are critical for SST operations, namely range, range-rate, and LOS measurement models. These models are essential for understanding how distances between satellites, their relative velocities, and their positions with respect to one another can be accurately determined primarily based on SST data.

RANGE MEASUREMENT MODEL

Radio-frequency based SST relies on the measurement of round-trip light time using phase or time measurements, as discussed previously in Chapter 2. Specifically, the essence of the two-way range measurement resides in computing the signal's round-trip transit time between two participating nodes. The calculation relies on a single clock located on the initiating participant to precisely determine the elapsed time of signal transit. Considering two spacecraft, each equipped with a transponder and antenna, a timeline representing the two-way range measurement is given in Figure 3.8. Based on this timeline, a two-way range measurement is given by:

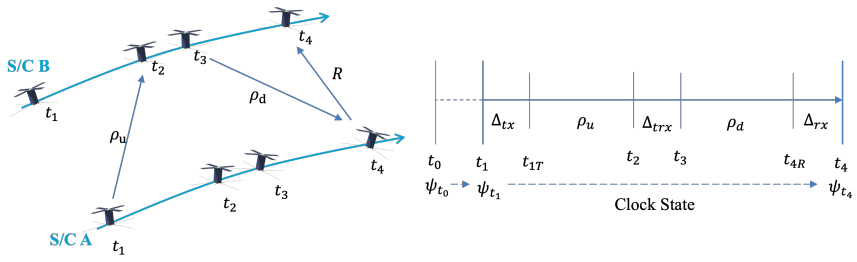

Figure 3.8: Two-way round-trip light time measurement.

$$\tau = \Delta_{tx} + \frac{\rho_u}{c} + \Delta_{trx} + \frac{\rho_d}{c} + \Delta_{rx} \tag{3.21}$$

where

$$\rho_u = c(t_2 - t_{1T}) = |\mathbf{r}_2(t_2) - \mathbf{r}_1(t_{1T})| \tag{3.22}$$

and

$$\rho_d = c(t_{4R} - t_3) = |\mathbf{r}_1(t_{4R}) - \mathbf{r}_2(t_3)| \tag{3.23}$$

where Δ_{tx} and Δ_{rx} are the transponder transmit and receive line delays on the S/C-A, respectively. The line delay on the S/C-B is Δ_{trx}. Both Eqn.3.22 and 3.23 need to be solved via the fixed-point iteration, which can be found in [117]. By including deterministic and stochastic clock errors, as well as systematic and random errors, the crosslink range model given in Eqn. 3.21 can be expressed as follows (see Figure 3.9):

$$\rho = \rho_u + \rho_d + c\,(\Delta_{tx} + \Delta_{rx}) + c\,\Delta_{trx} + c\sum_{l=0}^{2} \Delta\tau_c^l + c\delta t_s + \rho_{\text{noise}} \tag{3.24}$$

where $\Delta\tau_c^l$ represents the deterministic clock errors, mainly: bias, drift, and aging $l = 0, 1, 2$, respectively. The stochastic clock error is given as δt_s. It is worth noting that ρ_{noise} represents the thermal noise of the ranging system which, in general, is the dominant error source, as explained in Chapter 2. As an additional point worth mentioning, deterministic clock errors can be neglected, as they do not hold significant importance in two-way operations due to the quality clocks employed and the typically short signal travel time.

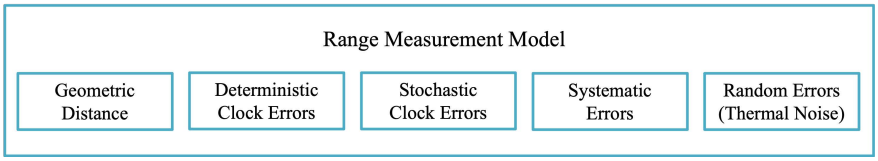

Figure 3.9: Range measurement model.

In some cases, such as error analysis, light-time delays are neglected in measurement models, leading to geometric measurement models. In this case, measurements are based on kinematics at a specific time. The geometric range measurement model in this context is expressed as follows:

$$\rho = |\mathbf{R}| + \rho_{\text{bias}} + \rho_{\text{noise}} = \sqrt{(\mathbf{r}_1 - \mathbf{r}_2) \cdot (\mathbf{r}_1 - \mathbf{r}_2)} + \rho_{\text{bias}} + \rho_{\text{noise}} \tag{3.25}$$

RANGE-RATE MEASUREMENT MODEL

This model outlines the relationship between the spacecraft's modeled velocity and the observed range rate, essentially capturing the rate at which the distance between the observer and the target spacecraft changes over time. The range rate, denoted as, $\dot{\rho}$, is expressed through the equation:

$$\dot{\rho} = \frac{\rho \cdot \dot{\rho}}{\rho} + \dot{\rho}_{\text{bias}} + \dot{\rho}_{\text{noise}} \tag{3.26}$$

where $\dot{\rho}$ represents the relative velocity vector between the observer and the target spacecraft. The equation accounts for the bias, $\dot{\rho}_{\text{bias}}$ and noise, $\dot{\rho}_{\text{noise}}$, in the measurement.

LINE-OF-SIGHT MEASUREMENT MODEL

The LOS measurement model quantifies the angular relationship between the observer and the target, specifically in terms of azimuth and elevation angles. These angles are modeled as:

$$\phi = \arctan\left(\frac{y_2 - y_1}{x_2 - x_1}\right) + \phi_{\text{bias}} + \phi_{\text{noise}} \tag{3.27}$$

$$\varphi = \arcsin\left(\frac{z_2 - z_1}{\rho}\right) + \varphi_{\text{bias}} + \varphi_{\text{noise}} \tag{3.28}$$

where ϕ and φ are the relative azimuth and elevation angles between the observer and the target, respectively. These equations incorporate biases ϕ_{bias}, φ_{bias} and noise ϕ_{noise}, φ_{noise}, reflecting the uncertainties in angle measurements. LOS vectors can be determined using time delay or phase shift of incoming radio signals, requiring at least three antennas to calculate two angles relative to a baseline, as explained in section 2.3. Relative optical measurements also provide a LOS solution with the potential for higher performances.

SST could possibly provides a full set of observables ρ_{SST}, $\dot{\rho}_{SST}$, ϕ_{SST} and φ_{SST}, representing range, range-rate, azimuth, and elevation measurements, respectively. Similarly, traditional ground-based radiometric measurements, including range $\rho_{i,GS}$ and range-rate $\dot{\rho}_{i,GS}$, follow the same modeling principles (Eqs. 3.25 and 3.26). Thus, the observation vector, combining both SST and ground-based measurements, can be represented as:

$$\mathbf{y} = \begin{bmatrix} \rho_{SST} & \dot{\rho}_{SST} & \phi_{SST} & \varphi_{SST} & \rho_{1,GS} & \dot{\rho}_{1,GS} & \rho_{2,GS} & \dot{\rho}_{2,GS} \end{bmatrix}^T \tag{3.29}$$

In essence, these measurement models are fundamental to accurately determining the spacecraft states, utilizing both SST and traditional ground-based observations to improve the precision and reliability of space mission operations.

MEASUREMENT ERROR MODELS

The accurate characterization of observation models plays a pivotal role in achieving precise OD. As highlighted earlier, the accuracy of measurements is constrained by various errors, emphasizing the necessity of carefully modeling and compensating for these inaccuracies to enhance the reliability of spacecraft navigation. In this study, the errors associated with range, range-rate, and LOS observations are systematically modeled, drawing upon the data presented in Table 2.5 of Chapter 2.

3.3.3. ESTIMATION MODELS

This section is dedicated to the estimation algorithms utilized within this study, building upon the previously discussed differences between sequential and batch data processing approaches. Given the advantages of sequential methods in providing near real-time navigation solutions, the focus of this study has shifted towards these techniques, particularly emphasizing the application of the Kalman filter [178]. This is a mathematical algorithm used for state estimation with recursive filtering that combines predictions from a mathematical model of a system with measurements to estimate the state of the system. This iterative process aims to minimize the mean square error between the predicted and the measured states, ultimately delivering an optimal estimate.

The Kalman filter's operational framework is divided into two key phases: the prediction step, which provides information on how the system evolves over time, taking into account factors such as the spacecraft motion and any uncertainty in the dynamics, and the update step, where measurement residuals are calculated as the difference between actual and computed or predicted measurements, and using such residuals to update the estimated state.

Given the fact that orbital dynamics have non-linear characteristics, this study employs non-linear variants of the Kalman filter, diverging from the basic assumption of the linear Kalman filter that dynamics and measurement equations can be represented by linear functions. There are several non-linear types of Kalman filters, optimized for different scenarios and variations of the estimation problem, which will be presented in the next subsections.

EXTENDED KALMAN FILTER (EKF)

The Extended Kalman Filter (EKF) is an extension of the linear Kalman filter and uses nonlinear functions for both dynamic and measurement equations. It extends the capabilities to handle nonlinear systems by approximating the nonlinear functions using a first-order Taylor series expansion, considering that the true spacecraft state $\mathbf{x}$ is close to the estimated state $\hat{\mathbf{x}}$. The essence of the EKF's methodology and its steps are summarized in Algorithm 1 [178].

where f is the system dynamics, $\mathbf{x}$ is the state vector, $\mathbf{h}$ is the measurement model, $\tilde{\omega}$ is the process noise, $\mathbf{v}$ is the measurement noise, P is the covariance matrix, K is the Kalman gain, Q and R are process noise and measurement noise covariance matrices, respectively.

ITERATED EXTENDED KALMAN FILTER (IEKF)

The Iterated Extended Kalman Filter (IEKF) follows a similar structure to the EKF and, in particular, it is an extension of the EKF iteratively refining the state estimation by im-

Algorithm 1: Extended Kalman Filter

Given: $P_0, \mathbf{x}_0, \tilde{\mathbf{y}}_k, Q, R_k$

Model:

$\dot{\mathbf{x}} = f(\mathbf{x}, \mathbf{u}, t) + \tilde{\omega}, \quad \tilde{\omega} \sim N(\mathbf{0}, Q)$

$\tilde{\mathbf{y}}_k = \mathbf{h}(\mathbf{x}_k) + \mathbf{v}_k, \quad \mathbf{v}_k \sim N(\mathbf{0}, R)$

Initialize:

$\hat{\mathbf{x}}_0 = E\{\hat{\mathbf{x}}_0\}$

$P_0 = E\left\{\tilde{\mathbf{x}}_0 \tilde{\mathbf{x}}_0^T\right\}$

Propagation:

$\dot{\hat{\mathbf{x}}} = f(\hat{\mathbf{x}}, \mathbf{u}, t)$

$\bar{P}_k = \Phi(t_k, t_{k-1}) P_{k-1} \Phi^T(t_k, t_{k-1}) + Q$

$\dot{\Phi}(t_k, t_{k-1}) = (\partial f(\hat{\mathbf{x}}, \mathbf{u}, t)/\partial \hat{\mathbf{x}}) \Phi(t_k, t_{k-1}), \quad \Phi(t_0, t_0) = I$

Update:

$K_k = \bar{P}_k \tilde{H}_k^T [\tilde{H}_k \bar{P}_k \tilde{H}_k^T + R_k]^{-1}, \quad \tilde{H}_k = \partial \mathbf{h}(\mathbf{x}_k)/\partial \mathbf{x}_k$

$\hat{\mathbf{x}}_k^+ = \hat{\mathbf{x}}_k^- + K_k [\tilde{\mathbf{y}}_k - \mathbf{h}(\hat{\mathbf{x}}_k^-)]$

$P_k = [I - K_k \tilde{H}_k] \bar{P}_k$

proving the linearization of the system dynamics. Local iterations are repeated in the update step each time, linearizing around the most recent estimate [174]. This iterative process aims to overcome the limitations of the initial linearization in the EKF and can provide a more accurate estimate. This could be the case where the system dynamics consists of significant nonlinearities: iterations continue until the estimate is no longer improved beyond a certain threshold or a maximum number of iterations is reached. Algorithm 2 presents the IEKF where the update step is repeated a predefined number of iterations N_i instead of using a threshold for error reduction, as this would make it hard to estimate the number of iterations.

ADAPTIVE EXTENDED KALMAN FILTER (AEKF)

The Adaptive Extended Kalman Filter (AEKF) is another extension of the EKF that adjusts the filter parameters based on the characteristics of the system or the quality of the measurement. It aims to improve the EKF performance by adapting to changes in the system or measurement conditions. Central to the AEKF's functionality is its capability to adaptively estimate the process noise covariance matrix Q and the measurement noise covariance matrix R. Traditionally, the process noise covariance matrix, Q, is determined through a trial-and-error method, necessitating extensive familiarity with the specific application to set it as a constant matrix appropriately. Similarly, the measurement noise covariance matrix, R, is typically fixed based on the precision of the measurement instruments involved. However, this fixed approach may not always be sufficient, especially in applications like data-aided ranging, where measurement accuracy can vary significantly under different conditions, thereby complicating the filter-tuning process.

There are various adaptive estimation approaches, and this work uses an innovation-based adaptive estimation strategy, derived from [179], being the difference between the

Algorithm 2: Iterated Extended Kalman Filter

Given: $P_0, \mathbf{x}_0, \tilde{\mathbf{y}}_k, Q, R_k, N_i$
Model:
$\dot{\mathbf{x}} = f(\mathbf{x}, \mathbf{u}, t) + \tilde{\omega}, \quad \tilde{\omega} \sim N(\mathbf{0}, Q)$
$\tilde{\mathbf{y}}_k = \mathbf{h}(\mathbf{x}_k) + \mathbf{v}_k, \quad \mathbf{v}_k \sim N(\mathbf{0}, R)$
Initialize:
$\hat{\mathbf{x}}_0 = E\{\hat{\mathbf{x}}_0\}$
$P_0 = E\{\tilde{\mathbf{x}}_0 \tilde{\mathbf{x}}_0^T\}$
Propagation:
$\dot{\hat{\mathbf{x}}} = f(\hat{\mathbf{x}}, \mathbf{u}, t)$
$\bar{P}_k = \Phi(t_k, t_{k-1}) P_{k-1} \Phi^T(t_k, t_{k-1}) + Q$
$\dot{\Phi}(t_k, t_{k-1}) = (\partial f(\hat{\mathbf{x}}, \mathbf{u}, t)/\partial \hat{\mathbf{x}})\, \Phi(t_k, t_{k-1}), \quad \Phi(t_0, t_0) = I$
Update:
while $i \geq N_i$ **do**
  $i \leftarrow i + 1$;
  $K_{k_i} = \bar{P}_k \tilde{H}_k^T [\tilde{H}_k \bar{P}_k \tilde{H}_k^T + R_k]^{-1}, \quad \tilde{H}_k = \partial \mathbf{h}(\mathbf{x}_k^+)/\partial \mathbf{x}_k^+$
  $\hat{\mathbf{x}}_{k_{i+1}}^+ = \hat{\mathbf{x}}_k^- + K_k[\tilde{\mathbf{y}}_k - \mathbf{h}(\hat{\mathbf{x}}_k^-) - \tilde{H}_k(\hat{\mathbf{x}}_k^- - \hat{\mathbf{x}}_{k_i}^+)]$
  $P_{k_{i+1}} = [I - K_k \tilde{H}_k] \bar{P}_k$
end

actual measurement and its predicted value:

$$\epsilon_k = \tilde{\mathbf{y}}_k - \mathbf{h}(\hat{\mathbf{x}}_k^+)$$

with residuals being the difference between the actual measurement and its estimated value:

$$\mathbf{d}_k = \tilde{\mathbf{y}}_k - \mathbf{h}(\hat{\mathbf{x}}_k^-)$$

Q and R are adjusted based on innovation and residual, respectively. This approach requires tuning a design parameter α, representing how the filter weights the previous estimates. One notable aspect of the AEKF is its flexibility; depending on the specific application, it may only adaptively estimate one of the noise covariance matrices, Q or R, not necessarily both. Moreover, the filter may start with the adaptive noise covariance estimation, and it can be stopped after a certain period of time (e.g., after convergence). In brief, AEKF is more robust against initial uncertainties in noise covariance matrices. This approach is given in Algorithm 3.

Building upon the AEKF, this study introduces the Adaptive Iterated Extended Kalman Filter (AIEKF), which combines local iterations from the IEKF with adaptive estimation of noise covariance matrices found in the AEKF. This hybrid approach allows for iterative linearization of $K_k, \mathbf{x}_k^+, P_k$ while also adaptively estimating Q and R based on innovation and residual. The iterative aspect enhances the filter's ability to cope with nonlinearities in the system, and the adaptive estimation ensures that the filter remains responsive to changes in system dynamics and measurement conditions.

Algorithm 3: Adaptive Extended Kalman Filter

Given: $P_0, \mathbf{x}_0, \tilde{\mathbf{y}}_k, Q_0, R_0, \alpha$

Model:

$\dot{\mathbf{x}} = f(\mathbf{x}, \mathbf{u}, t) + \tilde{\omega}, \quad \tilde{\omega} \sim N(\mathbf{0}, Q)$

$\tilde{\mathbf{y}}_k = \mathbf{h}(\mathbf{x}_k) + \mathbf{v}_k, \quad \mathbf{v}_k \sim N(\mathbf{0}, R)$

Initialize:

$\hat{\mathbf{x}}_0 = E\{\hat{\mathbf{x}}_0\}$

$P_0 = E\left\{\tilde{\mathbf{x}}_0 \tilde{\mathbf{x}}_0^T\right\}$

Propagation:

$\dot{\hat{\mathbf{x}}} = f(\hat{\mathbf{x}}, \mathbf{u}, t)$

$\bar{P}_k = \Phi(t_k, t_{k-1}) P_{k-1} \Phi^T(t_k, t_{k-1}) + Q_{k-1}$

$\dot{\Phi}(t_k, t_{k-1}) = (\partial f(\hat{\mathbf{x}}, \mathbf{u}, t)/\partial \hat{\mathbf{x}}) \Phi(t_k, t_{k-1}), \quad \Phi(t_0, t_0) = I$

Update:

$R_k = \alpha R_{k-1} + (1-\alpha)(\epsilon_k \epsilon_k^T + \tilde{H}_k \bar{P}_k \tilde{H}_k^T), \quad \tilde{H}_k = \partial \mathbf{h}(\mathbf{x}_k)/\partial \mathbf{x}_k, \quad \epsilon_k = [\tilde{\mathbf{y}}_k - \mathbf{h}(\hat{\mathbf{x}}_k^+)]$

$K_k = \bar{P}_k \tilde{H}_k^T [\tilde{H}_k \bar{P}_k \tilde{H}_k^T + R_k]^{-1}$

$\hat{\mathbf{x}}_k^+ = \hat{\mathbf{x}}_k^- + K_k \mathbf{d}_k, \quad \mathbf{d}_k = [\tilde{\mathbf{y}}_k - \mathbf{h}(\hat{\mathbf{x}}_k^-)]$

$P_k = [I - K_k \tilde{H}_k] \bar{P}_k$

$Q_k = \alpha Q_{k-1} + (1-\alpha)(K_k \mathbf{d}_k \mathbf{d}_k^T K_k^T)$

CONSIDER KALMAN FILTER (CKF)

In an estimation problem, accurately determining the state of a dynamical system presents significant challenges, primarily due to the inherent uncertainties in dynamical and measurement parameters. These uncertainties can significantly impact the accuracy and reliability of state estimation processes. There are three primary strategies for handling parameter uncertainties within the context of estimation: *neglecting* represents the state estimation by neglecting any uncertainties in the non-estimated dynamic and measurement model parameters. Secondly, *estimating* represents the state vector that is expanded by including dynamic and measurement model parameters. Lastly, *considering* represents the state vector is estimated, and dynamic and measurement model uncertainties are included in the estimation error covariance matrix. Estimating these parameters may become computationally expensive, particularly in state vectors with a large number of unknown parameters. More importantly, expanding the state vector may have an impact on the system observability and, thus, the estimation performance.

The Consider Kalman Filter (CKF), also known as the Schmidt Kalman Filter (SKF), follows the "considering uncertainties" approach by integrating parameter covariance into the estimation process. This is particularly useful for SST-based OD applications, where precise clock-related parameters, such as bias, play a critical role. The CKF methodology is presented in Algorithm 4, where C_k is the cross-covariance matrix, B_0 is the parameter covariance, b_0 is *a priori* parameter error. It should be noted that the CKF becomes the EKF in case of the zero parameter uncertainty.

UNSCENTED KALMAN FILTER (UKF)

The Unscented Kalman Filter (UKF) addresses the limitations of the EKF when the system is highly nonlinear where a first-order Taylor series approximation is not sufficient,

Algorithm 4: Consider Kalman Filter

Given: $P_0, B_0, C_0, \mathbf{x}_0, \mathbf{b}_k, \tilde{\mathbf{y}}_k, Q, R_k$

Model:

$\dot{\mathbf{x}} = f(\mathbf{x}, \mathbf{u}, t) + \tilde{\omega}, \quad \tilde{\omega} \sim N(\mathbf{0}, Q)$

$\tilde{\mathbf{y}}_k = \mathbf{h}(\mathbf{x}_k, \mathbf{b}_k) + \mathbf{v}_k, \quad \mathbf{v}_k \sim N(\mathbf{0}, R)$

Initialize:

$\hat{\mathbf{x}}_0 = E\{\hat{\mathbf{x}}_0\}$

$\mathbf{b}_0 = E\{\mathbf{b}_0\}$

$P_0 = E\{\tilde{\mathbf{x}}_0 \tilde{\mathbf{x}}_0^T\}$

$B_0 = E\{\mathbf{b}_0 \mathbf{b}_0^T\}$

$C_0 = E\{\tilde{\mathbf{x}}_0 \mathbf{b}_0^T\} = 0$

Propagation:

$\dot{\hat{\mathbf{x}}} = f(\hat{\mathbf{x}}, \mathbf{u}, t)$

$\bar{P}_k = \Phi(t_k, t_{k-1}) P_{k-1} \Phi^T(t_k, t_{k-1}) + Q$

$\dot{\Phi}(t_k, t_{k-1}) = (\partial f(\hat{\mathbf{x}}, \mathbf{u}, t)/\partial \hat{\mathbf{x}}) \Phi(t_k, t_{k-1}), \quad \Phi(t_0, t_0) = I$

$\bar{C}_k = \Phi(t_k, t_{k-1}) C_{k-1}$

Update:

$K_k = (\bar{P}_k \tilde{H}_k^T + \bar{C}_k N_k^T)[\tilde{H}_k \bar{P}_k \tilde{H}_k^T + N_k \bar{C}_k^T \tilde{H}_k^T + \tilde{H}_k \bar{C}_k N_k^T + N_k B_0 N_k^T + R_k]^{-1}$

$\tilde{H}_k = \partial \mathbf{h}(\mathbf{x}_k, \mathbf{b}_k)/\partial \mathbf{x}_k, \quad N_k = \partial \mathbf{h}(\mathbf{x}_k, \mathbf{b}_k)/\partial \mathbf{b}_k$

$\hat{\mathbf{x}}_k^+ = \hat{\mathbf{x}}_k^- + K_k[\tilde{\mathbf{y}}_k - \mathbf{h}(\hat{\mathbf{x}}_k^-, \mathbf{b}_k) - N_k \mathbf{b}_k]$

$P_k = [I - K_k \tilde{H}_k] \bar{P}_k - K_k N_k \bar{C}_k^T$

$C_k = \bar{C}_k - K_k(\tilde{H}_k \bar{C}_k + N_k B_0)$

leading to large errors and, thus, filter divergence. However, the UKF uses a deterministic sampling technique called the unscented transformation to capture the statistical properties of a nonlinear system. Different from the EKF, the UKF introduces different steps, starting with the calculation of $2N+1$ sigma points representing the distribution of the state vector (chosen around the current estimated state and capturing the distribution). A summary of UKF can be found in Algorithm 5. Key characteristics of the UKF are:

- Operating principle: it is based on the unscented transform (and no linearization is required).
- Accuracy: the UKF provides a more accurate state estimation than EKF for highly non-linear systems.
- Jacobians: One of the main benefits is that the UKF does not require any Jacobian calculations.
- Computational resources: the UKF requires more resources due to the increased number of sigma points. This results in a slower estimation process compared to the EKF.

The performance of the UKF is sensitive to the sigma points selection: optimal performance still requires considerations on the optimal choice of sigma points and tun-

ing parameters. In addition, local iterations can be applied in the measurement update step to build a derivative-free alternative to the IEKF, which is called Iterated Unscented Kalman Filter (IUKF).

Algorithm 5: Unscented Kalman Filter

Given: $P_0, \mathbf{x}_0, \tilde{\mathbf{y}}_k, Q, R_k$

Model:

$\dot{\mathbf{x}} = f(\mathbf{x}, \mathbf{u}, t) + \tilde{\omega}, \quad \tilde{\omega} \sim N(\mathbf{0}, Q)$

$\tilde{\mathbf{y}}_k = \mathbf{h}(\mathbf{x}_k) + \mathbf{v}_k, \quad \mathbf{v}_k \sim N(\mathbf{0}, R)$

Initialize:

$\hat{\mathbf{x}}_0 = E\{\hat{\mathbf{x}}_0\}$

$P_0 = E\left\{\tilde{\mathbf{x}}_0 \tilde{\mathbf{x}}_0^T\right\}$

Calculate:

$\chi_{k-1} = \left[\hat{\mathbf{x}}_{k-1} \quad \hat{\mathbf{x}}_{k-1} + \sqrt{(L+\lambda)\bar{P}_{k-1}} \quad \hat{\mathbf{x}}_{k-1} - \sqrt{(L+\lambda)\bar{P}_{k-1}}\right]$

Propagation:

$\hat{\chi} = f(\chi, \mathbf{u}, t)$

$\bar{\mathbf{x}}_k = \sum_{i=0}^{2L} W_i^m \hat{\chi}_i$

$W_0^m = \lambda/(L+\lambda),\ W_0^c = \lambda/(L+\lambda) + (1-\alpha^2+\beta),\ W_i^m = W_i^c = 1/2(L+\lambda),\ \lambda = L(\alpha^2-1)$

$\bar{P}_k = \sum_{i=0}^{2L} W_i^c [\chi_i - \hat{\mathbf{x}}_k][\chi_i - \hat{\mathbf{x}}_k]^T + Q$

$\hat{\mathbf{y}}_k = \sum_{i=0}^{2L} W_i^m \gamma_k^i, \quad \gamma_k = \mathbf{h}(\chi_{i,k})$

Update:

$P_{\tilde{y}_k \tilde{y}_k} = \sum_{i=0}^{2L} W_i^c [\gamma_{i,k} - \hat{\mathbf{y}}_k][\gamma_{i,k} - \hat{\mathbf{y}}_k]^T + R_k$

$P_{x_k y_k} = \sum_{i=0}^{2L} W_i^c [\chi_{i,k} - \hat{\mathbf{x}}_k][\gamma_{i,k} - \hat{\mathbf{y}}_k]^T$

$K_k = P_{x_k y_k} P_{\tilde{y}_k \tilde{y}_k}^{-1}$

$\hat{\mathbf{x}}_k^+ = \hat{\mathbf{x}}_k^- + K_k[\tilde{\mathbf{y}}_k - \hat{\mathbf{y}}_k]$

$P_k = \bar{P}_k - K_k P_{\tilde{y}_k \tilde{y}_k} K_k^T$

SMOOTHERS

In the context of estimation problems, a smoother is an algorithm used to improve the state estimation using all available observations. Filters take into account only past measurements and provide near-real-time estimates. However, smoothers use both past and future information with respect to the estimation epoch, which significantly improves the quality of state estimation. This advantage comes from the smoother's ability to mitigate the effects of measurement noise by integrating future data into the estimation process. Note that batch estimation algorithms, which process all available data in a single batch, can produce smoothed solutions in scenarios where there is no process noise. However, smoothers distinguish themselves by also accounting for process noise, an area where batch estimations may encounter difficulties. There are three types of smoothers [174]:

- Fixed-lag: This considers a fixed number of future measurements (thus a number of time steps referred to as the lag) to refine the estimates.

- Fixed-interval: This uses all measurements within a specified time interval to estimate the states in the interval.

- Fixed point: The state at a specific fixed point time is estimated based on measurements up to the current time.

In this work, the Rauch, Tung, and Striebel (RTS) fixed-interval smoother is studied since it is the most widely used algorithm for smoothing [174]. No smoother covariance is used to find the optimal estimate, and there is no need to store the forward filter covariance update and propagation (also called STM).

The RTS smoother operates in two steps: in the forward pass, it performs regular filtering, and in the backward pass, it combines filtered estimates and the smoother gain to provide a smoothed estimate independent of the backward covariance. A summary of the RTS fixed-interval smoother is presented in Algorithm 6 where $K_k^s, \hat{\mathbf{x}}_k^s$ and P_k^s are the smoother gain, estimate, and covariance, respectively.

Algorithm 6: RTS type Extended Kalman Smoother

Given: $P_0, \mathbf{x}_0, \tilde{\mathbf{y}}_k, Q, R_k$

Model:

$\dot{\mathbf{x}} = f(\mathbf{x}, \mathbf{u}, t) + \tilde{\omega}, \quad \tilde{\omega} \sim N(\mathbf{0}, Q)$

$\tilde{\mathbf{y}}_k = \mathbf{h}(\mathbf{x}_k) + \mathbf{v}_k, \quad \mathbf{v}_k \sim N(\mathbf{0}, R)$

Forward Initialize:

$\hat{\mathbf{x}}_0 = E\{\hat{\mathbf{x}}_0\}$

$P_0 = E\{\tilde{\mathbf{x}}_0 \tilde{\mathbf{x}}_0^T\}$

Forward Propagation:

$\dot{\hat{\mathbf{x}}} = f(\hat{\mathbf{x}}, \mathbf{u}, t)$

$\bar{P}_k = \Phi(t_k, t_{k-1}) P_{k-1} \Phi^T(t_k, t_{k-1}) + Q$

$\dot{\Phi}(t_k, t_{k-1}) = (\partial f(\mathbf{x}, \mathbf{u}, t)/\partial \mathbf{x}) \Phi(t_k, t_{k-1}), \quad \Phi(t_0, t_0) = I$

Forward Update:

$K_k = \bar{P}_k \tilde{H}_k^T [\tilde{H}_k \bar{P}_k \tilde{H}_k^T + R_k]^{-1}, \quad \tilde{H}_k = \partial \mathbf{h}(\mathbf{x}_k)/\partial \mathbf{x}_k$

$\hat{\mathbf{x}}_k^+ = \hat{\mathbf{x}}_k^- + K_k[\tilde{\mathbf{y}}_k - \mathbf{h}(\hat{\mathbf{x}}_k^-)]$

$P_k = [I - K_k \tilde{H}_k] \bar{P}_k$

Smoother Initialize:

$\hat{\mathbf{x}}_{B,N} = \hat{\mathbf{x}}_N^+$

$P_{B,N} = P_k$

Smoother Estimate:

$K_k^s = P_k \Phi^T(t_k, t_{k-1})(P_{k+1}^-)^{-1}$

$\hat{\mathbf{x}}_k^s = \hat{\mathbf{x}}_k^+ + K_k^s[\hat{\mathbf{x}}_{k+1}^s - \hat{\mathbf{x}}_k^-]$

$P_k^s = P_k + K_k^s[P_{k+1}^s - P_{k+1}^s](K_k^s)^T$

3.3.4. COMPUTATIONAL COMPLEXITY

The computational complexity of estimation algorithms plays a pivotal role in assessing their practicality and suitability for real-time applications. In this study, computational

complexity is defined by the number of Floating-point operations (FLOPs) per filter iteration [180]. This is a metric that serves as a reliable indicator of algorithm efficiency. If an algorithm is inefficient and consumes a lot of processing power for a given task, it may be less practical for real-time applications. In the previous sections, various estimation algorithms have been introduced for the specific estimation problem within SST-based OD. Since how many updates can be performed in a unit of time is directly related to the processor speed and computational complexity, it is important to investigate the number of FLOPs required per iteration of an estimation algorithm. It is also worth noting that FLOPs alone do not provide a complete picture of a system's overall performance, as other factors like memory and system architecture play significant roles. Nevertheless, FLOPs remain a valuable metric for assessing and comparing algorithms.

In general, arithmetic operations, common matrix operations, and others are counted in FLOPs. As an example, the number of FLOPs required to compute the product of two matrices with dimensions of $(m \times n)$ and $(n \times l)$ is given as $2mnl - ml$ (mnl products and $ml(n-1)$ summations). A summary of FLOPs operations can be found in Table 3.8 [180], [181].

Considering a SST-based OD application with a n-dimensional state vector and a m-dimensional observation vector, the complexity of filters used in this study is given in Table 3.9 and 3.10 under the following assumptions:

- Without taking advantage of the symmetric matrices such as the estimation error covariance matrix P, allowing only the upper triangular matrix to be computed.
- Without considering operations in the partial derivative calculations such as $\tilde{H}$, which can be calculated analytically or numerically.
- Without storing matrix/vector operations for later use.
- The n-dimensional state vector is larger than the m-dimensional observation vector and the b-dimensional consider parameter vector, i.e. $n \gg m, b$. This is typical in the SST-based OD application where $n \geq 12$, $m \leq 4$, $b \leq 3$ representing position/velocity states of the two spacecraft system, range/range-rate/angle (az/el) observations, and systematic clock bias/drift/aging consider parameters, respectively. Although this may confuse the reader that the number of measurements is significantly lower than the number of estimated parameters, this represents a single iteration in Kalman-type filters, which integrate each measurement directly into the estimation process.
- Without taking into account the matrix/vector operations of the non-linear functions such as $f(\hat{\mathbf{x}}, \mathbf{u}, t)$.

Figure 3.10 represents the number of FLOPs required for a single iteration of filters given in this study. As expected, EKF emerges as the most efficient algorithm among the given filters in case the estimated state vector consists of spacecraft states only. As the local number of iterations N increases, IEKF demands more computational time than others. Conversely, CKF offers advantages when systematic biases or similar systematic parameters are *considered* within the filter, resulting in a decrease in the size of the

Table 3.8: Matrix operations complexity [180], [181] (assumed $n \gg m, l$)

Description	Products	Summations	FLOPs	Order
Vector scaling ($\alpha a_{n\times 1}$)	n	-	n	n
Vector summation ($a_{n\times 1} + b_{n\times 1}$)	-	n	n	n
Matrix scaling ($\alpha A_{n\times m}$)	nm	-	nm	nm
Matrix summation ($A_{n\times m} + B_{n\times m}$)		nm	nm	nm
Matrix vector product ($A_{n\times m} b_{m\times 1}$)	nm	$n(m-1)$	$2nm-n$	$2nm$
Matrix-Matrix product ($A_{n\times m} B_{m\times l}$)	nml	$nl(m-1)$	$2nml-nl$	$2nml$
Matrix transpose ($A^T_{n\times n}$)	-	-	-	0
Matrix inverse ($A^{-1}_{n\times n}$)	$\frac{n^3}{2}+\frac{3n^2}{2}$	$\frac{n^3}{2}-\frac{n^2}{2}$	n^3+n^2+n	n^3

estimated state vector. Basically, CKF could be a possible alternative to EKF from a computational perspective.

Numerical analyses further validate these findings. Figure 3.11 presents the computational time required per filter iteration, with the EKF maintaining its position as the computationally optimal choice under simplified conditions. However, as the number of iterations increases, the IEKF becomes more computationally demanding. Interestingly, the UKF provided slightly higher computational times than expected, a deviation attributed to specific algorithm implementations.

A critical aspect not accounted for in this analysis is the processing time associated with nonlinear functions, which is especially relevant when comparing the UKF with the EKF. Since UKF calls state propagation $2n$ times more than EKF and does not use STM in calculations. It has been found that the computational time for the UKF is around six times longer than the one for the EKF in SST-based OD applications. It should be noted that this finding may vary with changes in the dynamical model.

Ultimately, this comprehensive analysis sheds light on the computational aspects of various estimation algorithms within the context of SST-based OD, providing a foundation for selecting the most appropriate algorithm based on computational efficiency.

3.4. SUMMARY

This chapter provided a comprehensive examination of the SST-based OD process, offering insights into the various models, challenges, and methodologies associated with this critical aspect of autonomous navigation. Starting with an overview of the general OD problem, the chapter delved into the differences between batch and sequential data processing algorithms, highlighting the advantages of autonomous operations and addressing the limitations of ground-based systems.

A detailed presentation of the SST-based autonomous OD method was provided, alongside a review of existing scientific literature in the field. This review not only provided the current state of research but also identified significant gaps in knowledge, setting the stage for the following sections of this dissertation. The chapter also outlined the specific OD requirements and goals for small satellite missions in deep space, emphasizing the importance of station-keeping analysis in evaluating OD performance.

Furthermore, the chapter introduced a variety of OD models, including high-fidelity

Table 3.9: Filter complexity where $n \gg m, b$

	Algorithm	FLOPs	Order
EKF	$\hat{\dot{\mathbf{x}}} = f(\hat{\mathbf{x}}, \mathbf{u}, t)$	N/A	$\mathcal{O}(f(\hat{\mathbf{x}}, \mathbf{u}, t))$
	$\bar{P}_k = \Phi(t_k, t_{k-1}) P_{k-1} \Phi^T(t_k, t_{k-1}) + Q$	$4n^3 - n^2$	$\mathcal{O}(4n^3)$
	$K_k = \bar{P}_k \tilde{H}_k^T [\tilde{H}_k \bar{P}_k \tilde{H}_k^T + R_k]^{-1}$	$m^3 + 4n^2 m + 2m^2(2n+1) + n$	$\mathcal{O}(4n^2 m)$
	$\hat{\mathbf{x}}_k^+ = \hat{\mathbf{x}}_k^- + K_k[\tilde{\mathbf{y}}_k - \mathbf{h}(\hat{\mathbf{x}}_k^-)]$	$2nm + m$	$\mathcal{O}(2nm)$
	$P_k = [I - K_k \tilde{H}_k] \bar{P}_k$	$2n^3 + 2n^2 m - mn$	$\mathcal{O}(2n^3)$
IEKF	$\hat{\dot{\mathbf{x}}} = f(\hat{\mathbf{x}}, \mathbf{u}, t)$	N/A	$\mathcal{O}(f(\hat{\mathbf{x}}, \mathbf{u}, t))$
	$\bar{P}_k = \Phi(t_k, t_{k-1}) P_{k-1} \Phi^T(t_k, t_{k-1}) + Q$	$4n^3 - n^2$	$\mathcal{O}(4n^3)$
	While $i \geq N_i$		
	$K_{k_i} = \bar{P}_k \tilde{H}_k^T [\tilde{H}_k \bar{P}_k \tilde{H}_k^T + R_k]^{-1}$	$N(m^3 + 4n^2 m + 2m^2(2n+1) + n)$	$\mathcal{O}(4Nn^2 m)$
	$\hat{\mathbf{x}}_{k_{i+1}}^+ = \hat{\mathbf{x}}_k^- + K_k[\tilde{\mathbf{y}}_k - \mathbf{h}(\hat{\mathbf{x}}_k^-) - \tilde{H}_k(\hat{\mathbf{x}}_k^- - \hat{\mathbf{x}}_{k_i}^+)]$	$N(4nm + 2n + 2m)$	$\mathcal{O}(4Nnm)$
	$P_{k_{i+1}} = [I - K_k \tilde{H}_k] \bar{P}_k$	$N(2n^3 + 2n^2 m - mn)$	$\mathcal{O}(2Nn^3)$
AEKF	$\hat{\dot{\mathbf{x}}} = f(\hat{\mathbf{x}}, \mathbf{u}, t)$	N/A	$\mathcal{O}(f(\hat{\mathbf{x}}, \mathbf{u}, t))$
	$\bar{P}_k = \Phi(t_k, t_{k-1}) P_{k-1} \Phi^T(t_k, t_{k-1}) + Q$	$4n^3 - n^2$	$\mathcal{O}(4n^3)$
	$R_k = \alpha R_{k-1} + (1-\alpha)(\epsilon_k \epsilon_k^T + \tilde{H}_k \bar{P}_k \tilde{H}_k^T)$	$2n^2 m + 2m^2(2+n) - 2m(1-2n)$	$\mathcal{O}(2n^2 m)$
	$K_k = \bar{P}_k \tilde{H}_k^T [\tilde{H}_k \bar{P}_k \tilde{H}_k^T + R_k]^{-1}$	$m^3 + 4n^2 m + 2m^2(2n+1) + n$	$\mathcal{O}(4n^2 m)$
	$\hat{\mathbf{x}}_k^+ = \hat{\mathbf{x}}_k^- + K_k[\tilde{\mathbf{y}}_k - \mathbf{h}(\hat{\mathbf{x}}_k^-)]$	$2nm + m$	$\mathcal{O}(2nm)$
	$P_k = [I - K_k \tilde{H}_k] \bar{P}_k$	$2n^3 + 2n^2 m - mn$	$\mathcal{O}(2n^3)$
	$Q_k = \alpha Q_{k-1} + (1-\alpha)(K_k \mathbf{d}_k \mathbf{d}_k^T K_k^T)$	$3n^2 + 2nm + m$	$\mathcal{O}(3n^2)$
CKF	$\hat{\dot{\mathbf{x}}} = f(\hat{\mathbf{x}}, \mathbf{u}, t)$	N/A	$\mathcal{O}(f(\hat{\mathbf{x}}, \mathbf{u}, t))$
	$\bar{P}_k = \Phi(t_k, t_{k-1}) P_{k-1} \Phi^T(t_k, t_{k-1}) + Q$	$4n^3 - n^2$	$\mathcal{O}(4n^3)$
	$\bar{C}_k = \Phi(t_k, t_{k-1}) C_{k-1}$	$2n^2 b - nb$	$\mathcal{O}(2n^2 b)$
	$K_k = (\bar{P}_k \tilde{H}_k^T + \bar{C}_k N_k^T)[\tilde{H}_k \bar{P}_k \tilde{H}_k^T + N_k \bar{C}_k^T \tilde{H}_k^T + \tilde{H}_k \bar{C}_k N_k^T + N_k B_0 N_k^T + R_k]^{-1}$	$m^3 + 4n^2 m + 6m^2 n + 4m^2 b + 2b^2 m + 5m^2 + 6nmb - 6nm - 4mb + 5m^2 + m$	$\mathcal{O}(4n^2 m)$
	$\hat{\mathbf{x}}_k^+ = \hat{\mathbf{x}}_k^- + K_k[\tilde{\mathbf{y}}_k - \mathbf{h}(\hat{\mathbf{x}}_k^-, \mathbf{b}_k) - N_k \mathbf{b}_k]$	$2nm + 2mb + m$	$\mathcal{O}(2nm)$
	$P_k = [I - K_k \tilde{H}_k] \bar{P}_k - K_k N_k \bar{C}_k^T$	$2n^3 + n^2(4m+1) + nm(2b-3)$	$\mathcal{O}(2n^3)$
	$C_k = \bar{C}_k - K_k(\tilde{H}_k \bar{C}_k + N_k B_0)$	$2mb^2 + 4nmb - 2mb + nb$	$\mathcal{O}(4nmb)$
UKF	$\chi_{k-1} = \left[\hat{\mathbf{x}}_{k-1} \quad \hat{\mathbf{x}}_{k-1} \pm \sqrt{(L+\lambda)\bar{P}_{k-1}}\right]$	$1/3n^3 + 1/2n^2 + 25/6n$	$\mathcal{O}(1/3n^3)$
	$\hat{\chi} = f(\chi, \mathbf{u}, t)$	N/A	$\mathcal{O}(2n\, f(\hat{\mathbf{x}}, \mathbf{u}, t))$
	$\bar{\mathbf{x}}_k = \sum_{i=0}^{2L} W_i^m \hat{\chi}_i$	$4n^2 - 2n$	$\mathcal{O}(4n^2)$
	$\bar{P}_k = \sum_{i=0}^{2L} W_i^c [\chi_i - \hat{\mathbf{x}}_k][\chi_i - \hat{\mathbf{x}}_k]^T + Q$	$6n^3 + 4n^2$	$\mathcal{O}(6n^3)$
	$\hat{\mathbf{y}}_k = \sum_{i=0}^{2L} W_i^m \gamma_k^i, \quad \gamma_k = \mathbf{h}(\chi_{i,k})$	$4m^2 n - m^2$	$\mathcal{O}(4m^2 n)$
	$P_{\tilde{y}_k \tilde{y}_k} = \sum_{i=0}^{2L} W_i^c [\gamma_{i,k} - \hat{\mathbf{y}}_k][\gamma_{i,k} - \hat{\mathbf{y}}_k]^T + R_k$	$6m^2 n + m^2 + 2mn$	$\mathcal{O}(6m^2 n)$
	$P_{x_k y_k} = \sum_{i=0}^{2L} W_i^c [\chi_{i,k} - \hat{\mathbf{x}}_k][\gamma_{i,k} - \hat{\mathbf{y}}_k]^T$	$4n^2 m + 2n^2 + 2nm$	$\mathcal{O}(4n^2 m)$
	$K_k = P_{x_k y_k} P_{\tilde{y}_k \tilde{y}_k}^{-1}$	$m^3 + m^2(n+1) + m(1-n)$	$\mathcal{O}(m^2(2n+1)$
	$\hat{\mathbf{x}}_k^+ = \hat{\mathbf{x}}_k^- + K_k[\tilde{\mathbf{y}}_k - \hat{\mathbf{y}}_k]$	$n(2m+1)$	$\mathcal{O}(2nm)$
	$P_k = \bar{P}_k - K_k P_{\tilde{y}_k \tilde{y}_k} K_k^T$	$n^2(2m+1) + 2m^2 n - 2nm$	$\mathcal{O}(n^2(2m+1))$

Table 3.10: A brief summary of the filter complexity (without taking into account non-linear dynamical functions, i.e. $\mathcal{O}(f(\hat{\mathbf{x}}, \mathbf{u}, t))$ and $\mathcal{O}(2n\, f(\hat{\mathbf{x}}, \mathbf{u}, t))$)

Algorithm	FLOPs	Order
EKF	$6n^3 + m^3 + n^2(6m-1) + 2m^2(2n+1) + nm + n + m$	$\mathcal{O}(6n^3)$
IEKF	$4n^3 - n^2 + N(2n^3 + m^3 + 6n^2 m + 2m^2(2n+1) + 3nm + 3n + 2m)$	$\mathcal{O}(4n^3 + N(2n^3))$
AEKF	$6n^3 + m^3 + 8n^2 m + 2n^2 + 6m^2(n+1) + 7nm + n$	$\mathcal{O}(6n^3)$
CKF	$6n^3 + m^3 + n^2(2b + 8m) + m^2(6n + 4b + 10) + 4b^2 m + nm(6b+5) + mb(6n-4) + 2m$	$\mathcal{O}(6n^3)$
UKF	$19/3n^3 + m^3 + n^2(23/2 + 6m) + m^2(12n+2) + n(19/6 + 3m) + m$	$\mathcal{O}(19/3n^3)$

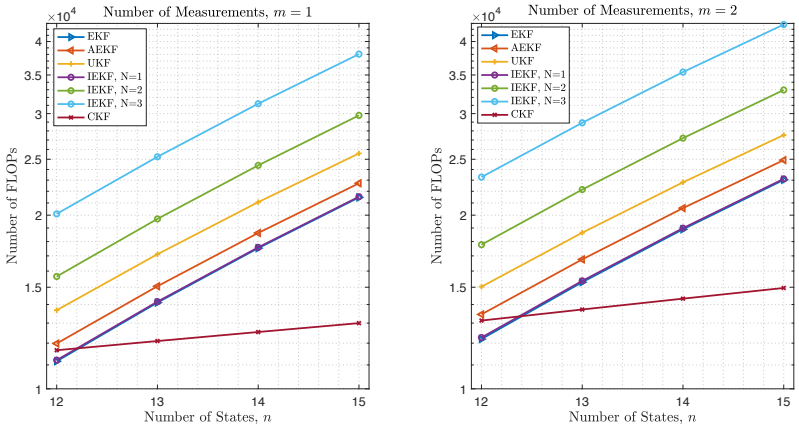

Figure 3.10: Number of FLOPs for the given filters under simplified dynamic conditions (see text). Note that CKF uses a fixed $n = 12$ plus $b = 0, 1, 2, 3$ as the number of states. However, EKF estimates these states e.g. $n = 13$ where systematic bias is estimated along with spacecraft dynamical states. $m = 1$ represents the "range-only" case, while $m = 2$ represents the "range and range-rate" measurements case.

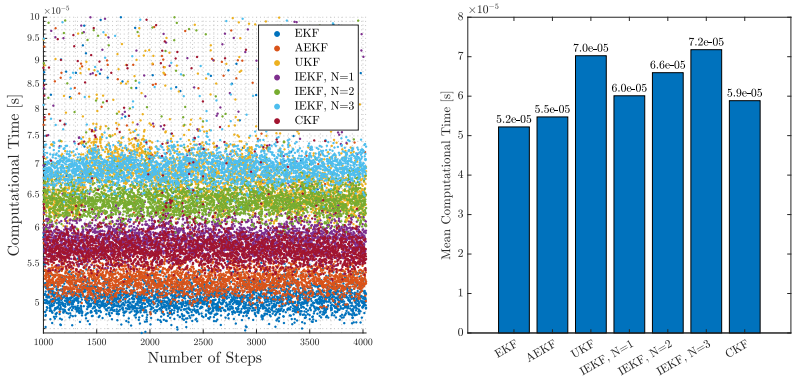

Figure 3.11: Comparison of computational time for the given filters under the simplified dynamic conditions.

dynamic models, the CRTBP, sources of dynamic modeling errors, and measurement models for range, range-rate, and LOS. Additionally, it covered several sequential data processing algorithms EKF, IEKF, AEKF, CKF, and UKF and smoothers, each with their respective advantages and disadvantages. Key findings from this chapter include:

- An extensive review and identification of gaps in the SST-based OD problem from various perspectives.
- Detailed OD requirements and goals for existing and future missions, accompanied by a station-keeping analysis.
- An extensive overview of SST-based OD models, dynamical models, measurement

models, and various filtering techniques, highlighting their computational needs based on analytical and numerical analyses.

This chapter aimed to address the research questions 1.a.: Autonomous navigation system requirements and 3.a.: Characteristics of SST-based OD, along with required OD models. Through this detailed examination, the chapter contributes valuable insights into advancing the field of autonomous OD, aiming for enhanced autonomy and efficiency in space missions.

4

Performance Analysis Methods

This chapter introduces the main performance analysis methods used in this dissertation. First, the concept of observability is outlined, accompanied by definitions and criteria for observability. Subsequently, various factors of observability, including the Observability Gramian, information matrix, degree of observability, and unobservability index, are presented. This chapter also covers a semi-analytical observability and covariance analysis for the Satellite-to-Satellite Tracking (SST)-based Orbit Determination (OD) within the Circular Restricted Three-body Problem (CRTBP), including analytical derivations for measurement sensitivity and Gramian matrices. Additionally, a method for comparing different observation data types from an observability perspective is introduced, offering a valuable tool for OD analyses. The chapter then proceeds to provide the Cramér-Rao Lower Bound (CRLB) for the OD problem relying on SST. Finally, the chapter presents the concepts of Monte Carlo simulation and covariance analysis, along with a discussion on these performance metrics, completing its comprehensive coverage of essential performance analysis methodologies.

Parts of this chapter have been published in:
E. Turan, S. Speretta, and E. Gill, "Performance analysis of crosslink radiometric measurement based autonomous orbit determination for cislunar small satellite formations", *Advances in Space Research*, vol. 72, no. 7, pp. 2710–2732, Oct. 2023. DOI: 10.1016/j.asr.2022.11.032

This chapter serves as a comprehensive guide to the key performance analysis methods employed in the study. It begins with an exploration of *observability*, a fundamental concept that assists the reliability of Orbit Determination (OD) solutions. Following this, a definition and the evaluation criteria for observability are laid out. Various methodologies for analyzing system observability are then discussed, including the use of observability Gramian, singular value decomposition-based methods, degrees of observability, and metrics for unobservability. Thereafter, Cramér-Rao Lower Bound (CRLB), Monte Carlo, and estimation error covariance analysis are introduced, each serving as integral tools for assessing and enhancing OD performance. Furthermore, an observation-type comparison is provided for the Satellite-to-Satellite Tracking (SST)-based autonomous OD problem presenting which observables, among them range, range-rate, or Line-of-Sight (LOS) measurements hold the key to more accurate state estimation. A discussion on performance metrics is provided, highlighting the pros and cons of each technique given in this study.

In brief, this chapter provides the analytical frameworks and critical insights necessary for achieving accurate OD, illustrating the methodologies that enable effective performance evaluation and optimization in the SST-based autonomous OD applications.

4.1. OBSERVABILITY ANALYSIS

Throughout this study, several performance analysis methods have been employed, with the observability analysis occupying a central position among them. Observability, in essence, refers to the system ability to estimate the spacecraft state, such as position and velocity, based on available observations. It is crucial at the system design level whether the system can accurately and reliably estimate the state variables. In particular, the observability analysis assesses whether the system state can be determined, in other words, if it is *observable*, based on available measurements. Furthermore, this approach delves into the complex relationship between system observability and the chosen observation type, introducing the impact of observation-related parameters like measurement accuracy. It helps to identify limitations in the system design and the relationship between the system accuracy and navigation system parameters.

Observability analysis methods are applicable across a broad spectrum of systems, from linear to non-linear, with the primary difference between applications lying in the formulation of the observability matrix, denoted by N. In the following paragraphs, first, the observability criteria and analysis methods are initially outlined for linearized systems, focusing on the construction of the observability matrix and the evaluation of system observability. These methods enable a clear assessment of whether every state variable of the system can be estimated from the inputs and outputs over a given time span. Transitioning to non-linear systems, a discussion is provided to address the complexities introduced by non-linear dynamics.

OBSERVABILITY GRAMIAN

The concept of the Observability Gramian plays a critical role in the evaluation of system observability. This analysis method typically involves evaluating the observability Gramian, known also as the observability matrix, which serves as a mathematical tool to determine if a system's internal state can be inferred from its external outputs.

The fundamental principle of observability is outlined in the following criterion: The system is observable at the time instant t_0 if and only if the observability Gramian is non-singular and thus a full rank matrix. The observability matrix, N is given as [115]:

$$N = \sum_{k=1}^{l} \Phi(t_k, t_0)^T \tilde{H}_k^T \tilde{H}_k \Phi(t_k, t_0) \tag{4.1}$$

where Φ denotes the STM from t_0 to t_k, illustrating how the system's state changes over time and $\tilde{H}$ symbolizes the matrix representing the partial derivatives of the observations with respect to the states at t_k expressed as $\tilde{H}_k = \partial \mathbf{h}(\mathbf{x}_k)/\partial \mathbf{x}_k$.

A theoretical analysis can be conducted using the observability Gramian to identify observable states or state combinations. Its assessment hinges on determining whether the observability Gramian possesses a full rank, which signifies that all its columns are linearly independent from one another. In such a scenario, the entire system can be considered observable, and every state can be accurately estimated using a navigation filter. However, when linearly dependent columns are present within the observability Gramian, this indicates the existence of unobservable states. In the cases where a linear combination of these dependent columns emerges, independent of other columns, it signifies the observability of the corresponding linear state combination. Consequently, the total number of observable states and state combinations aligns with the rank of the observability matrix, highlighting the pivotal role of the Gramian in understanding the observability characteristics of a given system.

INFORMATION MATRIX

Building on the foundational concepts introduced with the observability matrix, the information matrix, $\mathscr{I}$, represents another cornerstone in the system analysis, directly linked to the earlier discussions on the observability Gramian, Eq. 4.1. The information matrix serves as the inverse of the covariance matrix, thereby offering a quantitative measure of the information content captured over the analysis period. Its formulation can be expressed as [182]:

$$\mathscr{I} = \sum_{k=1}^{l} \Phi(t_k, t_0)^T \tilde{H}_k^T R_k \tilde{H}_k \Phi(t_k, t_0) \tag{4.2}$$

In this expression, R denotes the measurement noise covariance matrix at the time t_k, capturing the uncertainties associated with observational data. The information matrix, through its construction, provides a weighted assessment of system observability. This weighting becomes especially crucial under the assumption that the measurement noise covariance matrix, R, is consistent across the observed timeframe. This approach offers a robust framework for evaluating system observability under varying conditions of measurement noise.

DEGREE OF OBSERVABILITY

Both the observability Gramian, and the information matrix are essential tools for assessing the observability of a system, offering valuable insights into the system's capacity to yield accurate state estimations. In addition to assessing whether the system is

observable or not, the degree of observability is another aspect of the system design and analysis. High observability, thus, suggests that the state variables can accurately be estimated from the available measurements while a low observability implies that some state variables can not be estimated or can be weakly estimated, providing a quantitative measure of the system's observability dynamics. One common method employed for quantifying the degree of observability involves the following equation [183]:

$$\gamma = \frac{n}{\mathrm{Tr}[N_k^{-1}]} \tag{4.3}$$

where n represents the state vector's dimension and a larger value of γ signifies a higher degree of observability.

Additionally, the Condition Number (CN) serves as another pivotal metric, calculated for either the observability matrix, N, or the information matrix, $\mathscr{I}$, and is defined as the ratio of the matrix's largest singular value to its smallest non-zero singular value. This ratio provides insight into the system's sensitivity; a high condition number, $CN(N)$ or $CN(\mathscr{I})$, indicates that minor inputs can significantly affect the output, revealing ill-conditioning. Conversely, a lower condition number suggests well-conditioning, where the output remains relatively stable despite input variations.

Delving deeper into the system observability involves analyzing the eigenvalues and eigenvectors of the observability, N, or information ,$\mathscr{I}$, matrices through Singular Value Decomposition (SVD):

$$N = \mathrm{U}\Sigma\mathrm{V}^T \tag{4.4}$$

where U and V denote unitary matrices, while Σ contains the singular values arranged in descending order, e.g. $\Sigma_1 > \Sigma_2 > \cdots > \Sigma_{12}$ where the state vectors consist of position and velocity states of a formation consisted of two-spacecraft. The eigenvector associated with the highest eigenvalue highlights the direction of maximum information content, thereby identifying the most observable state direction. By evaluating the entire spectrum of eigenvalues and their corresponding eigenvectors, it is possible to order the states from most to least observable. In this context, the condition number is defined as:

$$CN(N) = \frac{\Sigma_1}{\Sigma_{12}} \tag{4.5}$$

Furthermore, to understand the specific impact of observations at distinct moments at time t_i alone, one might consider the square root of the maximum eigenvalue of each 3 by 3 component of N_k, denoted as $\sqrt{\max \mathrm{eig}(N_{i,3\times3})}$. This approach offers insights into how individual observations contribute to the observability of position and velocity states within a satellite formation.

UNOBSERVABILITY

While the condition number offers valuable insights into the degree of observability, it primarily focuses on the ratio of the highest singular value to the smallest one, providing information about the most and least observable state components within the system. However, it does not provide a comprehensive picture of all states. Situations may arise where different system configurations exhibit the same condition number while yielding

significantly different estimation results due to the presence of other state redcomponents.

To delve deeper into the least observable states within a system, another observability metric known as the unobservability index comes into play. This is essentially the reciprocal of the smallest local singular value and is expressed as [184]:

$$UOI(N) = \frac{1}{\Sigma_{12}} \tag{4.6}$$

This metric offers valuable insights into the system least observable state and is particularly useful when the objective is ensuring all states within a system surpass a certain observability threshold. Since it provides an observability assessment from the worst-case perspective, it sheds light on the states that are most vulnerable to limited observability. It is important to note that, unlike the CN, the Unobservability Index (UOI) does not increase with the addition of more observations, making it a suitable choice when evaluating the potential impact of observation noise on estimation errors, especially if the index is high.

It should be noted that the observability of a nonlinear system can be analyzed based on Lie derivatives [90], [185]. In this case, the system dynamics remain nonlinear, but linearization is still necessary for the measurement equations. Similar analysis methods, including the CN, UOI, and SVD can be applied to the observability matrix derived from Lie derivatives. The observability matrix N for a nonlinear system is given as [183]:

$$N = \begin{bmatrix} \mathrm{d}L_f^0\mathbf{h}(\mathbf{x}) \\ \mathrm{d}L_f^1\mathbf{h}(\mathbf{x}) \\ \vdots \\ \mathrm{d}L_f^{n-1}\mathbf{h}(\mathbf{x}) \end{bmatrix} \tag{4.7}$$

where n and $\mathbf{h}(\mathbf{x})$ represent the dimension of the state vector and the observation vector, respectively. Additionally, $\mathrm{d}L_f^k\mathbf{h}(\mathbf{x})$ is the kth order Lie derivative given as:

$$\mathrm{d}L_f^0\mathbf{h}(\mathbf{x}) = \mathbf{h}(\mathbf{x})L_f^k\mathbf{h}(\mathbf{x}) = \frac{\partial(L_f^{k-1}\mathbf{h}(\mathbf{x}))}{\partial\mathbf{x}} f(\mathbf{x}), \quad k = 1,2,...,n-1$$

SEMI-ANALYTICAL OBSERVABILITY ANALYSIS FOR SST-BASED OD WITHIN THE CRTBP

In the context of assessing the system observability for the SST-based OD problem within the CRTBP, a comprehensive approach can be employed, combining analytical derivations with numerical methods to evaluate observability. Moreover, CRLB can be assessed semi-analytically by inverting the information matrix. In particular, this part of the dissertation shows how SST provides an absolute state estimation within the CRTBP from an observability perspective.

Analytically, the process begins with the derivation of the observations as a function of the state vector, which is critical for mapping the relationship between measurements and states. This follows the calculation of the gradient matrix G, which comprises the partial derivatives of the acceleration vectors with respect to the state vector. These

derivations are essential for understanding how changes in the spacecraft's state provide an observable system within the CRTBP model. As a reminder, the CRTBP dynamics given in Eq. 3.15-3.17:

$$\ddot{x} - 2\dot{y} = x - (1-\mu)\frac{x+\mu}{r_1^3} - \mu\frac{x+\mu-1}{r_2^3}$$
$$\ddot{y} + 2\dot{x} = (1 - \frac{1-\mu}{r_1^3} - \frac{\mu}{r_2^3})y$$
$$\ddot{z} = (\frac{\mu-1}{r_1^3} - \frac{\mu}{r_2^3})z$$

where $r_1 = \sqrt{(x+\mu)^2 + y^2 + z^2}$ and $r_2 = \sqrt{(x+\mu-1)^2 + y^2 + z^2}$. Once again, the state vector is given in Eq. 3.1:

$$\mathbf{x} = \begin{bmatrix} \mathbf{r}_1 & \mathbf{v}_1 & \mathbf{r}_2 & \mathbf{v}_2 \end{bmatrix}^T \tag{4.8}$$

where $\mathbf{r}_i$ and $\mathbf{v}_i$ represent the position and velocity states of two spacecraft within a formation, $i = 1, 2$. For the purpose of observability analysis, the observation matrix, $\tilde{H}$, needs to be transformed through the STM between epochs, formulated as:

$$H_k = \tilde{H}_k \Phi(t_k, t_0) \tag{4.9}$$

where $\tilde{H}$ symbolizes the matrix representing the partial derivatives of the observations with respect to the states at t_k expressed as $\tilde{H}_k = \partial \mathbf{h}(\mathbf{x}_k)/\partial \mathbf{x}_k$ and Φ denotes the STM from t_k to t_0, illustrating how the system's state changes over time from t_k back to the initial state at t_0.

In a practical scenario, such as a range-only measurement case, i.e., ρ, involving a two-spacecraft system and considering the STM derived based on a second order Taylor series expansion at $t = t_0$, the components of H_k can be determined as follows (see Appendix B for further details):

$$H_k = \begin{bmatrix}
\frac{(x_1-x_2)+\frac{T_s^2}{2}(\frac{\partial \ddot{x}_1}{\partial x_1}x_1 - \frac{\partial \ddot{x}_1}{\partial x_1}x_2 + \frac{\partial \ddot{y}_1}{\partial x_1}y_1 - \frac{\partial \ddot{y}_1}{\partial x_1}y_2 + \frac{\partial \ddot{z}_1}{\partial x_1}z_1 - \frac{\partial \ddot{z}_1}{\partial x_1}z_2)}{\rho} \\
\frac{(y_1-y_2)+\frac{T_s^2}{2}(\frac{\partial \ddot{x}_1}{\partial y_1}x_1 - \frac{\partial \ddot{x}_1}{\partial y_1}x_2 + \frac{\partial \ddot{y}_1}{\partial y_1}y_1 - \frac{\partial \ddot{y}_1}{\partial y_1}y_2 + \frac{\partial \ddot{z}_1}{\partial y_1}z_1 - \frac{\partial \ddot{z}_1}{\partial y_1}z_2)}{\rho} \\
\frac{(z_1-z_2)+\frac{T_s^2}{2}(\frac{\partial \ddot{x}_1}{\partial z_1}x_1 - \frac{\partial \ddot{x}_1}{\partial z_1}x_2 + \frac{\partial \ddot{y}_1}{\partial z_1}y_1 - \frac{\partial \ddot{y}_1}{\partial z_1}y_2 + \frac{\partial \ddot{z}_1}{\partial z_1}z_1 - \frac{\partial \ddot{z}_1}{\partial z_1}z_2)}{\rho} \\
\frac{T_s(x_1-x_2+T_s y_1 - T_s y_2)}{\rho} \\
\frac{T_s(y_1-y_2+T_s x_1 - T_s x_2)}{\rho} \\
\frac{T_s(z_1-z_2)}{\rho} \\
-\frac{\left((x_1-x_2)+\frac{T_s^2}{2}(\frac{\partial \ddot{x}_2}{\partial x_2}x_1 - \frac{\partial \ddot{x}_2}{\partial x_2}x_2 + \frac{\partial \ddot{y}_2}{\partial x_2}y_1 - \frac{\partial \ddot{y}_2}{\partial x_2}y_2 + \frac{\partial \ddot{z}_2}{\partial x_2}z_1 - \frac{\partial \ddot{z}_2}{\partial x_2}z_2)\right)}{\rho} \\
-\frac{\left((y_1-y_2)+\frac{T_s^2}{2}(\frac{\partial \ddot{x}_2}{\partial y_2}x_1 - \frac{\partial \ddot{x}_2}{\partial y_2}x_2 + \frac{\partial \ddot{y}_2}{\partial y_2}y_1 - \frac{\partial \ddot{y}_2}{\partial y_2}y_2 + \frac{\partial \ddot{z}_2}{\partial y_2}z_1 - \frac{\partial \ddot{z}_2}{\partial y_2}z_2)\right)}{\rho} \\
-\frac{\left((z_1-z_2)+\frac{T_s^2}{2}(\frac{\partial \ddot{x}_2}{\partial z_2}x_1 - \frac{\partial \ddot{x}_2}{\partial z_2}x_2 + \frac{\partial \ddot{y}_2}{\partial z_2}y_1 - \frac{\partial \ddot{y}_2}{\partial z_2}y_2 + \frac{\partial \ddot{z}_2}{\partial z_2}z_1 - \frac{\partial \ddot{z}_2}{\partial z_2}z_2)\right)}{\rho} \\
-\frac{T_s(x_1-x_2+T_s y_1 - T_s y_2)}{\rho} \\
-\frac{T_s(y_1-y_2+T_s x_1 - T_s x_2)}{\rho} \\
-\frac{T_s(z_1-z_2)}{\rho}
\end{bmatrix}^T \tag{4.10}$$

where $T_s = t_k - t_0$ and $\partial\ddot{\mathbf{x}}_i/\partial\mathbf{x}_i$ for the spacecraft number $i = 1,2$:

$$
\begin{aligned}
\frac{\partial \ddot{x}_i}{\partial x_i} &= \frac{(\mu-1)}{{r_1}^3} - \frac{\mu}{{r_2}^3} + \frac{3\mu(\mu+x_i-1)(\mu+x_i-1)}{{r_2}^5} - \frac{3(\mu+x_i)(\mu+x_i)(\mu-1)}{{r_1}^5} + 1 \\
\frac{\partial \ddot{x}_i}{\partial y_i} &= \frac{3\,\mu\,y_i(\mu+x_i-1)}{{r_2}^5} - \frac{3y_i(\mu+x_i)(\mu-1)}{{r_1}^5} \\
\frac{\partial \ddot{x}_i}{\partial z_i} &= \frac{3\,\mu\,z_i(\mu+x_i-1)}{{r_2}^5} - \frac{3z_i(\mu+x_i)(\mu-1)}{{r_1}^5} \\
\frac{\partial \ddot{y}_i}{\partial x_i} &= -y_i\left(\frac{3(\mu+x_i)(\mu-1)}{{r_1}^5} + \frac{3\mu(\mu+x_i-1)}{{r_2}^5}\right) \\
\frac{\partial \ddot{y}_i}{\partial y_i} &= \frac{(\mu-1)}{{r_1}^3} + y_i\left(\frac{3\,\mu\,y_i}{{r_2}^5} - \frac{3y_i(\mu-1)}{{r_1}^5}\right) - \frac{\mu}{{r_2}^3} + 1 \\
\frac{\partial \ddot{y}_i}{\partial z_i} &= y_i\left(\frac{3\,\mu\,z_i}{{r_2}^5} - \frac{3\,z_i(\mu-1)}{{r_1}^5}\right) \\
\frac{\partial \ddot{z}_i}{\partial x_i} &= -z_i\left(\frac{3(\mu+x_i)(\mu-1)}{{r_1}^5} - \frac{3\mu(\mu+x_i-1)}{{r_2}^5}\right) \\
\frac{\partial \ddot{z}_i}{\partial y_i} &= z_i\left(\frac{3\,\mu\,y_i}{{r_2}^5} - \frac{3\,y_i(\mu-1)}{{r_1}^5}\right) \\
\frac{\partial \ddot{z}_i}{\partial z_i} &= \frac{\mu-1}{{r_1}^3} + z_i\left(\frac{3\,\mu\,z_i}{{r_2}^5} - \frac{3\,z_i(\mu-1)}{{r_1}^5}\right) - \frac{\mu}{{r_2}^3}
\end{aligned}
\tag{4.11}
$$

In the range-only case, as given above, the positional components $(H_k^{\mathbf{r}_1}, H_k^{\mathbf{r}_2})$ are different from each other, while many columns of $\tilde{H}_k$ exhibit equal magnitude but opposite signs, for instance, $\tilde{H}_k^{y_1} = -\tilde{H}_k^{y_2}$, i.e., $\partial\dot{\rho}/\partial y_1 = -\partial\dot{\rho}/\partial y_2$. This would make the rows of the information and observability matrices dependent. As stated in [11], differences in the state transition matrix, $\Phi(t_k, t_0)$ make H_k and thus the information and observability matrices positive definite. These differences are noticeable in certain elements, such as $H_k^{y_1}$, which contains $\partial\ddot{\mathbf{r}}_i/\partial y_1$ and $H_k^{y_2}$ which involves $\partial\ddot{\mathbf{r}}_2/\partial y_2$. Different orbital regions may exhibit unique STM characteristics, potentially resulting in an observable system. It is worth noting that Eq. 4.10 is derived based on a second-order Taylor series expansion at $t = t_0$. This simplified formulation makes the velocity components linearly dependent, e.g., $H_k^{\dot{x}_1} = -H_k^{\dot{x}_2}$. However, if the third order terms are added into the STM, e.g., $A^3 \cdot (t_i - t_0)^3/3!$, the velocity components are different from each other, e.g. $H_k^{\dot{x}_1} \neq -H_k^{\dot{x}_2}$:

$$
H_k^{\dot{x}_1} = \frac{T_s(6x_1 - 6\,x_2 + 6T_s y_1 - 6T_s y_2 + {T_s}^2(4x_1 - 4x_2 + 4\frac{\partial \ddot{x}_1}{\partial x_1}x_1 - \frac{\partial \ddot{x}_1}{\partial x_1}x_2 + \frac{\partial \ddot{y}_1}{\partial x_1}y_1 - \frac{\partial \ddot{y}_1}{\partial x_1}y_2 + \frac{\partial \ddot{z}_1}{\partial x_1}z_1 - \frac{\partial \ddot{z}_1}{\partial x_1}z_2)\,)}{6\rho} \tag{4.12}
$$

$$
H_k^{\dot{x}_2} = -\frac{T_s(6x_1 - 6x_2 + 6T_s y_1 - 6T_s y_2 + {T_s}^2(4x_1 - 4x_2 + 4\frac{\partial \ddot{x}_2}{\partial x_2}x_2 - \frac{\partial \ddot{x}_2}{\partial x_2}x_2 + \frac{\partial \ddot{y}_2}{\partial x_2}y_1 - \frac{\partial \ddot{y}_2}{\partial x_2}y_2 + \frac{\partial \ddot{z}_2}{\partial x_2}z_1 - \frac{\partial \ddot{z}_2}{\partial x_2}z_2)\,)}{6\rho} \tag{4.13}
$$

The extra terms are partial derivatives of $\ddot{\mathbf{r}}_1$ with respect to x_1 in $H_k^{\dot{x}_1}$ and $\ddot{\mathbf{r}}_2$ with respect to x_2 in $H_k^{\dot{x}_2}$, showing the terms are not identical and, thus the columns are in-

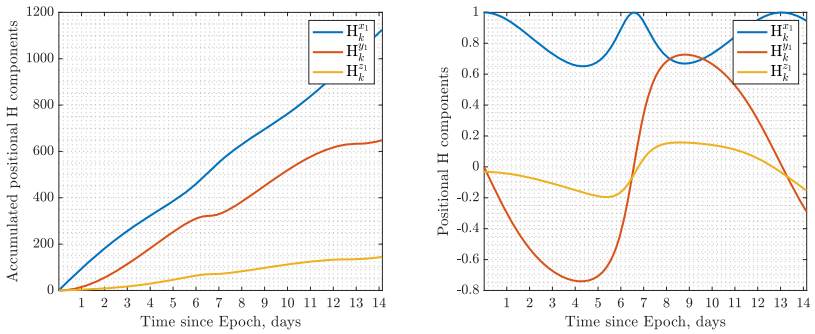

Figure 4.1: Information obtained by satellite-to-satellite observations. Left: Accumulated absolute information. Right: Instantaneous information.

dependent, clearly highlighting a second order approximation is not sufficient for this application.

Having established the distinct nature of the components within H_k, further investigation can be done: The equations given above indicate a clear connection between the inter-satellite distance ρ and the relative position between satellites $\boldsymbol{r}_1 - \boldsymbol{r}_2$. For instance, the x-positional component of the first spacecraft within H_k, denoted as $H_k^{x_1}$, is directly related to the difference in x-coordinates between two satellites, $x_1 - x_2$, and the pseudorange ρ. Since the covariance matrix is the inverse of the information matrix, maximizing all the components of H_k would be highly advantageous. By numerically propagating spacecraft states using the equations provided by Eq. 3.15-3.17 and employing the analytical derivations provided in Eq.4.10, it becomes possible to determine the cumulative information offered by observations over the course of a simulation. Figure 4.1 presents the accumulated information regarding the EML2 Halo orbiter position states within the context of the range-only EML1 Halo-to-EML2 Halo orbital configuration (see Table 3.7 for initial conditions): It reveals that there has been a steady increase in the collected information and shows that the least information is collected in the z-axis, i.e., $H_k^{z_1}$. These figures show that the information collected depends on the relative geometry between satellites and changes in the acceleration acting on the spacecraft with respect to corresponding positional states, e.g., $\ddot{\mathbf{r}}_1/\mathbf{r_1}$. It should be noted at this point there is no significant difference observed between the semi-analytical approach via Eq. 4.10 and the fully numerical approach: only a 0.0176% difference is observed on $H_k^{x_1}$ between these two approaches, cross-validating both approaches.

The approximated STM, Eq. B.12 given in Appendix, can be written in a more compact form including the gradient matrix G. Considering only one of the spacecraft states, the differential equation is defined, once again, Eq. 3.19, by:

$$\dot{\Phi}(t_k, t_0) = A(\mathrm{t})\Phi(t_k, t_0) = \frac{\partial F(\mathbf{x}, t)}{\partial \mathbf{x}}\Phi(t_k, t_0) = \begin{bmatrix} 0_{3\times3} & I_{3\times3} \\ G(t) & 2\Omega \end{bmatrix}\Phi(t_k, t_0) \tag{4.14}$$

where

$$G(t) = \begin{bmatrix} \frac{\partial \ddot{x}}{\partial x} & \frac{\partial \ddot{x}}{\partial y} & \frac{\partial \ddot{x}}{\partial z} \\ \frac{\partial \ddot{y}}{\partial x} & \frac{\partial \ddot{y}}{\partial y} & \frac{\partial \ddot{y}}{\partial z} \\ \frac{\partial \ddot{z}}{\partial x} & \frac{\partial \ddot{z}}{\partial y} & \frac{\partial \ddot{z}}{\partial z} \end{bmatrix} \qquad \Omega = \begin{bmatrix} 0 & 1 & 0 \\ -1 & 0 & 0 \\ 0 & 0 & 0 \end{bmatrix} \qquad \Phi(t_0, t_0) = I_{6\text{x}6} \tag{4.15}$$

The Taylor series expansion at $t = t_k$ for $\Phi(t_k, t_0)$ is:

$$\begin{aligned} \Phi(t_k, t_0) = &\begin{bmatrix} I & 0 \\ 0 & I \end{bmatrix} + \begin{bmatrix} 0 & I \\ G & 2\Omega \end{bmatrix} \Delta t + \begin{bmatrix} G & 2\Omega \\ 2\Omega G & G + 4\Omega^2 \end{bmatrix} \frac{\Delta t^2}{2} \\ &+ \begin{bmatrix} 2\Omega G & G + 4\Omega^2 \\ G^2 + 4\Omega^2 G & 2\Omega G + 2G\Omega + 8\Omega^2 \end{bmatrix} \frac{\Delta t^3}{6} \\ &+ \begin{bmatrix} G^2 + 4\Omega^2 G & 2\Omega G + 4\Omega G\Omega + 4G\Omega^2 + 16\Omega^3 \\ 2\Omega G^2 + 2G\Omega G + 8\Omega^2 G & G^2 + 4\Omega^2 G + 4\Omega G\Omega + 4G\Omega^2 + 16\Omega^3 \end{bmatrix} \frac{\Delta t^4}{24} + \mathcal{O}(A^5) \end{aligned} \tag{4.16}$$

where $\Delta t = t_k - t_0$. The Taylor expansion for the 3×3 position and velocity sub-matrices of the STM by ignoring the higher order terms are (i.e. $\mathcal{O}(A^5)$):

$$\Phi_{rr} = \frac{\partial \mathbf{r}}{\partial \mathbf{r}_0} = I + G\frac{\Delta t^2}{2} + (2\Omega G)\frac{\Delta t^3}{6} + (G^2 + 4\Omega^2 G)\frac{\Delta t^4}{24} \tag{4.17}$$

$$\Phi_{rv} = \frac{\partial \mathbf{r}}{\partial \mathbf{v}_0} = I\Delta t + \Omega \Delta t^2 + (G + 4\Omega^2)\frac{\Delta t^3}{6} + (2\Omega G + 4\Omega G\Omega + 4G\Omega^2 + 16\Omega^3)\frac{\Delta t^4}{24} \tag{4.18}$$

$$\Phi_{vr} = \frac{\partial \mathbf{v}}{\partial \mathbf{r}_0} = I + G\Delta t + \Omega G \Delta t^2 + (G^2 + 4\Omega^2 G)\frac{\Delta t^3}{6} + (2\Omega G^2 + 2G\Omega G + 8\Omega^2 G)\frac{\Delta t^4}{24} \tag{4.19}$$

$$\begin{aligned} \Phi_{vv} = \frac{\partial \mathbf{v}}{\partial \mathbf{v}_0} = &2\Omega \Delta t + (G + 4\Omega^2)\frac{\Delta t^2}{2} + (2\Omega G + 2G\Omega + 8\Omega^2)\frac{\Delta t^3}{6} \\ &+ (G^2 + 4\Omega^2 G + 4\Omega G\Omega + 4G\Omega^2 + 16\Omega^3)\frac{\Delta t^4}{24} \end{aligned} \tag{4.20}$$

Finally, $\Phi(t_k, t_0)$ is given as:

$$\Phi(t_k, t_0) \approx \begin{bmatrix} \Phi_{rr} & \Phi_{rv} \\ \Phi_{vr} & \Phi_{vv} \end{bmatrix} \tag{4.21}$$

To evaluate the performance of Eq. 4.21 with respect to the numerically derived STM, a comparison is detailed in Appendix C. It should be noted that Eq. 4.21 is given for only one of the spacecraft, necessitating calculations for both spacecraft, $i = 1, 2$:

$$\Phi(t_k, t_0) = \begin{bmatrix} \Phi_1(t_k, t_0) & 0_{6\times6} \\ 0_{6\times6} & \Phi_2(t_k, t_0) \end{bmatrix} \tag{4.22}$$

$\tilde{H}$ can be written in the following form of derivation with respect to the position and velocity vectors considering crosslink geometric range observations:

$$\tilde{H} = \begin{bmatrix} \frac{\partial \rho}{\partial \mathbf{r_1}} & \frac{\partial \rho}{\partial \mathbf{v_1}} & \frac{\partial \rho}{\partial \mathbf{r_2}} & \frac{\partial \rho}{\partial \mathbf{v_2}} \end{bmatrix} = \begin{bmatrix} \frac{\partial \rho}{\partial \mathbf{r_1}} & 0_{1\times3} & \frac{\partial \rho}{\partial \mathbf{r_2}} & 0_{1\times3} \end{bmatrix} \tag{4.23}$$

Basically, H can be found as:

$$H = \tilde{H}\Phi(t_k, t_0) = \begin{bmatrix} \frac{\partial \rho}{\partial \mathbf{r_1}} & 0_{1\times 3} & \frac{\partial \rho}{\partial \mathbf{r_2}} & 0_{1\times 3} \end{bmatrix} \begin{bmatrix} \begin{bmatrix} \Phi_{1,rr} & \Phi_{1,rv} \\ \Phi_{1,vr} & \Phi_{1,vv} \end{bmatrix} & 0_{6\times 6} \\ 0_{6\times 6} & \begin{bmatrix} \Phi_{2,rr} & \Phi_{2,rv} \\ \Phi_{2,vr} & \Phi_{2,vv} \end{bmatrix} \end{bmatrix} \tag{4.24}$$
$$= \begin{bmatrix} \frac{\partial \rho}{\partial \mathbf{r_1}}\Phi_{1,rr} & \frac{\partial \rho}{\partial \mathbf{r_1}}\Phi_{1,rv} & \frac{\partial \rho}{\partial \mathbf{r_2}}\Phi_{2,rr} & \frac{\partial \rho}{\partial \mathbf{r_2}}\Phi_{2,rv} \end{bmatrix}$$

If Eq. 4.24 is further expanded by a second-order approximation, Eq. 4.10 would be resulting. In Eq. 4.24, the velocity related terms are given as $(\partial\rho/\partial\mathbf{r_1})\Phi_{1,rv}$ and $(\partial\rho/\partial\mathbf{r_2})\Phi_{2,rv}$ respectively. As it can be seen from Eq.4.18, there is a null gradient matrix $G(t)$ related terms in Φ_{rv} until the third order expansion (e.g., $\Phi_{rv} = I\Delta t + \Omega\Delta^2$). This is why velocity-related terms given in H are linearly dependent in the second-order approximation, as discussed previously.

Now both the observability Gramian N, given in Eq. 4.1, and the information matrix $\mathcal{I}$, given in Eq. 4.2, can be derived with the information given above. It is known that the inverse of the information matrix, Eq. 4.2, is the covariance matrix, $P = \mathcal{I}^{-1}$:

$$P = \mathcal{I}^{-1} = \begin{bmatrix} \mathcal{I}_1 & \mathcal{I}_{1,2} \\ \mathcal{I}_{1,2} & \mathcal{I}_2 \end{bmatrix}^{-1} \tag{4.25}$$

where

$$\mathcal{I}_1 = \begin{bmatrix} \mathcal{I}_{rr,1} & \mathcal{I}_{rv,1} \\ \mathcal{I}_{rv,1} & \mathcal{I}_{vv,1} \end{bmatrix}$$

It is critical that the Schur complement of the block D in the matrix M can be determined using the specified matrix inversion approach [186]:

$$M^{-1} = \begin{bmatrix} (M/D)^{-1} & -(M/D)^{-1}BD^{-1} \\ -D^{-1}C(M/D)^{-1} & D^{-1} + D^{-1}C(M/D)^{-1}BD^{-1} \end{bmatrix} \tag{4.26}$$

where

$$M = \begin{bmatrix} A & B \\ C & D \end{bmatrix}, \text{ and } M/D = A - BD^{-1}C$$

A specific sub-block of the state estimation covariance matrix can be investigated in detail by applying Eq. 4.26. Here, if the positional state covariances of one of the spacecraft are the point of interest, i.e., $P_{rr,1}$ with a size of 3×3, the following can be written:

$$P_{rr,1} = (A - BD^{-1}C)^{-1} \tag{4.27}$$

where

$$A = \frac{1}{\sigma_\rho^2}\left[\Phi_{1,rr}^T \frac{\partial \rho}{\partial \mathbf{r_1}}^T \frac{\partial \rho}{\partial \mathbf{r_1}}\Phi_{1,rr}\right]_{3\times 3} \tag{4.28}$$

$$B = C^T = \frac{1}{\sigma_\rho^2}\left[\Phi_{1,rr}^T \frac{\partial \rho}{\partial \mathbf{r_1}}^T \frac{\partial \rho}{\partial \mathbf{r_1}}\Phi_{1,rv} \quad \Phi_{1,rr}^T \frac{\partial \rho}{\partial \mathbf{r_1}}^T \frac{\partial \rho}{\partial \mathbf{r_2}}\Phi_{2,rr} \quad \Phi_{1,rr}^T \frac{\partial \rho}{\partial \mathbf{r_1}}^T \frac{\partial \rho}{\partial \mathbf{r_2}}\Phi_{2,rv}\right]_{3\times 9} \tag{4.29}$$

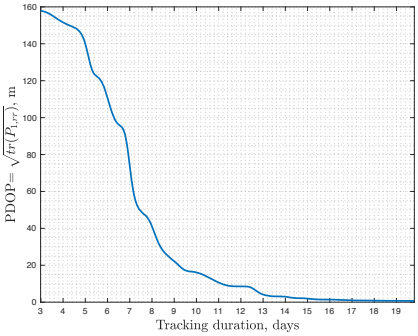

Figure 4.2: The uncertainty in the initial position estimation of the first spacecraft within the EML1-to-EML2 Halo orbiter scenario. $P_{0,rr}$ is provided as 100 km^2 for each state component. The initial conditions are given in Table 3.7

$$D = \frac{1}{\sigma_\rho^2}\begin{bmatrix} \Phi_{1,rv}^T \frac{\partial\rho}{\partial\mathbf{r_1}}^T \frac{\partial\rho}{\partial\mathbf{r_1}} \Phi_{1,rv} & \Phi_{1,rv}^T \frac{\partial\rho}{\partial\mathbf{r_1}}^T \frac{\partial\rho}{\partial\mathbf{r_2}} \Phi_{2,rr} & \Phi_{1,rv}^T \frac{\partial\rho}{\partial\mathbf{r_1}}^T \frac{\partial\rho}{\partial\mathbf{r_2}} \Phi_{2,rv} \\ \Phi_{2,rr}^T \frac{\partial\rho}{\partial\mathbf{r_2}}^T \frac{\partial\rho}{\partial\mathbf{r_1}} \Phi_{1,rv} & \Phi_{2,rr}^T \frac{\partial\rho}{\partial\mathbf{r_2}}^T \frac{\partial\rho}{\partial\mathbf{r_2}} \Phi_{2,rr} & \Phi_{2,rr}^T \frac{\partial\rho}{\partial\mathbf{r_2}}^T \frac{\partial\rho}{\partial\mathbf{r_2}} \Phi_{2,rv} \\ \Phi_{2,rv}^T \frac{\partial\rho}{\partial\mathbf{r_2}}^T \frac{\partial\rho}{\partial\mathbf{r_1}} \Phi_{1,rv} & \Phi_{2,rv}^T \frac{\partial\rho}{\partial\mathbf{r_2}}^T \frac{\partial\rho}{\partial\mathbf{r_2}} \Phi_{2,rr} & \Phi_{2,rv}^T \frac{\partial\rho}{\partial\mathbf{r_2}}^T \frac{\partial\rho}{\partial\mathbf{r_2}} \Phi_{2,rv} \end{bmatrix}_{9\times 9} \tag{4.30}$$

Eq. 4.27 represents the uncertainty in the initial position estimation of the first spacecraft via inverting the information matrix. STMs and measurement sensitivity matrix are given in Eq. 4.17-4.20 and Eq. 4.23, respectively. The measurement noise uncertainty, σ_ρ^2, is provided in Chapter 2. In brief, the position estimation specifically depends on the following: $\Phi_{i,rr}$, $\Phi_{i,rv}$, $\partial\rho/\partial\mathbf{r_i}$ for the spacecraft $i = 1,2$ and σ_ρ^2. Figure 4.2 shows an example case where the initial position uncertainty of the first spacecraft is calculated using Eq. 4.27 and represented by the Position Dilution of Precision (PDOP) metric, i.e. $\sqrt{\sigma_{1,x}^2 + \sigma_{1,y}^2 + \sigma_{1,z}^2}$, based on SST between EML1 and EML2 Halo orbiters (see Table 3.7 for initial conditions).

In a similar way, the observation effectiveness of the position state components alone, i.e., $\mathbf{r}_i$ of the spacecraft $i = 1,2$, can be calculated from:

$$\delta\mathscr{I}_{\mathbf{r},ij}(t_k) = \frac{1}{\sigma_\rho}\sqrt{\text{row}_j(\Phi_{i,rr}^T(t_k,t_0))(\frac{\partial\rho}{\partial\mathbf{r}_i})^T(\frac{\partial\rho}{\partial\mathbf{r}_i})\text{col}_j(\Phi_{i,rr}(t_k,t_0))} \tag{4.31}$$

and for the velocity states alone, x_i, y_i, z_i of the spacecraft $i = 1,2$:

$$\delta\mathscr{I}_{\mathbf{v},ij}(t_k) = \frac{1}{\sigma_\rho}\sqrt{\text{row}_j(\Phi_{i,rv}^T(t_k,t_0))(\frac{\partial\rho}{\partial\mathbf{r}_i})^T(\frac{\partial\rho}{\partial\mathbf{r}_i})\text{col}_j(\Phi_{i,rv}(t_k,t_0))} \tag{4.32}$$

where subscript j indicates element number e.g., $j = 1$ for x as a first state component. As it can be seen, the observation effectiveness, thus the estimation accuracy, is directly related to the direction of observation and the STM. It approximates how a slight

deviation in state variables propagates along the trajectory. In particular, it is advantageous from the estimation perspective if measurement vectors are not perpendicular to these deviations.

In this subsection $\tilde{H}_k$ is given for range, range-rate, and LOS angle measurements, although H_k is illustrated solely for the range measurement case due to the complexity of other measurement models. The first element of the range-rate model, $H^{x_1}_{\dot{\rho},k}$, is given below as an example. In a similar way, other Jacobian matrices, $H_{\dot{\rho},k}$, $H_{\phi,k}$ and $H_{\varphi,k}$, can be calculated.

$$
\begin{aligned}
H^{x_1}_{\dot{\rho},k} = &\left(\frac{\partial \ddot{x}_k}{\partial x_k}\frac{{T_s}^2}{2}+1\right)\left(\frac{(\dot{x}_1-\dot{x}_2)\,\rho^2-(x_1-x_2)\;\boldsymbol{\rho}\cdot\dot{\boldsymbol{\rho}}}{\rho^3}\right)+\left(\frac{\partial \ddot{y}_k}{\partial x_k}\frac{{T_s}^2}{2}\right)\left(\frac{\left(\dot{y}_1-\dot{y}_2\right)\rho^2-\left(y_1-y_2\right)\;\boldsymbol{\rho}\cdot\dot{\boldsymbol{\rho}}}{\rho^3}\right)\\
&+\left(\frac{\partial \ddot{z}_k}{\partial x_k}\frac{{T_s}^2}{2}\right)\left(\frac{(\dot{z}_1-\dot{z}_2)\,\rho^2-(z_1-z_2)\;\boldsymbol{\rho}\cdot\dot{\boldsymbol{\rho}}}{\rho^3}\right)+\left(\frac{\partial \ddot{y}_k}{\partial x_k}{T_s}^2+\frac{\partial \ddot{x}_k}{\partial x_k}T_s\right)\left(\frac{(x_1-x_2)}{\rho}\right)\\
&+\left(\frac{\partial \ddot{x}_k}{\partial x_k}{T_s}^2+\frac{\partial \ddot{y}_k}{\partial x_k}T_s\right)\left(\frac{\left(y_1-y_2\right)}{\rho}\right)+\left(T_s\frac{\partial \ddot{z}_k}{\partial x_k}\right)\left(\frac{(z_1-z_2)}{\rho}\right)
\end{aligned}
\tag{4.33}
$$

OBSERVATION TYPE COMPARISON

In the SST-based OD methodologies within this dissertation, a detailed comparison between observation types, specifically, range, range-rate, and LOS measurements, has been undertaken. This comparison is crucial for determining which observation data type optimizes OD performance given a specific tracking system's capabilities, mission objectives, and available measurement technologies. It is important to note that combining different sensors, and thus observation data types, can improve the estimation accuracy and reliability.

While section 2.3 has already discussed how LOS angles can be derived from range measurements and the relationship between the range error and the LOS measurement error, this section focuses primarily on the relationship between range and range-rate measurements. A quantitative approach, similar to one described in [187], is adopted in this section: a SNR criterion is formulated for an observable h (ρ or $\dot{\rho}$) and estimated states $\mathbf{x}$ can be calculated as follows:

$$
\Psi_{h,k} = \left|\frac{1}{\sigma_h}H_k\right| \tag{4.34}
$$

where σ_h is the noise level of the measurement h. Basically, the following figure of merit is defined to compare the relative sensitivity of range and range-rate observables to estimated states $\mathbf{x}$:

$$
\Xi_{\mathbf{x}} = \frac{\Psi_\rho}{\Psi_{\dot{\rho}}} \tag{4.35}
$$

A value of $\Xi_{\mathbf{x}} < 1$ indicates that range-rate observations offer a feasible alternative to range observations for estimating $\mathbf{x}$, suggesting a direct comparison of the observability Gramian across time epochs and incorporating realistic relative measurement error

parameters. To contextualize this comparison, the relation between range and range-rate observation errors is examined, defining the ranging error through the conventional tone-based ranging and calculating the phase error on the major tone, f_{MT} in radians as [130]:

$$\sigma_\phi = \sqrt{\frac{2B_n}{2\frac{S}{N_0}}} \tag{4.36}$$

where $2B_n$ Bi-lateral loop bandwidth, S/N_0, signal-to-noise ratio in dB Hz. Basically, the phase noise on the major ranging tone results in a range measurement error by multiplying the wavelength of the ranging signal, $\lambda_{MT}/2\pi$ as:

$$\sigma_\rho = \sigma_\phi \frac{\lambda_{MT}}{2\pi} \tag{4.37}$$

As an illustrative example, a 30 dBHz signal-to-noise ratio on the major tone with 0.1 Hz loop bandwidth would yield a 0.32 m ranging error. Doppler data noise, expressed in phase noise in radians, translates to range-rate noise via the following equation [117]:

$$\sigma_{\dot\rho} = \frac{\sqrt{2}c}{2\,G\,f_t\,t_c}\frac{\sigma_\varphi}{2\pi} \tag{4.38}$$

with c velocity of light, G transponder ratio, f_t, transmitted frequency, t_c, integration time, σ_φ phase noise in radians. Thus, the ratio of range and range-rate error, ζ, can be found by dividing Eq. 4.37 to 4.38:

$$\zeta = \frac{\sigma_\rho}{\sigma_{\dot\rho}} = \sqrt{2}\,G\,\frac{f_t}{f_{MT}}\,t_c \tag{4.39}$$

As an example for an S-band system, a 1 m ranging error would be equal to 0.3 mm/s range-rate error with 1 s integration on the same ranging/Doppler unit.

Employing this Eq. 4.39, the comparison between range-only and range-rate-only navigation systems is feasible, offering a realistic framework for assessment. Now, Eq. 4.35 can be rewritten as:

$$\Xi_k^i = \frac{1}{\zeta}\left|\frac{H_\rho^i}{H_{\dot\rho}^i}\right| \tag{4.40}$$

where i represents the state number and k represents time step.

4.2. CRAMÉR-RAO LOWER BOUND

In the OD field, understanding how accurately a spacecraft state can be estimated is crucial, especially when assessing compliance with navigation requirements. The CRLB plays a pivotal role in this regard as it establishes a fundamental limit on the variance of any unbiased estimator [188]. This limit is determined by the Fisher information matrix and quantifies the best attainable accuracy for estimating a parameter given a set

of observations. Importantly, this lower bound can be used as a tool for assessing the feasibility of meeting navigation requirements:

$$P_k \geq \mathscr{I}_k^{-1} \tag{4.41}$$

This study focuses on the SST-based OD and state estimation systems, emphasizing real-time state estimation. Consequently, the Fisher information matrix is given here within the context of a sequential filter, and is represented as follows [109]:

$$\mathscr{I}_k = (\Phi(t_k, t_{k-1}) \mathscr{I}_{k-1}^{-1} \Phi^T(t_k, t_{k-1}))^{-1} + H_k^T R_k^{-1} H_k, \qquad \mathscr{I}_0 = P_0^{-1} \tag{4.42}$$

It is worth noting that this equation shares similarities with Eq. 4.2. Here, the total information at the current time is equal to the sum of previous information (first part of Eq. 4.42) and the new information available at t_k (second part of Eq. 4.42). This differs from Eq. 4.2, where information at each time step is mapped back to the initial epoch t_0.

A particularly useful metric for performance analysis in this context is the mean RSS CRLB, which offers a comprehensive measure of the system's uncertainty in both position and velocity states over a specified time frame. This metric, by averaging the position and velocity state uncertainties RSS($\sqrt{\text{diag}(P_{pos/vel})}$), reflects the average maximum uncertainty attainable across both spacecraft in the formation. It thus captures the system characteristics, influenced by various factors, including orbital dynamics (Φ), observation (H) type, geometric configuration, measurement precision (R), and observation interval.

4.3. MONTE CARLO ANALYSIS

The Monte Carlo Analysis serves as a pivotal performance evaluation method, particularly suited for the complexities inherent in navigation systems design. This computational technique, through its reliance on random sampling and iterative simulations, offers a robust mechanism for conducting sensitivity and probabilistic analyses. It is useful in situations where analytical solutions are difficult to obtain. Within the scope of this study, Monte Carlo simulations are employed to assess estimation errors in each kth time step, for the Nth simulation. The RMS true estimation error is calculated using the following equation:

$$RMSE_k = \sqrt{\frac{1}{N} \sum_{i=0}^{N} (\mathbf{x}_k - \hat{\mathbf{x}}_k)(\mathbf{x}_k - \hat{\mathbf{x}}_k)^T} \tag{4.43}$$

where $\mathbf{x}_k$ and $\hat{\mathbf{x}}_k$ represent true state vector and estimated state vector, respectively. In addition to the estimation error, i.e., $\Delta\mathbf{e} = \mathbf{x}_k - \hat{\mathbf{x}}_k$, the difference between true state, $\mathbf{x}_k$ and nominal orbit, $\bar{\mathbf{x}}_k$, can be calculated in a similar way, representing actual state deviation, i.e., $\Delta\mathbf{x}_k = \mathbf{x}_k - \bar{\mathbf{x}}_k$. A typical Monte Carlo simulation framework for OD accuracy assessment can be seen in Figure 4.3. It should be noted that the selection of the number of simulations hinges on the desired level of confidence in the analysis results.

4.4. OTHER TECHNIQUES

Beyond the methodologies already explored, the study incorporates additional analysis techniques to assess the accuracy of the system estimation.

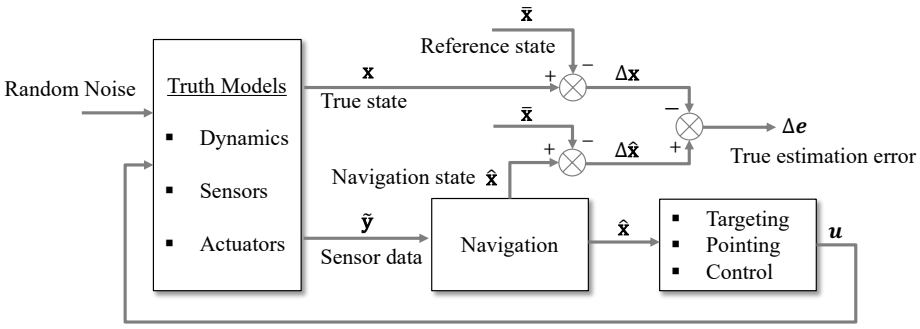

Figure 4.3: A typical Monte Carlo simulation framework for orbit determination accuracy assessment [189].

In this context, covariance and consider covariance analyses provide insights into the estimation algorithms performance and the impact of the various parameters on the OD process. Among these, covariance and consider covariance analyses stand out as instrumental in analyzing the performance of estimation algorithms and their sensitivity to various OD parameters.

The covariance analysis delves into the process of analyzing the covariance matrices associated with the estimated parameters and variables. It provides insights into the uncertainties and correlations between the estimated states. These covariance matrices are usually computed during the estimation process, as detailed in section 3.3.3. It is worth noting that representing the estimation uncertainty in the multi-spacecraft system can be a challenging task. The following metric can be used to compute the length of the largest axis of the error ellipsoid representing the uncertainty in the state estimation:

$$\beta_i = 3\max(\sqrt{\lambda}_j) \tag{4.44}$$

where λ_j for $j = 1,2,3$ are the eigenvalues of $P_{i_{3\times3}}$ representing the position and velocity sub-matrices and the average value of the N spacecraft system.

$$\beta_{ave} = \frac{1}{N}\sum_{k=1}^{N}\frac{1}{n}\sum_{i=1}^{n}\beta_i \tag{4.45}$$

where n is number of β values during the simulation. Considering a formation formed by N spacecraft, average value β_{ave} can be calculated over their $\bar{\beta}$ values.

The consider covariance analysis, on the other hand, focuses on the influence of systematic errors on the OD process, errors that remain unaffected by the volume of collected data [117]. Systematic errors limit the achievable OD performances, necessitating a thorough assessment to evaluate the system's accuracy realistically. A sequential approach to consider covariance analysis, detailed in the study (see Section 3.3.3), offers a framework for evaluating these impacts systematically.

Together with filtering results, covariance analyses provide an assessment of the accuracy and consistency of the state estimation.

4.5. DISCUSSION ON PERFORMANCE METRICS

The previous sections of this chapter have introduced a variety of performance analysis tools crucial for evaluating SST-based OD capabilities. A brief summary of these methods is provided in Table 4.1. Each tool is designed to meet specific system design needs, with some tools potentially overlapping in functionality. For instance, observability analysis offers valuable insights into estimation performances by highlighting the accuracy potential of OD solutions in highly observable systems. Similarly, the CRLB sheds light on the optimal performance achievable by an estimation filter, serving as a theoretical limit for the OD performance. Understanding the suitable application context for each method is essential, as is recognizing any limitations that could influence the system performance. The following paragraphs of this section provide insights into these aspects.

Table 4.1: A summary of performance analysis methods

Method	Description	Key equations
Observability Analysis	Observability Gramian	$N = \sum_{k=1}^{l} \Phi(t_k, t_0)^T \tilde{H}_k^T \tilde{H}_k \Phi(t_k, t_0)$
	Information Matrix	$\mathscr{I} = \sum_{k=1}^{l} \Phi(t_k, t_0)^T \tilde{H}_k^T R_k \tilde{H}_k \Phi(t_k, t_0)$
	Degree of Observability	$\gamma = \frac{n}{\mathrm{Tr}[N(\bar{1}_k^1]}$
	Unobservability index	$CN(N) = \frac{\Sigma_1}{\Sigma_{12}}$ where $N = \mathrm{U}\Sigma\mathrm{V}^T$
	Observation type comparison	$UOI(N) = \frac{1}{\Sigma_{12}}$
		$\Xi_k^i = \frac{1}{\zeta} \left\lvert \frac{H_\rho^i}{H_\rho^j} \right\rvert$
Cramér-Rao Lower Bound	Sequential processing	$\mathscr{I}_k = (\Phi(t_k, t_{k-1}) \mathscr{I}_{k-1}^{-1} \Phi^T(t_k, t_{k-1}))^{-1} + H_k^T R_k^{-1} H_k$
Monte Carlo Analysis		$RMSE_k = \sqrt{\frac{1}{N} \sum_{i=0}^{N} (\mathbf{x}_k - \hat{\mathbf{x}}_k)(\mathbf{x}_k - \hat{\mathbf{x}}_k)^T}$
Covariance Analysis	Covariance Matrix Consider Covariance Matrix	see Section 3.3.3

Observability, particularly in the context of SST-based OD, is closely linked to system performance, with specific orbital configurations and observation geometries playing a pivotal role in determining overall estimation accuracy. Observability analysis varies in approach, from investigating the observability Gramian to determine system observability at specific times, along with observable state or state combinations. It is possible to analyze any system analytically in this way. However, in certain cases, orbital dynamics are modeled based on high-fidelity dynamics, including gravitational accelerations based on spherical harmonics, solar radiation pressure, and other relevant models. In this case, it is quite challenging to perform analytical analysis, leading a numerical analysis to be conducted. However, analytical analysis can be straightforward in simpler scenarios, such as those assuming a single point mass gravitational source, especially for an interplanetary cruise phase of a satellite formation. In addition, a semi-analytical approach can be performed, blending analytical derivations with numerical solutions to deal with the complexity of real-world applications.

Regardless of the chosen approach, examining the eigenvalues of the observability matrix provides insights into the system's characteristics. Comparing various orbital configurations through their eigenvalues provides crucial information, enabling system optimization for specific mission requirements. For instance, in an SST-based OD framework involving a two-spacecraft formation, the focus may be on accurately

navigating only one of the spacecraft for scientific purposes. This narrows the interest to six states, position and velocity, of the relevant spacecraft, guiding optimization of orbital design or tracking intervals accordingly. Moreover, certain mission configurations might necessitate accurate estimation of only a subset of states, such as position and velocity in the along-track direction. It is important to note that while eigenvalue analysis enables comparison across different configurations or within states themselves, it does not provide knowledge on whether navigation requirements will be met.

When it comes to representing findings in OD performance analysis, CN and UOI emerge as significant metrics, each with its distinct advantages and limitations. The CN, defined as the ratio of the highest eigenvalue to the lowest one in a system, serves as a crucial metric but comes with notable limitations. One significant drawback is its inability to account for states not directly related to the eigenvalues being considered. This can lead to scenarios where systems with identical CNs exhibit different estimation performances due to the distribution of intermediate eigenvalues, either being placed towards the highest or the lowest eigenvalue, thus affecting overall system observability and estimation accuracy. Moreover, the CN's reliance on the ratio of eigenvalues implies it may increase over time. Conversely, the UOI, which tends to decrease over time, offers a distinct perspective by focusing on the system's least observable state but falls short in providing a comprehensive view of the system's other states. Nonetheless, UOI can be particularly useful in scenarios where system requirements necessitate all states exceed a certain observability threshold. Similar to this, a CN threshold can be defined for a given problem. For instance, SST-based OD within CRTBP requires CN to be less than 1×10^{16} for the problem to be observable [11]. Both CN and UOI metrics have been thoroughly examined in Chapter 5, underscoring their value at the system design level. It is crucial to recognize that relying on a single metric may result in misleading conclusions; thus, a comprehensive analysis that includes both CN and UOI is recommended to gain a full understanding of system observability.

Observability analysis extends beyond these metrics, enabling comparisons across different navigation data types and orbital configurations as introduced in this chapter and presented corresponding results in Chapter 5. For instance, different orbital configurations can be compared by searching the optimal CN, UOI, or a similar metric providing information on the degree of observability. Such analysis is vital when designing orbits for satellite formations consisting of two or more spacecraft, where the objective often includes maximizing the observability of the system. Despite the utility of these metrics, the information matrix-based approaches offer a similar, weighted assessment of the observability. The inverse of the information matrix is essential in deriving the CRLB.

The CRLB stands out by quantifying the minimum estimation uncertainty attainable by a filter for a given system configuration, thereby providing a limit for the highest potential estimation performance, as discussed in the previous sections. CRLB derived metrics are particularly valuable as they directly indicate the feasibility of meeting specific system requirements. Prior to the development of any filter, a thorough assessment of the CRLB is essential, ensuring that the designed filter is capable of achieving the desired performance levels. As such, CRLB not only serves as a measure of potential filter performance but also bridges the gap between system observability and filter perfor-

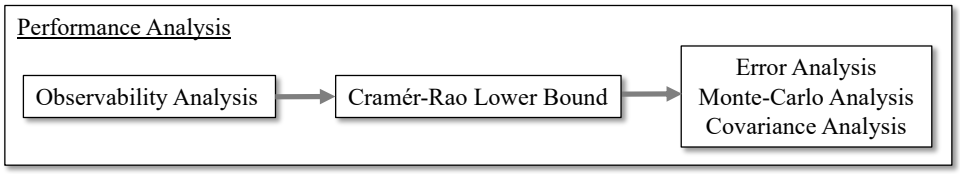

Figure 4.4: Performance Analysis Framework, highlighting that observability analysis provides insights into the system at hand, estimations shed light on expected OD performances, and CRLB bridges the gap between observability and filter performances.

mance (see Figure 4.4). This approach is applied extensively and discussed in Chapter 5.

Regardless of a system's observability, understanding the expected performance of the filter is essential. A suboptimal filter design could result in estimation outcomes that fall short of expectations. Here, Monte-Carlo simulations play a critical role by offering statistical insights into the expected filter performance across various system configurations. This method is particularly effective for examining the sensitivity of filter parameters, such as the adaptability of the measurement noise covariance matrix. Although beneficial, the main drawback of this method is its computational intensity and the necessity for a substantial number of runs to obtain statistically significant results, a process detailed in Chapter 5. Determining a number of runs for meaningful statistical outcomes remains a challenge, particularly within OD contexts, yet assessing estimation error variations across multiple simulations can be one of the possible ways.

Covariance analysis offers a straightforward alternative, providing expected estimation values without necessitating extensive simulations. While it primarily reflects estimation uncertainty rather than estimation error, the necessity for Monte-Carlo simulations for detailed accuracy assessment remains. An advantage of covariance and its variants, e.g. consider covariance analysis, is the ability to evaluate the impact of systematic errors on performance, facilitating the optimization of design parameters, such as orbital configurations or tracking intervals for satellite formations. For instance, Chapter 6 applies these insights, utilizing Particle Swarm Optimization (PSO) to optimize tracking windows.

In brief, Table 4.2 summarizes the advantages and disadvantages of each approach, highlighting their applications throughout the study. It underscores the critical role these methodologies play in evaluating and enhancing system performance for SST-based OD applications.

Table 4.2: A brief summary of performance analysis methods along with the advantages and disadvantages of each approach, highlighting their applications throughout the study.

Method	Advantages	Disadvantages	Applications
Observability Analysis	+ Provides insights into whether the system states can be accurately estimated. + Helps in identifying observable and unobservable states, guiding system design and sensor placement. + Can be used to compare different orbital configurations and their impact on the system's performance. + Can be used to optimize orbital configurations, tracking windows for satellite formations.	- Analytical approaches may not be feasible for complex systems with high-fidelity dynamics requiring numerical methods. - Does not provide absolute assurance of meeting navigation requirements. - Relying solely on either the CN or UOI may not provide a full understanding of the system observability, requiring a combined evaluation of both metrics.	See Section 4.1, 5.1, 5.5
Cramér-Rao Lower Bound	+ Offers a theoretical limit for the lowest possible estimation uncertainty, aiding in filter design. + Directly indicates the feasibility of meeting specific system requirements. + Useful for comparing the potential performance of different estimation filters.	- Provides a lower bound on variance, which might not always be achievable in practice.	See Section 5.1, 5.2, 5.6
Monte-Carlo Analysis	+ Provides statistical insights into expected estimation performance under various conditions. + Useful for assessing the sensitivity of filter parameters and their impact on filter performance. + Can simulate real-world scenarios and account for random errors and uncertainties.	- Computationally intensive, requiring a significant number of simulation runs for statistical significance. - Determining the adequate number of runs for meaningful outcomes can be challenging.	See Section 5.2, 5.3, 5.4,
Covariance Analysis	+ Offers an assessment of estimation uncertainty without the need for extensive simulations. + Can evaluate the impact of systematic errors on estimation performance. + Useful for preliminary filter performance evaluation and design optimization. + Directly indicates the feasibility of meeting specific system requirements.	- Does not directly provide estimation accuracy, only the expected uncertainty.	See Section 5.1, 5.2, 5.4, 5.5, 5.6, 5.7, 6.1

4.6. SUMMARY

This chapter provided a comprehensive introduction to the main performance analysis methods used in this dissertation. First, the concept of observability is given along with definitions and observability criteria. Thereafter, observability Gramian, information matrix, degree of observability, and unobservability index are presented. A semi-analytical observability analysis for the SST-based OD problem within the CRTBP is provided, including analytical derivations for measurement sensitivity and Gramian matrices, along with the corresponding CRLB. Additionally, the chapter introduced how to compare observation data types from the observability perspective. The introduction of Monte Carlo simulations and covariance analysis as pivotal tools for performance evaluation underscores the chapter's comprehensive approach to system analysis. Lastly, the chapter extends to a critical evaluation of performance metrics, discussing their advantages and disadvantages and underscoring their relevance across the study.

Addressing the third research question—How can we describe the fundamental aspects and design principles of a SST-based OD system for satellite formations in deep space?—this chapter aimed to answer the first sub-part of this research question (3.a): -Provide system performance analysis techniques-. This chapter undertakes a detailed exploration of these methods and sets a solid foundation for the subsequent chapter, which aims to delve into the rest of the research question on how various factors—such as orbital configuration, dynamical environment and errors, measurement geometry, accuracy, precision, and interval, as well as considerations like clock bias, drift, aging, navigation filter selection, design, parameters, number of spacecraft, and network topology—affect overall system performance.

5

AUTONOMOUS NAVIGATION PERFORMANCE FOR SATELLITE FORMATIONS IN DEEP SPACE

This chapter presents a comprehensive analysis on Satellite-to-Satellite Tracking (SST)-based Orbit Determination (OD) for satellite formations across various conditions. It extensively covers the three main core elements of OD: dynamics, measurements, and estimation, offering insights into the details of each aspect. The initial focus is on performance analysis within the two-body problem, addressing the sensitivity of orbital parameters and observation data types. Subsequently, the chapter delves into the three-body problem, investigating the dynamics of the OD process. It then proceeds to examine measurement effects, including errors and various strategies to handle measurement bias and clock parameters. The relationships between OD performance and observation SST data types are outlined, along with filtering performances. In addition, the chapter offers a detailed analysis of a realistic lunar mission scenario and further provides lunar network topologies, such as mesh and centralized architectures, for three or more satellite formations. The chapter concludes with an analysis of a small celestial body scenario and an interplanetary cruise phase of a formation, covering specific aspects of the OD problem.

Parts of this chapter have been published in:
E. Turan, S. Speretta, and E. Gill, "Performance analysis of crosslink radiometric measurement based autonomous orbit determination for cislunar small satellite formations", *Advances in Space Research*, vol. 72, no. 7, pp. 2710–2732, Oct. 2023. DOI: 10.1016/j.asr.2022.11.032
E. Turan, S. Speretta, and E. Gill, "Performance analysis of radiometric autonomous navigation for lunar satellite network topologies", English, 11th International Workshop on Satellite Constellations and Formation Flying,, IWSCFF2022 ; Conference date: 07-06-2022 Through 08-06-2022, 2022
E. Turan, S. Speretta, and E. Gill, "Radiometric autonomous navigation for cislunar satellite formations", English, Presented at the NAVITEC 2022 conference; NAVITEC 2022 ; Conference date: 05-04-2022 Through 07-04-2022, 2022
E. Turan, S. Speretta, and E. Gill, "Autonomous Crosslink Radionavigation for a Lunar CubeSat Mission", *Frontiers in Space Technologies*, vol. 3, pp. 1–12, Jun. 2022. DOI: 10.3389/frspt.2022.919311

This chapter offers an extensive analysis of SST-based autonomous OD performance, spanning various orbital regimes, scenarios, and measurement methods, along with various aspects of navigation parameters. Initially, it highlights various orbital dynamic configurations, shedding light on their impacts, followed by a detailed exposition of filtering performances. Subsequently, it provides an analysis presenting the impact of systematic and random errors on the OD performance. This is followed by a detailed exploration of network topologies, encompassing both mesh and centralized configurations. Lastly, the chapter provides an insightful evaluation of SST-based OD performance, both in the proximity of a small celestial body and during interplanetary cruises.

5.1. DYNAMICAL CONFIGURATIONS

In this section, various orbital dynamic configurations are studied. To begin, SST-based OD within the two-body problem is introduced, shedding light on its performance and applicability. Notably, CRLB is studied in the context of the two-body problem as well as a high-fidelity dynamic model, providing valuable comparative results. Subsequently, the section presents notable OD performances in the three-body problem, highlighting a range of orbital configurations that offer insights into performance from both observability and OD perspectives.

5.1.1. ORBIT DETERMINATION WITHIN THE TWO-BODY PROBLEM

In classical mechanics, the two-body problem refers to a simplified scenario in which two-point masses, typically a larger central body and a small orbiting body, interact solely through their gravitational forces. As explained in the previous chapter, SST-based absolute OD within a two-spacecraft formation is not a fully observable system under the two-body dynamics. Various two-body orbital configurations have been studied in [108] for the range-only and in [111] for the angle-only cases, respectively. To illustrate the functioning of SST-based OD in near-Earth and deep space scenarios, an analysis of its operation within the two-body dynamics is presented first since it serves as a foundation for understanding more complex dynamics, such as N-body dynamics and perturbed orbits. For this purpose, a simplified case is presented where two spacecraft orbit around the primary, Earth in this case, under two-body dynamics. It is known from previous studies [11], [108] that similar orbital parameters among satellites in a formation can significantly impact observability and consequently estimation performance. Hence, this analysis involves changing the orbital parameters of one spacecraft to identify which orbital parameter affects the system more than the other. Considering a specific orbital configuration for the chief spacecraft characterized by a circular orbit with a semi-major axis of $a = 7000$ km and an inclination of $i = 50$ deg, while other orbital elements are set to zero, Table 5.1 represents the observability metrics, CN and UOI, and the average position and velocity CRLB 1σ uncertainty (RSS), i.e., $\bar{\sigma}_r$ and $\bar{\sigma}_v$, for three different observation cases and various orbital configurations. The general case given represents the baseline scenario where two satellites are on the same orbital plane, sharing identical sizes, shapes, and orientations. Here, different size, inclination and shape represent a different orbital element for one of the node in the formation each time as 10 000 km, 30 deg, 0.2, respectively. In addition, mean anomalies are not identical in all

Table 5.1: The SST-based absolute OD performance within the two-body problem. CN and UOI stand for condition number and unobservability index, respectively. Averaged position and velocity uncertainties $\bar{\sigma}_r$ and $\bar{\sigma}_v$ are based on values after the converged phase.

Orbital configurations	**Observation type**	**CN**	**UOI**	$\bar{\sigma}_r$ [m]	$\bar{\sigma}_v$ [m/s]
General case	Range-only	1.15×10^{22}	4.59×10^{11}	4.15×10^{4}	44.73
	Range-rate only	6.35×10^{21}	6.26×10^{16}	3.95×10^{5}	425.79
	Angle only	1.39×10^{17}	1.07×10^{20}	1.87×10^{5}	202.36
Different size, $a_1 \neq a_2$	Range-only	5.41×10^{20}	9.72×10^{9}	4.11×10^{3}	3.38
	Range-rate only	1.86×10^{21}	2.10×10^{16}	4.08×10^{3}	3.37
	Angle only	7.27×10^{8}	7.06×10^{11}	493.09	0.40
Different inclination, $i_1 \neq i_2$	Range-only	7.07×10^{16}	3.12×10^{6}	256.97	0.27
	Range-rate only	6.80×10^{17}	8.23×10^{12}	257.08	0.27
	Angle only	6.23×10^{9}	6.07×10^{12}	636.95	0.65
Different shape, $e_1 \neq e_2$	Range-only	1.79×10^{33}	3.05×10^{11}	6.15×10^{3}	6.97
	Range-rate only	4.01×10^{33}	7.70×10^{16}	2.58×10^{3}	2.74
	Angle only	3.29×10^{20}	2.10×10^{11}	500.58	0.50
All different	Range-only	8.75×10^{10}	1.32	199.07	0.15
	Range-rate only	1.57×10^{11}	1.13×10^{6}	199.08	0.15
	Angle only	4.44×10^{8}	5.95×10^{11}	454.75	0.37

these cases. In this analysis, simulation parameters are set to 10 km position and 10 m/s velocity initial uncertainty (1σ), and 1 days of simulation duration, along with 180 sec measurement interval.

Table 5.1 provides a comprehensive overview of the impact of various orbital configurations and observation types on system performance. Typically, orbital planes can be different (non-coplanar, $i_1 \leq i_2$), or with different sizes ($a_1 \leq a_2$), or with different shapes ($e_1 \leq e_2$). Furthermore, these configurations can be further expanded by considering additional factors, such as the relative orientation of the orbital planes, which are described by the difference of longitude of ascending nodes, argument of periapsides, and inclinations within the two spacecraft formation. Circular orbits with different size and shape can also be integrated into these setups. Additionally, sensor fusion has the potential to expand the current configuration as typically range and range-rate data are collected together. However, representing these combinations and their corresponding results is not a trivial task, hence the table focuses on relatively concise configurations. Notably, the key finding here is that differences in orbital dynamics tend to improve system observability, consequently leading to reduced estimation uncertainty, aligning with findings from earlier research [108], [111]. Specifically, considering these orbital configurations, the most dominant effect is due to the inclination and thereafter orbital shape and size regardless of the observation type used.

To assess the impact of orbital size and shape along with various data types on system performance within the two-body problem, a simulation was performed exploring varying values within the range 6750 km< a <35 000 km and 0< e <0.5. Figure 5.1 shows the results for the three different observation data-type cases. Specifically, in the case of the Earth-orbiting scenario within the two-body problem, SST range and range-rate data show lower sensitivity to changes in altitude, while inertial angle measurements showed a marked increase in sensitivity to altitude variations. Remarkably, the data suggested

that the orbital shape (eccentricity) had a negligible influence on the OD performance, varying SST data types, with a slight performance enhancement noted as eccentricity increased.

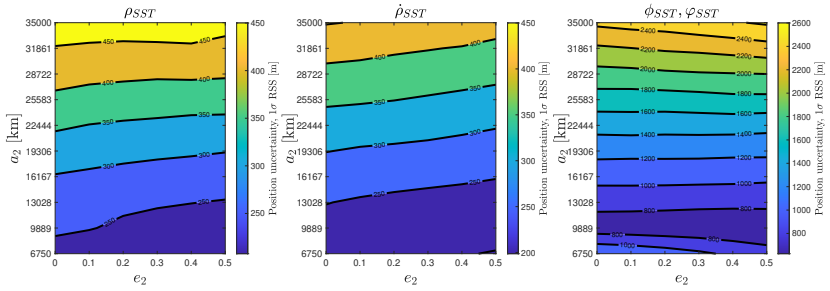

Figure 5.1: CRLB position uncertainty (1σ RSS) based on various relative orbital and observation configurations. ($a_1 = 6750\,\text{km}$, $e_1 = 0.1$)

5

Further exploration into the importance of including perturbations in the model for enhanced system observability involved a comparative analysis between the simplistic two-body dynamic model and a high-fidelity model incorporating perturbations such as SRP and gravitational effects from other celestial bodies, notably the Sun and the Moon. As depicted in Figure 5.2, the analysis conclusively showed that the incorporation of these perturbations significantly improves system observability, thus reducing estimation uncertainty. Particularly, Figure 5.3 underscores the notable improvements in estimation accuracy that high-fidelity dynamics offer over the simplified two-body scenario. The simulations revealed enhancements in position estimation accuracy by factors ranging from 1.6 to 2.8, with even more pronounced improvements—up to sevenfold—observed post-convergence phase. These benefits were especially evident in scenarios involving highly elliptical orbits or large inter-satellite distances, where the differences in dynamics provide useful information to the navigation filter. In conclusion, the findings highlight several key insights:

- Non-coplanar configurations significantly outperform coplanar ones, with orbital sizes and shapes playing crucial roles.
- SST range and range-rate data show lower sensitivity to altitude changes compared to inertial angle data. All observation types showed minimal sensitivity to changes in orbital shape.
- Incorporating perturbations into the two-body dynamics model significantly lowers estimation uncertainty, typically yielding at least a twofold improvement in performance.

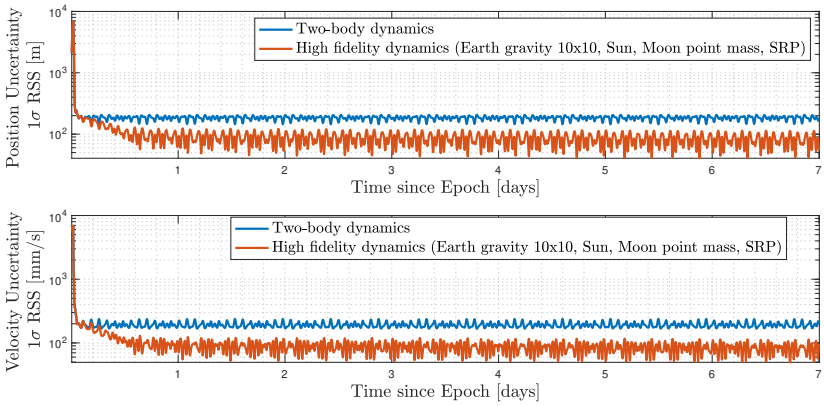

Figure 5.2: CRLB uncertainty (1σ RSS) for two-body and high-fidelity dynamics, including range-only measurements, representing more useful information that the high-fidelity dynamical case can collect. Note that CRLB is given here within a sequential filter, representing the limit of a real-time estimation.

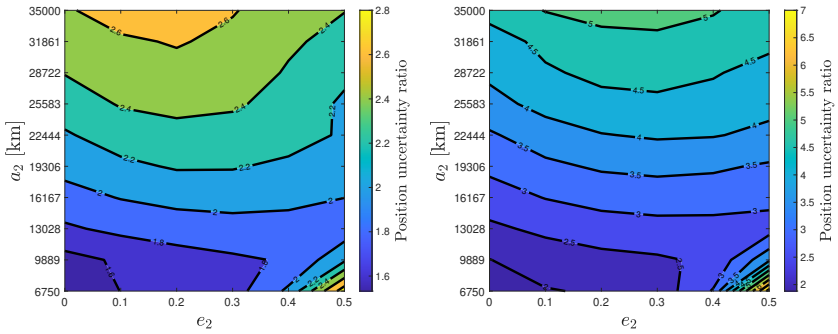

Figure 5.3: Ratio of the CRLB uncertainties (1σ RSS) for two-body and high-fidelity dynamical cases (Range-only measurements). Left: Uncertainty averaged across the entire simulation duration. Right: Uncertainty averaged post-convergence phase. Comparing these left and right figures provides insights into the convergence speed.

5.1.2. ORBIT DETERMINATION WITHIN THE THREE-BODY PROBLEM

This section delves into the SST-based OD problem within the context of the three-body problem, which involves the dynamic interaction of three bodies influenced by their gravitational forces. Building upon the prior research on SST-based OD in the three-body problem, this section extends the current understanding of the OD problem, offering valuable insights into its performance from both the observability and estimation perspectives through the CRTBP.

In this comprehensive analysis, 16 distinct orbital configurations are meticulously examined. These configurations encompass a variety of orbits, such as southern and northern Halo orbits at both L1 and L2 Lagrangian points, Lyapunov orbits around these points, and specific Lunar orbits, including elliptical and polar-circular trajectories. The

inclusion of two non-coplanar orbits between L1 and L2 Halo points underscores the diverse range of scenarios considered, providing a broad spectrum of data for observability and estimation performance evaluation. Notably, coplanar orbits are excluded from this study due to their potential influence on system observability and the OD performance.

Each of the highlighted orbital configurations, as depicted in Figure 3.7 and initial conditions given in Table 3.7 (see Chapter 3), contributes uniquely to the analysis. Among these, the Lunar elliptical orbit closely reflects the orbital parameters of the upcoming Lunar Pathfinder mission, with an inclination of 57 deg, a semi-major axis of 5735 km, and an eccentricity of 0.61. Furthermore, a polar-circular orbit has been investigated with a 95 deg inclination and a 5735 km semi-major axis. The detailed series of 120 simulation scenarios across all possible pairwise combinations of these orbits facilitates a deep dive into each specific case, considering a-priori covariance matrix with an assigned 1 km position and 1 m/s velocity 1σ uncertainty for each state component.

Table 5.2: Position uncertainty (1σ) RSS CRLB, [m], averaged after post-convergence.

	L2 Southern Halo.a	L2 Southern Halo.b	L2 Northern Halo.a	L2 Northern Halo.a	L1 Southern Halo.a	L1 Southern Halo.b	L1 Northern Halo.a	L1 Northern Halo.a	Lunar Elliptical	Lunar Polar Circular	L2 Southern NRHO	L1 Southern NRHO	L2 Northern NRHO	L1 Northern NRHO	L2 Lyapunov	L1 Lyapunov
L2 Southern Halo.a		45.54	1.03e6	40.81	19.23	31.95	41.47	53.50	0.69	0.60	1.79	2.37	1.21	4.29	10.47	13.98
L2 Southern Halo.b			40.81	1.51e7	15.34	23.38	35.73	46.73	0.64	0.59	1.91	2.24	1.26	3.34	9.98	10.70
L2 Northern Halo.a				45.54	41.47	53.50	19.23	31.95	0.73	0.62	1.21	4.29	1.79	2.37	10.47	13.98
L2 Northern Halo.b					35.73	46.73	15.34	23.38	0.70	0.60	1.26	3.34	1.91	2.24	9.98	10.70
L1 Southern Halo.a						115	1.87e5	33.61	0.54	0.54	2.08	5.56	1.96	2.58	9.13	7.01
L1 Southern Halo.b							33.61	3.86e5	0.53	0.54	1.95	4.78	1.73	2.56	7.42	7.84
L1 Northern Halo.a								115	0.58	0.53	1.92	2.58	2.08	5.56	9.13	7.01
L1 Northern Halo.a									0.60	0.53	1.73	2.56	1.95	4.78	7.42	7.84
Lunar Elliptical										4.19	0.96	1.90	1.03	1.85	10.08	12.56
Lunar Polar Circular											0.96	1.70	0.96	1.73	14.69	20.58
L2 Southern NRHO												0.92	1.32e7	3.45	3.50	3.17
L1 Southern NRHO													3.45	9.20e5	5.33	3.23
L2 Northern NRHO														0.92	3.50	3.17
L1 Northern NRHO															5.33	3.23
L2 Lyapunov																1.71e5
L1 Lyapunov																

Table 5.2 highlights that optimal performance is achieved when the satellite formation is composed of lunar orbiters, particularly those in lunar elliptical orbits. When comparing SST between halo-to-halo orbital configurations and lunar-halo cases, it becomes evident that the latter offers significantly more accurate results. This can be attributed to lunar orbiters having shorter orbital periods, which in turn facilitates superior observation geometry, enabling data collection along all axes within a shorter time frame.

In halo orbital configurations, when orbiting at different Lagrangian points, having similar orbital orientations (e.g., southern halo) leads to enhanced accuracy. On the contrary, for orbiters placed around the same Lagrangian points, different orbital orientations yield more accurate results. Notably, tracking between Lyapunov orbits does not yield a fully observable system due to the lack of out-of-plane motion.

Furthermore, a general trend emerges, indicating that larger inter-satellite separations provide an increased accuracy. Further details regarding the selected orbital configurations and their corresponding observability and estimation uncertainty results are

Table 5.3: Selected orbital configurations and corresponding OD performances. Values given in parenthesis represent the averaged ones after half of the simulation. CN, UOI, and CR stand for condition number, unobservability index, and convergence ratio, respectively.

Chief	Deputy	CN	UOI	CR	$\bar{\sigma}_r$ [m]	$\bar{\sigma}_v$ [m/s]
EML2 Northern Halo.a	Lunar Elliptical	1.49×10^{7}	1.1×10^{-2}	99.97	86 (0.918)	0.010 (4.19×10^{-5})
EML1 Northern Halo.a	Lunar Elliptical	3.14×10^{7}	7.9×10^{-4}	99.97	122 (0.745)	0.010 (4.43×10^{-5})
EML1 Northern Halo.a	Lunar Circular	3.21×10^{7}	8.2×10^{-4}	99.97	151 (0.679)	0.011 (3.57×10^{-5})
EML1 Northern Halo.a	EML1 Northern NRHO	1.12×10^{8}	4.6×10^{-3}	99.94	6835 (11.053)	0.092 (6.91×10^{-5})
EML1 Northern Halo.a	EML2 Northern Halo.b	8.26×10^{8}	1.6×10^{-2}	99.77	6866 (25.464)	0.097 (1.80×10^{-4})
EML2 Northern Halo.a	EML2 Northern Halo.b	1.18×10^{9}	8.3×10^{-1}	98.92	17775 (72.892)	0.152 (4.47×10^{-4})
EML2 Northern Halo.a	EML1 Lyapunov	4.67×10^{8}	2.4×10^{-1}	99.74	9045 (23.758)	0.097 (1.42×10^{-4})

presented in Table 5.3. It is important to highlight that the analysis includes averaged values across the whole simulation as well as post-convergence averages. This approach helps to get some insights into the convergence rate of the system. For example, when the post-convergence performances appear similar but the overall simulation averages differ significantly, it suggests that the system with the larger average over the entire simulation exhibits a slower rate of convergence. This detail is particularly critical in mission scenarios where tracking opportunities are limited, necessitating rapid convergence to meet operational demands. It is also worth noting that a smaller CN and UOI is preferable to a lower value. However, when comparing formations consisting of both halo and lunar elliptical orbits (i.e. EML2 Halo to Lunar and EML1 to Lunar), a situation is observed where one case provided a lower CN, while the other yielded a lower UOI. This shows that the least observable state has a higher uncertainty in the EM2 Halo-Lunar case than the EML1 Halo-Lunar case, suggesting that relying solely on the CN or UOI for evaluating system performance can be misleading, emphasizing the necessity to consider both observability metrics. Furthermore, the Convergence Ratio (CR) metric should be interpreted with caution, as state uncertainty may fluctuate over time, and comparing uncertainty at the end of the simulation with the one at the beginning can potentially yield misleading information. As discussed in Chapter 4 and considering the analysis given in this section, different metrics may be applied, depending on the specific goals of the analysis, with observability metrics aiding in sensitivity analysis and the CRLB offering insights into the best achievable estimation performance.

Since the previous analysis consisted of limited Halo orbital configurations, a further investigation has been done, focusing on southern Halo orbits characterized by a Jacobi constant, C_j, between 2.99 and 3.15 within L_1 and L_2 points, as illustrated in Figure 5.4. This analysis, excluding northern Halo orbits due to similar performance outcomes, reveals that there has been a slight decrease in the estimation uncertainty around shorter periodic orbits (high Jacobi constant), as illustrated in Figure 5.5. What can be clearly seen in this figure is the continual decrease in the estimation performance towards longer periodic orbits (low Jacobi constant). In other words, system performance is likely to improve when the orbital out-of-plane amplitude is maximized. This is true for both northern and southern halo orbits, in line with previous studies [11].

The same analysis given above is performed for the SST scenario involving the Lunar elliptical orbiter and EM Southern Halo orbiters. Figure 5.6 reveals that there has been a gradual increase in the estimation uncertainty when the orbital out-of-plane ampli-

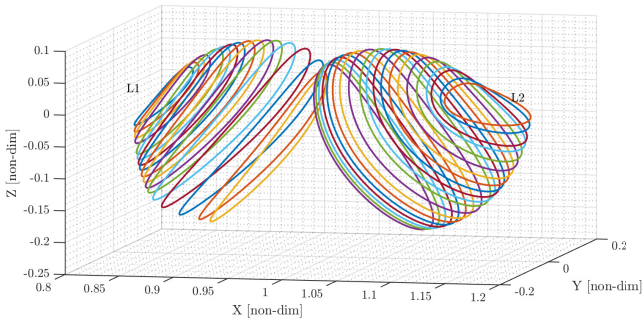

Figure 5.4: Orbital configurations for the EM Halo/Halo tracking scenario.

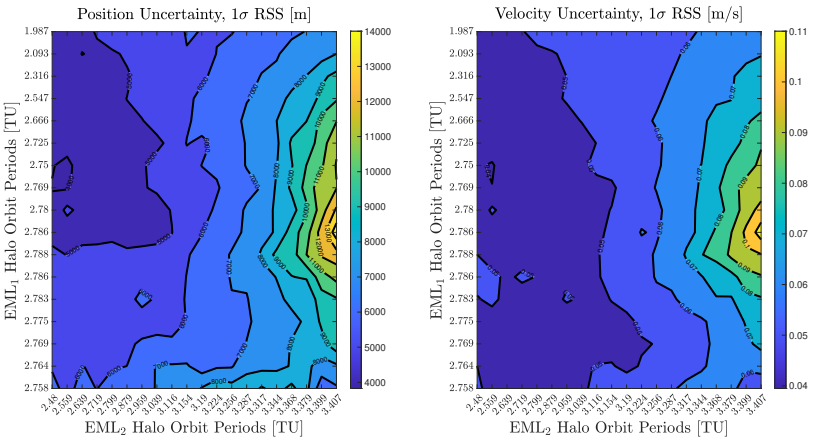

Figure 5.5: Estimated state uncertainty (1σ RSS) for the EM Halo/Halo tracking scenario.

tude tends to the maximum value. This suggests that large orbital separations could be beneficial for Halo/Lunar configurations.

In conclusion, the examination of SST-based OD within the three-body problem yields several key takeaways:

- A cislunar satellite formation consisting of a Lunar orbiter provides superior SST-based OD performance within the three-body problem.
- Proximity formations result in less accurate outcomes, while larger separations contribute to higher accuracy.
- Shorter periodic orbital configurations in the halo-only case yield lower estimation uncertainty.
- Satellite formations with distinct dynamic characteristics offer advantages for SST-based OD.

- Relying solely on the CN or UOI for evaluating system performance can be misleading, highlighting the necessity to consider both metrics.

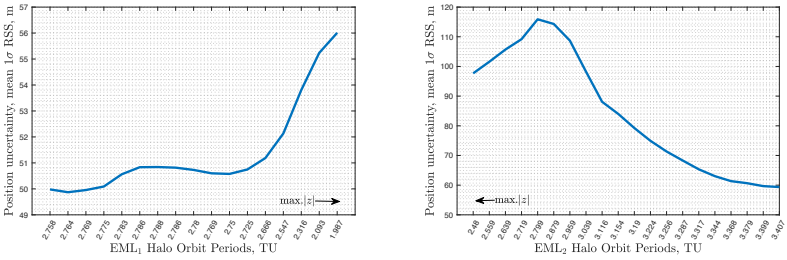

Figure 5.6: Estimated state uncertainty (1σ RSS) for the EM Halo/Lunar tracking scenario, highlighting that shorter periodic orbital configurations lead to reduced state uncertainty.

Thus far, this section has reviewed one of the key aspects of the SST-based OD problem: dynamical configurations. The findings have shed light on how various orbital setups influence OD performance within the two- and three-body problem providing valuable insights into observability and estimation uncertainties. However, a comprehensive understanding of the SST-based OD problem necessitates delving into another crucial aspect: the impact of measurements on the OD performance.

5.2. DATA TYPES AND THEIR ROLES IN ORBIT DETERMINATION

This section delves into the influence of observational data on OD performance, highlighting the critical role of measurement types and their accuracy. As previously emphasized, the CRLB stands as a direct reflection of the measurement type and its associated accuracy. In particular, the system's performance can be investigated in detail by analyzing CRLB with various measurement errors. Unsurprisingly, an increase in measurement error leads to a decrease in estimation performance. However, it is crucial to investigate the rate of this increase, as certain orbital configurations may exhibit higher sensitivity to measurement errors than others, limiting the applicability of certain SST techniques within specific scenarios. Furthermore, an essential aspect remains in identifying the most effective observation data type that provides optimal state estimation. Therefore, a comprehensive evaluation of the measurement is crucial in optimizing the overall performance and precision of the estimation process.

5.2.1. MEASUREMENT ERRORS

In this section, the focus shifts to analyzing the performance of SST-based autonomous OD systems under the influence of measurement errors, specifically examining range-only measurements. An extensive study across various orbital configurations reveals critical insights into how system performance fluctuates with measurement accuracy, as detailed in Table 5.4. A notable observation from this analysis is the significant impact of measurement errors on less observable orbital configurations (see the previous section), where uncertainty levels increase rapidly.

Table 5.4: The impact of varying measurement errors on orbit determination accuracy (Range-only scenario, CRLB analysis). The convergence rate indicates the trend derived from a linear regression analysis (Values in parentheses denote the performance metrics averaged post-convergence phase)

Chief	Deputy	Measurement Error	$\bar{\sigma}_r$ [m]	$\bar{\sigma}_v$ [m/s]	Slope
EML2 Southern Halo a.	Lunar Elliptical	1 m	83.55 (0.41)	0.0088 (2.45e-5)	0.34
		10 m	219.91 (4.10)	0.0153 (2.45e-4)	
		100 m	546.93 (34.79)	0.0266 (0.0023)	
EML1 Southern Halo a.	Lunar Elliptical	1m	54.45 (0.32)	0.0074 (1.78e-5)	0.26
		10 m	170.94 (3.25)	0.0154 (1.78e-4)	
		100 m	485.23 (27.25)	0.0352 (0.0017)	
EML2 Southern Halo a.	EML1 Southern Halo b.	1 m	6.03e3 (13.63)	0.0909 (8.37e-5)	2.39
		10 m	1.20e4 (65.54)	0.1377 (4.12e-4)	
		100 m	2.50e4 (263.82)	0.2185 (0.0015)	
EML2 Southern Halo a.	EML2 Southern Halo b.	1 m	1.51e4 (34.70)	0.1380 (1.77e-4)	6.76
		10 m	2.81e4 (150.55)	0.2140 (8.02e-4)	
		100 m	4.83e4 (728.31)	0.3479 (0.0036)	
Lunar Elliptical	EML2 Southern NRHO	1 m	71.48 (0.55)	0.0081 (2.20e-5)	0.30
		10 m	201.10 (5.17)	0.0146 (2.15e-4)	
		100 m	565.28 (31.73)	0.0292 (0.0019)	
Lunar Elliptical	EML2 Lyapunov	1 m	87.71 (6.21)	0.0083 (8.41e-5)	1.12
		10 m	227.65 (23.77)	0.0150 (3.66e-4)	
		100 m	618.16 (120.56)	0.0287 (0.0025)	

In contrast, systems with highly observable configurations, such as formations comprising EML1 and lunar orbiters, exhibit a lower sensitivity to high measurement errors. This suggests that even ranging systems with lower accuracy—like those utilizing data-aided ranging at reduced data rates—could be viable for missions with such advantageous orbital configurations. To quantify the sensitivity of these systems to measurement inaccuracies, the analysis presents the increase rate, which is calculated based on average position uncertainty from the converged OD solutions. This increase rate showcases a consistent trend across different metrics presented previously. Additionally, UOI could be an alternative to the increase rate provided in this section since it provides insights into states that are most vulnerable to limited observability, with the least observable state being affected the most by high measurement errors. In summary, this analysis underscores that:

- Satellite formations involving lunar orbiters exhibit a lower sensitivity to measurement errors, primarily due to their highly observable geometrical configurations.

UNDERWEIGHTED OR OVERWEIGHTED MEASUREMENT NOISE COVARIANCE

Another crucial consideration in the assessment of the navigation system relates to the potential impact of ill-conceived measurement noise, σ_{SST}, and thus the corresponding noise covariance matrix, R. This is expected to cause a degradation of navigation system performance, particularly in cases where SST relies on a ranging method characterized by high measurement errors. Thus, this part is conducted in response to the need to understand the system behavior in cases where the measurement noise covariance matrix is underweighted or overweighted. With this aim in mind, the noise covariance matrix is set to $\sigma_\rho^2 = (3\,\text{m})^2$, deviating from the actual measurement noise level of $1\sigma_\rho = 10\,\text{m}$, and the system response has been studied for a cislunar mission scenario (EML2 Halo-Lunar

formation). Notably, the AEKF showcases its adaptability and superior performance in accommodating these cases, as indicated in Figure 5.7. What stands out in Figure 5.7 is that AEKF provides superior performance over standard filters, as expected, while the miscalibrated filter exhibits noticeable fluctuations. Adaptive estimation of the measurement noise covariance matrix is given in Figure 5.8, representing an accurate solution.

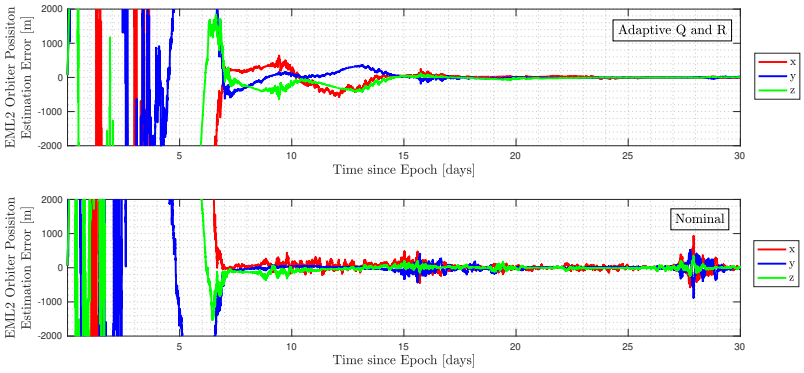

Figure 5.7: Contrast between adaptive estimation of measurement noise covariance and underweighted measurement noise covariance cases, demonstrating the superiority of adaptive estimation in achieving stable results.

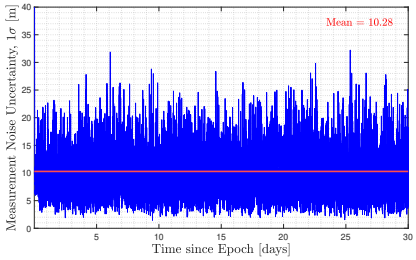

Figure 5.8: Adaptive estimation of the measurement noise uncertainty (range-only)

5.2.2. MEASUREMENT BIAS

The previous section has provided insights into measurement errors and corresponding impacts on the OD performance. In this section, the focus shifts to the critical consideration of measurement bias and its impact on system performance. This critical issue has been discussed in Section 3.3.3, outlining three bias handling strategies: neglected, estimated, and considered approaches within the context of the SST-based OD problem. The bias estimation strategy needs the expansion of the state vector to incorporate a bias

component, ρ_{bias}, thereby requiring the expansion of $\tilde{H}$ and Φ as follows:

$$\tilde{H} = \begin{bmatrix} \frac{\partial \mathbf{h}}{\partial \mathbf{r_1}} & \frac{\partial \mathbf{h}}{\partial \mathbf{v_1}} & \frac{\partial \mathbf{h}}{\partial \mathbf{r_2}} & \frac{\partial \mathbf{h}}{\partial \mathbf{v_2}} & 1 \end{bmatrix} \qquad \Phi(t_k, t_{k-1}) = \begin{bmatrix} \Phi_{\mathbf{Y}} & 0 \\ 0 & 1 \end{bmatrix}$$

As for the considered approach, the specific time-invariant measurement bias case is studied assuming that the consider parameter, b_k, is constant and the bias covariance matrix, B_k, is time-invariant.

Through simulations involving different orbital configurations, such as Halo/Halo and Halo/Lunar orbiter pairings, the impact of measurement bias on OD performance is assessed. Initial findings, illustrated in Figures 5.9 and 5.10, indicate a notable performance decline when biases are neglected. Remarkably, both the considered and estimated approaches yield comparable results when provided with accurate a-priori information about the bias. However, in the Halo/Halo configuration, the estimated bias approach results in decreased performance, a trend that can potentially be attributed to the adverse impact of an expanded state estimation vector on system observability. This issue is particularly pronounced in less observable configurations like Halo/Halo, where expanding the state vector further reduces the estimation accuracy. An exploration of whether the considered approach yields similar performance under inaccurate a-priori information (consider parameter) reveals that such inaccuracies may indeed lead to performance degradation, as presented in Figure 5.11. This underlines the critical importance of precise a-priori information in managing measurement biases effectively within SST-based OD systems.

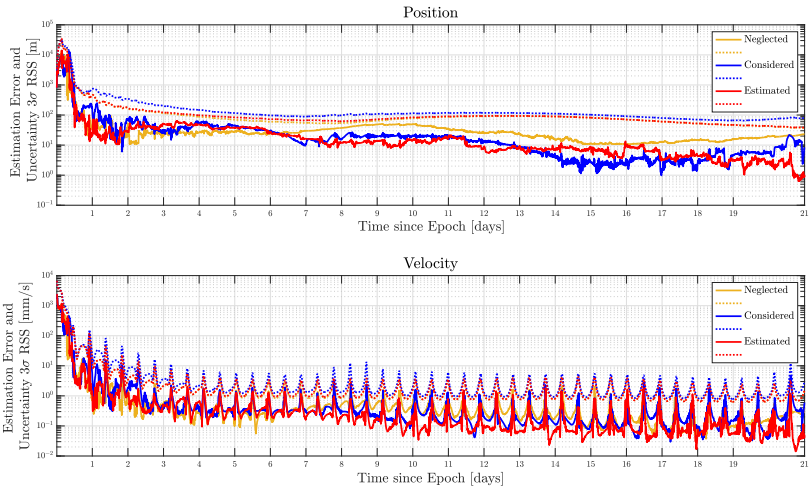

Figure 5.9: A case study illustration: analysis of three distinct bias handling strategies—neglecting, estimating, and considering approaches (Halo/Lunar configuration, with a 10 m systematic bias).

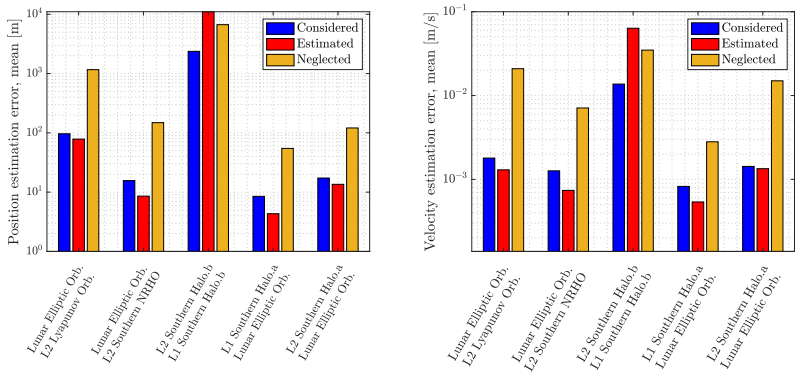

Figure 5.10: Comparison of bias management strategies across distinct orbital configurations (Monte Carlo analysis). Both estimated and considered approaches yield comparable results, with the estimation of bias adversely affecting state estimation accuracy in Halo/Halo configurations.

5

INSIGHTS FROM LONG-TERM MISSION PERFORMANCE

In the case of a real cislunar mission scenario with extended duration, e.g. >30 days, state estimation can be significantly impacted by other factors. This is particularly relevant when tracking periods are constrained by other operational requirements, such as telemetry and telecommand windows. Consider a scenario (Halo-Lunar) in which the SST period and thus the OD period is scheduled once every 4 days, each lasting for 1 day, with a subsequent Station-Keeping Maneuver (SKM) planned right after the OD period, aiming for a position (target point) 3 days ahead the current position (resulting in no SST for the following 3 days). In this configuration, OD can be performed for a full day once every 4 days. As this process involves real-time state estimation, OD cut-off period (time difference between OD solution and Delta-V execution) can be eliminated. Furthermore, it is thought that the very first SKM can be executed once the filter has converged, although determining the precise moment of convergence in practice can be challenging. Consequently, the initial SKM is planned for day 10.

Analysis of such a mission scenario demonstrates that within a span of 10 days, measurement biases can be accurately estimated, ensuring filter convergence and thereby enhancing OD accuracy, as depicted in Figures 5.12 and 5.13. Conversely, scenarios that the neglecting measurement bias tend to result in filter divergence, underscoring the critical importance of either estimating or considering measurement bias within the OD process, as further evidenced by the comparative consider performance illustrated in Figure 5.14.

From these observations, several key insights emerge:

- The estimation of measurement bias, or its treatment as a consider parameter, is indispensable in the OD process. The choice between estimating or considering the bias hinges on the specific demands of the mission scenario, with the estimated approach being more suited to formations such as Lunar/Halo, and the consider approach being preferable for Halo/Halo formations.

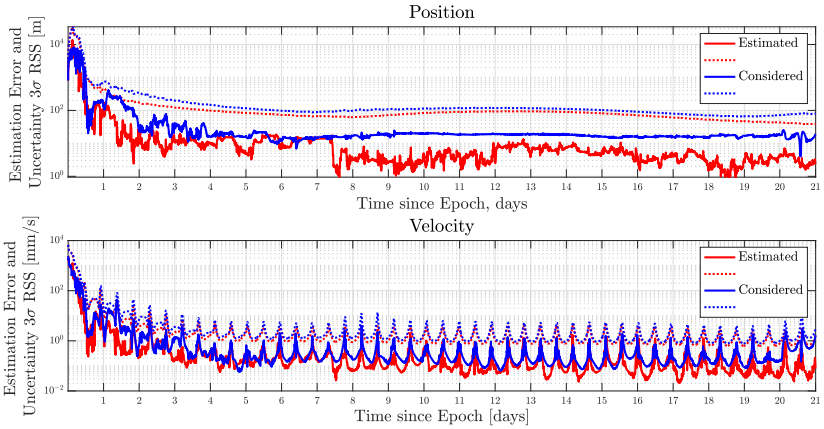

Figure 5.11: An example scenario: comparison of considered and estimated bias handling approaches (Lunar/Halo configuration, 20 m systematic bias, inaccurate a-priori consider parameter value)

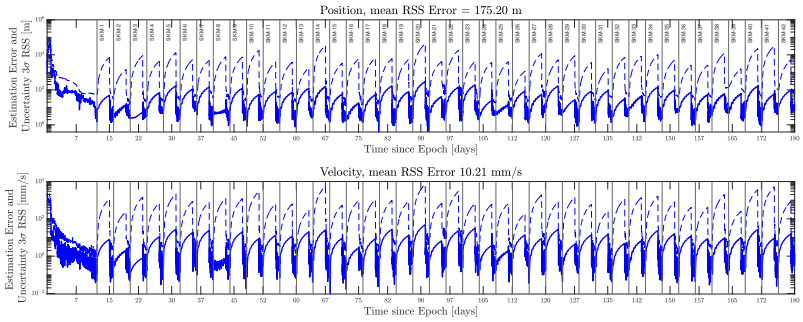

Figure 5.12: State estimation performance in the case of extended mission duration, including the estimated bias strategy.

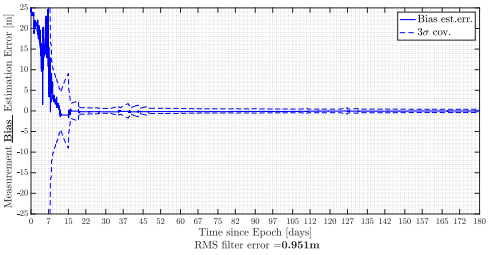

Figure 5.13: Measurement bias estimates in the case of extended mission duration.

The analysis underscores the critical role of measurement bias management in the OD process, highlighting that a detailed approach, depending on the mission require-

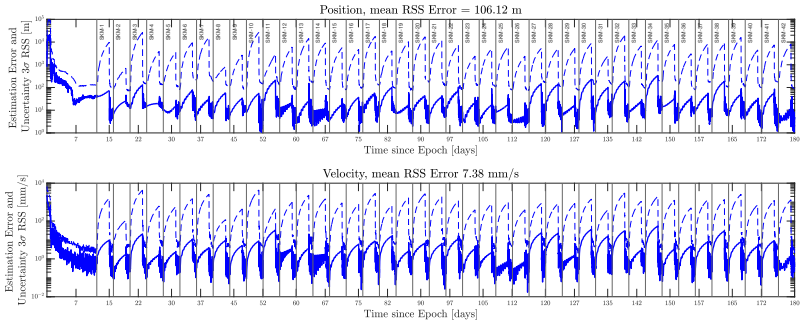

Figure 5.14: State estimation performance in the case of extended mission duration, including the considered bias strategy.

ments, is essential for optimizing system performance.

5

5.2.3. CLOCK PARAMETERS

The following part of this study analyzes in greater detail the effects of clock drift and aging in measurements. As described previously in Chapter 2, clock-related parameters, bias, drift, and aging, could cause errors in SST measurements, especially in one-way operations, as considered in this section. Similarly to systematic bias, these parameters could be modeled and estimated along with the spacecraft states. By incorporating deterministic clock errors—bias, denoted as $\Delta\tau_c^{(0)}$, drift, denoted as $\Delta\tau_c^{(1)}$, and aging denoted as $\Delta\tau_c^{(2)}$, with a deterministic clock error model of $\delta t_c = \sum_{i=0}^{2} \Delta\tau_c{}^{(i)}(t-t_0)^i$—into the estimated state vector, this part of the study aims to investigate their influence on system performance. In this context, the measurement sensitivity matrix and STM can be formed as follows:

$$\tilde{H} = \begin{bmatrix} \frac{\partial \mathbf{h}}{\partial \mathbf{r_1}} & \frac{\partial \mathbf{h}}{\partial \mathbf{v_1}} & \frac{\partial \mathbf{h}}{\partial \mathbf{r_2}} & \frac{\partial \mathbf{h}}{\partial \mathbf{v_2}} & 1 & (t-t_0) & (t-t_0)^2 \end{bmatrix} \qquad \Phi(t_k, t_{k-1}) = \begin{bmatrix} \Phi_{\mathbf{Y}} & 0 \\ 0 & \mathbf{I}_{3\times 3} \end{bmatrix}$$

Utilizing parameters reflective of the LRO, characterized by 1×10^{-4} s (30 000 m) clock bias, 6.9×10^{-8} s/s (20.7 m/s) clock drift, and 1.9×10^{-17} 1/s (5.6×10^{-9} m/s^2) clock aging, the study explores the feasibility of estimating these clock-related parameters alongside spacecraft states. As presented in Figure 5.15, EKF estimates and smoother solutions, particularly those derived from the RTS-type smoother, reveal that filtering of constant measurement biases has not been improved by smoothing. Conversely, neglecting these parameters in separate simulations precipitated diverged OD solutions, underscoring their significance. Furthermore, the exploration into the effects of expanding the state vector with additional clock parameters reveals a consistent increase in position/velocity estimation errors, as presented in Table 5.5, suggesting a potential trade-off between the expansion of the state vector and estimation accuracy. It is possible that these results may underestimate the role of measurement geometry and are somewhat limited by the given clock parameters. Thus, these findings cannot be extrapolated to all mission scenarios. However, it should be noted that this mission scenario is a typical Halo/Lunar

Table 5.5: The impact of expanding the estimated state vector on the estimation performance (Monte-Carlo), demonstrating a noticeable change in estimation errors for position and velocity. This reveals the balance required when enhancing the state vector with systematic parameters, indicating a trade-off between comprehensive state modeling and maintained estimation accuracy.

Estimated Parameters	**Mean RSS Pos Est. Err. [m]**	**Mean RSS Vel Est. Err. [m/s]**	**Mean Bias Est. Err. [m]**	**Mean Drift Est. Err. [m/s]**	**Mean Aging Est. Err. [m/s^2]**
None	72.80	0.007	N/A	N/A	N/A
Systematic Bias	80.77	0.007	0.37	N/A	N/A
Systematic Bias - Drift	94.70	0.008	0.52	2.45e-5	N/A
Systematic Bias - Drift - Aging	294.39	0.016	0.68	5.45e-5	2.51e-9

case representing a highly observable system.

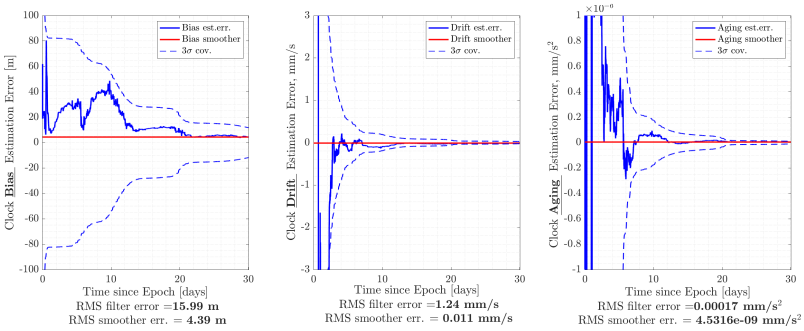

Figure 5.15: Extended Kalman Filter and Smoother Clock Parameter Estimates

In the case of an extended mission duration including SKM, clock parameters could be estimated accurately. The scenario given in the previous section has been considered here to test whether the system is capable of estimating these parameters for the long data arc. Figure 5.16 and 5.17 represent the spacecraft's state and clock parameter estimates for a 180 days scenario. What can be seen is that estimated clock parameters converge to actual values within 60 days due to the OD gaps caused by other operations. This is also the reason for the fluctuations in the estimation covariance. Even though gaps are not critical, a reasonable approach to tackle this problem could be to extend the very first OD period.

It is concluded that the real-time estimation of clock drift and aging across the entire mission duration may not offer a distinct advantage, particularly considering the potential impact on the position/velocity state estimation performance. Given the advancements in clock technology, periodic estimation of these parameters could suffice for system calibration, supplemented by offline data-processing algorithms to adjust for clock-related errors over time. The application of onboard smoothers, as discussed, could further refine the calibration process, especially in anticipation of SKM requirements. This nuanced understanding of clock-related parameters in SST-based OD emphasizes the need for cautious interpretation of these results, given their reliance on the specific mission scenario analyzed.

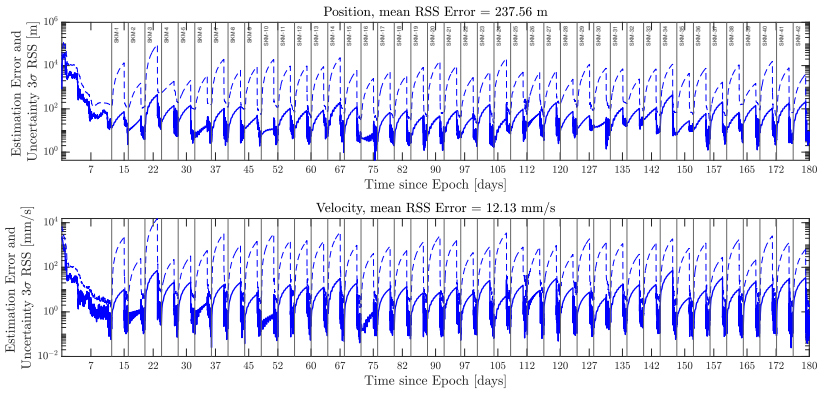

Figure 5.16: State estimation performance in the case of extended mission duration, including clock parameters.

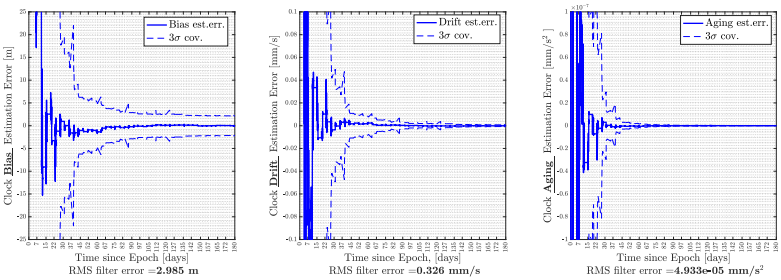

Figure 5.17: Clock parameter estimates in the case of extended mission.

5.2.4. OBSERVATION DATA TYPE

This section explores the relationship between observation data types—specifically range, range-rate, and angle data—and OD performance within various orbital configurations. Recognizing the distinct influences each data type exerts on system performance, a comprehensive comparison has been undertaken to ascertain the conditions under which each observation type yields superior state estimations. Recognizing the infeasibility of comparing high-error range data against low-error range-rate data (or vice versa), this analysis seeks to establish a fair basis for comparison among all observation types under equivalent orbital and measurement geometries, as discussed in earlier sections, e.g. Section 4.1 presented how to derive relationships between observation types.

To this end, the CRLB for range-only (σ_ρ =1 m), range-rate-only ($\sigma_{\dot{\rho}}$ =1 mm/s), and angle-only ($\sigma_{\phi_{SST}}, \sigma_{\varphi_{SST}}$ =40 arcsec) measurements were compared (see Chapter 2 for further details), taking into account the same orbital parameters and measurement setups. It was crucial to consider the different convergence rates of each observation type; hence, comparisons were made post-convergence (beyond day 10). The findings, depicted in Figure 5.18, highlight a general trend of increasing position uncertainty across certain geometries, regardless of the chosen observation type.

Another important aspect of this problem is related to understanding the relationship between observation data types in terms of OD performances. As presented in Figure 5.19 (see Eq. 4.35 for further details), findings indicate that the OD performance parity between SST-based range and range-rate systems is situated within a range-rate error spectrum of 0.04 mm/s to 0.14 mm/s for a corresponding range error of σ_ρ =1 m. Similarly, for angle-only measurements, an equivalent OD performance within a range error of σ_ρ =1 m is achievable within an angle measurement error range of 0.02 arcsec to 1.76 arcsec. These results may position the range-only observation system as potentially more advantageous compared to its range-rate-only and angle-only counterparts, considering the relative ease of attaining a 1 m accuracy in range measurements with respect to achieving 0.14 mm/s or 1.76 arcsec accuracy in range-rate and angle measurements, respectively, especially in less favorable geometric scenarios.

However, it is imperative to approach these conclusions with a degree of caution. The analysis given here has not accounted for the influence of measurement biases, which could significantly impact the system's performance. Thus, while the preliminary insights suggest a possible preference for range-only systems under certain conditions, a comprehensive evaluation inclusive of measurement biases remains essential for a full understanding of the optimal observation data type for enhancing OD performance.

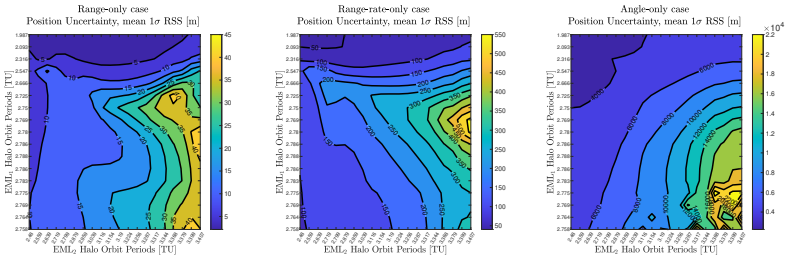

Figure 5.18: SST-based OD performances after the post-convergence for Halo/Halo orbital configurations based on various observation data types, demonstrating how each observation data type uniquely influences the performance.

5.3. FILTERING SELECTION

Having covered the dynamic and measurement aspects in the previous sections, the subsequent investigation focuses on estimation aspects. This section explores the relationship between filter selection and OD performance. Emphasizing the critical role of filters within the OD process, it examines how the selection of sequential data processing filters aligns with the potential for achieving optimal state estimation accuracy, as determined by the CRLB. Focusing on an array of sequential filters — including the EKF, AEKF, IEKF, AIEKF, UKF, and IUKF— this analysis primarily targets the estimation of spacecraft states within a two-spacecraft formation. It should be noted that CKF has not been studied in this part, as its performance has already been discussed in sections 5.2.2 and 5.2.3, respectively.

Figure 5.20 provides the performance of these filters within a defined Halo/Halo SST-based OD scenario. Contrary to initial expectations, this study did not find a significant

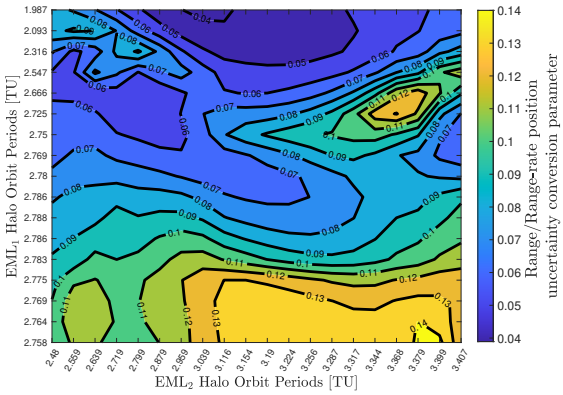

Figure 5.19: Comparison parameter for various orbital configurations, highlighting the SST-based OD performance parity between range and range-rate systems is situated within a range-rate error spectrum of 0.04 mm/s to 0.14 mm/s for a corresponding range error of σ_ρ =1 m.

difference between filters, although iterated solutions provided slightly better performances in certain regions. It should be noted that re-linearisation during IEKF and IUKF does not mean better performances in terms of convergence and estimation, as stated in [193]. What stands out in the figure is that adaptive approaches didn't provide as similar performances as other techniques. This is due to the fact that other methods have been provided with the correct priori process noise covariance matrix.

The findings reported here suggest that there is no significant difference between filters for the SST-based OD problem within the CRTBP. It is important to bear in mind that these findings cannot be extrapolated to high-fidelity dynamical cases.

5.4. A LUNAR CUBESAT SCENARIO

In the previous sections, comprehensive analyses were conducted to assess the OD performance within the CRTBP framework. This section, however, aims to provide a more realistic mission scenario and SST-based OD performance within the cislunar space. With this aim in mind, this part of the study presents the autonomous navigation performances of the selected mission scenario: Lunar Meteoroid Impact Observer (LUMIO), via the inter-satellite link between LPF and the LUMIO CubeSat. A simulation-based analysis will determine the achievable OD accuracy, considering realistic radio frequency measurement errors derived from the Phase-A study inter-satellite link design, which is a design not originally intended for crosslink navigation purposes. The mission features a 12U CubeSat in a Halo orbit at the EML2 to observe, quantify, and characterize meteoroid impacts on the Lunar farside by detecting their flashes [171]. The mission aims to determine the spatial and temporal characteristics of meteoroids impacting the Lunar surface to characterize their flux. The operational orbit for LUMIO has been selected as a quasi-periodic halo orbit with a Jacobi constant C_j = 3.09 [171]. The LUMIO Phase-B study is ongoing at the time of writing this dissertation. It is noteworthy to mention that certain parts of this section have been previously presented in

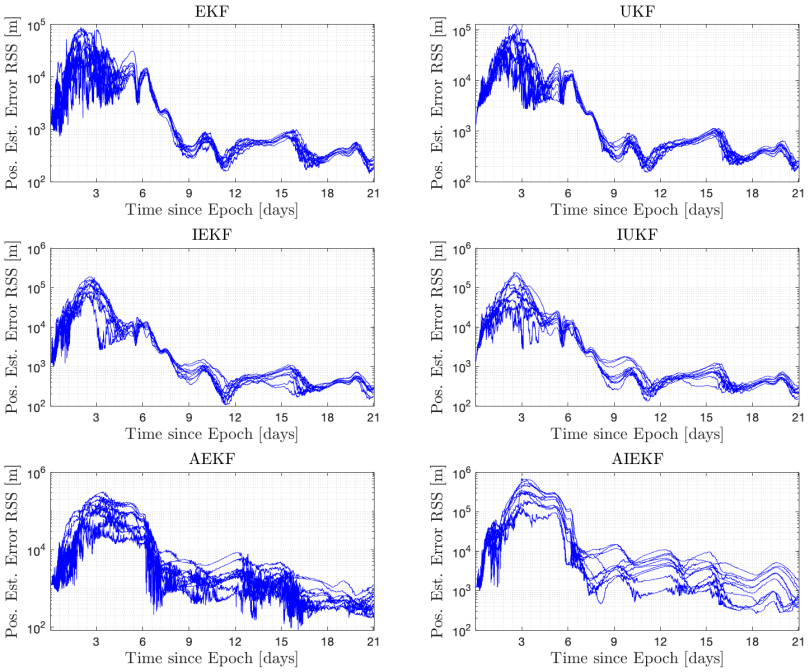

Figure 5.20: Filtering performance for the Halo-to-Halo SST-based autonomous OD scenario within the CRTBP, including 10 Monte-Carlo runs.

[192].

The operational framework of the radiometric navigation system integrates the pre-existing hardware of the communication system, featuring a combination of ISL and DTE links. Notably, the DTE link is primarily designed for payload data downlink, including capabilities for ranging and tracking under nominal conditions. This study adopts the OD requirements of achieving 1 km positional and 1 cm/s velocity accuracies, parameters that align with previous ground-based radiometric navigation analyses presented in [80], which demonstrated that utilizing tracking stations like Cebreros, ESTRACK, or the Sardinia Deep Space Antenna for scheduled 3 hours per tracks once every 7 + 7 + 14 days could meet these accuracy levels.

Conversely, the ISL aims to offer a redundant commanding link without involving a dedicated deep-space class ground station but reusing commercial resources. Such a link provides optimal performances in terms of visibility, despite the fact that data rates are quite limited. Functioning as a relay satellite, the SSTL LPF spacecraft plays a pivotal role in this configuration. Depending on the relative distance, between a minimum of 31 000 km and a maximum of 89 000 km, data rates are expected in the order of 0.5 kbps-4 kbps based on S-band, 9 dBW EIRP link, including a 3 dB safety margin [80].

Within the LUMIO mission framework, the focus shifts to accurately estimating the

Table 5.6: Radiometric parameters considered in the Lunar mission scenario. Downlink and Uplink stand for LPF-to-LUMIO and LUMIO-to-LPF, respectively. See Chapter 2 for further details about measurement errors.

	Parameter	Value	
		Downlink	Uplink
Inter-Satellite Link (ISL) Budget	Frequency, f	2200 MHz	2100 MHz
	TX power, P_t	3 dBW	3 dBW
	TX path losses, L_t	1 dB	1 dB
	TX antenna gain, G_t	6.5 dBi	23.6 dBi
	Polarisation loss, L_p	0.5 dB	0.5 dB
	Data rate	4000 bps	500 bps
	Required E_b/N_0	2.5 dB	2.5 dB
	Link Margin	3 dB	3 dB
Radiometric Measurement Parameters (ISL)	Symbol rate, $1/T_{sd}$	4000 sps	2700 sps
	Correletor integration time, T_l	0.5 s	
	Symbol-to-noise ratio, E_s/N_0	−1 dB	
	Modulation	BPSK	
	Transponding ratio, G	1	
	Range clock frequency, f_{rc}	1 MHz	
	Ranging code	T2B	
	Ranging clock power over noise spectral density, P_{rc}/N_0	25 dBHz	
	Loop Bandwidth, B_L	1 Hz	
	Chip rate difference, Δf_{chip}	100 Hz	
Measurement Errors 1σ, two-way, (ISL)	Conventional PN ranging error	2.98 m	
	Time-derived ranging error	102.44 m	
	Range-rate error	0.97 mm/s	

dynamical states (position and velocity) of both LUMIO and LPF. Utilizing two-way operations for baseline measurements, the mission scenario delves into analyzing performance under two distinct measurement error frameworks: One reflecting the high accuracy typically associated with conventional pseudo-noise ranging methods and another mirroring the challenges posed by low data-rate, data-aided ranging methods. A pivotal step in enhancing the mission's navigational accuracy involved reconfiguring the radiometric parameters to suit the demands of the SST-based OD, notably improving upon the initial configuration that yielded a 2700 m 1σ ranging accuracy. This optimization hinged on augmenting the uplink data rate and symbol duration through an enhanced antenna configuration and increased transmit power. Based on the specific link parameters given for both spacecraft, range and range-rate measurement errors are calculated and presented in Table 5.6.

In terms of the initial state errors and uncertainty, the onboard navigation filter can be initiated via a ground-based navigation solution, a key aspect that has been extensively examined during the LUMIO Phase-A design study. A ground-based tracking session spanning 7 hours, by the Sardinia Deep Space Antenna, based on range and range-

rate measurements characterized by errors of 1 m range and 0.33 mm/s range-rate with a measurement bias of 2.5 m results in 0.11 km and 0.95 cm/s position and velocity errors with 1σ uncertainty of 1.65 km and 4.7 cm/s, respectively (Batch-Least squares). Basically, this initial estimation from the single tracking session can be used to initialize the navigation system onboard. Although a similar ground-based state estimation has not been conducted for LPF, it is reasonable to assume that ground-based state estimation for LPF aligns with the same order of magnitude. It should also be noted that ground-based tracking is used to initialize the on-board filter. However, it has not been integrated into any of the SST-based OD scenarios given in this section.

In brief, the initial filter uncertainty is set to 1000 m for each position state and 1 cm/s for each velocity state, respectively. The spherical harmonic 15×15 gravity model of the Earth alongside point mass models for the Sun and the Moon have been used in the filter. A simple cannonball model is assumed for SRP. Regarding this, surface areas are set to 3 m^2 and 0.41 m^2, and reflectivity coefficients are set to 1.8 and 1.08, respectively. Measurements are corrupted by 10 m bias representing uncalibrated instrumental delays. Measurement errors, on the other hand, are set to the values given in Table 5.6. The process/measurement noise state compensation is arranged according to the adaptive estimation approach given in section 3.3.3, with the tuning parameter α set to 0.4 to optimize performance. During the filtering process, the local iterations are applied in a repetitive process till the estimate is no longer improved, with the number of iterations set to 3. Overall, AIEKF is implemented as an estimation filter for this particular scenario. As a side note, LUMIO's OD requirement is 1000 m for position and 0.01 m/s for velocity, respectively. This has been taken as the baseline goal for this study. Table 5.7 lists all the simulation parameters used within these analyses.

The initial assessments focused on a baseline scenario employing the conventional PN ranging method, demonstrating the SST-based on-board absolute state estimation of both the LUMIO and LPF spacecraft. Considering a simplified scenario where no measurement bias, measurement noise covariance uncertainty, process noise uncertainty, and orbit insertion errors are assumed, the navigation filter estimates the true states of LUMIO in the order of 10 m for position and 1 mm/s velocity, respectively. LPF states are estimated within the order of 10 m position and 1 cm/s velocity, respectively. Figure 5.21 represents the estimation results of the very first two weeks of the OD process (without any SKM). As can be seen, the filter converges to the true values approximately one week into the simulation. This is due to the fact that the halo orbit has a period of around 14 days, with the half-orbit serving optimal fit for the L2 orbiter. Additionally, fluctuations in the estimation results are related to the LPF dynamics. Notably, the position estimation tends to converge when LPF approaches the periselene, but diverges as it approaches the aposelene, highlighting LPF velocity states can not be accurately estimated when the spacecraft is close to the periselene due to the spacecraft's highly changing velocity. Therefore, it would be beneficial to perform SST near-periselene and not exactly at the closest and farthest point to the Moon. This finding aligns with the challenges of ground-based tracking near periselene, as highlighted by other research in the domain [194].

Expanding upon the initial findings, the exploration of a mission duration of one year and the influence of operational interruptions on SST performance adds additional lay-

Table 5.7: Summary of the simulation and spacecraft parameters considered in the Lunar mission scenario. See Chapter 3 for dynamical and measurement models.

	Parameters / Values
Ephemeris	JPL DE440
Reference Frame	Earth Centered Inertial
Simulation Epoch	01 January 2024 12:00:00
Force Models	Earth gravity 15x15 spherical harmonics Lunar gravity - point mass Sun gravity - point mass
Solar Radiation Pressure	Lunar orbiter, 3 m^2, C_r1.8 L2 Halo orbiter, 0.41 m^2, C_r1.08
Initial State Covariance	Position states 1σ, 1 km Velocity states 1σ, 1 cm/s Systematic Bias 1σ, 3 km
Initial State Error	Position states 500 m Velocity states 1 cm/s Systematic Bias 300 m
Measurement Error	See Table 5.6
Measurement Bias	10 m
Measurement Rate	1/180 s
Measurement Noise Covariance	20% underweighted, Adaptively
Process Noise Covariance	Trial-and-error, Adaptively
SST window	1 day once every 4 days (Initial 7 days)
Orbit Insertion error	500 m and 1 cm/s into each state
SKM Execution error	1%, $\epsilon_{exe} \sim \mathcal{N}(0, \sigma^2_{exe})$

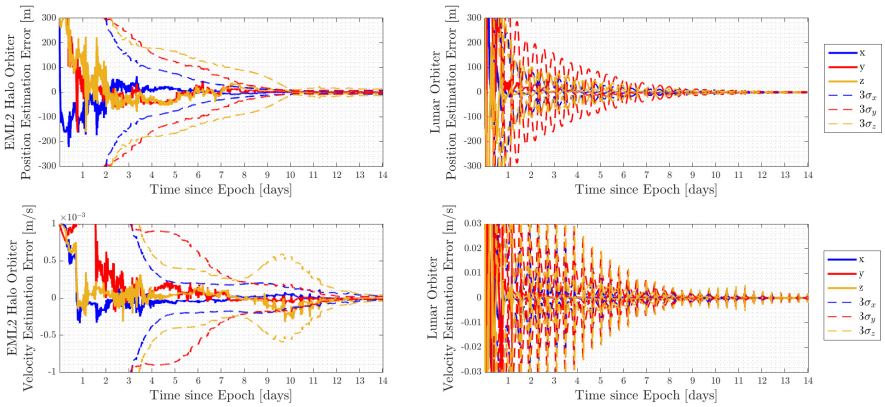

Figure 5.21: Kalman-type filtering performance for the Lunar CubeSat simplified mission scenario considering the PN ranging as a SST method.

5

ers of complexity. As stated previously, telemetry, telecommand, and/or SKM periods affect the overall system performance. If the overall goal is estimating the LUMIO's position/velocity within predefined values during the full mission (e.g., 1 km and 1 cm/s for this study), then this would require SST planing with caution. Another need would be having an accurate estimate just before SKM instead of a full mission duration. While the process of designing the optimal tracking windows remains beyond the scope of this section, a fixed interval tracking is assumed mainly once every 4 days for a duration of 1 day. Figure 5.22 illustrates the OD performance (with errors lower than 100 m and 1 cm/s), highlighting that 1 day of constant SST provides an OD solution sufficient to compensate for errors resulting from the 3 days of tracking gap. This gap might be increased to minimize the number of SST and thus OD periods. However, this would also affect the Delta-V budget since OD periods are planned just before SKM. Another approach would be to minimize the SST duration. Moreover, the study dived into optimizing SST duration, seeking the minimal tracking period necessary to comply with the navigation requirements. Through a detailed sensitivity analysis, it was observed that around 12 hours of tracking once every 4 days are sufficient to meet the OD requirements. This highlights the potential for reducing the duration of SST operations, thereby conserving resources and streamlining mission operations without compromising navigational needs. An important thing to bear in mind is that distributing the measurements over the orbit, in general, provides the best results. Thus, this finding may not be observed in other mission scenarios.

The next analysis delves into the impact of high measurement errors on OD performance, considering the data-aided ranging as the SST approach. As already highlighted, modulating the ranging signal reduces the power available for telemetry and, thus, the supported telemetry data rates. It might be an issue to perform ranging and telemetry sessions during the same time window. However, data-aided ranging, distinguished by its integration into the telemetry stream, emerges as a strategic solution to the operational challenge of concurrent ranging and telemetry activities. This method not only

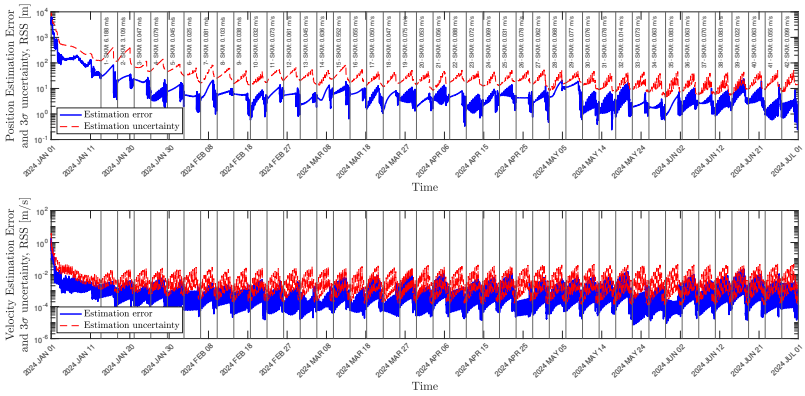

Figure 5.22: Kalman-type filtering performance for the Lunar CubeSat scenario, considering the PN ranging as a SST method. Vertical lines represent the Delta-V budget.

simplifies the communication system's design but also minimizes the power demands on the spacecraft, presenting an efficient alternative for missions operating within tight power budgets.

The performance evaluation of the OD system under conditions of high measurement error—characteristic of low-rate data-aided ranging—reveals an interesting outcome. Despite the relatively large measurement noise, with a standard deviation of σ_ρ =100 m, the OD system demonstrates acceptable performances, maintaining compliance with the mission's requirements for position and velocity accuracy, as presented in Figure 5.23. This finding underscores the robustness of the OD method employed, illustrating its capability to derive accurate state estimations even in the face of significant measurement uncertainties.

However, one of the interesting findings is the significant influence of Delta-V execution errors on the system's overall performance. The findings indicate that inaccuracies in executing SKMs exert a large impact on estimation accuracy, up to a degree of three times. The observed increase in error could be attributed to neglected/non-considered SKM execution in the filter.

LOST-IN-SPACE

This thesis has meticulously explored the SST-based autonomous OD in overcoming operational challenges that might affect the mission's success. A particular emphasis has been placed on scenarios that could disrupt the continuity of operations, such as lost-in-space situations, propulsion system failures, or communication system faults. Among these, the lost-in-space scenario emerges as critically significant from an OD perspective due to its direct impact on the ability to perform OD and, consequently, SKM. It is believed that this scenario is more critical than others from the OD perspective. For instance, missing a certain SKM can be mitigated by locating the target points at some time in the future after any subsequent SKM. This would allow an extended operation in case of any SKM execution failure. Although SKM can be performed without the OD period

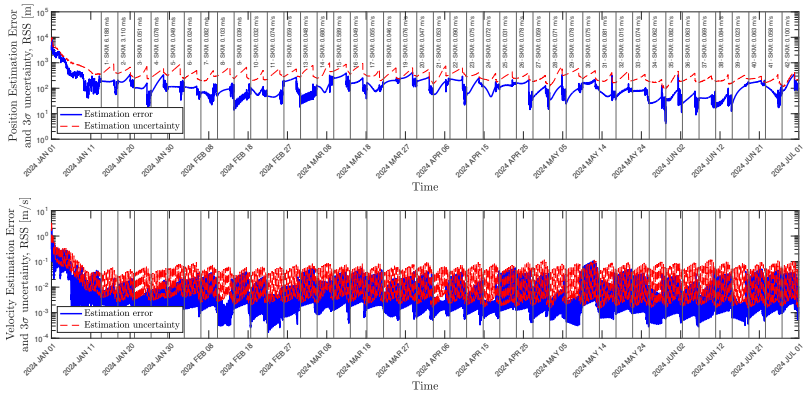

Figure 5.23: Kalman-type filtering performance for the Lunar CubeSat scenario considering the data-aided ranging as a SST method

(without measurement update), this would result in higher Delta-Vs.

The resilience of the SST-based autonomous OD approach lies in its cooperative nature, allowing for on-board filtering calculations to be performed across different nodes within the satellite formation (exchanging navigation solutions). This flexibility ensures that a system failure in one node can be compensated for by another, maintaining operational continuity through mutual support and information exchange. Such a setup offers a backup solution against potential disruptions, ensuring that critical functions can proceed with minimal interruption. In this context, lost-in-space is considered as a time interval without having any SST and, thus, measurement update during the mission operations. It should be noted that this implies a scenario for only one of the nodes being lost in the network.

To illustrate the robustness of SST-based autonomous OD systems against lost-in-space scenarios, the study simulates a system failure extending over a two-week period in the middle of the mission. Despite this interruption, the filter effectively leverages prior information to accurately estimate the spacecraft's position and velocity once normal operations resume, demonstrating the system's capacity for rapid recovery post-disruption, as illustrated in Figure 5.24. It should also be noted that this resilience can be further enhanced by the ability to utilize relative distance information from SST as an initial guess for re-initializing the on-board filter, particularly beneficial for Lagrangian point orbiters, considering relatively short-term lost-in-space scenarios. By analyzing SST range data over half an orbit, the system can deduce crucial information about the spacecraft's coarse location from the reference orbit based on observed maximum and minimum relative distances, offering a simple approach to establishing OD accuracy in the case of a lost-in-space event.

This section not only offers a detailed examination of SST-based autonomous OD as a potential alternative to traditional ground-based navigation methods, even under high measurement errors, but also highlights the system's adaptability to operational uncertainties. As the discussion progresses to include the addition of an extra space-

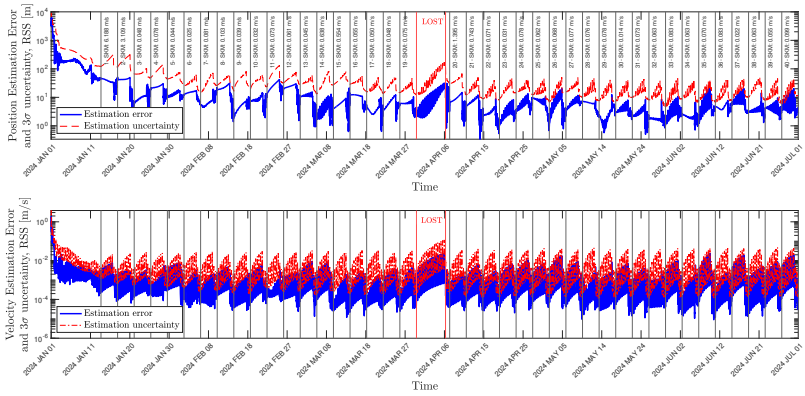

Figure 5.24: Kalman-type filtering performance for the Lunar CubeSat scenario considering the data-aided ranging as a SST method and two weeks of the lost period starting from day 90

craft to the satellite formation, the potential for further enhancing system robustness and operational flexibility becomes a focal point, promising to improve the efficiency of autonomous navigation in the cislunar environment.

5.5. NETWORK TOPOLOGIES

The evolution of satellite formations, particularly the incorporation of more than three spacecraft, marks a shift towards enhancing operational efficiency and mission objectives. The integration of additional spacecraft into satellite formations is increasingly recognized for its potential to harmonize mission operations and extend operational capabilities. This trend towards larger formations underscores the growing importance of advanced network topologies in facilitating robust and flexible mission architectures.

In small satellite missions, especially those operating in the lunar vicinity, the traditional one-hop link configuration via a mothercraft serves as the cornerstone for payload data transfer to Earth, establishing a centralized or star topology. This approach, while effective for simplifying communication strategies, presents limitations in the flexibility and redundancy of the network. The concept of mesh or distributed topology introduces another layer by enabling direct interactions between all spacecraft in the formation. Unlike the star topology that relies heavily on a central node for communication, the mesh topology's performance is distributed across the network, potentially enhancing the robustness and resilience of mission operations. This distributed approach is particularly beneficial for SST-based autonomous OD, utilizing existing communication links for improved navigation performance.

Introducing three or more spacecraft into a lunar satellite network raises interesting considerations for optimal orbital configurations and, thus, observation geometry. It is expected that a mesh topology would outperform a star topology in terms of OD performance due to the additional links, providing extra navigational information. However, the actual degree of improvement remains a subject for a detailed investigation. The in-

clusion of three or more spacecraft in a formation, especially within a low observability configuration, e.g. Halo/Halo formation, may pose challenges to system performance. The expansion of the estimated state vector to accommodate this additional node could adversely impact system observability and, consequently, estimation accuracy. Moreover, the performance of the OD system may fluctuate within the same relative geometry between spacecraft, depending on the chosen chief configuration in a star topology. Deciding which spacecraft undertakes the observation collection and executes the onboard OD process becomes a pivotal consideration in maximizing system performance.

There are various communication topologies for satellite formations including star (centralized), mesh (distributed), or hierarchical (hybrid) topology. In this section, the hierarchical topology, characterized by its multi-layered structure incorporating two or more star networks, is not studied due to the main focus being on a three-spacecraft scenario. A schematic representation of both centralized and mesh topologies in Figure 5.25 provides a visual framework for understanding these configurations.

Through a performance analysis of SST-based autonomous OD within various lunar satellite network topologies, this section aims to show the operational advantages and challenges of each configuration. By leveraging the optimal orbital geometries, the study seeks to mitigate the geometric constraints imposed by ground-based navigation in the Earth-Moon system. The findings are anticipated to offer valuable insights into the benefits of mesh topology and guidance on selecting the central node in star configurations, thereby supporting decision-making processes for future lunar missions, involving satellite formations.

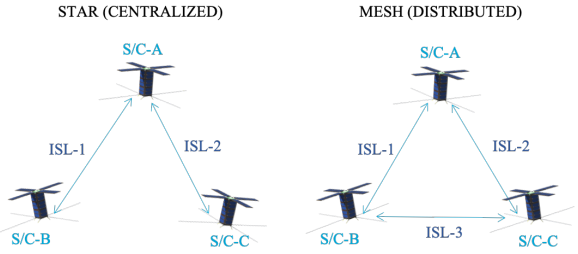

Figure 5.25: Diagram illustrating centralized and mesh network configurations for a three-spacecraft scenario. Indicated arrows show potential communication paths, highlighting whether links are bidirectional or unidirectional, originating from a primary spacecraft or encompassing all members of the network.

Building upon the information given above, the centralized topology, characterized by its reliance on a central node or mothercraft, offers simplicity in design but carries the risk of a single point of failure. Any failure in the mothercraft could put the entire mission's communication/navigation capabilities at risk, highlighting the critical nature of the central node's reliability. Conversely, the mesh topology offers robustness against individual spacecraft failures. However, as the number of spacecraft within the network increases, the complexity of managing the mest topology increases significantly, especially when considering the exponential increase in the number of connections required (considering the N number of spacecraft, $N-1$ versus $N(N-1)/2$ connections required for the centralized and mesh topologies, respectively).

To analyze the SST-based OD within these topologies, simulations are conducted to evaluate the performance of centralized and mesh configurations in lunar satellite networks. The number of ISLs are set at two connections for centralized topologies and three for mesh configurations (see Figure 5.26). The analysis extends to explore 560 combinations for the mesh topology, based on N orbital configurations taken K at a time without repetition, $\binom{N}{K} = \frac{N!}{K!(N-K)!}$ and $560 \times 3 = 1680$ combinations for the centralized topology when including the selection of a central node. The simulation, extending over 28 days, aims to cover 1.5 times the longest orbital period identified within the selected configurations, thus ensuring a comprehensive assessment of each topology's performance over a significant portion of the mission's duration. The assumption of a 1σ measurement error of 3 m for inter-satellite range measurements, without the introduction of biases, standardizes the evaluation criteria across all configurations.

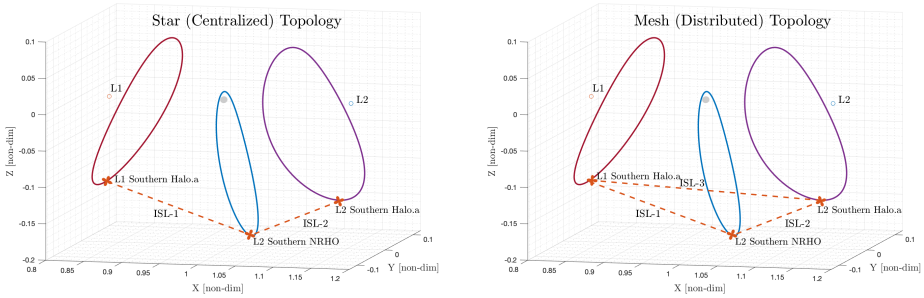

Figure 5.26: Representation of centralized and mesh network topologies for the three Spacecraft case in the cislunar vicinity.

5.5.1. CENTRALIZED TOPOLOGY

In an illustrative scenario highlighting the centralized topology's performance for autonomous OD, three spacecraft, specifically the L_1 southern Halo a., L_2 southern NRHO (central node), and L_2 southern Halo a., are chosen to demonstrate the expected outcomes in such applications (see trajectories in Figure 5.26). The results presented in Figure 5.27 reveal that the crosslink range measurements facilitated by the ISL between the L2 NRHO and the L1 and L2 Halos enable the system to achieve position estimation uncertainties (1σ) below 150 m and velocity estimation uncertainties (1σ) below 8 mm/s for all spacecraft involved after six days from the start of the mission.

Notably, the position states of the NRHO spacecraft are more precisely estimated as it nears periselene, although this precision does not extend to its velocity states. A period of six days from the initial epoch is identified as sufficient to attain stable estimation results. The condition number and unobservability index values, 9.82×10^{11}, 4.76×10^{8} respectively, indicate that the problem remains observable. This type of application requires the condition number to be less than 10^{16} for the problem to be observable [11].

An examination of $\beta_{ave-pos}$ and $\beta_{ave-vel}$, which stand at 756 m and 5.44 mm/s respectively, offers insight into the average uncertainties 3σ across the spacecraft within the formation.

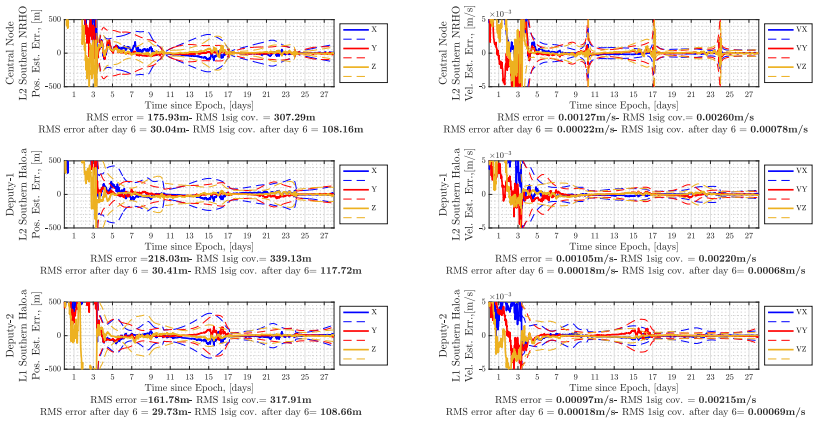

Figure 5.27: State estimation results within a centralized topology configuration (selected case study)

5

Subsequent analysis of the centralized topology's performance, as depicted in Figures 5.28, highlights that combinations involving lunar elliptical or polar-circular orbiters yield superior results compared to other configurations. Specifically, configurations including the Lunar elliptical orbiter exhibit marginally better performance, especially in terms of velocity estimations, over those incorporating the Lunar polar-circular orbiter.

Conversely, configurations limited to L1 or L2 Halos exhibited higher estimation errors due to similar orbital periods and relative position changes, which resulted in certain directions being poorly observable, especially those involving spacecraft in close proximity. Moreover, topologies constituted by Lyapunov orbits fail to yield accurate results due to the lack of out-of-plane motion despite the significant inter-satellite distances, underscoring the challenges of ensuring comprehensive observability across all directions.

Selected configurations detailed in Table 5.8 further illustrate that the most effective centralized topologies are those characterized by larger inter-satellite distances and significant differences in orbital periods. Such configurations enhance the performance of centralized topologies, particularly when comprising Lunar orbiters and/or Halo orbiters positioned at distinct Lagrangian points. An exemplary centralized topology might involve a Lunar elliptical orbiter, an L1 southern Halo orbiter, and an L2 northern Halo orbiter, leveraging the diversity in their orbital dynamics to optimize OD performance within the lunar vicinity.

5.5.2. MESH TOPOLOGY

The exploration of mesh topology in lunar satellite formations yields significant insights into the performance advantages offered by distributed configurations. State estimation outcomes for mesh topologies surpass those observed in centralized topologies, a benefit attributed to the added navigational data provided by an additional inter-satellite link.

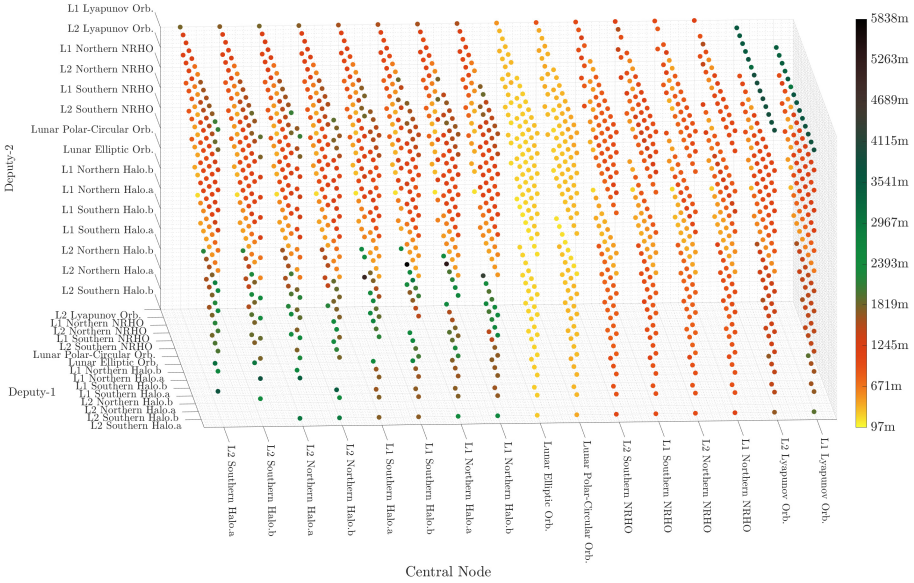

Figure 5.28: $\beta_{ave-pos}$ results for the centralized topology. Each dot signifies a unique centralized topology instance, with color coding indicating the level of estimation uncertainty.

Table 5.8: Selected mesh and network topologies consisted of three S/C. Note that S/C-A is the central node in the centralized topology and, thus, there is no SST between S/C-B and S/C-C. CN and UOI stand for condition number and unobservability index, respectively.

S/C-A	S/C-B	S/C-C	Topology	CN	UOI	$\beta_{ave-pos}$,[m]	$\beta_{ave-vel}$,[cm/s]
Lunar Elliptic Orb.	L1 Southern Halo.a	L2 Northern Halo.a	Centralized	6.99×10^{6}	1.3×10^{-3}	337	2.54
			Mesh	2.00×10^{7}	7.4×10^{-4}	186	1.62
Lunar Polar-Circular Orb.	L1 Southern Halo.a	L2 Northern Halo.a	Centralized	7.30×10^{6}	1.3×10^{-3}	467	2.75
			Mesh	1.98×10^{7}	7.3×10^{-4}	298	2.08
L1 Northern NRHO	L1 Southern Halo.a	L2 Northern Halo.a	Centralized	1.69×10^{7}	4×10^{-3}	12350	14.38
			Mesh	2.58×10^{7}	10×10^{-4}	4423	8.14
L1 Lyapunov Orb.	L1 Northern NRHO	L2 Southern Halo.b	Centralized	1.15×10^{7}	4.6×10^{-3}	10197	13.08
			Mesh	1.94×10^{7}	43×10^{-4}	3412	6.99
L2 Northern Halo.b	L1 Northern Halo.a	L1 Northern Halo.b	Centralized	1.95×10^{8}	11×10^{-3}	10780	13.74
			Mesh	1.23×10^{7}	32×10^{-4}	4500	7.97
L2 Southern Halo.b	L2 Northern Halo.a	L2 Northern Halo.b	Centralized	6.65×10^{7}	37×10^{-3}	22905	18.37
			Mesh	3.66×10^{7}	89×10^{-4}	7940	9.72

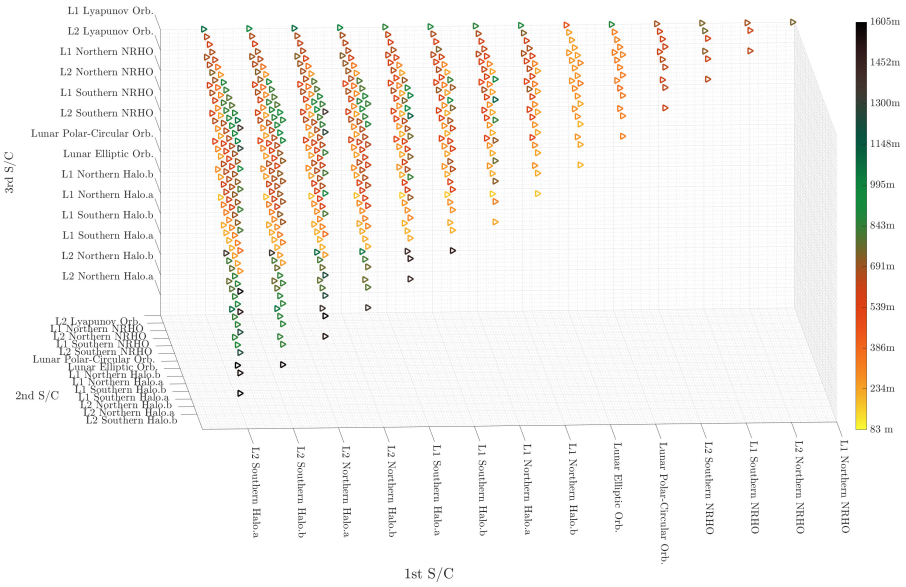

Figure 5.29: $\beta_{ave-pos}$ levels across various mesh topology configurations, depicted by dots. The color gradient reflects the degree of uncertainty in each scenario, illustrating fewer instances due to the inherently limited number of combinations in mesh topologies compared to centralized ones.

Figure 5.29 represents state estimation results under mesh topology, underscoring optimal performance achievements when the topology includes Lunar orbiters. Conversely, formations exclusively comprising L1 or L2 Halos fall short in matching these superior performances.

Selected mesh topology configurations, detailed in Table 5.8, present marginal performance enhancements when formed by Lunar orbiters compared to their centralized counterparts with the same geometrical configurations. Notably, a minimum of 10% improvement in performance has been realized in these instances. Mesh topologies comprising solely of Halo orbiters, however, derive more substantial benefits from the extra link, providing approximately a 55% overall improvement in performance metrics such as mean $\beta_{ave-pol}$ across all combinations considered in this study.

Further analysis into the addition of a third spacecraft unveils methodologies for optimizing the third orbital selection as a central node. By fixing two spacecraft and varying the third, performance metrics such as the CN, UOI, or overall state uncertainty based on the CRLB can guide towards an optimal third orbit solution. Figure 5.30 explores the inclusion of a third spacecraft within a Halo/Halo centralized topology, indicating that orbits with shorter periods tend to yield better overall performance (see Figure 5.31 for corresponding trajectories).

In this comprehensive study, which explored 560 mesh and 1680 centralized topologies across various orbital configurations, mesh topologies have consistently offered improved state estimation. This outcome aligns with expectations, attributing the enhance-

ment to the additional information data facilitated by extra inter-satellite links. The study further confirms that topologies with shorter orbital periods generally lead to better and faster-converging state estimations. This is due to the fact that crosslink measurements provide all the necessary information to the filter to determine the complete spacecraft states about the full trajectory that the orbiter with the shorter period would have. Additionally, configurations featuring longer inter-satellite distances tend to outperform those with closer proximity.

In conclusion, lunar satellite network topologies that incorporate large inter-satellite distances and shorter orbital periods are best to leverage autonomous navigation systems effectively. Such autonomous OD systems hold promise for future lunar networks comprising relay satellites and multiple collaborative assets. These systems aim to reduce mission costs, enhance performance, and improve reliability without heavily relying on ground-based tracking. While autonomy levels may necessitate occasional corrections, the overall system design ensures reduced dependence on ground support, facilitating a more flexible and efficient space exploration framework.

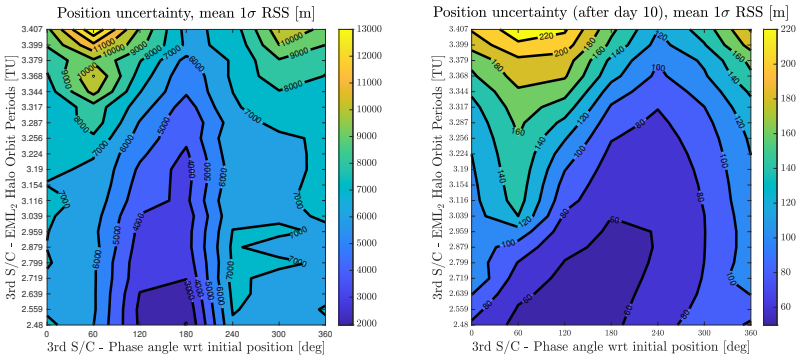

Figure 5.30: The impact of 3rd S/C within the centralized topology based on various phase angles and EML2 Halo orbits.

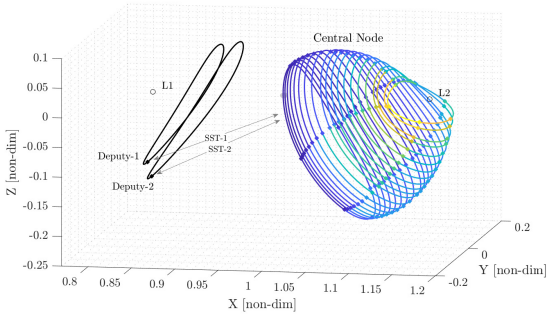

Figure 5.31: The central node in the three S/C EML2 Halo orbit scenario within the centralized topology. Color gradient indicates the level of uncertainty (blue=low uncertainty, yellow=high uncertainty)

Table 5.9: Selected mesh and network topologies consisted of four S/C. Note that S/C-A is the central node in the centralized topology, and thus, there is no SSTs between S/C-B and S/C-C, S/C-B and S/C-D, S/C-C, and S/C-D, respectively. CN and UOI stand for condition number and unobservability index, respectively.

S/C-A	S/C-B	S/C-C	S/C-D	Topology	CN	UOI	$\beta_{ave-pos}$ [m]	$\beta_{ave-vel}$ [cm/s]
Lunar Elliptic Orb.	L1 Southern Halo.a	L2 Northern Halo.a	L1 Northern Halo.a	Centralized	8.13×10^{6}	1.3×10^{-3}	288	1.93
				Mesh	1.70×10^{7}	4.8×10^{-4}	124	1.02
Lunar Polar-Circular Orb.	L1 Southern Halo.a	L2 Northern Halo.a	L1 Northern Halo.a	Centralized	7.29×10^{6}	1.3×10^{-3}	439	2.51
				Mesh	1.66×10^{7}	4.6×10^{-4}	172	1.29
L1 Northern NRHO	L1 Southern Halo.a	L2 Northern Halo.a	L1 Northern Halo.a	Centralized	1.68×10^{7}	3.9×10^{-3}	8720	11.73
				Mesh	2.04×10^{7}	6.2×10^{-4}	1447	4.37
L1 Lyapunov Orb.	L1 Northern NRHO	L2 Southern Halo.b	L1 Northern Halo.a	Centralized	1.81×10^{8}	4.1×10^{-3}	5881	9.40
				Mesh	2.02×10^{8}	36×10^{-4}	1429	4.21
L2 Northern Halo.b	L1 Northern Halo.a	L1 Northern Halo.b	L1 Southern Halo.a	Centralized	1.73×10^{8}	9.6×10^{-3}	7600	10.80
				Mesh	3.76×10^{7}	9.3×10^{-4}	1684	4.55
L2 Southern Halo.b	L2 Northern Halo.a	L2 Northern Halo.b	L1 Southern Halo.a	Centralized	2.30×10^{8}	1.3×10^{-2}	9126	11.86
				Mesh	4.71×10^{7}	10×10^{-4}	2850	5.89

5.5.3. MULTIPLE NODES

Expanding on satellite formations with more than three nodes, this section delves into the impact of adding additional nodes to network topologies on the system's overall performance. This inquiry is critical because, while an extra node introduces more information through an additional ISL, it could potentially diminish system observability. Hence, it is important to understand the full extent of the network topologies consisting of multiple nodes.

Given the vast number of potential combinations for systems with more than three nodes, detailed testing of each orbital and network configuration becomes impractical. For instance, a four-node network yields 1820 mesh topology combinations and quadruples to 7280 in centralized configurations. Therefore, this study narrows its focus to selected configurations, specifically targeting the most, moderately, and least observable mesh and centralized topologies (e.g., from highly to less perturbed orbits) previously identified from three-spacecraft systems, resulting in a total of twelve case studies.

The analysis revealed key insights, summarized in Table 5.9: Introducing shorter-period orbits (e.g., Lunar orbits) into less observable configurations significantly enhances the information available to the OD filter, contributing positively to the system's performance. Conversely, the addition of nodes in longer-period orbits (e.g., Halo orbits) did not yield noticeable improvements. This observation aligns with earlier findings suggesting that network topologies comprising orbits with shorter periods (highly perturbed orbits) generally offer better solutions for OD systems. This behavior underscores the importance of selecting optimal orbital configurations when expanding satellite networks, where the strategic addition of nodes in shorter periodic orbits can substantially improve observability and, by extension, the overall system performance.

These results highlight the relationship between the addition of nodes to a satellite network and its impact on OD capabilities. By carefully considering the orbital period and the inherent observability of potential new nodes, system designers can make informed decisions to enhance the functionality and effectiveness of space mission operations through optimized network topologies.

The most obvious finding to emerge from the analysis is that shorter periodic orbits added to the less observable configurations bring valuable information to the OD filter. On the other hand, having an additional longer periodic orbit did not show any significant improvement. These findings are consistent with the results from the previous

section.

5.6. A SMALL BODY SCENARIO

The exploration of small celestial bodies, such as asteroids and comets, constitutes a significant frontier in space missions, aiming to enrich our understanding of the solar system's origins and dynamics. A notable selection of missions—ranging from the Deep Space 1 flyby [195] of asteroid Braille, the NEAR Shoemaker's rendezvous [196] with asteroid Eros, LICIACube's observation asteroid Dimorphos after DART's impact [18], to the Hayabusa2 [197] and OSIRIS-REx [198] sample return missions targeting asteroids Ryugu and Bennu, respectively—demonstrates the diverse methodologies deployed in navigating these challenging environments. Future missions like Hera [199], set to explore the binary asteroid system of Didymos and Dimorphos, and the Comet Interceptor [51], designed to study a yet-to-be-discovered long-period comet, underscore the evolving landscape of exploration strategies.

Traditionally, ground-based tracking has been the backbone of OD strategies for deep-space missions. This approach has been augmented with additional navigation methods as missions demand higher accuracy and autonomy, especially when spacecraft approach their target bodies. For instance, the OSIRIS-REx mission utilized optical navigation as a primary data type during its close-range operations around asteroid Bennu, employing ground-based, centroid-based, and landmark-based optical tracking data throughout its various phases [172]. Such diversity in data types underscores the need for adaptable OD strategies to comply with the requirements of each mission phase.

The advent of missions focused on small bodies raises questions about the optimal use of observation data types and their impact on autonomous navigation system performance. This is especially critical for missions requiring close proximity operations, such as asteroid rendezvous, where onboard navigation systems must rely on a mix of ground-based tracking, crosslink radiometric tracking, optical tracking, and other data types. The relationship between these various observation data types and their influence on the effectiveness of autonomous navigation systems remains a not yet fully explored area in the context of missions around small bodies.

This study seeks to bridge this gap by conducting a comprehensive performance comparison of autonomous navigation systems using different sensor types and various orbital configurations around small bodies. Through a semi-analytical approach, this subsection delves into the CRLB analysis of various orbital and measurement configurations, beginning with simulation results around asteroid Eros. Subsequently, the investigation extends to asteroid Bennu, providing a comparative analysis of the system performance in differing orbital environments.

The objective is to clarify how different observation data types, when utilized in autonomous navigation systems and various orbital setups, affect the overall system performance in the unique operational contexts of small-body missions. By examining the outcomes of these analyses, the study aims to offer valuable insights into selecting and optimizing navigation systems for future missions, ensuring they are equipped to navigate the complex and varied environments of small celestial bodies effectively.

EROS

This section focuses on Eros as a primary case study. Acknowledging the insights from prior research and also from Section 5.1.1, the study highlights the potential limitations of circular orbits in enhancing the system's observability, particularly in scenarios involving two spacecraft orbiting the same celestial body. Moreover, it is suggested that non-coplanar configurations may offer superior state estimation capabilities compared to coplanar setups. Consequently, this analysis is devoted exclusively to non-coplanar orbital configurations to understand the impact of various orbital elements on the orbit determination performance more comprehensively.

The initial part of the analysis examines the influence of different orbital configurations on the CRLB, focusing on the variations in semi-major axis (a) (ranging from 30 km to 50 km) and eccentricity (e) (ranging from 0 to 0.3) for both spacecraft. The findings, depicted in Figure 5.32 as a color map, represent the mean CRLB position uncertainty (1σ RSS) across diverse orbital setups. Notably, each plotted value on the map is the outcome of analyzing various mean anomaly configurations, pinpointing the most favorable result within the given orbital configuration. The figure illustrates that both an increase in eccentricity (e) and semi-major axis (a) lead to improved performances.

Further analysis, illustrated in Figure 5.33, keeps the second spacecraft's states fixed with a semi-major axis of 30 km and an eccentricity of 0.014. The results underscore that both an increase in eccentricity and a decrease in the semi-major axis lead to improved state estimation and faster convergence of the navigation solution. Interestingly, circular orbital configurations at 30 km exhibit superior state estimation compared to eccentric configurations at 50 km. This superiority is attributed to the interaction of both spacecraft with the highly asymmetric gravity field of the asteroid, particularly when one spacecraft orbits closer to the asteroid. The analysis suggests that having a different orbital shape for the second spacecraft is advantageous for enhancing system performance.

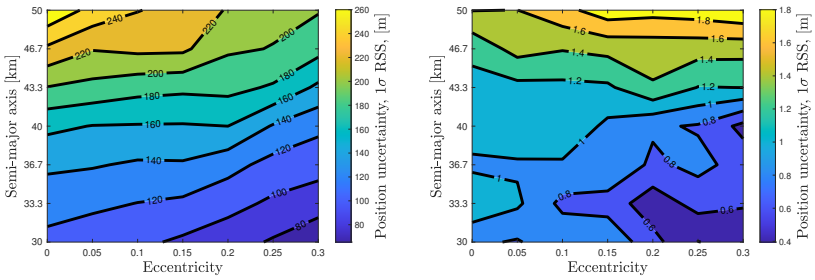

Figure 5.32: CRLB Position uncertainty (1σ RSS) based on various orbital configurations. Left: Uncertainty averaged across the entire simulation duration. Right: Uncertainty averaged after the converged phase. Comparing these left and right figures provides insights into the convergence speed.

The investigation also delves into the impact of mean anomaly on system performance. Figure 5.34 presents the position uncertainty for various mean anomaly configurations, demonstrating that mean anomalies of 0 degrees and 180 degrees for the second spacecraft lead to slower navigation solutions. Specifically, a configuration with a

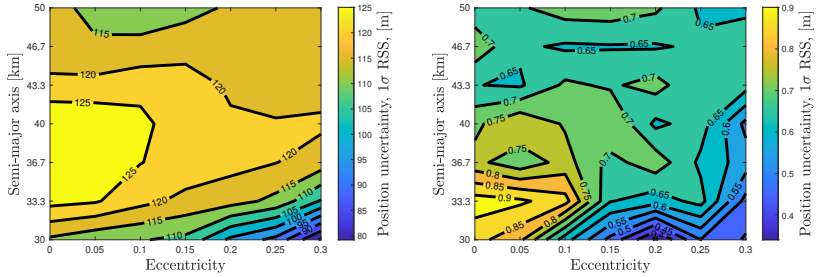

Figure 5.33: CRLB Position uncertainty (1σ RSS) based on various orbital configurations. In this case, the S/C-B orbit is fixed to $a = 30$ km. Left: Uncertainty averaged across the entire simulation duration. Right: Uncertainty averaged post-convergence phase.

180-degree mean anomaly tends to yield higher position uncertainties in the converged solution. This finding highlights the critical role of the initial relative geometry in influencing the OD performance, highlighting the necessity to carefully consider orbital configurations when designing autonomous navigation systems around small bodies like asteroids.

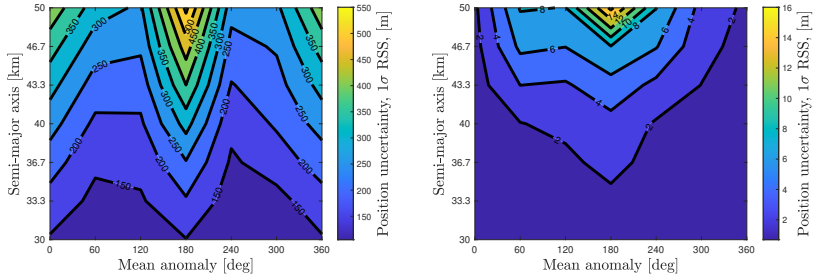

Figure 5.34: CRLB Position uncertainty (1σ RSS) based on various mean anomaly configurations. In this case, the S/C-B orbit is fixed to the mean anomaly of 0 deg. Left: Uncertainty averaged across the entire simulation duration. Right: Uncertainty averaged post-convergence phase.

In an extended analysis focusing on the comprehensive evaluation of various measurement methods and their impact on state estimation accuracy, Figure 5.35 sheds light on the CRLB for state uncertainty (1σ) across different observation techniques. These include inter-satellite range, range rate, angle (azimuth and elevation), ground-based range, range rate, and LOS celestial body tracking (azimuth and elevation). Based on the measurement errors outlined in Table 2.6, it was expected that integrating all measurement methods would yield the best system performance. Interestingly, the study observed negligible differences in performance between systems utilizing crosslink range-only measurements and those incorporating both range and range-rate measurements. This outcome underscores the higher utility of accurate range measurements (1 m, 1σ) over crosslink range-rate measurements (1 mm/s, 1σ) within the specific orbital configurations analyzed. Additionally, the implementation of LOS celestial body tracking did

not introduce any substantial new information, whereas ground-based measurements and inter-satellite angle measurements, when combined with range and range-rate data, achieved performance levels comparable to those of ground-based techniques. Figure 5.36 further illustrates CRLB position uncertainty based on various measurement methods and orbital configurations.

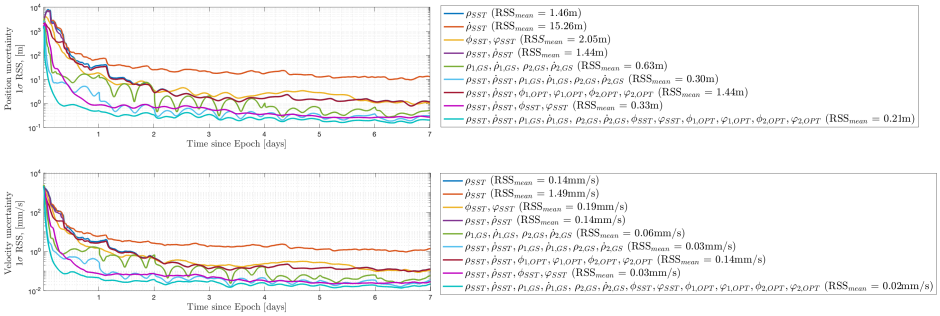

Figure 5.35: CRLB analysis of position uncertainty for different observation techniques. (Eros case study, RSS values averaged following convergence phase.)

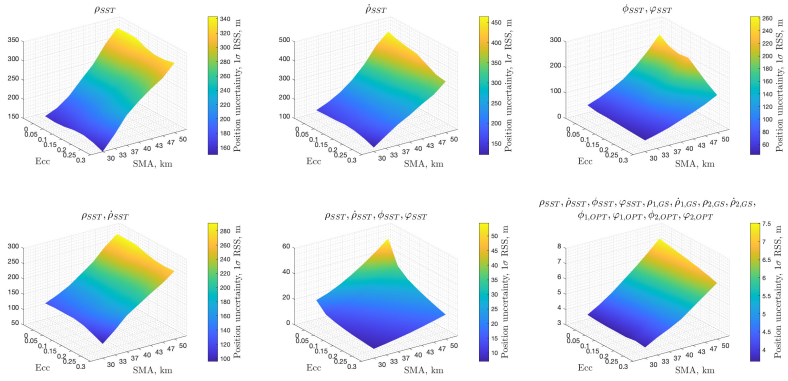

Figure 5.36: CRLB analysis of position uncertainty for different observation techniques and varying orbital configurations. RSS results are averaged over the full simulation.

The comparative study between different observation data types underscores the relative effectiveness based on their noise profiles. Through a specific case analysis, a threshold, β, has been explored for varying errors in inter-satellite range, range-rate, and angle measurements, with Figure 5.37 presenting the outcomes. For instance, the figure illustrates that in the range-rate-only case, a measurement accuracy spanning from 0.08 mm/s and 0.2 mm/s, depending on orbital configurations, matches the average performance achieved by a range-only system with a 1 m crosslink ranging accuracy after

the post-convergence phase. Typically, range-rate data facilitate slightly faster convergence in less observable orbital setups and marginally superior results in more observable configurations. It is noteworthy that specific geometrical configurations might favor one data type over another for enhanced state estimation. This comparative analysis extends to the relationship between satellite-to-satellite angle and range measurements. On the right-hand side of Figure 5.37, the outcomes indicate that an angle-only system, with accuracies ranging from 8 arcsec and 30 arcsec, can match the overall performance of a range-only system with a 1 m ranging error, depending on the orbital configuration. Particularly, angle-only systems may offer relatively improved performance in scenarios characterized by low a and high e orbital configurations.

Summarizing, this assessment underlines that a range-rate-only system with accuracies between 0.08 mm/s and 0.2 mm/s, as well as an inertial angle-only system with accuracies ranging from 8 arcsec and 30 arcsec, could potentially replicate the OD performance derived from a range-only system with a 1 m error (1σ).

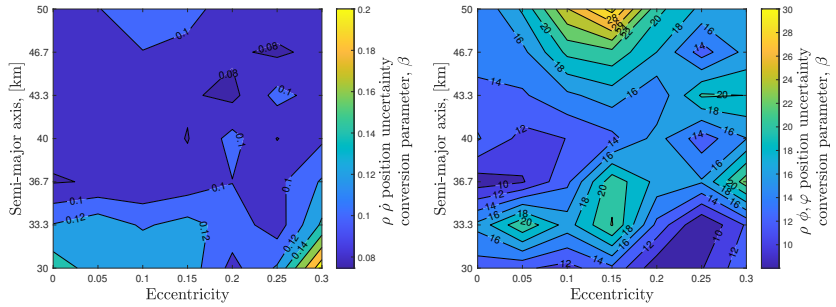

Figure 5.37: Comparison for crosslink navigation systems. Left panel: Performance of range-only versus range-rate-only systems. Right panel: Analysis of range-only compared to angle-only systems.

This study shows that variations in spacecraft characteristics such as area, mass, and reflectivity coefficient, C_r, within a formation can enhance navigation solutions for specific orbital configurations. This improvement is attributed to the differences in acceleration function and the STM, offering a unique navigation solution that leverages the asymmetrical gravity field for a fully observable system. Besides gravitational acceleration, solar radiation pressure also contributes to system observability, yet to a smaller extent. Exploiting these differences could involve forming satellite formations with varied surface areas, masses, and C_r values. A practical example could be a formation consisting of a deputy designed as a 6U CubeSat with a surface area of 0.5 m^2 and a mass of 22 kg. Figure 5.38 highlights the ratio of mean RSS CRLB uncertainty between formations comprising identical and differing surface area, mass, and C_r. In this scenario, one spacecraft adopts parameters from the NEAR Shoemaker spacecraft, with surface areas set to 1.7 m^2, 0.5 m^2, masses to 805 kg, 22 kg, and both with a C_r of 1.2. This configuration enabled achieving lower bounds for both position and velocity uncertainties, especially in low observable geometrical configurations (with higher a and lower e). Specifically, at greater a, the acceleration due to the asteroid's non-spherical body impacting both spacecraft is diminished compared to configurations with lower a. For instance, at a 50

km a, a circular orbiter experiences an acceleration of approximately 2×10^{-4} m/s^2 due to the primary body. Conversely, the differences in acceleration attributable to solar radiation pressure between spacecraft approximate 1.2×10^{-7} m/s^2, potentially reducing position uncertainty by up to 10 m overall.

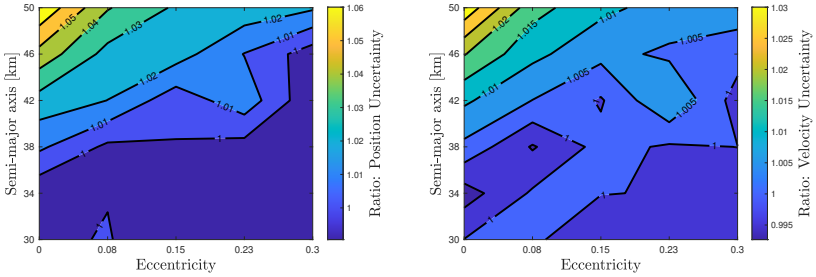

Figure 5.38: Ratio of mean RSS CRLB position and velocity uncertainties for the identical and different S/C parameters. Left: Averaged across the entire simulation duration. Right: Averaged post-convergence phase.

5

In terms of planet tracking, the standard scenario involved measuring relative angles (azimuth and elevation) between spacecraft and Jupiter and Mars. An additional case study explored the effects of tracking different planets on the system's performance. Table 5.10 details scenarios where two spacecraft track separate planets. As anticipated, tracking diverse planets does not introduce supplementary information to the position uncertainty. Nonetheless, it can influence the convergence speed, contingent on the initial relative geometry between spacecraft and planets. Essentially, obtaining relative angle measurements between planets and spacecraft can primarily aid in enhancing the convergence speed of the navigation solution.

Table 5.10: CRLB for position uncertainty difference based on various planet tracking configurations. Values in parenthesis stand for averaged after day 3.

		S/C-B			
		Sun	Earth	Mars	Jupiter
S/C-A	Sun	35.90 (3.56)	N/A	N/A	N/A
	Earth	35.03 (3.59)	37.66 (3.63)	N/A	N/A
	Mars	41.17 (3.60)	36.34 (3.64)	47.56 (3.65)	N/A
	Jupiter	45.55 (3.61)	44.13 (3.66)	50.81 (3.67)	58.98 (3.68)

BENNU

In this segment of the study, the focus shifts to Bennu as the primary body, adopting spacecraft orbital configurations with e of 0.14 and 0.01, and a of 1.5 km and 0.9 km, respectively, based on data from the OSIRIS-REx SPICE files. The evaluation of different measurement methodologies on system performance reveals their impact on the CRLB state uncertainty (1σ), as depicted in Figure 5.39. Utilizing identical measurement errors as previously specified (with the exception of $\sigma_{\phi_{SST}}, \sigma_{\varphi_{SST}}$ adjusted to 8.3 arcmin, considering the maximum inter-satellite distance around 3 km), it is noted that systems

utilizing range-only measurements outperform those based solely on range-rate measurements. This observation aligns with findings from prior analyses, with a notable distinction being the benefit of angle-only systems due to the close proximity formations, thereby slightly enriching the information. Given the specific orbital configuration under this section, it has been determined that a range-rate-only system with a measurement error of 0.05 mm/s, as well as an inertial angle-only system with an error of 28 arcmin, can achieve orbit determination performances comparable to that of a range-only system with a 1 m measurement error.

Moreover, the study revisits the influence of spacecraft mass and surface area on estimation performance, repeating findings similar to those around asteroid Eros. Considering the OSIRIS-REx spacecraft parameters with those of a beacon spacecraft—characterized by previously mentioned dimensions and reflective properties—an enhancement in position uncertainty reduction, approximately 2 meters overall, is observed. This improvement underscores the significant benefits of varying spacecraft characteristics within close formation flight around small celestial bodies, as illustrated in Figure 5.40.

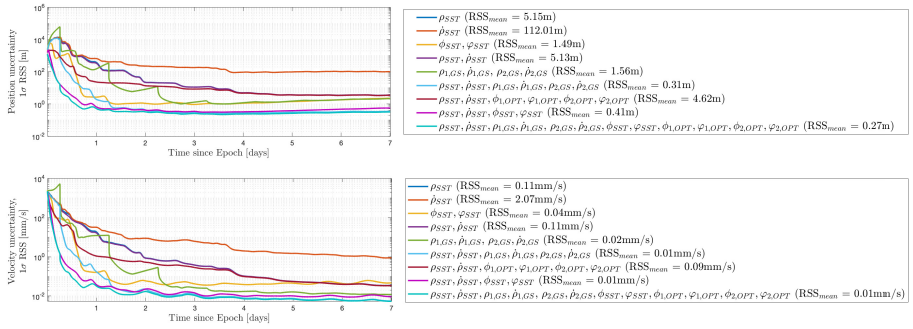

Figure 5.39: CRLB position and velocity uncertainties based on various measurement methods (Bennu scenario, RSS values are averaged after the converged phase)

ESTIMATION PERFORMANCE

This section primarily centered on the CRLB to present the potential impacts of various spacecraft and orbital parameters on navigation accuracy, sidelining the details of navigation filter design. Yet, a case study highlighted in Figure 5.41 delves into the operational efficacy of employing SST data, utilizing the AIEKF for its execution. Notably, this approach, despite augmenting computational demands by 10%, provided accurate mean RSS for both position and velocity estimations—approximately 10 m and 1 mm/s, respectively, after a duration of six hours. The analysis further supports earlier CRLB findings, indicating the advantageous impact of divergent spacecraft areas, masses, and reflectivity coefficients on the navigation solution. Moreover, Figure 5.42 compares the AIEKF with the AEKF, underscoring the superior accuracy afforded by iterative measurement updates within the filtering process over the standard adaptive approach.

Despite these insights, several limitations were identified, showing possibilities for future studies. Notably, the measurement geometry's influence on OD highlights the ab-

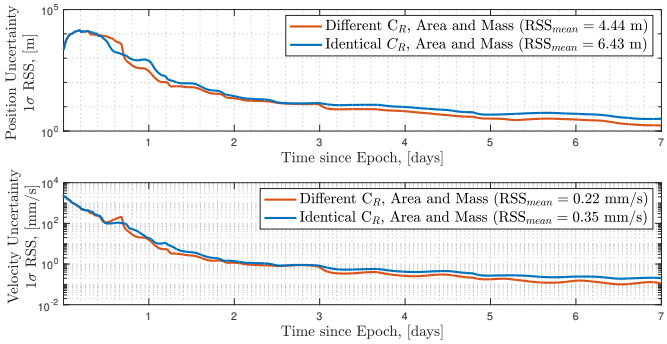

Figure 5.40: CRLB position and velocity uncertainties (Bennu scenario, RSS values are averaged post-convergence.)

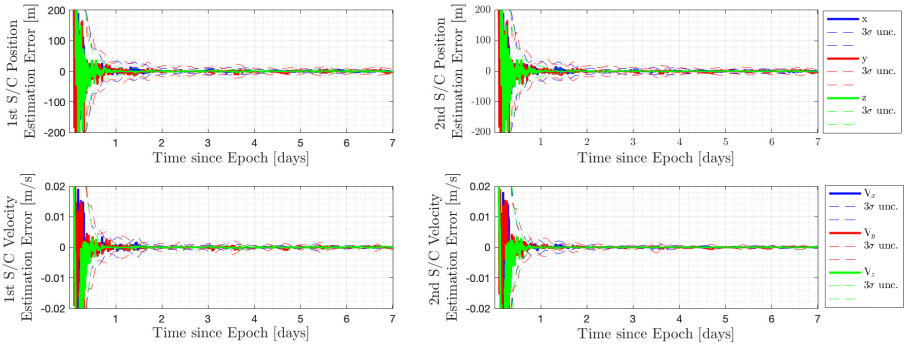

Figure 5.41: AIEKF Estimation performance (Eros scenario, based on SST range,range-rate, and angle measurements)

sence of an investigation into optimal tracking windows and ground station positioning, which could yield enhanced results. Furthermore, while the analysis touched upon the effects of orbital size and shape, it did not delve into the dynamics introduced by varying relative orbital orientations, a factor crucial to optimizing observability and, consequently, OD accuracy. An interesting direction for future research could involve identifying optimal relative orientations that minimize orbit determination errors.

Additionally, this study's reliance on a simplistic cannonball model for SRP overlooks the relationship between spacecraft attitude, SRP modeling, and their collective impact on orbital dynamics. Delving into high-fidelity SRP and orbital dynamics models could significantly enhance system performance insights. The study also skips the potential impacts of measurement bias on system performance, hinting at the utility of consider covariance analysis in future research. Addressing these limitations could vastly improve the understanding and application of autonomous navigation systems in missions exploring small solar system bodies.

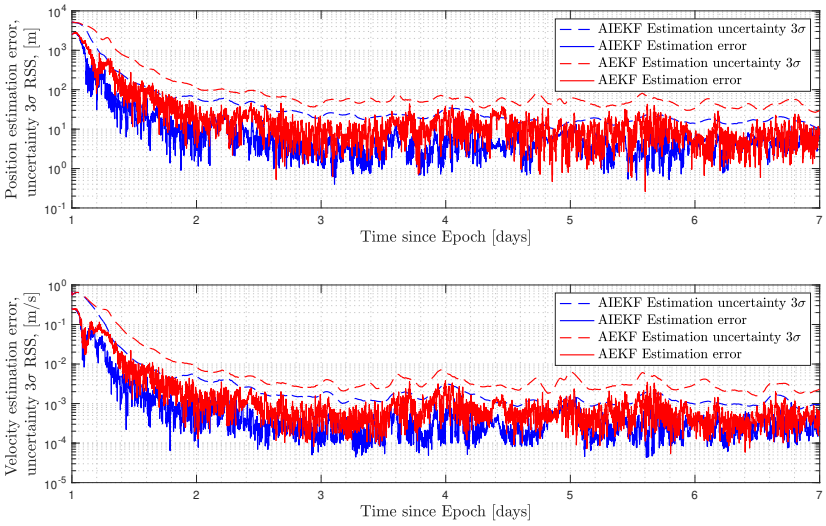

Figure 5.42: AIEKF and AEKF estimation performances given as RSS values (Eros scenario, based on SST range,range-rate, and angle measurements)

5.7. INTERPLANETARY CRUISE

This section delves into the unique challenges and performances of SST-based autonomous OD during the interplanetary cruise phase of a mission. Thus far, the thesis presented the SST-based autonomous OD performance around Earth (section 5.1.1), in cislunar space (section 5.1.1), and around small solar system bodies (section 5.6). It is highlighted that while inter-satellite observables often fall short of offering a fully observable system within the two-body problem context, incorporating SRP and other perturbations can somewhat enhance system observability. The interplanetary cruise phase presents a unique challenge: The accelerations influencing the formation exhibit similar magnitudes with insignificant differences. Consequently, this similarity could lead to certain states remaining unobservable, depending on the mission's geometric layout.

To illustrate this, the MarCO Cubesats mission serves as a case study, specifically chosen for its relevance and the availability of ephemeris data. This analysis utilized CRLB to simulate the mission's duration up to the Mars flyby. However, the findings revealed significant uncertainties in the order of 1×10^6 km in position and 1 km/s in velocity within the initial phase, a reduction to the order of 1×10^3 km and 0.1 km/s after nearly three months. These results underscore the limitation of relying solely on crosslink measurements for accurate state estimation during interplanetary cruises, presenting similar conclusions drawn for SST-based OD within the two-body problem framework.

The analysis suggests that integrating additional navigation data types, such as those derivable from onboard sensors like star trackers, into the filter could mitigate these limitations. A collaborative study, referenced [200] (co-authored), investigates the performance of combining SST-based radiometric OD with LOS optical navigation for satel-

lite formations on deep space cruises. The integration of these navigation techniques demonstrates promising enhancements in performance across different spacecraft architectures, leading to more robust and reliable autonomous navigation solutions in deep space missions.

5.8. SUMMARY

This chapter presented a comprehensive analysis on SST-based OD for satellite formations across various conditions. It addressed the three main core elements of OD: dynamic, measurement, and estimation, offering insights into the details of each aspect. Through meticulous examination, it began with analyzing the two-body problem, exploring the sensitivities tied to orbital parameters and observation data types assessing their implications on both estimation accuracy and system observability. Subsequently, the chapter delved into the three-body problem, investigating the dynamics of the OD process. It then proceeded to examine measurement effects, including measurement errors, underweighted/overweighted measurement noise covariance, and various strategies for handling measurement bias and clock parameters. The relationships between OD performance and observation data types, specifically range, range-rate, and angle, were outlined. Furthermore, the chapter highlighted the filtering performance, demonstrating how the system responds to distinct filtering algorithms. Additionally, the chapter presented a detailed analysis of a realistic mission scenario that aimed to utilize SST-based onboard OD. The chapter further provided network topologies, such as mesh and centralized topologies, for three or more satellite formations, with the aim of aiding future lunar networks composed of relay satellites and multiple assets, facilitating collaborative and autonomous operations to achieve enhanced cost efficiency, performance, and reliability. The chapter concludes with an analysis of a small body scenario and an interplanetary cruise phase, covering all possible aspects of the OD problem. The key takeaways from this comprehensive analysis can be given as follows:

Two-body Problem Insights:

- Non-coplanar configurations significantly outperform coplanar ones, with orbital sizes and shapes playing crucial roles.
- SST range and range-rate data show lower sensitivity to altitude changes compared to inertial angle data. All observation types showed minimal sensitivity to changes in orbital shape.
- Incorporating perturbations into the two-body dynamics model significantly reduces estimation uncertainty, typically yielding at least a twofold improvement.

Three-body Problem Findings:

- A cislunar satellite formation consisting of a Lunar orbiter yields superior SST-based OD performance over those composed solely of Lagrangian point orbiters.
- Larger separations and shorter periodic orbits are beneficial for SST-based OD performance in cislunar space, whereas closer formations and longer periodic orbits tend to reduce performance.

- Satellite formations having differences in their dynamics present advantages for SST-based OD.

Navigation Data Observations:

- A satellite formation consisting of lunar orbiters is less sensitive to measurement errors than Lagrangian point orbiters.
- A measurement bias must be estimated or handled as a consider parameter in the OD process. The choice between estimating or considering the bias hinges on the specific demands of the mission scenario, with the estimated approach being more suited to formations such as Lunar/Halo, and the consider approach being preferable for Halo/Halo formations.
- Estimating clock-related parameters may negatively impact the accuracy of position/velocity estimations.
- In a CRTBP Halo-only scenario, the SST-based OD performance parity between range and range-rate systems is situated within a range-rate error spectrum of 0.04 mm/s to 0.14 mm/s for a corresponding range error of 1 m. Similarly, for angle-only measurements, an equivalent OD performance with a range error of 1 m is achievable within an angle measurement error range of 0.02 arcsec to 1.76 arcsec.
- In a typical small body scenario, a range-rate-only system with accuracies between 0.08 mm/s and 0.2 mm/s, as well as an inertial angle-only system with accuracies ranging from 8 arcsec to 30 arcsec, could potentially replicate the OD performance by a range-only system with a 1 m error (1σ).

Network Topologies Insights:

- Lunar satellite network topologies, whether mesh or centralized, generally achieve the greatest benefit from autonomous navigation systems when they feature large inter-satellite links and short orbital periods.
- The integration of additional satellites into lunar network topologies tends to enhance overall system performance.

Small Body and Interplanetary Cruise Phase:

- Depending on the small celestial body, SST-based systems provide similar OD performances if measurement errors are in the order of 1 m range, 0.01 mm/s range-rate, and 10 arcsec inertial-angle. Distant planet tracking only affects the convergence speed. Ground-based tracking combined with crosslink radiometric measurements decreases the positional uncertainty by an order of magnitude. In addition, ground-based tracking only performance could be achieved by satellite-to-satellite tracking only. Relative angle measurements provided higher information if the orbital configuration is in a close formation.
- Regarding orbital configurations, an increase in eccentricity and a decrease in the semi-major axis may lead to improved state estimation and faster convergence of the navigation solution around small solar system bodies.

- Different S/C areas, mass, and reflectivity in the formation may lead to reduced state uncertainty by increasing the system observability.
- SST alone does not provide accurate state estimation for satellite formations in the interplanetary cruise phase.

General Observations:

- Relying solely on the Condition Number (CN) or Unobservability Index (UOI) for evaluating system performance may lead to misleading conclusions, necessitating a comprehensive approach that considers both metrics.
- There is no significant difference observed between different filtering techniques within the simplified three-body problem, though more advanced filters show improved performance in dealing with nonlinearity around small solar system bodies.
- A realistic cislunar mission scenario has been presented where even high measurement errors could provide an OD solution complying with the requirements.

6

Operational Strategies and Navigation Data Flow

This chapter introduces the operational aspects that are related to navigation crucial to a real mission scenario. It begins with a detailed investigation of tracking windows, emphasizing the importance of careful planning and exploring near-optimal solutions. The chapter then proceeds to present strategies for both on-board and off-board tracking planning. A comprehensive overview of the autonomous navigation data flow is provided, offering an implementation of on-board logic in a practical context. This chapter provides insights into the operational considerations essential for mission planning and execution.

Parts of this chapter have been published in:
E. Turan, S. Speretta, and E. Gill, "Particle swarm optimization based tracking window planning for cislunar orbiters performing autonomous radiometric navigation", English, in *Proceedings of the 74th International Astronautical Congress (IAC)*, 74th International Astronautical Congress (IAC), IAC 2023 ; Conference date: 02-10-2023 Through 06-10-2023, 2023

Satellite operations involve various tasks essential for the success of space missions, including Orbit Determination (OD), trajectory adjustments, communication, and data acquisition. Autonomous capabilities allow satellites to make decisions and perform tasks without human intervention. This shift not only boosts operational efficiency but also addresses challenges in managing satellites in space. It may enhance reliability, adaptability, and overall mission success. In both autonomous and non-autonomous operations, tracking window planning plays a pivotal role in the effective execution of satellite missions, with a primary focus on OD. These windows represent specific time intervals during which ground-based or space-based tracking systems can observe and collect navigation data. In autonomous operations, the planning of tracking windows becomes even more critical as satellites must independently schedule and optimize these periods for OD. Operational challenges arise from limited resources, varying orbital dynamics, visibility constraints, and the need for synchronization with ground-based tracking stations. Additionally, in non-autonomous scenarios, careful planning is essential to ensure ground-based operators can efficiently manage and execute tracking operations. The upcoming sections dive into tracking window planning, exploring near-optimal solutions, the significance of both on- and off-board tracking strategies, and a detailed data flow for autonomous navigation. These discussions contribute to a comprehensive understanding of the operational challenges faced in satellite missions and the advancements brought about by autonomous capabilities.

6.1. TRACKING WINDOWS

Tracking windows requires critical considerations since they dictate when SST operations should occur. This timing plays a crucial role because tracking windows can produce different OD performances, potentially causing navigation requirements to be unmet and resulting in mission failures. It is worth noting that well placed tracking windows can lead to nearly optimal OD results, which can translate to reduced propellant usage, simplifying mission operations, and prolonged mission duration. However, grouping tracking windows can also help reduce overall setup costs in tracking, such as antenna pointing, actually lowering the overall navigation cost.

In essence, the key is to determine the most advantageous time windows for collecting observations that will maximize the effectiveness of the navigation filter. While it is generally ideal to equally distribute measurements across the entire orbit, practical constraints may block continuous tracking. These constraints can result from operational phases like Telemetry & Telecommand (TTC) and station-keeping periods. In some cases, modulating the ranging signal with telemetry or telecommand signals is feasible, effectively creating a single window for telemetry, telecommand, and tracking. However, conventional ranging methods require a specific amount of on-board power dedicated to the ranging signal, potentially limiting the available telemetry power. Consequently, in small satellites with limited on-board power employing SST, planning operations into different time frames becomes a necessity, as can be seen in Figure 6.1a.

In addition, as previously explained in Chapter 2, there are alternative ranging techniques beyond conventional methods that streamline ranging operations, such as telemetry ranging or telemetry/telecommand ranging [122], [125]. In such cases, it becomes possible to eliminate the ranging signal altogether, allowing the entire power capacity to

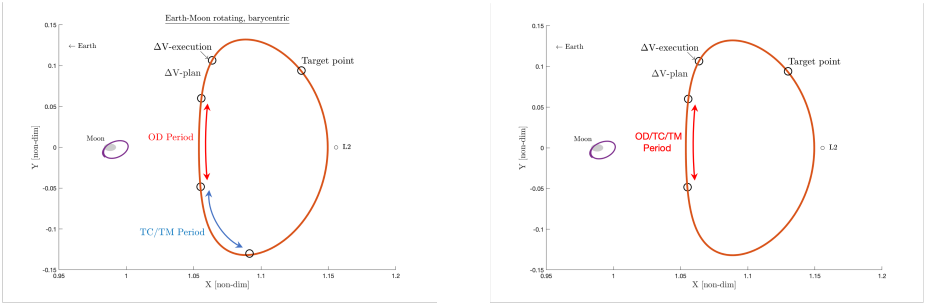

(a) Conventional ranging-based.

(b) Data-aided ranging-based.

Figure 6.1: Operational time windows.

be allocated for telemetry or telecommand transmissions. In these cases, the TTC and SST windows coincide, allowing all operations to be performed simultaneously, as illustrated in Figure 6.1b. Furthermore, if necessary, the total duration of SST/TTC/OD can be extended, resulting in more navigation data and telemetry transmission. Even in this scenario, the challenge is to find the optimal communication window that yields the best OD performance.

As pointed out in the previous sections, measurement geometry and, thus, tracking windows may affect the performance of the OD. Estimation performance could differ for the same number of measurements if tracking windows are not planned correctly. Consider a scenario where a Lunar orbiter and EML2 Halo orbiter perform SST in different time frames. Figure 6.2 represents OD results for two different tracking scenarios: when the Lunar orbiter is close to periselene and aposelene, respectively. The figure reveals that different tracking windows, including the same number of measurements, lead to different results. In this scenario, averaged position estimation uncertainties (1σ RSS) after the filter convergence between selected cases are around 3.2 m and 7.2 m, respectively. It should be noted that the difference could be marginal for different measurement geometries and orbital conditions.

In the previous study, [11] presented how SST can be planned using a simple strategy based on the relationship between the state uncertainty and the observation vector. Hill stated that observations are expected to be effective when inter-satellite measurement vectors are parallel with the axis of most uncertainty and less effective when vectors are perpendicular to the axis of most uncertainty, respectively. This has been investigated under the topic of observation effectiveness, which is the effectiveness of each observation to the filter (see section 4.1 for further details). Here, the SST planning is further studied from an on-board decision perspective, and the logic is discussed for implementation purposes.

A simple observation effectiveness scenario can be seen in Figure 6.3 where no useful information is observed in specific time frames. In particular, an error ellipsoid in each time step could be used to decide whether the current geometry could provide useful information to the filter. The figure shows the angle between the observation vector and the most uncertain positional direction. In other words, tracking windows could be

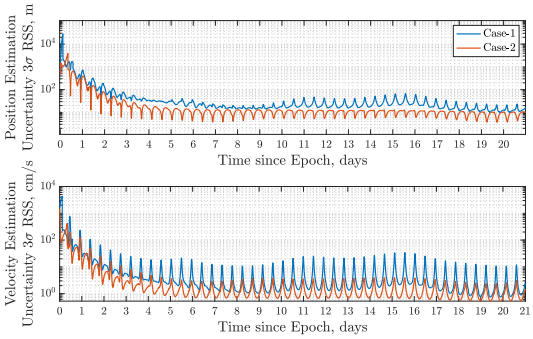

Figure 6.2: Lunar orbiter state estimation uncertainty for two-different tracking scenarios: Case-1 and Case-2 stand for tracking around aposelene and periselene, respectively.

planned based on this information, as discussed in [11].

SST-based OD can provide a real-time navigation solution for all the nodes in the system. If our interest is only in one of the nodes, then an error ellipsoid of the corresponding node could be used as a decision parameter for the SST windows. Consider a scenario where EML1 and EML2 Halo orbits perform SST and tracking windows are planned based on a design parameter defined in advance. A threshold value can trigger SST and thus the measurement update step in the estimation process. This leads to non-uniform SST using effective time-windows. In particular, if the angle between the most uncertain positional direction and the observation vector is lower than the given threshold, then SST takes action. This threshold needs to be determined on the ground based on mission requirements. Figure 6.4 presents the corresponding results with increasing

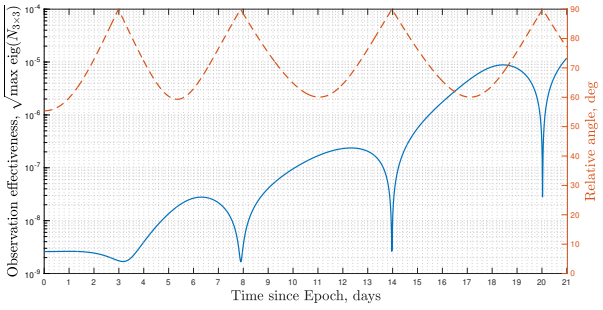

Figure 6.3: Obsevation effectiveness for an EML2 Halo orbiter formation and the angle between the most uncertain positional direction and the observation vector. Hill [11] originally proposed the analysis illustrated in this figure.

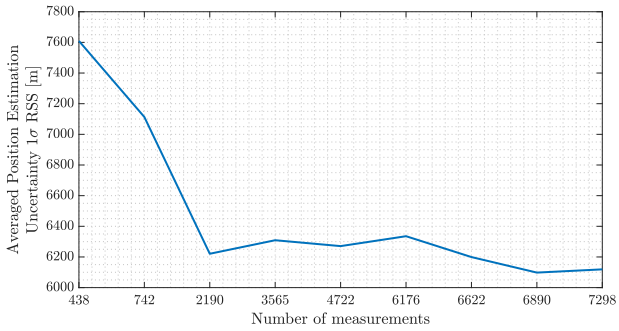

Figure 6.4: Averaged position uncertainty 1σ RSS for a Halo/Halo SST scenario. The x-axis represents the total number of measurements distributed over the full mission after five days of initial tracking according to the algorithm given in the study.

threshold values, allowing more measurements to be collected. However, no significant improvement is observed after a specific threshold. In other words, there is no benefit in collecting measurements at particular geometries. Similarly, on-board SST decisions can be planned: this would require only a design parameter, which can be found depending on mission requirements.

It should be noted that on-board tracking decisions based on this approach may still not be optimal considering operational constraints such as inter-satellite distance or data transfer windows. There might be no useful observation for a period in which tracking must be handled. Station-Keeping Maneuver (SKM) periods might have been planned for frequent intervals in which there might be no useful observation. Since measurement bias estimation is directly related to the number of measurements, it might be better to perform tracking as much as possible at the very beginning of a mission, in which, again, there might be no useful observation for orbital states. For such a complicated situation, another approach might provide a near-optimal solution for tracking windows. In the coming section, PSO-based tracking window planning will be presented in detail.

6.1.1. PARTICLE SWARM OPTIMIZATION-BASED TRACKING WINDOW PLANNING

This section offers a PSO-based offline tracking planning strategy for SST-based OD. PSO is an optimization algorithm inspired by the collective behavior of animals where a population of potential solutions, represented as particles, iteratively explores a search space [202]. Each particle adjusts its position and velocity based on its own experience and that of its peers. PSO efficiently navigates through complex, high-dimensional spaces to find near-optimal solutions. It is widely used in various fields due to its simplicity and effectiveness in tackling optimization and search problems.

There are various OD performance analysis metrics given in scientific literature that can be derived through methods such as Monte Carlo simulations, CRLB, or the observability analysis that includes observability indices, condition numbers, RMS or RSS po-

sition/velocity error or uncertainty (see Chapter 4 for further details). Any of these metrics can serve the same purpose as outlined in this research. However, for this study, the length of the largest axis of the error ellipsoid has been adopted as given in Eqn. 4.45.

In summary, PSO is used to minimize the overall position and velocity uncertainty by finding near-optimal tracking windows. In this context, the optimization problem is given as follows:

$$\begin{aligned} \min \quad & \beta_{av} = \frac{1}{2}\sum_{j=1}^{2}\frac{1}{n}\sum_{i=1}^{n} 3\max(\sqrt{\lambda}_j) \\ \text{s.t.} \quad & 0 < T_{SST} < T_{end} \end{aligned} \tag{6.1}$$

where λ_j for $j = 1,2$ are the eigenvalues of $P_{i_{3\times3}}$ representing the position and velocity sub-matrices, T_{SST} represents SST windows (timing points) with the number $w = 1,2,3$ (e.g., three tracking windows), while T_{end} is the simulation duration. It should be noted that, based on different scenarios, the constraints vary throughout this study, and more details are given in the following paragraphs.

In brief, the OD simulation starts with an array containing the initial times of each tracking window determined by the PSO particles. Subsequently, the filter utilizes SST observations obtained during these tracking windows with the starting times defined by the particles and a fixed tracking duration. As the simulation progresses, β_{av} is assigned to the respective particle, and this process continues until the maximum number of particles is achieved in the first iteration. In each iteration, the global fitness value (which represents the minimum position and velocity uncertainty) is stored until the maximum iteration count is reached. This process is given in Algorithm 7.

This section investigates autonomous on-board OD for cislunar formations: initial simulations will focus on a two-satellite formation that includes a satellite in an Earth-Moon L1 NRHO ($T = 7.83$ days, $C_j = 3.00$) and an L2 orbiter ($T = 14.14$ days, $C_j = 3.11$). Later simulations will include a second orbiter around the EML1 point ($T = 12.10$ days, $C_j = 3.10$). Detailed initial conditions can be found in Chapter 5. Telemetry ranging has been assumed as the inter-satellite ranging method simplifying the tracking operation, and measurement errors (1σ error of 10 m) have been considered without any bias. Each tracking window, as a reference set, spans a continuous 2 days period with measurements taken every 180 seconds within that window. To put this into context, an example taken from ground-based conventional PN tracking (assuming the T2B code) involves approximately 175 s for signal acquisition, 0.25 s to 500 s for signal correlation (including ambiguity solving) and user-defined measurement intervals on the major tone (e.g., 0.5 s). In practice, additional measurements can be conducted, and observations can be averaged after signal acquisition to improve accuracy. Given the total tracking window duration and the overall ranging sequence duration, a measurement cadence of 180 s is considered an appropriate choice.

It is important to note that the satellites within the formation have different orbital periods and, consequently, the measurement geometry continually changes over time, making it impossible to plan SST when one orbiter passes a specific point in its orbit and the other is at a completely different location. For example, the first orbiter may be in a high-velocity region in the NRHO, while the second orbiter is in a low-velocity region in the EML2 Halo orbit. Due to this variability, the trajectory was not divided into

Algorithm 7: PSO-based Tracking Windows: A Simplified Case.

Given: P_0, X_0, Q, N_k, LB, UB
Minimize:
$f(X)$, minimizing β_{av}
subject to $0 < T_{SST} < T_{end}$, $T_{SST} = [T_1, T_2, ..., T_l]$
Initialize: For each particle i in a swarm population size Ps
X_i a random vector within [LB UB]
V_i a random vector within [LB UB]
Evaluate the fitness $f(X_i)$=$\beta_{av,i}$
$pbest_i$ with a copy of $T_{SST,i}$
$gbest$ with a copy of $T_{SST,i}$ with the best fitness
while $k \geq N_k$ **do**
  $i \leftarrow i + 1$;
  Update V_i^k and X_i^k for each particle i by
  $V_i^{k+1} = wV_i^k + c_1 rand_1(pbest_i - X_i^k + c_2 rand_2(gbest - X_i^k))$
  $X_i^{k+1} = X_i^k + V_i^{k+1}$
  Evaluate fitness $f(X_i^k)$
  $pbest_i \leftarrow X_i^k$ if $f(pbest_i) < f(X_i^k)$
  $gbest \leftarrow X_i^k$ if $f(gbest) < f(X_i^k)$
end

separate segments, and the different combinations were not simulated. Instead, the PSO algorithm seeks a near-optimal solution, providing the best averaged OD uncertainty. To achieve this objective, six distinct scenarios are explored to identify the most favorable tracking windows under different conditions:

- Case-A: Four tracking arcs.
- Case-B: Four tracking arcs, each within four equally divided time windows.
- Case-C: A single tracking arc initiated after the convergence period.
- Case-D: A single tracking arc planned when the inter-satellite distance is less than 90 000 km.
- Case-E: Three tracking arcs incorporating measurement bias as a consider parameter.
- Case-F: Three tracking arcs for a satellite formation consisting of three spacecraft in a mesh topology, where all satellites are linked.

Regarding station-keeping strategies for Halo orbits, it is recommended to conduct three or four SKM per orbit [203]. Reflecting this, the nominal scenario, referred to as Case-A, incorporates four tracking sessions. Similarly, Case-B also has four tracking sessions, but these are distributed equally throughout the mission duration. Case-C introduces an initial orbit determination period. In Case-D, the focus shifts to considering

the inter-satellite distance as a critical operational constraint, which could influence the timing and frequency of tracking sessions. Case-E delves into the effects of measurement bias on tracking windows. Finally, Case-F presents a more complex scenario involving a satellite formation consisting of three spacecraft, adding another layer of complexity to the tracking strategies. Each of these cases presents a unique perspective on the operational challenges and considerations.

Simulation results are presented in the following subsections, starting from the nominal scenario and continuing by progressively adding more constraints.

CASE-A: NOMINAL

This presents the standard scenario in which the goal is to identify SST windows (a total of N) providing the best overall OD accuracy. Here, straightforward limitations are imposed, including tracking arcs, which must fall within the 0 to T_{end} range. Since three or four station-keepings are advised per Halo orbit [203], four tracking windows are selected, each comprising 1000 measurements taken at intervals of 180 seconds, resulting in approximately two days of continuous tracking. A further constraint was imposed to avoid overlapping two tracking windows: the PSO typically avoids this and would not provide optimal results. However, the constraint limits the search space and reduces the simulation time. To sum up, these constraints can be outlined as follows:

$$\begin{aligned} \min \quad & \beta_{av} \\ \text{s.t.} \quad & 0 < T_{SST} < T_{end} \\ & T_{SST} = [T_1, T_2, T_3, T_4] \\ & T_l = 2.08\,\text{days} \\ & T_{l+1} - T_l = 2.08\,\text{days} \end{aligned} \tag{6.2}$$

Figure 6.5 presents the comparison between equally distributed tracking windows and the tracking windows provided by the PSO technique: the colored vertical lines in the figure represent SST points for each approach. Basically, the PSO pushes the very first two tracking windows into the very initial phase of the mission, as expected, due to the high initial uncertainty in the system. However, distributing tracking arcs could not provide an accurate solution since the first tracking session was not long enough to capture valuable information. This results in a 6 km (3σ) increase in the overall position uncertainty.

This case was suitable for illustration since there were only four tracking sessions. However, almost two days of continuous tracking might be too long for small satellite missions. For this reason, in the second scenario, each tracking session is reduced to 10 hours (T_l = 10 hours), representing 200 measurements once every 180 s. Figure 6.6 and 6.7 illustrate what would happen in this scenario, showing a trend for the first figure, EML1 NRHO/EML2 Halo: pushing tracking windows into the very early phase of a mission to reduce the initial position uncertainty and distributing fewer tracking sessions at a later stage, since convergence had already been achieved. The second one, EML1 Halo/EML2 Halo, shows a trend of distributing tracking sessions throughout the mission.

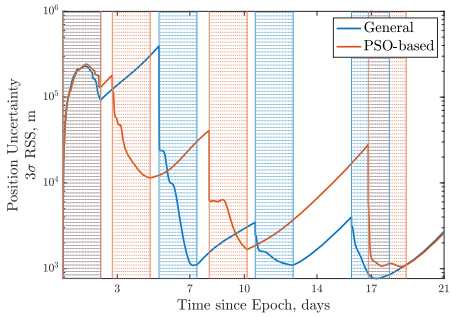

Figure 6.5: Comparison of PSO-based and equally distributed tracking windows (EML1 Halo/EML2 Halo case). Vertical lines represent SST points for each solution.

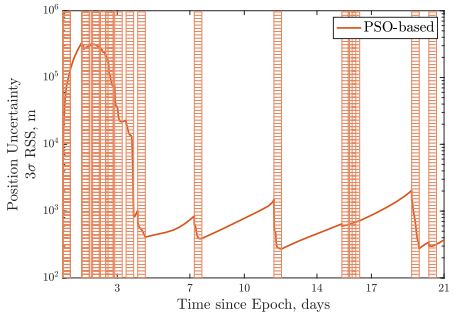

Figure 6.6: PSO-based SST windows and corresponding position uncertainty (EML1 NRHO/EML2 Halo case)

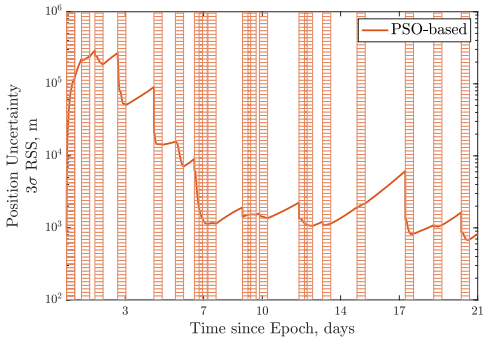

Figure 6.7: PSO-based SST windows and corresponding position uncertainty (EML1 Halo/EML2 Halo case).

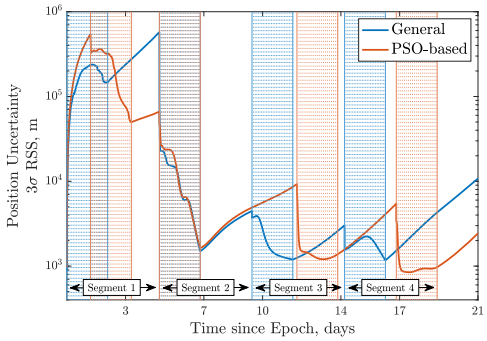

Figure 6.8: Comparison of PSO-based and equally distributed tracking windows (EML1 Halo/EML2 Halo case).

CASE-B: EQUALLY DIVIDED TIME WINDOWS

In the previous case, the tracking windows were distributed over the entire mission duration; however, there might be the need to have a tracking window at specific intervals due to mission constraints. This then requires one to divide the entire mission span into segments and place a tracking arc into each part, and the PSO can help find the best tracking windows for each corresponding segment. We can formulate the problem as follows:

$$
\begin{aligned}
\min \quad & \beta_{av} \\
\text{s.t.} \quad & 0 < T_{SST} < T_{end} \\
& T_{SST} = [T_1, T_2, T_3, T_4] \\
& LB = [0, 4.7, 9.4, 14.2]\,(\text{days}) \\
& UB = [4.7, 9.4, 14.2, 18.9]\,(\text{days}) \\
& T_l = 2.08\,\text{days} \\
& T_{l+1} - T_l = 2.08\,\text{days}
\end{aligned}
\tag{6.3}
$$

Figure 6.8 illustrates the corresponding result. It is interesting to see in this case that the PSO skipped the very first days and placed the first tracking arc around day 2. This means the relative geometry between satellites (thus, the measurement geometry) is better after around day two than the very first days, compensating for increased state uncertainty. Overall, around 4.5 km (3σ) positional improvement has been observed (26 m after the second tracking window).

CASE-C: AFTER THE CONVERGENCE PERIOD

Up to now, simulations have indicated the advantages of scheduling tracking windows during the initial phases of missions, primarily due to high initial uncertainties. From an operational perspective, an initial OD will be performed either from ground-based sources or from another external source, providing an initial state to the on-board filter. After the convergence period, the PSO can seek the near-optimal tracking window: a single tracking window starting after day 4, determined by running a separate simulation.

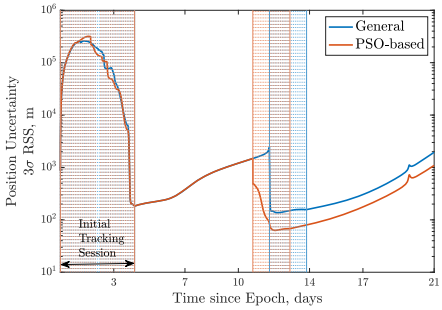

Figure 6.9: Comparison of PSO-based and nominal (midpoint) tracking windows (After convergence, EML1 NRHO/EML2 Halo case).

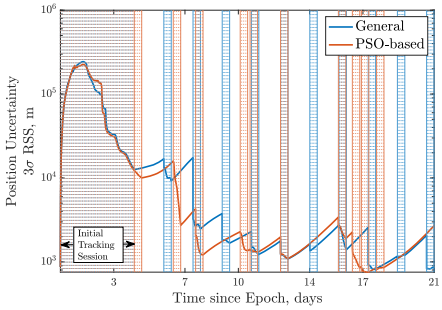

Figure 6.10: Comparison of PSO-based and equally distributed tracking windows (After the initial tracking session, EML1 Halo/EML2 Halo case).

The optimization problem can be defined as:

$$\begin{aligned} \min \quad & \beta_{av} \\ \text{s.t.} \quad & 0 < T_{SST} < T_{end} \\ & T_{SST} = T_1 \\ & LB = 4\,\text{days} \\ & UB = 18.92\,\text{days} \\ & T_l = 2.08\,\text{days} \end{aligned} \tag{6.4}$$

The comparison between a single tracking window found by the PSO and a midpoint selected tracking window is shown in Figure 6.9, where the PSO shifts the tracking window earlier than the midpoint of the mission, resulting in a better overall state uncertainty. In case the number of tracking windows is increased to ten, while each tracking session is reduced to 10 hours, the same pattern can be seen as given in Figure 6.10 ($\approx$125 m (3σ) positional improvement with the PSO).

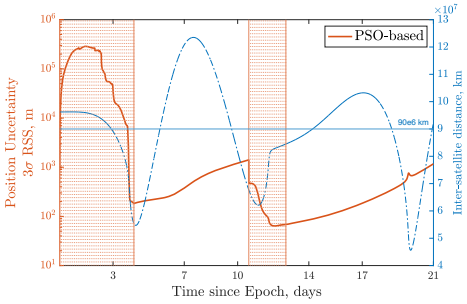

Figure 6.11: PSO-based tracking window planning under the distance constraint.

CASE-D: CONSTRAINED DISTANCE

Another operational constraint can be related to the communications system: inter-satellite distance can be limited due to the on-board power used for ranging. For such cases, the tracking windows may be restricted to short intervals only when the distance is lower than a specific value. In this case, the mean inter-satellite distance (90 000 km) is investigated and set as a constraint. Figure 6.11 illustrates the corresponding results, while the following equations represent the problem:

$$\begin{aligned} \min \quad & \beta_{av} \\ \text{s.t.} \quad & 0 < T_{SST} < T_{end} \\ & T_{SST} = [T_1, T_2, T_3] \\ & \rho \leq 90\,000\,\text{km} \\ & T_l = 2.08\,\text{days} \\ & T_{l+1} - T_l = 2.08\,\text{days} \end{aligned} \tag{6.5}$$

CASE-E: CONSIDERED BIAS

In Chapter 5 it has been shown that systematic bias significantly impacts measurement quality, consequently influencing the OD performance. There are various approaches to handling systematic biases, and one of them is implemented in this study using a CKF. In this case, the filter takes into account the impact of measurement bias, which has been assumed to be 10 m. The optimization problem is the same as given in Eqn. 6.2, the only difference being the covariance matrix in the filter.

Figure 6.12 presents the cases where both PSO-based tracking windows: the former considers measurement bias and incorporates it into the filter, while the latter does not. As shown, the PSO provides completely different solutions, highlighting that systematic biases can affect the tracking windows timing. It is worth noting that the average OD uncertainty is around 9773 m (3σ) for the considered bias case, while it is around 9665 m (3σ) for the no-bias scenario, as expected. Using the tracking window of the no-bias case instead of the tracking window of the considered case brings the average solution of 9933 m (3σ) when measurements are affected by a constant bias. This demonstrates

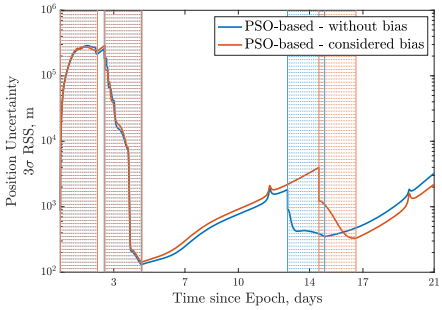

Figure 6.12: PSO-based tracking window planning under the measurement bias constraint.

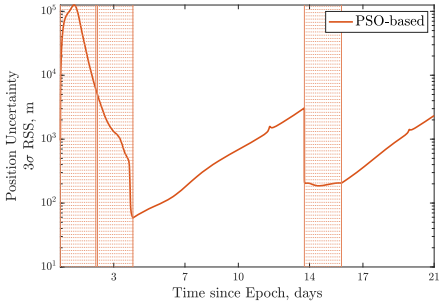

Figure 6.13: PSO-based tracking window planning for a satellite formation formed by 3 S/C in a mesh topology.

that measurement biases can impact OD uncertainty under specific geometries, leading the PSO to recommend a different time window to minimize overall OD uncertainty.

CASE-F: NETWORK TOPOLOGY

Adding a third satellite in a mesh topology to the cislunar formation leads to an optimization problem equivalent to the one expressed in Eqn. 6.2, with the sole difference being the size of the estimated state vector and the increased number of inter-satellite links (number of measurements). The PSO-driven SST windows are illustrated in Figure 6.13, where it is interesting to see that the final tracking window is long enough to maintain a stable uncertainty. In this case, conducting just a few hours of tracking would be sufficient. Still, it is worth noting that OD performance is more accurate (average 2141 m, 3σ) in the mesh topology due to the higher amount of links, allowing for more relaxed tracking durations.

In this section, it has been demonstrated that the PSO can provide an accurate solution for SST windows for cislunar satellite formations performing on-board OD. This algorithm can be used in advance on the ground to plan TTC windows. Although the given approach is applied only to the EML1 Halo/NRHO/L2 Halo case, this method applies to missions in different orbital regimes. It is worth noting that several limitations can be further investigated. In this section, the duration of tracking sessions is assumed

fixed, however, this can also be optimized for much more compact planning. Furthermore, ΔVs can be optimized by minimizing the local best OD estimations instead of minimizing the overall OD accuracy.

6.2. AUTONOMOUS ORBIT DETERMINATION DATA FLOW

This section provides a comprehensive overview of the autonomous navigation data flow, offering the implementation of on-board logic in a practical context. Building on the findings presented in the previous chapters, the objective is to enhance understanding from both implementation and system analysis perspectives. Figure 6.14 provides a simplified block diagram, while a more detailed representation is offered in Figure 6.15.

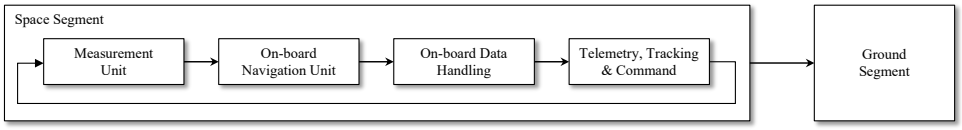

Figure 6.14: Simplified Autonomous Orbit Determination Data Flow.

The core components of the autonomous on-board navigation system include an estimation filter and a measurement unit. This relies on commands, or tracking planning, either obtained in advance from a ground source or autonomously decided on board. Ground-based tracking planning uses algorithms such as the PSO-based method, generating near-optimal solutions for tracking windows during various mission phases. These predefined time periods can then be transmitted from the ground to the spacecraft.

Alternatively, on-board decisions for tracking are feasible, as presented in the previous section. One such approach involves calculating the angle between the most uncertain direction and the measurement direction, enabling the identification of optimal time frames. However, both planning approaches demand careful consideration due to potential constraints imposed by TTC windows, scientific plannings, visibility constraints introducing mission-dependent variations. A comprehensive analysis of mission requirements, particularly those related to the navigation system, becomes imperative in such applications.

The measurement unit receives commands either from the ground or on-board, to perform SST. This radiometric measurement unit generates time-stamped range/range-rate navigation data, crucial for subsequent processing at the estimation unit. Chapter 2 provided detailed information on how SST works for satellite formations. From the timing perspective, measurements can be averaged to reduce noise. Considering a signal acquisition of approximately 175 s, which is assumed for ground-based tracking, signal correlation, and measurement intervals can be defined as 0.25 s to 500 s and 0.5 s, respectively, resulting in a measurement cadence of around 180 s. Increasing this duration could improve measurement quality, however, affects the number of measurements to be provided to the navigation filter.

The observations, processed through this timing framework, are then transmitted to the on-board data unit. The estimation unit reads the available observations and performs OD. As real-time estimation forms the basis of this work, a sequential-type fil-

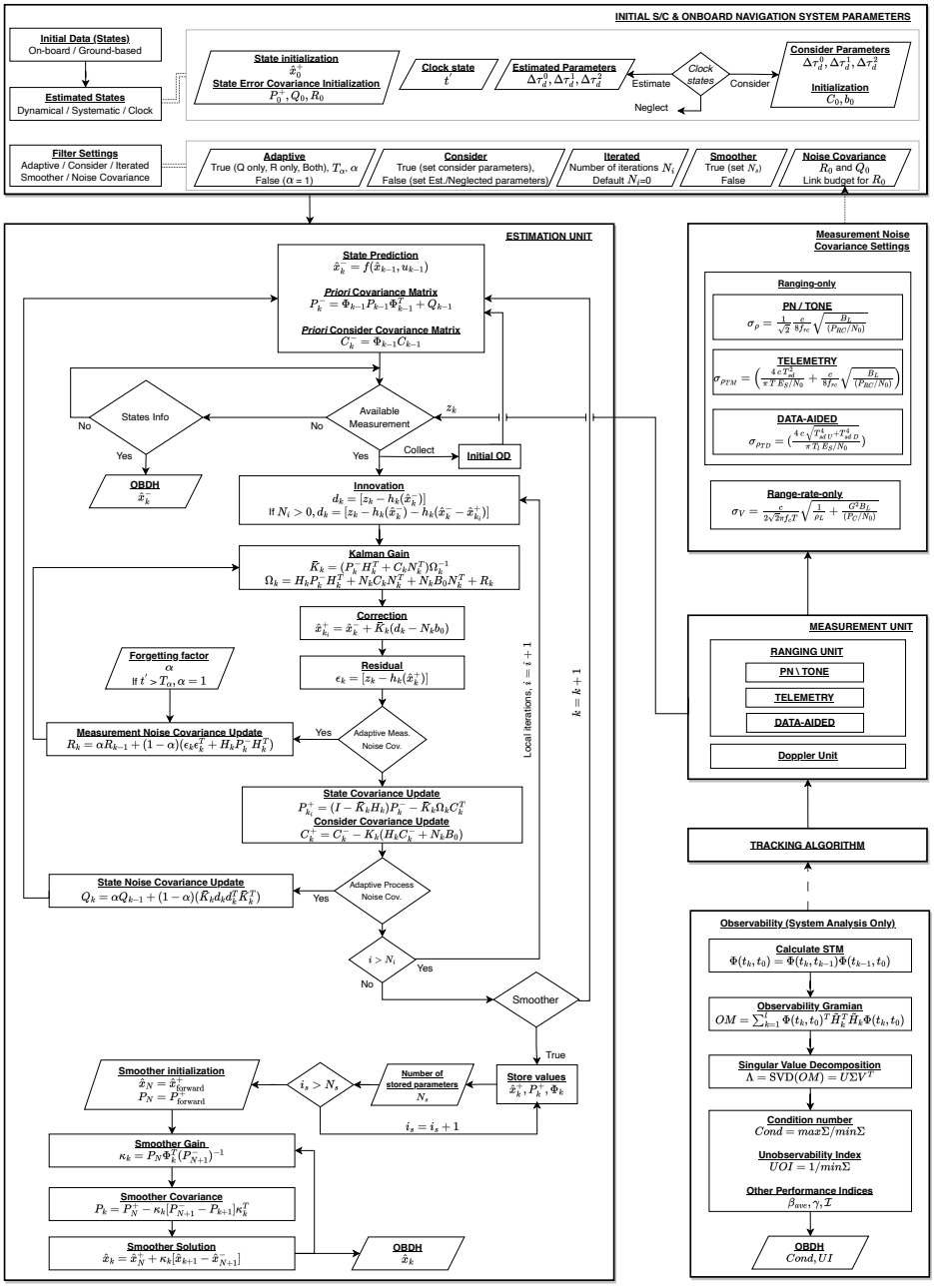

Figure 6.15: Detailed Satellite-to-Satellite Radio Tracking-based Autonomous Orbit Determination Data Flow.

tering approach is adopted, as discussed in Chapter 3. Even though measurements are intended to be processed in real-time, there will always be a lag processing in real-time measurements. However, as discussed in previous chapters, spacecraft states can be predicted.

To initialize the on-board navigation system, a ground or on-board command is essential. While this dissertation did not dive into initial OD, a viable approach involves leveraging information from carrier spacecraft or objects. In such scenarios, the on-board filter of the spacecraft being deployed utilizes the state vector of the carrier spacecraft. Such an approach can be particularly effective in scenarios where the deploying spacecraft has a well-determined orbit, providing a reliable reference point. Although potentially less accurate, this data could be sufficient for the on-board filter to converge into true states. It should be noted that this initialization could potentially consider the deployment dynamics depending on the mission scenario. EKF-type filters tend to diverge if the initial guesses are not close to true states. For this reason, it has been recommended to collect measurements at the very beginning of a mission and perform least-squares to initialize the Kalman-type filter. The on-board filter necessitates certain settings definition, primarily the states to be estimated: dynamical states, systematic errors, and clock parameters. Notably, bias, drift, and aging can be estimated, neglected, or estimated for certain intervals. The choice of the estimated state vector size impacts filter performance, illustrating the need for thoughtful consideration. Although not detailed in the presented data flow, it should be noted that station-keeping maneuvers, a routine aspect of mission operations, can be estimated, considered, or neglected, taking into account the inaccuracy of executed ΔVs.

It has been presented in Chapter 5 that consider filtering is more suitable for Halo / Halo formations, while estimating is preferable for Halo / Lunar formations, contingent on mission configuration. An essential aspect involves determining the initial process and measurement noise covariance matrices. The latter can be defined based on the communication link budget and weighted for expected performance depending on the selected ranging method. For various radiometric measurement methods, their expected performances are given in Figure 6.15. It should be noted that there is no need to modify weightings during the mission if the communication link budget is expected to be stable. However, there might be a case where a mission uses more than one communication data rate during operation (data-aided ranging only). In this case, measurement noise covariance uncertainties need to be edited accordingly. Basically, the spacecraft can autonomously adjust these matrices: this is called an adaptive estimation approach based on residuals, although this flexible method affects state estimation and may be stopped after a certain time period.

Furthermore, the estimation unit must also be aware of whether a smoother will be used, with flexibility for this decision throughout the mission. Depending on the chosen implementation, a smoother can yield a solution representing past states, necessitating the predefined definition of the number of stored parameters.

The Kalman-type filter illustrated in Figure 6.15 is a combination of EKF, CKF, AEKF, and IEKF introduced in this dissertation. The transitions between these algorithms hinge on specific settings: without a defined consider parameter, CKF turns into EKF. Activating the adaptive approach converts it into AEKF while incorporating local iterations

during the update step results in the filter adopting the characteristics of IEKF. These algorithms present varying complexities, as given in Chapter 3. Similarly, this type of flow can also be applied to UKF. The filter can provide state information once every predefined time interval to the data unit.

Although it might not be necessary to switch between filters during mission operations, certain phases could benefit from specific filters. For instance, the number of local iterations can be increased before the SKM following an OD period. This increases the number of operations, but leads to a more reliable solution. At the same time, the adaptive approach might be eliminated, providing a more stable solution. This can be done in practice by commanding parameter settings from the ground, e.g., iterations, thresholds, update rates etc. It is important to note that the presented data flow serves not only as a guide for implementation but also for error analysis, providing a comprehensive overview of mission analysis from a navigation perspective. It includes considerations such as weighting measurement errors, defining essential initial parameters, and presenting different filtering techniques. This autonomous SST-based OD data flow is a valuable resource for anyone interested in constructing such an OD system (See also Appendix D for the performance analysis toolbox).

6.3. SUMMARY

This chapter introduced the operational aspects crucial for a real mission scenario. It provided an in-depth investigation of tracking windows, emphasizing the significance of careful planning and exploring near-optimal solutions. The importance of strategic tracking planning, whether executed on-board or off-board, was thoroughly examined. A PSO-based algorithm was introduced, showing that a near-optimal solution could be derived based on different challenging operational constraints. The chapter further dived into the details of the autonomous navigation data flow, offering practical insights into implementing onboard logic while serving as a valuable tool for error analysis.

7

CONCLUSION

This concluding chapter contains key insights, findings and innovations from the previous chapters, providing a comprehensive summary of the research undertaken on autonomous Orbit Determination (OD) for small satellite missions in deep space and cislunar environments, focusing on Satellite-to-Satellite Tracking (SST). The chapter begins by summarizing the key findings, contributions, and answers to the research questions. This is followed by an outlook, where potential areas for future research are identified and discussed. These suggestions aim to further enhance the capabilities and efficiency of OD in future satellite formation missions beyond Earth.

7.1. SUMMARY

This dissertation investigated the autonomous Orbit Determination (OD) for deep space and cislunar small satellite missions, focusing on Satellite-to-Satellite Tracking (SST). It started with an extensive literature review on the historical and future context of small satellite missions in deep space (Chapter 1), highlighting the crucial role of cost-effective autonomous OD as an alternative to expensive ground-based tracking.

In Chapter 2, Satellite-to-Satellite Tracking (SST) was studied, examining its relevance in improving Distributed Space Systems (DSS) capabilities. An in-depth analysis of the three primary data types - range, range-rate, and LOS angles - derived from radiometric measurements is provided, along with their contributions to autonomous strategies.

Chapter 3 presented a detailed evaluation of the OD process, highlighting the differences between ground-based and SST-based strategies. This Chapter also critically evaluated existing literature and identified areas needing further research, especially from an OD perspective. This chapter also established navigation requirements for different mission scenarios and introduced various models based on SST, which include dynamical, measurement, and estimation aspects.

The following Chapter 4 focused on performance analysis methods critical for OD. Observability aspects were discussed in the context of SST-based operations within the Circular Restricted Three-body Problem (CRTBP), including analytical derivations for measurement sensitivity and Gramian matrices. The chapter concluded with CRLB and other performance analysis tools.

In Chapter 5, a comprehensive analysis of SST methods was conducted for formations under various conditions. The chapter delved into the dynamics, measurements, and estimation aspects of OD, examining the two-body and three-body problems, measurement errors, filtering performance, and the impact of different observation data types. This chapter also provided an in-depth analysis of realistic mission scenarios, including lunar missions, networks, and scenarios involving small celestial bodies and interplanetary cruises.

Finally, Chapter 6 shifted the focus to the operational aspects of real mission scenarios, exploring tracking windows and strategies for ground-based and on-board tracking planning. This provided practical insights into implementing on-board logic and operational constraints for mission planning and execution.

In summary, this dissertation has significantly extended the current understanding of SST-based autonomous OD for small satellite DSS missions in deep space and cislunar environments. This work has highlighted the crucial role of inter-satellite measurements and explored various aspects to improve system performance. Using a simple data-aided ranging method, SST provides a navigation approach meeting small satellite mission requirements. While considering the complexities and challenges presented in deep-space missions, this work offers a valuable resource for future research and practical applications for autonomous navigation. As the demand for small satellite missions in deep and cislunar space will grow, the contributions of this work will play a critical role in spacecraft navigation. In brief, this dissertation aimed to answer the following research questions:

- What are the current scientific and technological advances in autonomous navigation for deep space small satellites?

It was essential to first gain a comprehensive understanding of deep space navigation to address this research question. In recent years, there has been an increasing interest in utilizing small satellites for exploring cislunar and deep space. Traditionally, planetary navigation relies heavily on ground-based radiometric tracking, a method that, while effective, often results in high operational costs due to crowded communication networks and an extensive support required from mission operation teams. As we progress into a new era of deep space exploration, there is an increasing need for autonomous navigation systems that can operate independently of ground-based support.

This research question has been mainly answered in Chapter 1, providing a comprehensive review of recent advancements in autonomous navigation systems for deep space small satellites, underscoring autonomy as a key factor in enhancing mission capabilities. An analysis of 65 proposed missions (see appendix B), mainly targeting cislunar space and small celestial bodies for surface mapping and characterization purposes, revealed a predominant reliance on ground-based navigation, with only a few choosing autonomous methods. The chapter delved into various deep space navigation techniques suitable for small satellites, such as optical, X-ray pulsar, and satellite-to-satellite radio-tracking-based navigation, detailing their operational principles and common error sources. A comprehensive categorization for deep space navigation was provided from the perspective of data collection, autonomy, and methods (see Table 1.5), including their advantages, disadvantages, and mission examples (see Table 1.3). After that, the focus has been shifted to crosslink radiometric navigation, which integrates well with existing communication systems, offering a significant advantage in terms of adaptability for current missions (see Table 1.5). Considering missions around small bodies and cislunar space, this navigation method demonstrates accuracy within tens to hundreds of meters and millimeters per second in position and velocity, respectively (see Table 3.3). The survey results indicated that a majority of missions (>%58) utilize inter-satellite communication, with a significant portion able to benefit from autonomous crosslink radiometric navigation. This approach not only simplifies missions by reducing the distance for navigation measurements, thereby lowering accuracy demands and complexity, but also reduces overall mission cost. Moreover, autonomy opens up possibilities for new applications, particularly where direct communication with Earth is not feasible.

- What are the characteristics of a simple radio-tracking system for satellite formations in deep space?

This research question has been addressed in Chapter 2. The investigation primarily focused on various radio-frequency-based ranging methods, evaluating their effectiveness for satellite-to-satellite tracking. It has been found that ranging provides marginally superior navigation solutions compared to other observational data types, specifically in cislunar space. Consequently, the study focused on examining simple-ranging algorithms, supported by a detailed review of the existing literature. The chapter presented an extensive review of SST ranging methods, including their performance characteris-

tics, as illustrated in Figure 2.21. Key elements such as inter-satellite radio link, measurement error budgets, and error models were discussed, with a summarized overview provided in Table 2.5. A crucial finding of this research was the importance of a simple yet reliable ranging method, especially considering the limitations in communication power available for small satellites. Consequently, the study pivoted towards exploring the data-aided ranging algorithm. This method eliminates the need for separate ranging signals in the communication chain, offering a simplified approach over traditional ranging methods. The performance of this method was thoroughly examined, presenting that at high data rates, telemetry and telecommand signals could effectively substitute traditional ranging methods.

In brief, the research found data-aided or telemetry ranging methods to be more advantageous than conventional tone/PN ranging methods for small satellite formations in deep space. This is because traditional methods require a separate ranging signal, which reduces the power for telemetry, resulting in tracking and telemetry sessions in different time periods. In addition, the ranging system could benefit from the high transmission data rate in close proximity operations. However, data-aided methods offer a significant benefit by allowing simultaneous tracking and telemetry transmissions within the same time frame, allowing more navigation data to be collected. A pivotal factor influencing the choice of a data-aided ranging method is the data rate, with a threshold identified at higher than 10 kbps. The research concluded that even at lower data rates, data-aided ranging solutions are generally sufficient to meet the majority of navigational needs for deep space small satellites.

- How can we describe the fundamental aspects and design principles of a satellite-to-satellite tracking-based autonomous on-board orbit determination system for satellite formations?

To answer this research question, Chapters 3 to 6 delved deeply into the three main aspects of OD: dynamics, measurements, and estimation. This comprehensive investigation separates itself from traditional ground-based OD by focusing on the simultaneous and autonomous estimation of at least two spacecraft absolute states, relying solely on satellite-to-satellite tracking data. This approach closely links with the concept of autonomy, typically associated with on-board navigation, presenting a unique set of challenges.

From a dynamical perspective, this research examined various orbital configurations and their performances under different environmental and dynamical conditions. These ranged from the simplicity of two-body dynamics to the complexities of three-body interactions and high-fidelity dynamics. The findings underscored that there is no one-size-fits-all answer for different mission profiles and orbital configurations. Notably, close proximity operations tend to negatively impact OD performance as state differences become less observable within a given reference frame. Conversely, designing operational orbits with varied geometries can enhance the collection of useful observations. For instance, co-planar orbits or those with similar sizes and shapes tend to negatively impact the OD system more than non-coplanar orbits. This finding underscores the importance of diverse orbital configurations in improving observation quality and system performance.

A significant observation from this research is the advantage of modeling all perturbations in OD. This insight suggests that relying on simplified dynamics for on-board implementation may not be the most effective approach. Instead, incorporating high-fidelity dynamical models that account for various perturbations proves to be beneficial. The extent to which these dynamics are modeled is, however, related to the specific requirements of the mission. This balance between model complexity and mission needs is a crucial consideration in designing and implementing autonomous OD systems. The analysis clearly indicated that a more comprehensive approach to modeling dynamics, even at the cost of increased on-board computational requirements, can significantly enhance the accuracy of autonomous OD systems in satellite-to-satellite tracking scenarios.

Regarding measurements, the research showed that the orbital geometry significantly influences the system's observability and sensitivity to measurement errors. This implies that certain measurement methods might be unsuitable for specific mission scenarios and phases. For instance, satellite-to-satellite tracking with a lunar orbiter in cislunar space indicated that less accurate measurements could still suffice for navigation requirements, allowing for simpler data-aided ranging methods in such missions. Another vital aspect addressed was systematic errors. The analysis underscored the necessity of either estimating or considering biases in the navigation filter, as neglecting these could lead to significant inaccuracies. The approach to handling biases varies depending on the orbital configuration. Additionally, the research explored observation data types, revealing that the suitability of a particular data type for navigation depends heavily on the mission profile. Generally, range observations were found to offer better performance compared to range-rate and angle data. Thresholds for these observations were also established, providing guidance on focusing on certain navigation data types based on the mission's specific requirements and profile.

Finally, the aspect of estimation was addressed, completing the whole picture. Various filtering techniques were investigated for their performance capabilities and complexities. Adaptive approaches were found to be effective in managing uncertainties in dynamics and measurements, although they might affect the state estimation convergence speed. The research suggested switching between filters during mission operations. Depending on the mission configuration, the local iterations during the filter update step can be adjusted by increasing the total number of iterations for satellite formations in less observable configurations. As discussed in the previous paragraph, estimate or consider the systematic errors could be followed depending on the orbital configuration. As crucial as previous aspects, the research highlighted the critical role of tracking window planning, with measurement geometry emerging as a key performance driver. On-board and off-board strategies were discussed, presenting different ways of handling tracking planning.

In conclusion, this research question was answered as follows: The fundamental aspects of satellite-to-satellite tracking-based autonomous on-board OD systems revolve around dynamics, measurement, and estimation. In detail, the key elements are differences in spacecraft dynamics, observation geometry, and tracking windows. Regarding design principles, this research highlights that distinct differences in spacecraft dynamics and, thus, optimized observation geometry are pivotal for improved OD perfor-

mance. The measurement aspect has less effect on the system performance than the orbital aspect. In essence, even with a less accurate measurement system, the desired OD performance can be achieved by carefully designing the observation geometry (mission design).

7.2. INNOVATIONS

This dissertation has made several significant contributions to the autonomous navigation field for deep space small satellites. These contributions are summarized as follows:

Comprehensive Review of Autonomous Navigation for Deep Space Small Satellites An extensive review was provided in Chapter 1 and 2. As far as this author knows, there was no such review in the scientific literature by the time of publication [1]. This work has presented the current trends on small satellite missions in deep space along with advancements in autonomous navigation. By the writing of this dissertation, [1] was still one of the most downloaded articles from the journal Acta Astronautica.

Radiometric Tracking Chapter 2 details various radiometric measurement types used in ground-based and satellite-to-satellite tracking. The chapter discusses the performance, advantages, and disadvantages of these methods, with a particular focus on the benefits of data-aided ranging methods for satellite formations in cislunar and deep space environments.

Insights on Performance Metrics Various performance metrics exist in the field. However, it is somewhat unclear which metric is useful for a specific case and how to implement it. This posed challenges in the practical application and in effectively presenting and interpreting the results. To address this gap, Chapter 4 introduced specific metrics suitable for the study's focus, outlining their implementation, advantages, and disadvantages. It was found that relying solely on the Condition Number (CN) or Unobservability Index (UOI) for evaluating system performance may lead to misleading conclusions, necessitating a comprehensive approach that considers both metrics.

Exploring the Core Aspects of Orbit determination in Satellite-to-Satellite Tracking: This study addressed the OD problem from dynamics, measurement, and estimation perspectives, detailing each of these key elements for various mission considerations, extending the study done by [11]. A semi-analytical observability and covariance analysis were provided in Chapter 4, along with the detailed performance analysis in Chapter 5.

- **Dynamics: Understanding Orbital Configurations** Chapter 5 provided a detailed performance analysis for the orbit determination problem from the orbital configuration perspective. The role of high-fidelity dynamics in orbit determination was presented, revealing simplified dynamics limits the performance. It was found that satellite formations in cislunar space are less sensitive to measurement inaccuracies than the observation geometry. It was also found that consider filtering is

more suitable for Halo / Halo formations, while estimating is preferable for Halo / Lunar formations, depending on mission configuration. This research has, for the first time in literature, focused on network topologies consisting of three or more satellites performing SST-based OD. It was found that Lunar satellite network topologies, whether mesh or centralized, generally achieve the greatest benefit from autonomous navigation systems when they feature long inter-satellite links and short orbital periods. The integration of additional satellites into lunar network topologies is found to be effective in enhancing overall system performance.

- **Relationship between Navigation Data Types** A semi-analytical approach has been presented to analyze different data types. It has been shown that, in general, range observations were found to offer better performance compared to range-rate and angle data. It was found that in a CRTBP Halo-only scenario, the SST-based OD performance parity between range and range-rate systems is situated within a range-rate error spectrum of 0.04 mm/s to 0.14 mm/s for a corresponding range error of 1 m. Similarly, for angle-only measurements, an equivalent OD performance with a range error of 1 m is achievable within an angle measurement error range of 0.02 arcsec to 1.76 arcsec. In a typical small body scenario, a range-rate-only system with accuracies between 0.08 mm/s and 0.2 mm/s, as well as an inertial angle-only system with accuracies ranging from 8 arcsec to 30 arcsec, could potentially replicate the OD performance by a range-only system with a 1 m error (1σ). Studies on observation data types and thresholds for the SST-based OD problem have not existed before to the best knowledge of the author.

- **Estimation Perspective** To the best of this author's knowledge, there was no such study on SST-based OD implementing different sequential filters. This study provided an in-depth investigation, showing their complexities and use cases. It was found that there was no significant difference between different filtering techniques within the simplified three-body problem, though more advanced filters have shown improved performance in dealing with non-linearity around small solar system bodies.

A Realistic Mission Scenario In Chapter 5, a Lunar CubeSat study has been presented, detailing different aspects of the problem from link-budget analysis, measurement considerations, orbit determination, and station-keeping perspectives, presenting a systematic way to analyze the orbit determination performance. This part provides valuable insights into OD for similar mission concepts. The very first preliminary results of this mission scenario have been published in [192] where there was no such study on an EML2 Halo real-mission scenario focusing on various crosslink radiometric measurements and corresponding parameters along with autonomous operations. It has been shown that these types of missions could benefit from simple ranging methods for autonomous OD purposes.

Operational Aspects The final chapter addressed operational aspects, highlighting the importance of optimal tracking windows and presented an on-board data flow for the

purpose of error analysis and implementation. This part of the research offers practical guidance for the mission design and operational planning of deep space satellite formations. In this chapter, covariance analysis and PSO have been found to be adequate tools for designing tracking windows. This is the first time this approach has been proposed for use in optimizing tracking windows for state and bias estimation within those orbits in cislunar space.

7.3. FUTURE RESEARCH DIRECTIONS

The current study has made significant progress in understanding SST-based OD. However, several aspects remain unexplored and could be addressed in future research:

This work opened up areas for further exploration in the estimation aspect of SST-based OD. A significant area yet to be explored is the incorporation of consider parameters, particularly in scenarios where one satellite's (deputy) dynamical states are not estimated but rather those of another satellite (master). For instance, the interaction between a Lunar orbiter and a halo orbiter, with the lunar orbiter's states assumed as known with uncertainty (consider parameters), could be studied. This approach would focus on determining the halo orbiter's position, potentially on-board the halo orbiter itself, which could offer computational benefits. Additionally, this method may allow for the estimation of systematic errors without expanding the state dimension beyond that in the nominal two-spacecraft estimation problem. The expected performance and implications of this approach require further research.

Regarding the realistic mission scenario, the attitude of the spacecraft and its impact on inter-satellite communication and link budget analysis were not covered in detail. While the current study assumed continuous communication between the Halo orbiter and the Lunar data relay satellite, with the former always oriented toward the Moon, a more detailed analysis, including spacecraft orientation, is necessary. Furthermore, the impact of on-board clocks on time-tagging, affecting both measurement and state information, needs detailed investigation. Systematic errors in measurements are studied in detail but not the effects on state information. The influence of the master spacecraft clock on the overall system performance, particularly in multi-satellite formations, is another critical aspect that requires detailed research.

Tracking window planning in satellite formations is a very complex issue that needs careful examination. While near-optimal tracking windows based on observation effectiveness can be identified, the impact of scientific operations on these plans is a significant consideration. Flexible methods, such as PSO-based techniques, might offer near-optimal solutions that account for operational constraints. However, the ground-dependent nature of these solutions can cause challenges for autonomy. Alternative approaches, such as predefined tracking windows or decision algorithms based on mission geometry, could offer solutions but may lack autonomy and adaptability to mission changes. Additionally, exploring the integration of tracking windows with station-keeping intervals to minimize overall propellant consumption while considering the variability of these tracking intervals and, thus, the station-keeping intervals needs a detailed investigation.

Lastly, this study provided an overview of the data flow. However, it did not dive into the various efficient ways to implement these algorithms. Future work could focus on exploring different implementation strategies for these algorithms, considering factors such as computational efficiency, resource constraints, and real-time processing capabilities on spacecraft.

BIBLIOGRAPHY

[1] E. Turan, S. Speretta, and E. Gill, "Autonomous navigation for deep space small satellites: Scientific and technological advances", *Acta Astronautica*, vol. 193, pp. 56–74, Apr. 2022. DOI: 10.1016/j.actaastro.2021.12.030.

[2] "Dsn telecommunications link design handbook", Jet Propulsion Laboratory California Institute of Technology, Tech. Rep., 2018. [Online]. Available: http://deepspace.jpl.nasa.gov/dsndocs/810-005/.

[3] CCSDS, "Radio Frequency and Modulation Systems Part 1 Earth Stations and Spacecraft CCSDS 401.0-B-32", Tech. Rep., Oct. 2021, pp. 165–170. [Online]. Available: https://public.ccsds.org/Pubs/414x0g2.pdf.

[4] M. Sweeting, "Modern small satellites-changing the economics of space", *Proceedings of the IEEE*, vol. 106, no. 3, pp. 343–361, 2018.

[5] R. Walker, "Esa technology cubesats: Pushing the mission autonomy envelope", 2021.

[6] S. Bhaskaran, J. E. Riedel, and S. P. Synnott, "Autonomous optical navigation for interplanetary missions", in *Space Sciencecraft Control and Tracking in the New Millennium*, International Society for Optics and Photonics, vol. 2810, 1996, pp. 32–43.

[7] J. Riedel, S. Bhaskaran, S. Desai, *et al.*, "Using autonomous navigation for interplanetary missions: The validation of deep space 1 autonav", 2000.

[8] M. Chory, D. Hoffman, and J. LeMay, "Satellite autonomous navigation-status and history", *pln*, pp. 110–121, 1986.

[9] V. Franzese, P. D. Lizia, and F. Topputo, "Autonomous optical navigation for LUMIO mission", in *2018 Space Flight Mechanics Meeting*, American Institute of Aeronautics and Astronautics, Jan. 2018. DOI: 10.2514/6.2018-1977.

[10] D. Hestroffer, M. Agnan, B. Segret, *et al.*, "Birdy-interplanetary cubesat for planetary geodesy of small solar system bodies (sssb).", in *AGU fall meeting abstracts*, 2017.

[11] K. A.Hill, "Autonomous Navigation in Libration Point Orbits", Ph.D. dissertation, University of Colorado, 2007.

[12] A. R. Dahir, "Lost in space: Autonomous deep space navigation", Ph.D. dissertation, University of Colorado at Boulder, 2020.

[13] R. Funase, T. Inamori, S. Ikari, *et al.*, "One-year deep space flight result of the world's first full-scale 50kg-class deep space probe procyon and its future perspective", 2016.

[14] Y. Tsuda, M. Yoshikawa, M. Abe, H. Minamino, and S. Nakazawa, "System design of the hayabusa 2—asteroid sample return mission to 1999 JU3", *Acta Astronautica*, vol. 91, pp. 356–362, Oct. 2013. DOI: 10.1016/j.actaastro.2013.06.028.

[15] J. Biele and S. Ulamec, "Capabilities of philae, the rosetta lander", *Origin and Early Evolution of Comet Nuclei*, pp. 275–289, 2008.

[16] S. W. Asmar and S. Matousek, "Mars cube one (MarCO) shifting the paradigm in relay deep space operation", in *SpaceOps 2016 Conference*, American Institute of Aeronautics and Astronautics, May 2016. DOI: 10.2514/6.2016-2483.

[17] B. Cheetham, T. Gardner, A. Forsman, E. Kayser, and M. Clarkson, "CAPSTONE: A unique CubeSat platform for a navigation demonstration in cislunar space", in *ASCEND 2022*, American Institute of Aeronautics and Astronautics, Oct. 2022. DOI: 10.2514/6.2022-4382.

[18] E. Dotto, V. D. Corte, M. Amoroso, *et al.*, "LICIACube - the light italian cubesat for imaging of asteroids in support of the NASA DART mission towards asteroid (65803) didymos", *Planetary and Space Science*, vol. 199, p. 105 185, May 2021. DOI: 10.1016/j.pss.2021.105185.

[19] NASA, *What is lunar flashlight?*, (accessed Feb 2021), Oct. 2020. [Online]. Available: https://www.nasa.gov/directorates/spacetech/small_spacecraft/What_is_Lunar_Flashlight.

[20] NASA, *Artemis 1 secondary payloads, aes em-1 secondaries fact sheet*, (accessed June 2020), Apr. 2015. [Online]. Available: https://www.nasa.gov/sites/default/files/atoms/files/aes-secondaries-fs-v508c.pdf.

[21] C. Mercer, "Planetary science deep space smallsat studies", in *Lunar Planetary Science Conference Special Session, The Woodlands, Texas*, 2018.

[22] C. R. Mercer, "Small satellite missions for planetary science", 2019.

[23] NASA, *Nasa's space cubes: Small satellites provide big payoffs*, (accessed June 2020), Aug. 2017. [Online]. Available: https://www.nasa.gov/feature/nasa-s-space-cubes-small-satellites-provide-big-payoffs.

[24] M. Chandrashekhar, "Diminutive asteroid visitor using ion drive (david): A 6u-cubesat mission analysis of a near earth asteroid visit",

[25] NASA, *Europa clipper home page at nasa.* (accessed June 2020). [Online]. Available: https://europa.nasa.gov/mission/about/.

[26] B. Burgett, J. Long, P. Whaley, *et al.*, "Mini-maggie: Cubesat magnetism and gravity investigation at europa", in *Lunar and Planetary Science Conference*, vol. 47, 2016, p. 1928.

[27] A. E. Thelen, N. Chanover, J. Murphy, K. Rankin, and S. Stochaj, "A europa cubesat concept study for measuring atmospheric density and heavy ion flux", *Journal of Small Satellites*, vol. 6, pp. 591–607, 2017.

[28] T. Imken, B. Sherwood, J. Elliott, *et al.*, "Sylph-a smallsat probe concept engineered to answer europa's big question", 2016.

[29] M. Di Benedetto, L. Imperi, D. Durante, *et al.*, "Augmenting nasa europa clipper by a small probe: Europa tomography probe (etp) mission concept", Sep. 2016.

[30] R. Walker, D. Binns, C. Bramanti, *et al.*, "Deep-space CubeSats: Thinking inside the box", *Astronomy & Geophysics*, vol. 59, no. 5, pp. 524–530, Oct. 2018. DOI: 10.1093/astrogeo/aty232.

[31] T. Kohout, A. Näsilä, T. Tikka, *et al.*, "Feasibility of asteroid exploration using cubesats—aspect case study", *Advances in Space Research*, vol. 62, no. 8, pp. 2239–2244, 2018.

[32] F. Perez, D. Modenini, A. Vázquez, *et al.*, "Dustcube, a nanosatellite mission to binary asteroid 65803 didymos as part of the esa aim mission", *Advances in Space Research*, vol. 62, no. 12, pp. 3335–3356, 2018.

[33] GMV, *Aim industry days, cubata, cubesat at target asteroid*, (accessed June 2020), Feb. 2016. [Online]. Available: https://indico.esa.int/event/133/contributions/765/attachments/817/994/10_CUBATA.pdf.

[34] E. Vinterhav, *Aim/pals aim industry days*. [Online]. Available: https://indico.esa.int/event/133/contributions/762/attachments/847/1025/08_PALS.pdf.

[35] Ö. Karatekin, "The asteroid geophysical explorer (agex); a proposal to explore didymos system using cubesats", in *41st COSPAR Scientific Assembly*, vol. 41, 2016.

[36] P. Tortora, M. Zannoni, G. Gutierrez, P. Martino, and I. Carnelli, "Didymos gravity science through juventas satellite-to-satellite doppler tracking",

[37] S. Speretta, F. Topputo, J. Biggs, *et al.*, "LUMIO: Achieving autonomous operations for lunar exploration with a CubeSat", in *2018 SpaceOps Conference*, American Institute of Aeronautics and Astronautics, May 2018. DOI: 10.2514/6.2018-2599.

[38] C. Conigliaro, D. Calvi, L. Franchi, F. Stesina, and S. Corpino, "Design and analysis of an innovative cubesat thermal control system for biological experiment in lunar environment", in *Proceedings of the 69th International Astronautical Congress, Bremen, Germany*, 2018, pp. 1–5.

[39] M. Bentum, A.-J. Boonstra, M. Klein Wolt, *et al.*, "The cubesat low frequency explorer (cle) in lunar orbit", in *42nd COSPAR Scientific Assembly*, vol. 42, 2018.

[40] R. Kruzelecky, P. Murzionak, J. Lavoie, *et al.*, "Vmmo lunar volatile and mineralogy mapping orbiter", 48th International Conference on Environmental Systems, 2018.

[41] R. T. Rajan, S. Engelen, M. Bentum, and C. Verhoeven, "Orbiting low frequency array for radio astronomy", in *2011 Aerospace Conference*, IEEE, 2011, pp. 1–11.

[42] X. Chen, J. Burns, L. Koopmans, *et al.*, "Discovering the sky at the longest wavelengths with small satellite constellations", *arXiv preprint arXiv:1907.10853*, 2019.

[43] D. Spokesperson and M. K. Wolt, "A white paper for a low–frequency radio interferometer mission to explore the cosmological dark ages for the l2, l3 esa cosmic vision program", 2013.

[44] S. Wu, W. Chen, Y. Zhang, W. Baan, and T. An, "Sulfro: A swarm of nano-/micro-satellite at se l2 for space ultra-low frequency radio observatory", 2014.

[45] B. K. Malphrus, K. Z. Brown, J. Garcia, *et al.*, "The lunar IceCube EM-1 mission: Prospecting the moon for water ice", *IEEE Aerospace and Electronic Systems Magazine*, vol. 34, no. 4, pp. 6–14, Apr. 2019. DOI: 10.1109/maes.2019.2909384.

[46] A. Babuscia, K. Angkasa, B. Malphrus, and C. Hardgrove, "Development of telecommunications systems and ground support for em-1 interplanetary cubesats missions: Lunar icecube and lunah-map", 2017.

[47] M. V. Di Tana, C. Fiori, S. Simonetti, and S. Pirrotta, "Argomoon, a multipurpose cubesat platform for missions in moon vicinity and orbit", in *European Planetary Science Congress*, vol. 12, 2018.

[48] S. Campagnola, J. Hernando-Ayuso, K. Kakihara, *et al.*, "Mission analysis for the EM-1 CubeSats EQUULEUS and OMOTENASHI", *IEEE Aerospace and Electronic Systems Magazine*, vol. 34, no. 4, pp. 38–44, Apr. 2019. DOI: 10.1109/maes.2019.2916291.

[49] P. Clark, "Cubesats in cislunar space", 2018.

[50] K. Oguri, K. Oshima, S. Campagnola, *et al.*, "EQUULEUS trajectory design", *The Journal of the Astronautical Sciences*, Jan. 2020. DOI: 10.1007/s40295-019-00206-y.

[51] C. I. .-. P.-2. Proposal, "Comet interceptor:a mission to a dynamically new solar system object", Tech. Rep., (accessed June 2020). [Online]. Available: http://www.cometinterceptor.space/uploads/1/2/3/7/123778284/comet_interceptor_executive_summary.pdf.

[52] C. Hibbitts, B. Clyde, D. Blewett, *et al.*, "The lunar water mission: A psds3 feasibility study of a solar-electric propulsion small sat mission to characterize the water on the moon", in *Lunar and Planetary Science Conference*, vol. 49, 2018.

[53] D. Draper, J. Stopar, S. Lawrence, *et al.*, "The irregular mare patch exploration lander (impel) smallsat mission concept", in *Lunar and Planetary Science Conference*, vol. 49, 2018.

[54] S. Romaine, R. Kraft, K. Gendreau, *et al.*, "Cubesat x-ray telescope (cubex) for lunar elemental abundance mapping and millisecond x-ray pulsar navigation", in *42nd COSPAR Scientific Assembly*, vol. 42, 2018.

[55] J. Deller, E. Vilenius, O. Roders, *et al.*, "Asteroid in-situ interior investigation-3way: Understanding the formation processes and evolution of small solar system bodies", *EPSC*, vol. 2019, EPSC–DPS2019, 2019.

[56] J. H. Beau Bierhaus Ben Clark, *Ross (née, caesar)*, (accessed June 2020), Jan. 2018. [Online]. Available: https://www.lpi.usra.edu/sbag/meetings/jan2018/presentations/930-Bierhaus-Ross.pdf.

[57] I. Garrick-Bethell, C. Pieters, C. Russell, *et al.*, "Nanoswarm: A cubesat discovery mission to study space weathering, lunar magnetism, lunar water, and small-scale magnetospheres", in *Lunar and Planetary Science Conference*, vol. 46, 2015, p. 3000.

[58] J. Plescia, O. Barnouin, D. Richardson, *et al.*, "The asteroid probe experiment (apex) mission", 2017.

[59] N. Petro, E. Mazarico, X. Sun, J. Abshire, G. Neumann, and P. Lucey, "Miluv does it good—the mini lunar volatiles mission: A planetary science deep space smallsat study of a lunar orbiting mission", in *Lunar and Planetary Science Conference*, vol. 49, 2018.

[60] T. Stubbs, B. Malphrus, R. Hoyt, *et al.*, "Bi-sat observations of the lunar atmosphere above swirls (bolas): Tethered smallsat investigation of hydration and space weathering processes at the moon", in *Lunar and Planetary Science Conference*, vol. 49, 2018.

[61] C. Sotin, G. Avice, J. Baker, *et al.*, "Cupid's arrow: A small satellite concept to measure noble gases in venus' atmosphere", in *Lunar and Planetary Science Conference*, vol. 49, 2018.

[62] V. Cottini, S. Aslam, N. Gorius, *et al.*, "Cuve-cubesat uv experiment: Unveil venus' uv absorber with cubesat uv mapping spectrometer", in *15th Meeting of the Venus Exploration and Analysis Group (VEXAG)*, vol. 2061, 2017, p. 8044.

[63] NASA, *Nasa selects lockheed martin's lunir cubesat for artemis i secondary payload*, (accessed June 2020), Jan. 2016. [Online]. Available: https://www.nasa.gov/feature/nasa-selects-lockheed-martin-s-lunir-cubesat-for-artemis-i-secondary-payload.

[64] T. Kremic *et al.*, "Seismic and atmospheric exploration of venus (saeve) final report", Lunar and Planetary Institute, Tech. Rep., 2018.

[65] M. I. Desai, F. Allegrini, R. W. Ebert, *et al.*, "The CubeSat mission to study solar particles", *IEEE Aerospace and Electronic Systems Magazine*, vol. 34, no. 4, pp. 16–28, Apr. 2019. DOI: 10.1109/maes.2019.2917802.

[66] R. W. Ebert, F. Allegrini, F. Bagenal, *et al.*, "Jupiter magnetospheric boundary explorer (jumper)", in *2018 IEEE Aerospace Conference*, IEEE, 2018, pp. 1–17.

[67] NASA, *Biosentinel fact sheet*, (accessed June 2020), Apr. 2019. [Online]. Available: https://www.nasa.gov/sites/default/files/atoms/files/biosentinel_fact_sheet-16apr2019_508.pdf.

[68] T. Hewagama, S. Aslam, P. Clark, *et al.*, "Primitive object volatile explorer (prove)-waypoints and opportunistic deep space missions to comets", Mar. 2018. DOI: 10.1117/12.2321264.

[69] J. Sobtzak, E. Tianang, B. Branham, *et al.*, "A deep space radio communications link for cubesats: The cu-e3 communication subsystem", 2017.

[70] A. Didion, A. Komjathy, B. Sutin, *et al.*, "Remote sensing of venusian seismic activity with a small spacecraft, the vamos mission concept", in *2018 IEEE Aerospace Conference*, IEEE, 2018, pp. 1–14.

[71] S. H. Schaire, S. Altunc, Y. F. Wong, *et al.*, "Investigation into new ground based communications service offerings in response to smallsat trends", 2018.

[72] K. Sayanagi, R. Dillman, A. Simon, *et al.*, "Small next-generation atmospheric probe (snap) concept", 2017.

[73] R. L. Staehle, S. Spangelo, M. S. Lane, *et al.*, "Multiplying mars lander opportunities with marsdrop microlanders", 2015.

[74] L. Montabone, M. VanWoerkom, B. Cantor, *et al.*, "Mars aerosol tracker (mat): An areostationary cubesat to monitor dust storms and water ice clouds", in *Lunar and Planetary Science Conference*, vol. 49, 2018.

[75] K. V. Mani, A. Casado, V. Franzese, F. Topputo, and A. Cervone, "Systems design of mario: Stand-alone 16u cubesat from earth to mars", Oct. 2019.

[76] A. T. Klesh, J. Baker, and J. Krajewski, "Marco: Flight review and lessons learned", in *33rd Annual AIAA/USU Conference on Small Satellites*, 2019.

[77] A. Cook, A. Colaprete, J. Fisher, *et al.*, "The doppler wind and thermal sounder instrument for the aeolus mission concept to mars", *AGUFM*, vol. 2019, P11D–3487, 2019.

[78] R. Lillis, S. Curry, D. Larson, *et al.*, "Mars ion and sputtering escape network (misen)", in *2018 Plantary Science Deep Space SmallSat Mission Concepts Meeting*, 2018, pp. 1–19.

[79] M. Bappy, R. Huq, P. Das, and S. Siddique, "System design concept of mars intelligent imaging & atmospheric research cubesat constellation using distributed deep learning (miiar)", May 2019.

[80] S. Speretta, A. Cervone, A. Menicucci, *et al.*, "Designing the Radio Link for a Lunar CubeSat: the LUMIO case", 2021.

[81] S. Bhaskaran, N. Mastrodemos, J. E. Riedel, and S. P. Synnott, "Optical navigation for the stardust wild 2 encounter", in *18th International Symposium on Space Flight Dynamics*, vol. 548, 2004, p. 455.

[82] N. Mastrodemos, D. G. Kubitschek, and S. P. Synnott, "Autonomous navigation for the deep impact mission encounter with comet tempel 1", *Space Science Reviews*, vol. 117, no. 1-2, pp. 95–121, Mar. 2005. DOI: 10.1007/s11214-005-3394-4.

[83] S. Bhaskaran, "Autonomous navigation for deep space missions", American Institute of Aeronautics and Astronautics, Mar. 2012. DOI: 10.2514/6.2012-1267135.

[84] O. Camino, M. Alonso, D. Gestal, *et al.*, "Smart-1 operations experience and lessons learnt", *Acta Astronautica*, vol. 61, no. 1-6, pp. 203–222, 2007.

[85] T. Martin, A. Blazquez, E. Canalias, *et al.*, "Flight dynamics analysis for philae landing site selection", in *25th International Symposium on Space Flight Dynamics*, 2015.

[86] B. Segret, D. Hestroffer, G. Quinsac, M. Agnan, and J. Vannitsen, "On-board orbit determination for a deep space cubesat", in *International Symposium on Space Flight Dynamics*, 2017.

[87] T. Oshima, J. Kawaguchi, and S. Hagino, "The mission operations of hayabusa asteroid explorer", in *57th International Astronautical Congress*, 2006, pp. C1–6.

[88] B. Segret, J. Vannitsen, M. Agnan, *et al.*, "Birdy: An interplanetary cubesat to collect radiation data on the way to mars and back to prepare the future manned missions", in *Modeling, Systems Engineering, and Project Management for Astronomy VI*, International Society for Optics and Photonics, vol. 9150, 2014, 91501N.

[89] V. Franzese, F. Topputo, F. Ankersen, and R. Walker, "Deep-space optical navigation for m-ARGO mission", Oct. 2021. DOI: 10.1007/s40295-021-00286-9.

[90] J. Yim, J. Crassidis, and J. Junkins, "Autonomous orbit navigation of interplanetary spacecraft", in *Astrodynamics Specialist Conference*, American Institute of Aeronautics and Astronautics, Aug. 2000. DOI: 10.2514/6.2000-3936.

[91] A. Delépaut, P. Giordano, J. Ventura-Traveset, *et al.*, "Use of gnss for lunar missions and plans for lunar in-orbit development", *Advances in Space Research*, vol. 66, no. 12, pp. 2739–2756, 2020.

[92] S. Schaire, Y. Wong, G. Bussey, *et al.*, "Lunar and lagrangian point l1/l2 cubesat communication and navigation considerations", 2017.

[93] J. B. Berner, "Deep space network in the cubesat era", *IEEE Aerospace and Electronic Systems Magazine*, vol. 34, no. 4, pp. 46–54, 2019. DOI: 10.1109/MAES.2019.2913266.

[94] J. M. Rebordão, "Space optical navigation techniques: An overview", M. F. P. C. M. Costa, Ed., SPIE, Nov. 2013. DOI: 10.1117/12.2026063.

[95] C. J. G. David Folta, *Navigation overview strategic and technical aspects of planetary small satellite missions*, 3rd Planetary CubeSat Science Symposium Presentation Slides, Aug. 2018.

[96] C. J. Gramling, *Planetary cubesats deep space navigation*, 4th Planetary CubeSat Science Symposium Presentation, Jun. 2019.

[97] W. M. Owen Jr, "Methods of optical navigation", 2011.

[98] A. Team, J. Riedel, S. Bhaskaran, *et al.*, "Autonomous optical navigation (autonav) ds1 technology validation report", *Jet Propulsion Laboratory, California Institute of Technology*, 2000.

[99] V. H. Adams and M. A. Peck, "Interplanetary optical navigation", in *AIAA Guidance, Navigation, and Control Conference*, American Institute of Aeronautics and Astronautics, Jan. 2016. DOI: 10.2514/6.2016-2093.

[100] V. H. Adams and M. A. Peck, "Lost in space and time", in *AIAA Guidance, Navigation, and Control Conference*, American Institute of Aeronautics and Astronautics, Jan. 2017. DOI: 10.2514/6.2017-1030.

[101] S. I. Sheikh, D. J. Pines, P. S. Ray, K. S. Wood, M. N. Lovellette, and M. T. Wolff, "Spacecraft navigation using x-ray pulsars", vol. 29, no. 1, pp. 49–63, Jan. 2006. DOI: 10.2514/1.13331.

[102] L. B. Winternitz, M. A. Hassouneh, J. W. Mitchell, *et al.*, "SEXTANT x-ray pulsar navigation demonstration: Additional on-orbit results", in *2018 SpaceOps Conference*, American Institute of Aeronautics and Astronautics, May 2018. DOI: 10.2514/6.2018-2538.

[103] J. E. Hanson, "Principles of x-ray navigation", Tech. Rep., Mar. 2006. DOI: 10.2172/877425.

[104] J. Dong, "Pulsar navigation in the solar system", Dec. 2008. arXiv: 0812.2635 [astro-ph].

[105] L. Markley, "Autonomous satellite navigation using landmarks", vol. -1, Jul. 1981.

[106] F. Markley, "Autonomous navigation using landmark and intersatellite data", in *Astrodynamics conference*, 1987, p. 1987.

[107] L. Iess, M. D. Benedetto, N. James, M. Mercolino, L. Simone, and P. Tortora, "Astra: Interdisciplinary study on enhancement of the end-to-end accuracy for spacecraft tracking techniques", *Acta Astronautica*, vol. 94, no. 2, pp. 699–707, Feb. 2014. DOI: 10.1016/j.actaastro.2013.06.011.

[108] T. Qin, D. Qiao, and M. Macdonald, "Relative orbit determination using only intersatellite range measurements", *Journal of Guidance, Control, and Dynamics*, vol. 42, no. 3, pp. 703–710, Mar. 2019. DOI: 10.2514/1.g003819.

[109] J. Leonard, B. Jones, E. Villalba, and G. Born, "Absolute Orbit Determination and Gravity Field Recovery for 433 Eros Using Satellite-to-Satellite Tracking", in *AIAA/AAS Astrodynamics Specialist Conference*, American Institute of Aeronautics and Astronautics, Aug. 2012. DOI: 10.2514/6.2012-4877.

[110] Z. Li, Y. Wang, and W. Zheng, "Observability analysis of autonomous navigation using inter-satellite range: An orbital dynamics perspective", *Acta Astronautica*, vol. 170, pp. 577–585, May 2020. DOI: 10.1016/j.actaastro.2020.02.023.

[111] X. Zhou, T. Qin, M. Macdonald, and D. Qiao, "Observability analysis of cooperative orbit determination using inertial inter-spacecraft angle measurements", *Acta Astronautica*, vol. 210, pp. 289–302, Sep. 2023. DOI: 10.1016/j.actaastro.2023.05.019.

[112] E. Turan, S. Speretta, and E. Gill, "Autonomous Navigation Performance of Cislunar Orbits considering High Crosslink Measurement Errors", in *2022 IEEE Aerospace Conference (AERO)*, IEEE, Mar. 2022, pp. 1–11. DOI: 10.1109/aero53065.2022.9843772.

[113] E. Turan, S. Speretta, and E. Gill, "Performance analysis of crosslink radiometric measurement based autonomous orbit determination for cislunar small satellite formations", *Advances in Space Research*, vol. 72, no. 7, pp. 2710–2732, Oct. 2023. DOI: 10.1016/j.asr.2022.11.032.

[114] C. L. Thornton and J. S. Border, *Radiometric tracking techniques for deep-space navigation*. John Wiley & Sons, 2003.

[115] M. D., "Autonomous relative navigation for small spacecraft.", Ph.D. dissertation, Delft University of Tecnology, 2014.

[116] S. Bertone, C. Le Poncin-Lafitte, P. Rosenblatt, V. Lainey, J.-C. Marty, and M.-C. Angonin, "Impact analysis of the transponder time delay on radio-tracking observables", *Advances in space research*, vol. 61, no. 1, pp. 89–96, 2018.

[117] O. Montenbruck and E. Gill, *Satellite Orbits*. Springer Berlin, Heidelberg, 2000. DOI: 10.1007/978-3-642-58351-3.

[118] K. Andrews, J. Hamkins, S. Shambayati, and V. Vilnrotter, "Telemetry-based ranging", in *2010 IEEE Aerospace Conference*, IEEE, 2010, pp. 1–16.

[119] H. W. Baugh, "Sequential ranging: How it works", *NASA STI/Recon Technical Report N*, vol. 94, p. 13 796, 1993.

[120] J. Berner and S. Bryant, "Operations comparison of deep space ranging types: Sequential tone vs. pseudo-noise", in *Proceedings, IEEE Aerospace Conference*, IEEE. DOI: 10.1109/aero.2002.1035264.

[121] E. C. for Space Standardization, "Ecss-e-st-50-02c - ranging and doppler tracking", Tech. Rep., 2018.

[122] J. Hamkins, P. Kinman, H. Xie, V. Vilnrotter, and S. Dolinar, "Telemetry ranging: Concepts", *IPNPR*, vol. 42, pp. 1–20, 2015.

[123] J. Hennawy, N. Adams, E. Sanchez, *et al.*, "Telemetry ranging using software-defined radios", in *2015 IEEE Aerospace Conference*, IEEE, Mar. 2015. DOI: 10.1109/aero.2015.7119178.

[124] The Consultative Committee for Space Data Systems (CCSDS), "Pseudo-Noise (PN) Ranging Systems", Tech. Rep., 2014.

[125] V. Vilnrotter and J. Hamkins, "Telecommand/telemetry ranging for deep-space applications", in *2019 IEEE Aerospace Conference*, IEEE, 2019, pp. 1–10.

[126] P. Grenfell, "Systems performance analysis for autonomous spacecraft navigation within satellite constellations using intersatellite optical communications links", Ph.D. dissertation, Massachusetts Institute of Technology, 2024.

[127] J. B. Berner, S. H. Bryant, and P. W. Kinman, "Range measurement as practiced in the deep space network", *Proceedings of the IEEE*, vol. 95, no. 11, pp. 2202–2214, Nov. 2007. DOI: 10.1109/jproc.2007.905128.

[128] S. E. S. European Telecommunications Standards Institute and S. (SES), "Satellite earth stations and systems (ses);technical analysis of spread spectrum solutions-for telemetry command and ranging (tcr)of geostationary communications satellites", Tech. Rep., 2001. [Online]. Available: https://www.etsi.org/deliver/etsi_tr/101900_101999/101956/01.01.01_60/tr_101956v010101p.pdf.

[129] M. B. Mwakyanjala, M. R. Emami, and J. van de Beek, "Functional analysis of software-defined radio baseband for satellite ground operations", *Journal of Spacecraft and Rockets*, vol. 56, no. 2, pp. 458–475, Mar. 2019. DOI: 10.2514/1.a34333.

[130] Zodiac Data Systems, *Cortex CRT. Quantum user manual*. 2014.

[131] Y. Bar-Sever, E. Burt, K.-M. Cheung, *et al.*, "Architectures and technology investment priorities for positioning, navigation, and timing at the moon and mars",

[132] M. R. Thompson, A. Forsman, S. Chikine, *et al.*, "Cislunar navigation technology demonstrations on the CAPSTONE mission", in *The International Technical Meeting of the The Institute of Navigation*, Institute of Navigation, Feb. 2022. DOI: 10.33012/2022.18208.

[133] E. C. J. R. Centre., *Chip-scale atomic clocks: physics, technologies, and applications*. Publications Office, 2021. DOI: 10.2760/278540.

[134] M. M. Rybak, P. Axelrad, J. Seubert, and T. Ely, "Chip scale atomic clock–driven one-way radiometric tracking for low-earth-orbit CubeSat navigation", *Journal of Spacecraft and Rockets*, vol. 58, no. 1, pp. 200–209, Jan. 2021. DOI: 10.2514/1.a34684.

[135] J. Seubert, E. Gustafson, M. Jesick, *et al.*, "Orbit determination for the mars 2020 mission", in *AAS/AIAA Astrodynamics Specialist Conference, AAS Paper*, 2021, pp. 21–503.

[136] C. T. C. C. for Space Data Systems, "Proximity-1 space link protocol - data link layer recommended standard", Tech. Rep., July 2020.

[137] S. Woo, J. Gao, and D. Mills, "Space network time distribution and synchronization protocol development for mars proximity link", in *SpaceOps 2010 Conference*, American Institute of Aeronautics and Astronautics, Apr. 2010. DOI: 10.2514/6.2010-2360.

[138] *Time synchronization for space data links*, 2012. [Online]. Available: http://www.cis.udel.edu/~mills/proximity.html.

[139] D. L. Mills, *Computer network time synchronization: the network time protocol*. CRC press, 2006.

[140] G. Iraci and C. Gnam, "An open source radio for low cost small satellite ranging", Aug. 2018.

[141] C. Foster, H. Hallam, and J. Mason, "Orbit determination and differential-drag control of planet labs cubesat constellations", Sep. 2015. arXiv: http://arxiv.org/abs/1509.03270v1 [physics.space-ph].

[142] W. Fehse, *Automated Rendezvous and Docking of Spacecraft* (Cambridge Aerospace Series), M. J. Rycroft and W. Shyy, Eds. Cambridge University Press, The Edinburgh Building, Cambridge, United Kingdom, 2003. DOI: 10.1017/CBO9780511543388.

[143] A. Tiainen, *Inter-satellite link antennas: Review and the near future*, 2017.

[144] S. Papais, B. J. Hockman, S. Bandyopadhyay, R. R. Karimi, S. Bhaskaran, and I. A. Nesnas, "Architecture trades for accessing small bodies with an autonomous small spacecraft", in *2020 IEEE Aerospace Conference*, IEEE, 2020, pp. 1–20.

[145] R. Funase, H. Koizumi, S. Nakasuka, *et al.*, "50kg-class deep space exploration technology demonstration micro-spacecraft procyon", 2014.

[146] M. Kobayashi, "Iris deep-space transponder for sls em-1 cubesat missions", 2017.

[147] J. P. Laboratory, *Iris v2 cubesat deep-space transponder (iris)*, Jan. 2019. [Online]. Available: https://www.jpl.nasa.gov/cubesat/missions/iris.php.

[148] D. Sorensen, T. Russell, T. Neilsen, J. Hunt, and Z. Towfic, "Iris transponder enhancements for deep space and lunar operations", 2022.

[149] T. Gardnera, "Capstone: A unique cubesat platform operating in cislunar space tom gardnera*, brad cheethama, jeff parkera, alec forsmana, ethan kaysera, michael thompsona, connor otta, lauren demoudta, matt bolligera, arlen kama, keith thompsonb, tristan latchub, rebecca rogersb, brennan bryantc, tomas svitekc", 2022.

[150] T. Ely, Z. Towfic, and D. Sorensen, "Formulation and characterization of one-way radiometric tracking with the iris radio using a chip-scale atomic clock", *NAVIGATION: Journal of the Institute of Navigation*, vol. 71, no. 1, 2024.

[151] T. Hashimoto, T. Yamada, M. Otsuki, *et al.*, "Nano semihard moon lander: OMOTENASHI", *IEEE Aerospace and Electronic Systems Magazine*, vol. 34, no. 9, pp. 20–30, Sep. 2019. DOI: 10.1109/maes.2019.2923311.

[152] S. Palo, D. O'Connor, E. DeVito, R. Kohnert, G. Crum, and S. Altunc, "Expanding cubesat capabilities with a low cost transceiver", 2014.

[153] M. M. Kobayashi, S. Holmes, A. Yarlagadda, *et al.*, "The iris deep-space transponder for the SLS EM-1 secondary payloads", *IEEE Aerospace and Electronic Systems Magazine*, vol. 34, no. 9, pp. 34–44, Sep. 2019. DOI: 10.1109/maes.2019.2905923.

[154] M. R. Maheshwarappa and C. P. Bridges, "Software defined radios for small satellites", in *2014 NASA/ESA Conference on Adaptive Hardware and Systems (AHS)*, IEEE, 2014, pp. 172–179.

[155] C. Loisel, C. Dudal, O. Bompis, *et al.*, "Intersatellite links for rosetta/philae, hayabusa-2/mascot, and next-gen miniaturized isl in s and ka band",

[156] H. Goldberg, Ö. Karatekin, B. Ritter, *et al.*, "The juventas cubesat in support of esa's hera mission to the asteroid didymos", 2019.

[157] G. Dynamics, *Small deep space transponder*, http://gdmissionsystems.com (Accessed 04 December 2020).

[158] M. B. O'Neill, C. B. Haskins, and B. M. Bubnash, "Advances in deep space radios", in *2017 IEEE MTT-S International Microwave Symposium (IMS)*, IEEE, 2017, pp. 398–401.

[159] M. Pugh, I. Kuperman, F. Aguirre, *et al.*, "The universal space transponder: A next generation software defined radio", in *2017 IEEE Aerospace Conference*, IEEE, 2017, pp. 1–14.

[160] CCSDS, "Navigation data - definitions and conventions ccsds 500.0-g-4", Tech. Rep., 2019.

[161] J. Raol and N. Sinha, "On the orbit determination problem", *IEEE Transactions on Aerospace and Electronic Systems*, vol. AES-21, no. 3, pp. 274–291, May 1985. DOI: 10.1109/taes.1985.310558.

[162] R. E. Kalman, "A new approach to linear filtering and prediction problems", *Journal of Basic Engineering*, vol. 82, no. 1, pp. 35–45, Mar. 1960. DOI: 10.1115/1.3662552.

[163] D. A. Vallado, *Fundamentals of Astrodynamics and Applications, Second Edition (Space Technology Library, Volume 12) (Space Technology Library)*. Springer, 2001, p. 980, ISBN: 9780792369035.

[164] E. C. for Space Standardization, "Ecss-e-70-11a space engineering space segment operability", Tech. Rep., Aug. 5, 2005.

[165] K. Hill and G. H. Born, "Autonomous Interplanetary Orbit Determination Using Satellite-to-Satellite Tracking", *Journal of Guidance, Control, and Dynamics*, vol. 30, no. 3, pp. 679–686, May 2007. DOI: 10.2514/1.24574.

[166] K. Hill, J. Parker, G. Born, and N. Demandante, "A Lunar L2 Navigation, Communication, and Gravity Mission", in *AIAA/AAS Astrodynamics Specialist Conference and Exhibit*, American Institute of Aeronautics and Astronautics, Aug. 2006. DOI: 10.2514/6.2006-6662.

[167] S. Hesar, J. Parker, J. Mcmahon, and G. Born, "Small Body Gravity Field Estimation Using LiAISON Supplemented Optical Navigation", in *38th Annual AAS Rocky Mountain Section Guidance and Control Conference Conference*, Breckenridge, CO, Jan. 2015, pp. 41–54.

[168] W. Wang, L. Shu, J. Liu, and Y. Gao, "Joint navigation performance of distant retrograde orbits and cislunar orbits via LiAISON considering dynamic and clock model errors", *Navigation*, vol. 66, no. 4, pp. 781–802, Dec. 2019. DOI: 10.1002/navi.340.

[169] J. M. Leonard, "Supporting Crewed Missions using LiAISON Navigation in the Earth-Moon System", Ph.D. dissertation, University of Colorado, 2015.

[170] K. Fujimoto, N. Stacey, and J. M. Turner, "Stereoscopic Image Velocimetry as a Measurement Type For Autonomous Asteroid Gravimetry", in *AIAA/AAS Astrodynamics Specialist Conference*, American Institute of Aeronautics and Astronautics, Sep. 2016, pp. 1–12. DOI: 10.2514/6.2016-5566.

[171] A. Cervone, F. Topputo, S. Speretta, *et al.*, "LUMIO: A CubeSat for observing and characterizing micro-meteoroid impacts on the lunar far side", *Acta Astronautica*, vol. 195, pp. 309–317, Jun. 2022. DOI: 10.1016/j.actaastro.2022.03.032.

[172] P. G. Antreasian, C. D. Adam, K. Berry, *et al.*, "OSIRIS-REx proximity operations and navigation performance at bennu", in *AIAA SCITECH 2022 Forum*, American Institute of Aeronautics and Astronautics, Jan. 2022. DOI: 10.2514/6.2022-2470.

[173] K. Oguri, K. Kakihara, S. Campagnola, *et al.*, "Equuleus mission analysys: Design of the science orbit phase", in *26th International Symposium on Space Flight Dynamics*, 2017, pp. 1–7.

[174] J. L. Crassidis and J. L. Junkins, *Optimal estimation of dynamic systems*. CRC press, 2011.

[175] H. Curtis, *Orbital Mechanics for Engineering Students*. Elsevier LTD, Oxford, Aug. 2020, 780 pp., ISBN: 0128240253. [Online]. Available: https://www.ebook.de/de/product/41219397/howard_curtis_orbital_mechanics_for_engineering_students.html.

[176] J. G. Daniel, "Generating Periodic Orbits in the Circular Restricted Three-Body Problem with Applications to Lunar South Pole Coverage", M.S. thesis, MSc thesis, Purdue University, West Lafayette, Indiana, 2006.

[177] K. C. Howell, "Three-dimensional, periodic, ?halo? orbits", *Celestial Mechanics*, vol. 32, no. 1, pp. 53–71, Jan. 1984. DOI: 10.1007/bf01358403.

[178] B. Tapley, B. E. Schutz, and G. H. Born, *Statistical Orbit Determination*. Elsevier Academic Press, Burlington, USA, 2004, ISBN: 9780126836301. DOI: 10.1016/B978-0-12-683630-1.X5019-X.

[179] S. Akhlaghi, N. Zhou, and Z. Huang, "Adaptive adjustment of noise covariance in kalman filter for dynamic state estimation", in *2017 IEEE Power & Energy Society General Meeting*, IEEE, Jul. 2017. DOI: 10.1109/pesgm.2017.8273755.

[180] A. Valade, P. Acco, P. Grabolosa, and J.-Y. Fourniols, "A study about kalman filters applied to embedded sensors", *Sensors*, vol. 17, no. 12, p. 2810, Dec. 2017. DOI: 10.3390/s17122810.

[181] R. Hunger, *Floating point operations in matrix-vector calculus*. Munich University of Technology, Inst. for Circuit Theory and Signal . . ., 2005, vol. 2019.

[182] A. D. Dianetti, R. Weisman, and J. L. Crassidis, "Observability analysis for improved space object characterization", *Journal of Guidance, Control, and Dynamics*, vol. 41, no. 1, pp. 137–148, Jan. 2018. DOI: 10.2514/1.g002229.

[183] D. Wang, M. Li, X. Huang, and X. Zhang, *Spacecraft Autonomous Navigation Technologies Based on Multi-source Information Fusion*. Springer Singapore, 2021. DOI: 10.1007/978-981-15-4879-6.

[184] A. J. Krener and K. Ide, "Measures of unobservability", in *Proceedings of the 48h IEEE Conference on Decision and Control (CDC) held jointly with 2009 28th Chinese Control Conference*, IEEE, Dec. 2009. DOI: 10.1109/cdc.2009.5400067.

[185] K. Yano, *The theory of Lie derivatives and its applications*. Courier Dover Publications, 2020.

[186] T. Ely, S. Bhaskaran, N. Bradley, T. J. W. Lazio, and T. Martin-Mur, "Comparison of deep space navigation using optical imaging, pulsar time-of-arrival tracking, and/or radiometric tracking", *The Journal of the Astronautical Sciences*, vol. 69, no. 2, pp. 385–472, Apr. 2022. DOI: 10.1007/s40295-021-00290-z.

[187] D. Dirkx, I. Prochazka, S. Bauer, *et al.*, "Laser and radio tracking for planetary science missions—a comparison", *Journal of Geodesy*, vol. 93, no. 11, pp. 2410–2411, Jul. 2018. DOI: 10.1007/s00190-018-1171-x.

[188] H. Cramér, *Mathematical methods of statistics*. Princeton university press, 1999, vol. 26.

[189] D. K. Geller, "Linear covariance techniques for orbital rendezvous analysis and autonomous onboard mission planning", *Journal of Guidance, Control, and Dynamics*, vol. 29, no. 6, pp. 1404–1414, Nov. 2006, ISSN: 1533-3884. DOI: 10.2514/1.19447.

[190] E. Turan, S. Speretta, and E. Gill, "Performance analysis of radiometric autonomous navigation for lunar satellite network topologies", English, 11th International Workshop on Satellite Constellations and Formation Flying,, IWSCFF2022 ; Conference date: 07-06-2022 Through 08-06-2022, 2022.

[191] E. Turan, S. Speretta, and E. Gill, "Radiometric autonomous navigation for cislunar satellite formations", English, Presented at the NAVITEC 2022 conference; NAVITEC 2022 ; Conference date: 05-04-2022 Through 07-04-2022, 2022.

[192] E. Turan, S. Speretta, and E. Gill, "Autonomous Crosslink Radionavigation for a Lunar CubeSat Mission", *Frontiers in Space Technologies*, vol. 3, pp. 1–12, Jun. 2022. DOI: 10.3389/frspt.2022.919311.

[193] J. Havlik and O. Straka, "Performance evaluation of iterated extended kalman filter with variable step-length", *Journal of Physics: Conference Series*, vol. 659, p. 012 022, Nov. 2015. DOI: 10.1088/1742-6596/659/1/012022.

[194] C. Ott, M. Bolliger, M. Thompson, N. P. Ré, and D. C. Davis, "Range biases, measurement noise, and perilune accuracy in near rectilinear halo orbit navigation", in *AIAA Scitech 2022 Forum*, 2022, p. 0999.

[195] M. D. Rayman, P. Varghese, D. H. Lehman, and L. L. Livesay, "Results from the deep space 1 technology validation mission", *Acta Astronautica*, vol. 47, no. 2-9, pp. 475–487, Jul. 2000. DOI: 10.1016/s0094-5765(00)00087-4.

[196] A. F. Cheng, A. G. Santo, K. J. Heeres, *et al.*, "Near-earth asteroid rendezvous: Mission overview", *Journal of Geophysical Research: Planets*, vol. 102, no. E10, pp. 23 695–23 708, Oct. 1997. DOI: 10.1029/96je03364.

[197] S.-i. Watanabe, Y. Tsuda, M. Yoshikawa, S. Tanaka, T. Saiki, and S. Nakazawa, "Hayabusa2 mission overview", *Space Science Reviews*, vol. 208, no. 1-4, pp. 3–16, Jun. 2017. DOI: 10.1007/s11214-017-0377-1.

[198] D. S. Lauretta, S. S. Balram-Knutson, E. Beshore, *et al.*, "OSIRIS-REx: Sample return from asteroid (101955) bennu", *Space Science Reviews*, vol. 212, no. 1-2, pp. 925–984, Aug. 2017. DOI: 10.1007/s11214-017-0405-1.

[199] P. Michel, M. Küppers, A. C. Bagatin, *et al.*, "The ESA hera mission: Detailed characterization of the DART impact outcome and of the binary asteroid (65803) didymos", *The Planetary Science Journal*, vol. 3, no. 7, p. 160, Jul. 2022. DOI: 10.3847/psj/ac6f52.

[200] S. Casini, E. Turan, A. Cervone, B. Monna, and P. Visser, "Combined optical line-of-sight and crosslink radiometric navigation for distributed deep-space systems", *Scientific Reports*, vol. 13, no. 1, Sep. 2023. DOI: 10.1038/s41598-023-43339-9.

[201] E. Turan, S. Speretta, and E. Gill, "Particle swarm optimization based tracking window planning for cislunar orbiters performing autonomous radiometric navigation", English, in *Proceedings of the 74th International Astronautical Congress (IAC)*, 74th International Astronautical Congress (IAC), IAC 2023 ; Conference date: 02-10-2023 Through 06-10-2023, 2023.

[202] J. Kennedy and R. Eberhart, "Particle swarm optimization", in *Proceedings of ICNN'95 - International Conference on Neural Networks*, IEEE. DOI: 10.1109/icnn.1995.488968.

[203] E. Geipel, "Halo orbit determination, integration, and station keeping", 2019.

A

Deep Space Small Satellite Missions

This appendix provides additional information about the various missions analyzed throughout this dissertation. Detailed in Table A.1, the list includes essential aspects of each mission, offering a comprehensive overview for easy reference. For each mission, the table outlines the mission's name, the form factor of the satellites involved, and the leading organizations. Additionally, the destination of each mission is specified, highlighting the targeted locations. Primary objectives of these missions are also included, shedding light on the specific goals and scientific pursuits each mission aims to achieve. Lastly, corresponding references are provided for each mission, allowing readers to find specific details and gather further insights.

Table A.1: List of all studied small satellite missions

Mission ID	Size	Organization	Destination	Objectives	Reference
Lunar IceCube	6U	Morehead State University	Cislunar	Search for water on the Moon from a low-perigee highly inclined lunar orbit	[45]
LunaH-Map	6U	Arizona State University	Cislunar	Search for hydrogen on the permanently shadowed lunar crates	[46]
Lunar Flashlight	6U	NASA Jet Propulsion Lab. and Marshall Space Flight Center	Cislunar	Search for ice deposits and identifying favorable locations	[20]
NEA Scout	6U	NASA Jet Propulsion Lab. and Marshall Space Flight Center	Cislunar	Take pictures of the asteroid 1991 VG and observe its position in space using a solar sail propulsion	[20]
CuSP	6U	Southwest Research Institute	Cislunar	Study dynamic particles and magnetic fields in near-Earth orbit, and support space weather research	[65]
LunIR	6U	Lockheed Martin	Cislunar	Perform a lunar flyby taking images of the lunar surface and its environment for remote sensing, site selection observations, and to surface characterization	[63]
OMOTENASHI	6U	JAXA, University of Tokyo	Cislunar	Demonstrate a lunar semi-hard landing by a CubeSat and observe the radiation environment and soil mechanics	[48]
EQUULEUS	6U	JAXA, University of Tokyo	Cislunar	Demonstrate trajectory control techniques, and to observe the Moon from Earth-Moon L2	[50]
BioSentinel	6U	NASA Ames Research Center	Cislunar	Measure the impact of space radiation on living organisms over long duration	[67]
ArgoMoon	6U	Argotec, Italian Space Agency	Cislunar	Taking pictures of the SLS secondary propulsion stage and the Moon and the surrounding environment	[47]
Cislunar Explorers	6U	Cornell University	Cislunar	Demonstrate the water electrolysis propulsion and autonomous optical navigation technologies	[49]
CU-E3	6U	University of Colorado	Lunar Flyby	Demonstrate long-distance (more than 4 million km) communications	[69]
Team Miles	6U	Team Miles Tampa Hackerspace	Lunar Flyby	Demonstrate long-distance communications with a software-defined radio operating in the S-band and navigation capability using plasma thrusters	[71]
M-ARGO	6U	ESA	Small Bodies	Rendezvous with an asteroid, characterise its physical properties and assess potential for resource exploitation	[30]
HALO	6U	NASA Glenn Research Center	Cislunar	Survey the surface of the Moon andto observe the impinging solar wind and the reflected ion component	[23]

DAVID	6U	NASA Glenn Research Center	Small Bodies	investigate an asteroid, 2001 GP2, which is the smallest asteroid investigated by previous missions	[23]
MAT	Mid ESPA	Space Science Institute, Exo Terra Resource, Malin Space Science Systems, NASA GSFC, CNRS/LMD	Mars	Observe the temporal evolution of dust storms and water ice clouds and to detect changes in surface physicalproperties throughout the diurnal cycle	[74]
CUVE	12U	University of Maryland, NASA GSFC	Venus	Measure the ultraviolet light absorption to understand the Venus atmospheric dynamics	[62]
JUMPER	N/A	Southwest Research Institute NASA JPL, CU LASP	Jupiter	Understand the solar wind's interaction with Jupiter's magnetosphere and to determine its energetic neutral atomemissions	[66]
PrOVE	Mid ESPA	University of Maryland, NASA GSFC, JPL	Jupiter	Perform a close flyby of a new and Jupiter familycomet and study surface structure and volatile inventory	[68]
Ross	6U	Lockheed Martin, Uni. of Hawaii, Malin Space Science Systems, SETI Institute	Small Bodies	Obtain fundamentaldata on size, shape and structure during flyby to different Near Earth Objects	[56]
VAMOS	ESPA	NASA Jet Propulsion Lab., Uni. of Illinois, Uni. of Michigan, CNES, DLR	Jupiter	Determine the global seismic activity of Venus	[70]
WATER	ESPA	John Hopkins Applied Physics Laboratory, NASA GRC, GSFC, MSFC	Cislunar	Characterize water on the surface of the Moon including its chemical form, and distribution	[52]
CubeX	12U	Smithsonian Astrophysical Observatory, Harvard Uni., MIT, Carnegie Inst., of Washington., GSFC, Birkbeck College, Uni. of Arizona, NASA Ames RS	Cislunar	Identify and spatially map lunar crust and demonstrate semi-autonomous deep space navigation using X-raypulsars with a X-ray telescope	[54]
IMPEL	ESPA	NASA Johnson Space Center	Cislunar	Explore a site of potentially recent volcanism on the Moon	[53]
MARIO	16U	Politecnico di Milano	Mars	Perform thermal radiation imaging and to establish long-distance X-band communication link withthe Earth	[75]
ASPECT	3U	VTT, University of Helsinki, Aalto University, ESA	Small Bodies	Map the surface composition of the asteroid, to characterize possible landing sites, and evaluatesurface areas and objects for sample return	[31]
DustCube	3U	University of Vigo, University of Bologna, MICOS, ESA	Small Bodies	Characterize the natural dustenvironment and ejected plume due to high speed impact on the asteroid and imaging of the Didymoon before, during and after impact	[32]

CUBATA	3U	GMV, University of La Sapienza, INTA, ESA	Small Bodies	Determine the gravity field of the Didymos before and after impact with Doppler shift provided due to the relative line-of-sight velocity between the two spacecraft and to observe the impact from two different viewpoints	[33]
PALS	3U	Swedish Institute of Space Physics, KTH, DLR, IEEC, AAC Microtec, ESA	Small Bodies	Characterizesurface structure and magnetisation, and observe impact plume	[34]
AGEX	3U	ROB, ISAE Supaero, Emxys, Antwerp Space, ESA	Small Bodies	Measure mass during the descent and landing, anddetermination of dynamical state, local gravity before and after impact	[35]
Juventas	6U	GMV, Astronika, Brno University, CSRC, ESA	Small Bodies	Characterize the gravity field and internal structure and to determine the surface and the dynamical properties of Didymos	[36]
MILANI	6U	IRF, KTH, RSL, Aalto Uni. VTT Research Center, Uni. of Helsinki, DLR Bremen, SSC, ESA	Small Bodies	Map the surface composition and internal structure of Didymos	[36]
LUMIO	12U	Politecnico di Milano, TU Delft, EPFL, S&T Norway,	Cislunar	Observe, quantify and characterizemeteroid impacts on the Lunar farside by detecting their impact flashes with an optical camera	[37]
VMMO	12U	MPB Communications, University of Surrey, Lends R&D, University of Winnipeg, ESA	Cislunar	Search for water ice deposits in permanently shadowed craters at the south pole	[40]
MoonCare	12U	Von Karman Institute, DLR, Tyvak International, Politecnico di Torino	Cislunar	Characterize and study the lunar radiation and its effect on microorganisms	[38]
CLE	12U	ISIS bv, ASTRON, Radboud Uni. Nijmegen, Uni. Twente, TU Delft	Cislunar	Demonstrate radio astronomy below 30MHz in lunar radio quiet zone	[39]
Cupid's Arrow	Pr.	NASA Jet Propulsion Lab., CalTech, Georgia Tech., Uni. Nancy	Venus	Measure noble gases around Venus	[61]
SAEVe	Pr.	NASA Glenn Research Center, Imperial College London, Wesleyan Uni., Lunar and Planetary Institute NASA JPL, Uni. of Oxford	Jupiter	Determinegeophysical activity of Venus	[64]

SNAP	Pr.	Hampton University, NASA Langley RC, JPL, Uni. of California Berkeley, Purdue Uni.	Uranus	Examine the physical and chemical processes in the Uranus atmosphere	[72]
Mini-Maggie	3U	University of Alaska, NASA Jet Propulsion Lab.	Europa	Characterize the magnetic field and gravity around Europa	[26]
DARCSIDE	3U	New Mexico State University	Europa	Perform singlelow-altitude pass above Europa and measure atmospheric density and heavy ion flux	[27]
Sylph	Pr.	Cornell University	Europa	Sample a presumed plume on Europa by performing single 2km altitude flyby above thesurface	[28]
ETP	Pr.	Italian Space Agency	Europa	Measure the magnetic field at different orbital and rotational frequencies, rotational state and tidal information with an inter-satellite link enabled by a transponder	[29]
B1	Pr.	JAXA	Small Bodies	Encounter and fly closer to take a multi-dimensional picture of the comet	[51]
B2	Pr.	ESA	Small Bodies	Encounter and fly closer to take a multi-dimensional picture of the comet	[51]
BIRDY-T	3U	Paris Observatory CERES, Uni. PSL, Odysseus Space SA	Small Bodies	Fly small solar system body to observe the sizeand shape and perform radio science experiment with an inter-satellite link between a mother-spacecraft andthe CubeSat	[10]
AI3	16U	Uni. of Kiel, Max Planck Institute for Solar System Research	Small Bodies	Characterize of an asteroid, by making use of inter-satellite link, and detect the seismic wave after an impactevent produced by an impactor,	[55]
MarsDrop	Pr.	NASA JPL, Aerospace Corporation, Planetary Science Institute	Mars	Take instruments to difficult sites inaccessible for large landers and rovers	[73]
NanoSWARM	3U	Uni. of California Santa Cruz UCLA, MIT, UC Berkeley, APL, Ames, JPL, Tyvak, KASI Northrop Grumman	Cislunar	Understand mechanisms of space weathering, near surface water formation and the origin of planetary magnetism	[57]
MarCO	6U	NASA Jet Propulsion Lab.	Mars	Fly independently to Mars and act as a relay during InSight's entry, descent and landing phase	[76]
MISEN	Mid ESPA	UC Berkeley SSL, UCLA ESS, Tyvak LLC, Advanced Space LLC	Mars	Characterize the magnitude, global patterns and real-time response tospace weather of ion escape at Mars	[78]
MiLuV	ESPA	NASA Goddard Space Flight Center	Cislunar	Map lunar volatiles by using a lunar ice spectrometer	[59]

APEX	Pr.	Johns Hopkins Uni., Arizona State Uni., Sandia National Lab., Uni. Maryland	Small Bodies	Determine the interior structure of an asteroid, Apophis, to understand its origin and evolution	[58]
PRISM	12U	NASA GSFC, Morehead St. Uni., JHU APL, Uni. of Iowa, Georgia Institute of Tech., NASA JPL	Small Bodies	Investigate Phobos and Deimos with an ion mass spectrometer	[49]
Aeolus	24U	NASA Ames Research Center	Mars	Produce global wind speed may, determine the global energy balance and measure atmospheric aerosol at Mars	[77]
BOLAS	12U	NASA GSFC, Morehead State Uni., Tethers Unlimited, Busek	Cislunar	Investigate the hydration and space weathering processes at the Moon	[60]
OLFAR	N/A	ASTRON	Cislunar	Investigate frequency ranges between 30kHz - 30MHz at Lunar orbit or Sun-Earth L4-L5	[41]
DSL	N/A	Radboud University Nijmegen, CAS-SHAO	Cislunar	Explore frequency range between 100KHz - 50MHz at Sun-Earth L2 with 8 spacecrafts	[42]
DEx	N/A	Radboud University Nijmegen	Sun-Earth L2	Investigate frequency ranges between100KHz - 80MHz and 1MHz-100MHz respectively at Sun-Earth L2	[43]
LICIACube	6U	Italian Space Agency	Small Bodies	Perform an autonomous flyby of the Didymos system, testify the DART impact, obtaining multiple images of the impact site and Dimorphos.	[18]
SULFRO	2U	Shanghai Engineering Centre for Microsatellites	Sun-Earth L2	Investigate frequency ranges between 100KHz - 80MHz and 1MHz-100MHz respectively at Sun-Earth L2	[44]
MIIAR	6U	North South University	Mars	Study of Mars surface using hyperspectral imaging and act as relay satellites between surface assets and the Earth	[79]
MMO	6U	Malin Space Science Systems	Mars	Measure the Mars atmosphere in visible and infrared wavelengths from Mars orbit and serve as a relay for Mars surface based missions	[24]
CAPSTONE	12U	Advanced Space	Cislunar	Demonstrate the reliability of innovative spacecraft-to-spacecraft navigation solutions as well as communication capabilities with Earth	[17]

B

Observability Matrix Components: Derivatives and Approximations

This appendix introduces the partial derivatives of measurements, along with the detailed parts of the observability matrix.

The foundation of this analysis is the derivation of partial derivatives with respect to the state vectors of spacecraft within a formation, focusing on three primary observables: Geometric range, range-rate, and inertial angle. Since the Satellite-to-Satellite Tracking (SST)-based OD process involves the position and velocity states of two spacecraft within a formation, the state vector is given as:

$$\mathbf{x} = \begin{bmatrix} \mathbf{r}_1 & \mathbf{v}_1 & \mathbf{r}_2 & \mathbf{v}_2 \end{bmatrix}^T \tag{B.1}$$

where $\mathbf{r}_i$ and $\mathbf{v}_i$ represent the position and velocity states of two spacecraft within a formation, $i = 1,2$. As a reminder for the observation matrix, $\tilde{H}$, including all these navigation data types:

$$\tilde{H} = \frac{\partial y}{\partial \mathbf{x}} = \begin{bmatrix} \frac{\partial \rho_{SST}}{\partial \mathbf{x}} & \frac{\partial \dot{\rho}_{SST}}{\partial \mathbf{x}} & \frac{\partial \phi_{SST}}{\partial \mathbf{x}} & \frac{\partial \varphi_{SST}}{\partial \mathbf{x}} & \frac{\partial \rho_{GS}}{\partial \mathbf{x}} & \frac{\partial \dot{\rho}_{GS}}{\partial \mathbf{x}} \end{bmatrix} \tag{B.2}$$

The SST-based geometric range, range-rate, and inertial angle measurement partial derivatives with respect to the spacecraft states are:

$$\tilde{H}_\rho = \begin{bmatrix} \frac{(x_1-x_2)}{\rho} & \frac{(y_1-y_2)}{\rho} & \frac{(z_1-z_2)}{\rho} & 0_{1\times 3} & \frac{-(x_1-x_2)}{\rho} & \frac{-(y_1-y_2)}{\rho} & \frac{-(z_1-z_2)}{\rho} & 0_{1\times 3} \end{bmatrix} \tag{B.3}$$

B

$$\tilde{H}_{\dot{\rho}} = \begin{bmatrix} \frac{(\dot{x}_1-\dot{x}_2)}{\rho} - \frac{(x_1-x_2)\left((x_1-x_2)(\dot{x}_1-\dot{x}_2)+(y_1-y_2)(\dot{y}_1-\dot{y}_2)+(z_1-z_2)(\dot{z}_1-\dot{z}_2)\right)}{\rho^3} \\ \frac{(\dot{y}_1-\dot{y}_2)}{\rho} - \frac{(y_1-y_2)\left((x_1-x_2)(\dot{x}_1-\dot{x}_2)+(y_1-y_2)(\dot{y}_1-\dot{y}_2)+(z_1-z_2)(\dot{z}_1-\dot{z}_2)\right)}{\rho^3} \\ \frac{(\dot{z}_1-\dot{z}_2)}{\rho} - \frac{(z_1-z_2)\left((x_1-x_2)(\dot{x}_1-\dot{x}_2)+(y_1-y_2)(\dot{y}_1-\dot{y}_2)+(z_1-z_2)(\dot{z}_1-\dot{z}_2)\right)}{\rho^3} \\ \frac{(x_1-x_2)}{\rho} \\ \frac{(y_1-y_2)}{\rho} \\ \frac{(z_1-z_2)}{\rho} \\ -\frac{(\dot{x}_1-\dot{x}_2)}{\rho} + \frac{(x_1-x_2)\left((x_1-x_2)(\dot{x}_1-\dot{x}_2)+(y_1-y_2)(\dot{y}_1-\dot{y}_2)+(z_1-z_2)(\dot{z}_1-\dot{z}_2)\right)}{\rho^3} \\ -\frac{(\dot{y}_1-\dot{y}_2)}{\rho} + \frac{(y_1-y_2)\left((x_1-x_2)(\dot{x}_1-\dot{x}_2)+(y_1-y_2)(\dot{y}_1-\dot{y}_2)+(z_1-z_2)(\dot{z}_1-\dot{z}_2)\right)}{\rho^3} \\ -\frac{(\dot{z}_1-\dot{z}_2)}{\rho} + \frac{(z_1-z_2)\left((x_1-x_2)(\dot{x}_1-\dot{x}_2)+(y_1-y_2)(\dot{y}_1-\dot{y}_2)+(z_1-z_2)(\dot{z}_1-\dot{z}_2)\right)}{\rho^3} \\ -\frac{(x_1-x_2)}{\rho} \\ -\frac{(y_1-y_2)}{\rho} \\ -\frac{(z_1-z_2)}{\rho} \end{bmatrix}^T \tag{B.4}$$

$$\tilde{H}_{\phi} = \begin{bmatrix} \frac{-(y_1-y_2)}{(x_1-x_2)^2\left(\frac{(y_1-y_2)^2}{(x_1-x_2)^2}+1\right)} & \frac{1}{(x_1-x_2)\left(\frac{(y_1-y_2)^2}{(x_1-x_2)^2}+1\right)} & 0_{1\times 4} & \frac{(y_1-y_2)}{(x_1-x_2)^2\left(\frac{(y_1-y_2)^2}{(x_1-x_2)^2}+1\right)} & \frac{-1}{(x_1-x_2)\left(\frac{(y_1-y_2)^2}{(x_1-x_2)^2}+1\right)} & 0_{1\times 4} \end{bmatrix} \tag{B.5}$$

$$\tilde{H}_{\varphi} = \begin{bmatrix} \frac{(2x_1-2x_2)(z_1-z_2)}{(2(1-(z_1-z_2)^2/((x_1-x_2)^2+(y_1-y_2)^2+(z_1-z_2)^2))^{1/2}((x_1-x_2)^2+(y_1-y_2)^2+(z_1-z_2)^2)^{3/2})} \\ \frac{(2y_1-2y_2)(z_1-z_2)}{(2(1-(z_1-z_2)^2/((x_1-x_2)^2+(y_1-y_2)^2+(z_1-z_2)^2))^{1/2}((x_1-x_2)^2+(y_1-y_2)^2+(z_1-z_2)^2)^{3/2})} \\ \frac{-(x_1^2-2x_1x_2+x_2^2+y_1^2-2y_1y_2+y_2^2)}{(1-(z_1-z_2)^2/((x_1-x_2)^2+(y_1-y_2)^2+(z_1-z_2)^2))^{1/2}((x_1-x_2)^2+(y_1-y_2)^2+(z_1-z_2)^2)^{3/2}} \\ 0_{3\times 1} \\ \frac{-(2x_1-2x_2)(z_1-z_2)}{(2(1-(z_1-z_2)^2/((x_1-x_2)^2+(y_1-y_2)^2+(z_1-z_2)^2))^{1/2}((x_1-x_2)^2+(y_1-y_2)^2+(z_1-z_2)^2)^{3/2})} \\ \frac{-(2y_1-2y_2)(z_1-z_2)}{(2(1-(z_1-z_2)^2/((x_1-x_2)^2+(y_1-y_2)^2+(z_1-z_2)^2))^{1/2}((x_1-x_2)^2+(y_1-y_2)^2+(z_1-z_2)^2)^{3/2})} \\ \frac{(x_1^2-2x_1x_2+x_2^2+y_1^2-2y_1y_2+y_2^2)}{(1-(z_1-z_2)^2/((x_1-x_2)^2+(y_1-y_2)^2+(z_1-z_2)^2))^{1/2}((x_1-x_2)^2+(y_1-y_2)^2+(z_1-z_2)^2)^{3/2}} \\ 0_{3\times 1} \end{bmatrix}^T \tag{B.6}$$

For ground-based measurements, the geometric range and range-rate measurement partial derivatives, $\tilde{H}_{\rho_{GS}}$ and $\tilde{H}_{\dot{\rho}_{GS}}$, are derived similarly from B.3 and B.4, with the distinction that partials related to the non-tracked spacecraft are set to zero. This differentiation acknowledges the scenario where only one spacecraft in the formation is being tracked from the ground.

In the observability analysis, $\tilde{H}$ must be mapped to the initial epoch t_0 through the STM as:

$$H_k = \tilde{H}_k \Phi(t_k, t_0) \tag{B.7}$$

Considering a formation formed by two spacecraft $i = 1, 2$, the STM is given by:

$$\dot{\Phi}(t, t_k) = A(\mathrm{t})\Phi(t, t_k) = \frac{\partial F(\mathbf{x}^*, t)}{\partial \mathbf{x}} \Phi(t, t_k), \qquad \Phi(t_0, t_0) = I_{12\mathrm{x}12} \tag{B.8}$$

where

$$A(t) = \frac{\partial F(\mathbf{x},t)}{\partial \mathbf{x}} = \begin{bmatrix} \frac{\partial \dot{x}_1}{\partial x_1} & \frac{\partial \dot{x}_1}{\partial y_1} & \frac{\partial \dot{x}_1}{\partial z_1} & \cdots & \frac{\partial \dot{x}_1}{\partial \dot{z}_2} \\ \frac{\partial \dot{y}_1}{\partial x_1} & \frac{\partial \dot{y}_1}{\partial y_1} & \frac{\partial \dot{y}_1}{\partial z_1} & & \\ \frac{\partial \dot{z}_1}{\partial x_1} & \frac{\partial \dot{z}_1}{\partial y_1} & \frac{\partial \dot{z}_1}{\partial z_1} & & \vdots \\ \vdots & & & \ddots & \\ \frac{\partial \ddot{z}_2}{\partial x_1} & & \cdots & & \frac{\partial \ddot{z}_2}{\partial \dot{z}_2} \end{bmatrix}$$

$$= \begin{bmatrix} & 0_{3\times3} & & & I_{3\times3} & & & & \\ \frac{\partial \ddot{x}_1}{\partial x_1} & \frac{\partial \ddot{x}_1}{\partial y_1} & \frac{\partial \ddot{x}_1}{\partial z_1} & 0 & 2 & 0 & & 0_{6\times6} & \\ \frac{\partial \ddot{y}_1}{\partial x_1} & \frac{\partial \ddot{y}_1}{\partial y_1} & \frac{\partial \ddot{y}_1}{\partial z_1} & -2 & 0 & 0 & & & \\ \frac{\partial \ddot{z}_1}{\partial x_1} & \frac{\partial \ddot{z}_1}{\partial y_1} & \frac{\partial \ddot{z}_1}{\partial z_1} & 0 & 0 & 0 & & & \\ & & & & & & 0_{3\times3} & & I_{3\times3} \\ & 0_{6\times6} & & & & & \frac{\partial \ddot{x}_2}{\partial x_2} & \frac{\partial \ddot{x}_2}{\partial y_2} & \frac{\partial \ddot{x}_2}{\partial z_2} & 0 & 2 & 0 \\ & & & & & & \frac{\partial \ddot{y}_2}{\partial x_2} & \frac{\partial \ddot{y}_2}{\partial y_2} & \frac{\partial \ddot{y}_2}{\partial z_2} & -2 & 0 & 0 \\ & & & & & & \frac{\partial \ddot{z}_2}{\partial x_2} & \frac{\partial \ddot{z}_2}{\partial y_2} & \frac{\partial \ddot{z}_2}{\partial z_2} & 0 & 0 & 0 \end{bmatrix} \tag{B.9}$$

and

$$\begin{aligned}
\frac{\partial \ddot{x}_i}{\partial x_i} &= \frac{(\mu-1)}{{r_1}^3} - \frac{\mu}{{r_2}^3} + \frac{3\mu(\mu+x_i-1)(\mu+x_i-1)}{{r_2}^5} - \frac{3(\mu+x_i)(\mu+x_i)(\mu-1)}{{r_1}^5} + 1 \\
\frac{\partial \ddot{x}_i}{\partial y_i} &= \frac{3\,\mu\,y_i(\mu+x_i-1)}{{r_2}^5} - \frac{3y_i(\mu+x_i)(\mu-1)}{{r_1}^5} \\
\frac{\partial \ddot{x}_i}{\partial z_i} &= \frac{3\,\mu\,z_i(\mu+x_i-1)}{{r_2}^5} - \frac{3z_i(\mu+x_i)(\mu-1)}{{r_1}^5} \\
\frac{\partial \ddot{y}_i}{\partial x_i} &= -y_i\left(\frac{3(\mu+x_i)(\mu-1)}{{r_1}^5} + \frac{3\mu(\mu+x_i-1)}{{r_2}^5}\right) \\
\frac{\partial \ddot{y}_i}{\partial y_i} &= \frac{(\mu-1)}{{r_1}^3} + y_i\left(\frac{3\,\mu\,y_i}{{r_2}^5} - \frac{3y_i(\mu-1)}{{r_1}^5}\right) - \frac{\mu}{{r_2}^3} + 1 \\
\frac{\partial \ddot{y}_i}{\partial z_i} &= y_i\left(\frac{3\,\mu\,z_i}{{r_2}^5} - \frac{3\,z_i(\mu-1)}{{r_1}^5}\right) \\
\frac{\partial \ddot{z}_i}{\partial x_i} &= -z_i\left(\frac{3(\mu+x_i)(\mu-1)}{{r_1}^5} - \frac{3\mu(\mu+x_i-1)}{{r_2}^5}\right) \\
\frac{\partial \ddot{z}_i}{\partial y_i} &= z_i\left(\frac{3\,\mu\,y_i}{{r_2}^5} - \frac{3\,y_i(\mu-1)}{{r_1}^5}\right) \\
\frac{\partial \ddot{z}_i}{\partial z_i} &= \frac{\mu-1}{{r_1}^3} + z_i\left(\frac{3\,\mu\,z_i}{{r_2}^5} - \frac{3\,z_i(\mu-1)}{{r_1}^5}\right) - \frac{\mu}{{r_2}^3}
\end{aligned} \tag{B.10}$$

Moreover, each component of the STM can be given as:

$$\dot{\Phi}_{m,n}(t_k,t_0) = \Phi_{m+3,\,n}(t_k,t_0)$$

$$\text{e.g., } \dot{\Phi}_{1,1}(t_k,t_0) = \Phi_{4,\,1}(t_k,t_0)$$

where $m = 1,2,3,7,8,9$ and $n = 1,2,...,12$ and,

$$\begin{aligned}
\dot{\Phi}_{4,n}(t_k,t_0) &= 2\Phi_{5,n}(t_k,t_0) + \frac{\partial \ddot{x}_1}{\partial x_1}\Phi_{1,n}(t_k,t_0) + \frac{\partial \ddot{x}_1}{\partial y_1}\Phi_{2,n}(t_k,t_0) + \frac{\partial \ddot{x}_1}{\partial z_1}\Phi_{3,n}(t_k,t_0)\\
\dot{\Phi}_{5,n}(t_k,t_0) &= 2\Phi_{4,\,n}(t_k,t_0) + \frac{\partial \ddot{y}_1}{\partial x_1}\Phi_{1,n}(t_k,t_0) + \frac{\partial \ddot{y}_1}{\partial y_1}\Phi_{2,n}(t_k,t_0) + \frac{\partial \ddot{y}_1}{\partial z_1}\Phi_{3,n}(t_k,t_0)\\
\dot{\Phi}_{6,n}(t_k,t_0) &= \frac{\partial \ddot{z}_1}{\partial x_1}\Phi_{1,n}(t_k,t_0) + \frac{\partial \ddot{z}_1}{\partial y_1}\Phi_{2,n}(t_k,t_0) + \frac{\partial \ddot{z}_1}{\partial z_1}\Phi_{3,n}(t_k,t_0)\\
\dot{\Phi}_{10,n}(t_k,t_0) &= 2\Phi_{11,\,n}(t_k,t_0) + \frac{\partial \ddot{x}_2}{\partial x_2}\Phi_{7,n}(t_k,t_0) + \frac{\partial \ddot{x}_2}{\partial y_2}\Phi_{8,n}(t_k,t_0) + \frac{\partial \ddot{x}_2}{\partial z_2}\Phi_{9,n}(t_k,t_0)\\
\dot{\Phi}_{11,n}(t_k,t_0) &= 2\Phi_{12,\,n}(t_k,t_0) + \frac{\partial \ddot{y}_2}{\partial x_2}\Phi_{7,n}(t_k,t_0) + \frac{\partial \ddot{y}_2}{\partial y_2}\Phi_{8,n}(t_k,t_0) + \frac{\partial \ddot{y}_2}{\partial z_2}\Phi_{9,n}(t_k,t_0)\\
\dot{\Phi}_{12,n}(t_k,t_0) &= \frac{\partial \ddot{z}_2}{\partial x_2}\Phi_{7,n}(t_k,t_0) + \frac{\partial \ddot{z}_2}{\partial y_2}\Phi_{8,n}(t_k,t_0) + \frac{\partial \ddot{z}_2}{\partial z_2}\Phi_{9,n}(t_k,t_0)\\
\text{e.g., } \dot{\Phi}_{4,1}(t_k,t_0) &= 2\Phi_{5,\,1}(t_k,t_0) + \frac{\partial \ddot{x}_1}{\partial x_1}\Phi_{1,1}(t_k,t_0) + \frac{\partial \ddot{x}_1}{\partial y_1}\Phi_{2,1}(t_k,t_0) + \frac{\partial \ddot{x}_1}{\partial z_1}\Phi_{3,1}(t_k,t_0)
\end{aligned} \tag{B.11}$$

where $m = 4,5,6,10,11,12$ and $n = 1,2,...,12$. Due to the complexity of solving these coupled equations analytically, the study outlines an approximation strategy for scenarios where the time difference between t and t_0 is minimal. This approximation relies on expanding the STM, into a series, simplifying the process by considering only terms up to the second order. This approach is mathematically represented as follows:

$$\Phi(t_k,t_0) = I_{12\text{x}12} + A\cdot(t_k-t_0) + \frac{A^2\cdot(t_k-t_0)^2}{2!} + ... \tag{B.12}$$

Finally, the STM is given as:

$$\Phi(t_k,t_0) = \begin{bmatrix} M_1 & 0_{6\text{x}6} \\ 0_{6\text{x}6} & M_2 \end{bmatrix} \tag{B.13}$$

where matrices M_1 and M_2 can be found by:

$$M_k = \begin{bmatrix}
\frac{\partial \ddot{x}_k}{\partial x_k}\frac{{T_s}^2}{2}+1 & \frac{\partial \ddot{x}_k}{\partial y_k}\frac{{T_s}^2}{2} & \frac{\partial \ddot{x}_k}{\partial z_k}\frac{{T_s}^2}{2} & T_s & {T_s}^2 & 0\\
\frac{\partial \ddot{y}_k}{\partial x_k}\frac{{T_s}^2}{2} & \frac{\partial \ddot{y}_k}{\partial y_k}\frac{{T_s}^2}{2}+1 & \frac{\partial \ddot{y}_k}{\partial z_k}\frac{{T_s}^2}{2} & {T_s}^2 & T_s & 0\\
\frac{\partial \ddot{z}_k}{\partial x_k}\frac{{T_s}^2}{2} & \frac{\partial \ddot{z}_k}{\partial y_k}\frac{{T_s}^2}{2} & \frac{\partial \ddot{z}_k}{\partial z_k}\frac{{T_s}^2}{2}+1 & 0 & 0 & T_s\\
\frac{\partial \ddot{y}_k}{\partial x_k}{T_s}^2+\frac{\partial \ddot{x}_k}{\partial x_k}T_s & \frac{\partial \ddot{y}_k}{\partial y_k}{T_s}^2+\frac{\partial \ddot{x}_k}{\partial y_k}T_s & \frac{\partial \ddot{y}_k}{\partial z_k}{T_s}^2+\frac{\partial \ddot{x}_k}{\partial z_k}T_s & \frac{{T_s}^2}{2}\left(\frac{\partial \ddot{x}_k}{\partial x_k}+4\right)+1 & \frac{\partial \ddot{x}_k}{\partial y_k}\frac{{T_s}^2}{2}+2T_s & \frac{{T_s}^2}{2}\frac{\partial \ddot{x}_k}{\partial z_k}\\
\frac{\partial \ddot{x}_k}{\partial x_k}{T_s}^2+\frac{\partial \ddot{y}_k}{\partial x_k}T_s & \frac{\partial \ddot{x}_k}{\partial y_k}{T_s}^2+\frac{\partial \ddot{y}_k}{\partial y_k}T_s & \frac{\partial \ddot{x}_k}{\partial z_k}{T_s}^2+\frac{\partial \ddot{y}_1}{\partial z_1}T_s & \frac{\partial \ddot{y}_k}{\partial x_k}\frac{{T_s}^2}{2}+2T_s & \frac{{T_s}^2}{2}\left(\frac{\partial \ddot{y}_k}{\partial y_k}+4\right)+1 & \frac{{T_s}^2}{2}\frac{\partial \ddot{y}_k}{\partial z_k}\\
T_s\frac{\partial \ddot{z}_k}{\partial x_k} & T_s\frac{\partial \ddot{z}_k}{\partial y_k} & T_s\frac{\partial \ddot{z}_k}{\partial z_k} & \frac{{T_s}^2}{2}\frac{\partial \ddot{z}_1}{\partial x_1} & \frac{{T_s}^2}{2}\frac{\partial \ddot{z}_1}{\partial y_1} & \frac{{T_s}^2}{2}\frac{\partial \ddot{z}_k}{\partial z_k}+1
\end{bmatrix} \tag{B.14}$$

with $T_s = t_k - t_0$ and the partial derivatives given the equation are presented in Eq. B.8. Finally, Eq. (B.7), $H_k = \tilde{H}_k\Phi(t_k,t_0)$ can be calculated as given in Eq. 4.10.

C

State Transition Matrix Comparison

In Orbit Determination (OD) process, the State Transition Matrix (STM) emerges as a pivotal element, mapping the states between epochs. This appendix introduces a comparison between the STM generated through a numerical integrator, specifically ODE113 in Matlab, and an approximated method outlined in Section 4.1.

The baseline of this comparison is the relative error parameter, ϵ, defined as the normalized sum of absolute differences between each element of the numerically integrated $\bar{\Phi}_{ij}$ and its approximated counterpart (Φ_{ij}. This parameter is calculated over all elements of the STM, providing a quantitative measure of the approximation method's accuracy against the reference set by the numerical integrator:

$$\epsilon = \frac{1}{36} \sum_{i=1}^{6} \sum_{j=1}^{6} \left| \frac{(\Phi_{ij} - \bar{\Phi}_{ij})}{\bar{\Phi}_{ij}} \right| \tag{C.1}$$

The analysis is carried out for two different orbital configurations, the Earth-Moon L2 and the Earth-Moon L1 Southern Halo orbits, over a period of 7 days. These orbits were selected for their different dynamical characteristics, offering a comprehensive test case for the comparative study. Initial conditions for these orbits are detailed in Table 3.7.

Table C.1: Performance investigation of the approximated STM.

$\Delta t(s)$	ϵ for the EML2 Halo Orbiter		ϵ for the EML1 Halo Orbiter	
	RMSE	1σ STD	RMSE	1σ STD
10	9.29×10^{-10}	7.54×10^{-10}	1.75×10^{-9}	1.13×10^{-9}
60	6.44×10^{-9}	1.64×10^{-8}	1.22×10^{-8}	2.83×10^{-8}
100	1.42×10^{-8}	3.89×10^{-8}	2.65×10^{-8}	6.70×10^{-8}
600	6.95×10^{-8}	5.54×10^{-7}	1.31×10^{-7}	9.68×10^{-7}

Table C.1 presents the Root Mean Square (RMS) errors and their standard deviations calculated for varying step sizes within the numerical integration process. A lower RMS error and a smaller standard deviation indicate a closer match between the approximated and the numerically integrated STMs, suggesting that the approximation method can reliably replicate the dynamics captured by the numerical integrator.

D

PERFORMANCE ANALYSIS TOOLBOX

In this dissertation, the OD models were developed from scratch using MATLAB, avoiding reliance on commercial software. This approach allowed for a comprehensive exploration of models ranging from simplistic to high-fidelity, tailored specifically to facilitate autonomous onboard OD via SST. The toolbox, considered as a *living project*, is continually evolving, reflecting ongoing development efforts aimed at enhancing its capabilities and reliability, aiming for practical implementation.

Currently, the toolbox is equipped to support a range of SST-based geometrical observations including range, range-rate, and angle data types. It calculates required matrices, such as partial derivatives of these observables relative to the estimated state vectors, crucial for OD. The inclusion of radiometric observables extends the toolbox's capability, allowing an exploration of how OD solutions respond to variations in radiometric parameters, for sensitivity analysis purposes. The dissertation introduced several estimation algorithms (see Chapter 3), all of which are incorporated into the toolbox.

Various analysis methods such as CRLB, Observability, Monte-Carlo, and Covariance analyses (see Chapter 4) are integrated within the toolbox. These features enable detailed performance assessments and help identify the most effective network topologies, particularly as the number of satellites within a formation increases. This capability is particularly beneficial for designing robust satellite networks.

Looking ahead, there are plans to make the toolbox accessible to externals interested in leveraging its capabilities for their mission analyses. This initiative aims to encourage broader collaboration and innovation in the field of autonomous navigation. For those interested in exploring the toolbox further, Figure D.1 offers several screenshots of the simplified version of this toolbox, and more detailed information can be obtained by contacting the author directly.

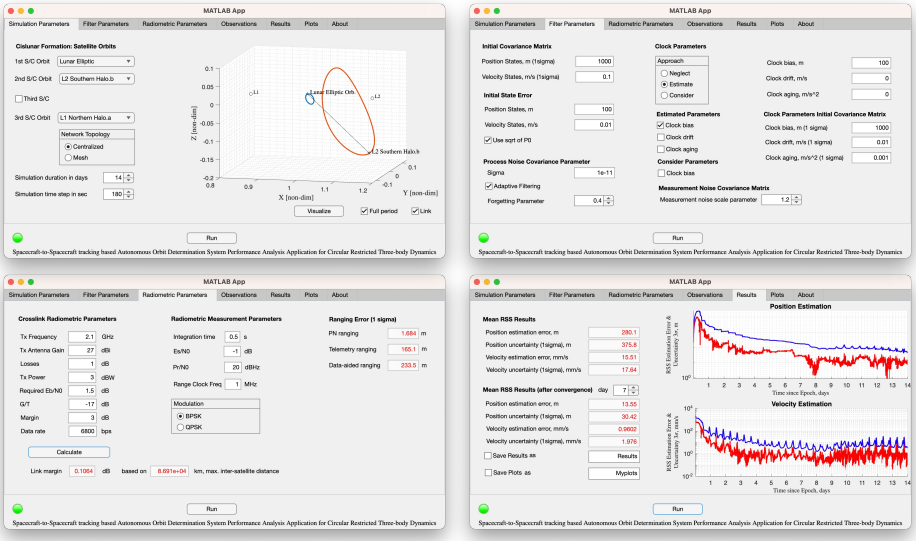

Figure D.1: Simplified version of the SST-based Autonomous OD Performance Analysis Toolbox, considering the CRTBP as dynamics.

List of Publications

Journal Papers

3. **Turan, E.**, Speretta, S., and Gill, E. (2023) *Performance analysis of crosslink radiometric measurement based autonomous orbit determination for cislunar small satellite formations*, Advances in Space Research

2. **Turan, E.**, Speretta, S., and Gill, E. (2022) *Autonomous Crosslink Radionavigation for a Lunar CubeSat Mission*, Frontiers in Space Technologies, Vol. 3 pp. 1-12.

1. **Turan, E.**, Speretta, S., and Gill, E. (2022) *Autonomous navigation for deep space small satellites: Scientific and technological advances*, Acta Astronautica, 193, pp. 56-74.

Conference Papers

4. **Turan, E.**, Speretta, S. & Gill, E. (2023) *"Particle Swarm Optimization based Tracking Window Planning for Cislunar Orbiters Performing Autonomous Radiometric Navigation*, the 74th International Astronautical Conference, Baku, Azerbaijan

3. **Turan, E.**, Speretta, S. & Gill, E. (2022) *Performance Analysis of Radiometric Autonomous Navigation for Lunar Satellite Network Topologies*, 11th International Workshop on Satellite Constellations and Formation Flying, Milan, Italy

2. **Turan, E.**, Speretta, S. & Gill, E. (2022) *Radiometric autonomous navigation for cislunar satellite Formations*, NAVITEC 2022, ESA Online Event

1. **Turan, E.**, Speretta, S. & Gill, E. (2022) *Autonomous Navigation Performance of Cislunar Orbits considering High Crosslink Measurement Errors*, 2022 IEEE Aerospace Conference, Montana, USA, 2022 (Peer-reviewed)

Additional Publications

Journal Papers

3. Casini, S., **Turan, E.**, Cervone, A. & Visser, P. (2023) *Combined optical line-of-sight and crosslink radiometric navigation for distributed deep-space systems*, Scientific Reports volume 13, 16253.

2. Topputo, F., Merisio, G., Cervone, A., Speretta, S., Menicucci, A., **Turan, E.**, Bertels, E., Vennekens, J., Walker, R., & More Authors (2022). *Meteoroids detection with the LUMIO lunar CubeSat*, Icarus, 389, 19 pp., 115213

1. Cervone, A., Topputo, F., Speretta, S., Menicucci, A., **Turan, E.**, Di Lizia, P., Massari, M., Costa, E., Bertels, E., & More Authors (2022) *LUMIO: A CubeSat for observing and characterizing micro-meteoroid impacts on the Lunar far side*, Acta Astronautica, 195, 309-317.

CONFERENCE PAPERS

2. Speretta, S., **Turan, E.**, Cervone, A., Menicucci, A., Topputo, F., Franzese, V., Giordano, C., Merisio, G., Di Lizia, P., & More Authors (2022). *LUMIO: A CubeSat to Monitor Micro-meteroid Impacts on the Lunar Farside* 2022 IEEE Aerospace Conference, Montana, USA, 2022 (Peer-reviewed)

1. Speretta, S., Cervone, A., Menicucci, A., **Turan, E.**, Bertels, E., Bosman, B. N., & Topputo, F. (2021). *Designing the Radio Link for a Lunar CubeSat: the LUMIO Case*, the 72nd International Astronautical Conference, Dubai, United Arab Emirates